

This item was submitted to Loughborough University as a PhD thesis by the author and is made available in the Institutional Repository (<https://dspace.lboro.ac.uk/>) under the following Creative Commons Licence conditions.



For the full text of this licence, please go to:
<http://creativecommons.org/licenses/by-nc-nd/2.5/>

BLDSC no:- DX 77879

LOUGHBOROUGH
UNIVERSITY OF TECHNOLOGY
LIBRARY

AUTHOR/FILING TITLE

KNEESHAW, J A

ACCESSION/COPY NO.

015107/02

VOL. NO.

CLASS MARK

- 5 NOV 1998

- 4 DEC 1998

1 5 JAN 1999

2 5 FEB 1999

LOAN COPY

001 5107 02



THE CORROSION BEHAVIOUR OF Fe-Cr-Ni ALLOYS
IN COMPLEX HIGH TEMPERATURE GASEOUS ATMOSPHERES
CONTAINING THE REACTANTS OXYGEN, SULPHUR
AND CARBON

by

JONATHAN ANDREW KNEESHAW, B.Sc., B.Eng.

A Doctoral Thesis submitted in partial fulfilment
of the requirements for the award of
Doctor of Philosophy
of the Loughborough University of Technology, U.K.,
based on research carried out at the
Commission of the European Communities Joint Research Centre,
Petten, Netherlands.

JUNE, 1987.

© by J. A. Kneeshaw, 1987.

Loughborough University of Technology Library	
Date	Jan 88
Class	
Acc. No.	015107/02

ABSTRACT

Title of Thesis: The corrosion behaviour of Fe-Cr-Ni Alloys in complex high temperature gaseous atmospheres containing the reactants oxygen, sulphur and carbon.

Author: J. A. Kneeshaw

A systematic in-depth study has been undertaken to establish the corrosion mechanism of a Model 25Cr-35Ni-Fe alloy and four commercial alloys HP40Nb, AISI314, HP40Al and Alloy 800H in low oxygen, high sulphur and carbon containing environments typically found in coal gasification and fluidised bed combustion processes.

A review of present knowledge of corrosion processes in purely oxidizing, sulphidizing and carburizing environments and multiple reactant carburizing/oxidizing, carburizing/sulphidizing and oxidizing/sulphidizing environments is given.

The experimental programme was designed to establish the role of sulphur on the corrosion process by studying corrosion mechanisms in a sulphur-free H_2 -7%CO-1.5% H_2O gas, a low sulphur H_2 -7%CO-1.5% H_2O -0.2% H_2S gas ($pS_2 = 10^{-8}$ bar), and a high sulphur H_2 -7%CO-1.5% H_2O -0.6% H_2S gas ($pS_2 = 10^{-8}$ bar) at 800°C. All three environments had a constant partial pressure of oxygen ($pO_2 = 10^{-21}$ bar) and carbon activity ($a_c = 0.3$).

In the sulphur-free gas the Model alloy formed a thin uniform Cr_2O_3 layer which grew at a constant parabolic rate throughout the exposure period of 0 - 5000 hours. Surface working increased the growth rate and thickness of the Cr_2O_3 layer but created a large number of cracks and pores which allowed carbon containing gaseous species to diffuse through the oxide to form carbide precipitates in the alloy substrate. Alloying additions of Si promoted the formation of an inner SiO_2 layer which reduced the corrosion rate by cutting off the outward diffusion of Cr, Mn and Fe. Alloying additions of Mn promoted the formation of an additional outer (Mn,Fe) Cr_2O_4 layer. The 3.5% Al content of the HP40Al was insufficient to form a complete Al_2O_3 layer. Alloy 800H was susceptible to localised internal oxidation.

Adding a low level of sulphur (0.2% H_2S) to the gas increased the corrosion rate of the Model alloy in the initial stages. This rate gradually slowed down before becoming parabolic after 1000 - 2000 hours. This was due to the nucleation of sulphides in addition to oxides. The oxides and sulphides grew side by side until the oxides overgrew the sulphides to form a complete Cr_2O_3 layer which cut off further ingress of sulphur from the gas. The entrapped sulphides promoted localized thickening of the oxide layer. Eventually the sulphur redistributed from the sulphides in the scale to internal sulphide precipitates in the alloy with the corrosion rate returning to that of the sulphur-free gas for the rest of the exposure period (5000 hours total).

In the commercial alloys the internal sulphide precipitates prevented the inner SiO_2 layer becoming complete. Sulphur doped the (Mn,Fe) Cr_2O_4 outer layer and the intermediate Cr_2O_3 layer formed from the spinel layer, increasing the number of cation vacancies and the growth rate of the scale. These factors caused a massive Cr depletion of the alloy substrate after several thousand hours. The internal carbides became unstable which led to a massive amount of internal attack and a dramatic increase (breakaway) in the corrosion rate. Due to its thickness and the presence of SiO_2 inner layer the external scale became susceptible to spallation. If this occurred the oxides and sulphides nucleated on the alloy surface

again but insufficient Cr was available for the oxides to overgrow the sulphides. The sulphides therefore grew to form a fast growing non-protective sulphide scale which soon led to catastrophic failure of the alloy.

Increasing the level of sulphur in the gas to 0.6% H₂S caused oxides and sulphides to nucleate on the surface, but in this² case the sulphides overgrew the oxides to form thick fast growing non-protective sulphide scales on all the alloys.

Key words: High temperature corrosion, oxidation, sulphidation, carburization, breakaway corrosion, coal gasification, fluidized bed combustion, Fe-Cr-Ni alloys.

ACKNOWLEDGEMENTS

Mr. J. F. Norton for supervision, encouragement and enthusiasm for this work.

Prof. I. A. Menzies for helpful suggestions and constructive advice particularly concerning the writing of the thesis.

S. Canetoli and F. Gandrey for assistance with the corrosion experiments and helping to assemble some of the figures.

L. Blidegn and G.D. Dickson (Laboratory Manager) for assistance with the corrosion experiments.

Ph. Glaude (X-ray diffraction), M. Moulaert (E.P.M.A.), G. von Birgelen (ESCA-AUGER), K. Schuster and P. Frampton (Metallography), D. Ross (EPMA Loughborough), F. Page (SEM Loughborough) for their structural analysis work.

J. Blom for developing and printing the photographs.

L. Brahy and D.G. Kneeshaw for typing the manuscript.

D.B. Bottomley (former senior boursier) for passing on a vast amount of knowledge in the first year of this project.

R. Edwards (Chauffeur), and M.F. Stroosnijder (Minder) for transport, protection and helpful discussions.

K. E. Beck, F. Frank, V. Guttmann, R.C. Hurst, E. Lang, A.S. McAllister, P. Tambuyser and N. Taylor for helpful discussions.

E. Bullock and R. Fordham for reading sections of the manuscript.

G. Kemeny and J.B. Marriott for assistance in dealing with administrative difficulties.

"Mr. Micron" (P. Pex) for the markers.

E.D. Hondros (Director of J.R.C. Petten) and M. Van de Voorde (Head of Materials Division) for permission to carry out the work within the Petten Laboratories.

Department DG XII of the Commission of the European Communities for financial support.

D.R. Gabe for bringing this rather unique opportunity to my attention.

DECLARATION

The original contents of this thesis are
the sole responsibility of the author.

VOLUME 1

CONTENTS

	Page
1. INTRODUCTION	1
2. REVIEW OF THE RELEVANT LITERATURE	5
2.1 Technological Requirements	5
2.2 Corrosion Processes in Single Reactant Gaseous Environments	22
2.2.1 Oxidation	22
2.2.2 Sulphidation	59
2.2.3 Carburization	83
2.3 Corrosion Processes in Multiple Reactant Gaseous Environments	98
2.3.1 Thermodynamic Considerations	98
2.3.2 Carburization/Oxidation	114
2.3.3 Carburization/Sulphidation	126
2.3.4 Sulphidation/Oxidation	132
2.4 Research Requirements Emerging from the Literature Review	172
3. EXPERIMENTAL	174
3.1 Materials and their Preparation	174
3.2 Gases and their Thermodynamic Characterisation	178
3.3 Corrosion Autoclaves and Experimental Procedures	179
3.4 Analytical Techniques	182
4. RESULTS AND THEIR INTERPRETATION	205
4.1 Oxidation Governed Regime at 800°C	206
4.1.1 Model 25Cr-35Ni-Fe Alloy	206
a) Sulphur-free gas	206
b) 0.2% H ₂ S gas	211
Summary	223
4.1.2 HP40Nb	262
a) Sulphur-free gas	263
b) 0.2% H ₂ S gas	269
Summary	277
4.1.3 AISI314	316
a) Sulphur-free gas	317
b) 0.2% H ₂ S gas	320
Summary	325

4.1.4	HP40Al	354
	a) Sulphur-free gas	355
	b) 0.2% H ₂ S gas	358
	Summary	362
4.2	Sulphidation Governed Regime at 800°C	387
4.2.1	Model 25Cr-35Ni-Fe Alloy in the 0.6% H ₂ S gas	387
4.2.2	HP40Nb in the 0.6% H ₂ S gas	401
4.2.3	HP40Al in the 0.6% H ₂ S gas	417
4.3	A Preliminary Investigation on Alloy 800H at 800°C	436
	a) Sulphur-free gas	436
	b) 0.2% H ₂ S gas	440
	c) 0.6% H ₂ S gas	445
	d) 2.0% H ₂ S gas	452
5.	DISCUSSION	482
5.1	Corrosion Mechanisms in the sulphur-free gas	482
5.2	Corrosion Mechanisms in the low sulphur 0.2% H ₂ S gas	496
5.3	Corrosion Mechanisms in the high sulphur 0.6% H ₂ S gas	510
5.4	Recommendations for Technological Applications	513
6.	CONCLUSIONS	517
7.	SUGGESTIONS FOR FURTHER WORK	520

1. INTRODUCTION

Complex environments of the type encountered in advanced coal conversion processes such as gasifiers and fluidised bed combustors can be very aggressive to metallic materials at high temperatures. These environments often contain low oxygen levels, high levels of sulphur-containing species, in addition to carburizing species. It is therefore possible for oxidation, sulphidation and carburization to occur either independently or in association with each other. Whereas oxidation can be beneficial by forming protective oxide scales on the alloy, sulphidation can lead to rapid corrosive attack with the possible catastrophic failure of components. Carburisation can aggravate the situation by affecting the formation and growth of oxide scales and by assisting the sulphidation process. There is thus a requirement for a detailed mechanistic understanding of the corrosion processes in such environments so that reliable predictions can be made for long-term materials behaviour. This should lead to better design of process plant and, in turn, safe and reliable operation in service.

The majority of the research carried out in such environments to date has been concentrated in gases which contain relatively high levels of sulphur where sulphidation processes dominate and high corrosion rates make conventional high temperature alloys unusable. Only a limited amount of work has taken place in gases containing low levels of sulphur where oxidation processes tend to dominate. In this case the initial corrosion rate is often low but after long exposure periods a transition to much more rapid rates takes place. This phenomenon is known as 'breakaway' but until now the reasons for this in these complex multi-reactant environments have not been established. The roles of carbon, surface finish and Si additions to alloys have also received little attention.

The aim of this thesis has therefore been to carry out an in-depth systematic study to establish the factors which can lead to breakaway in gases containing low levels of sulphur and to determine in detail the

role alloy composition, carbon activity and surface finish can have on this phenomenon. This was achieved by :

- (i) Selecting a simple Model 25Cr-35Ni-Fe alloy which contains sufficient chromium to form a protective Cr_2O_3 surface layer.
- (ii) Selecting two commercial alloys, HP40Nb and AISI 314, which contain silicon levels of 1.2 % and 2 % respectively and have the potential to form an additional SiO_2 layer.
- (iii) Selecting another commercial alloy, HP40Al, which contains an additional 3.5 % Al addition thereby offering the possibility to form a layer containing Al_2O_3 .
- (iv) Preparing specimens of these alloys to two standard conditions : a work-free electropolished condition and a surface worked '180 grit' condition.
- (v) Exposing these specimens to a sulphur-free H_2 -7%CO-1.5% H_2O gas at 800°C ($p_{\text{O}_2} = 10^{-21}$ bar, $a_c = 0.3$) for periods ranging from 5 minutes through to 5000 hours. This enabled the corrosion kinetics and mechanisms to be established in the absence of sulphur.
- (vi) Exposing specimens to a low sulphur containing H_2 -7%CO-1.5% H_2O -0.2% H_2S gas at 800°C ($p_{\text{O}_2} = 10^{-21}$ bar, $a_c = 0.3$, $p_{\text{S}_2} = 10^{-9}$ bar) for exposure periods ranging from 5 minutes through to 5000 hours. This determined how the presence of sulphur changed the corrosion kinetics and mechanisms and led to breakaway on some alloys after several thousand hours.
- (vii) Exposing specimens to a high sulphur containing H_2 -7%CO-1.5% H_2O -0.6% H_2S gas at 800°C ($p_{\text{O}_2} = 10^{-21}$ bar, $a_c = 0.3$, $p_{\text{S}_2} = 10^{-8}$ bar) for exposure periods ranging from 5 minutes through to 1000 hours. This illustrated the severity of corrosive attack should breakaway occur.

(viii) An additional study on Alloy 800H was also included because of its importance as a high temperature alloy with good mechanical properties.

The literature review in chapter 2 surveys the materials requirements in coal conversion processes. The review then summarizes present knowledge of high temperature corrosion processes firstly in single reactant environments and secondly in environments containing more than one reactant. A section is also included on the use of thermodynamics to aid the understanding of corrosion processes in these complex environments. Finally a summary of the research requirements emerging from the review is given.

The experimental section in chapter 3 describes the materials, gases and testing techniques used in this study. A description is also given of the various analytical techniques such as optical metallography, E.P.M.A., X-ray diffraction, ESCA-AUGER and SEM which were used to examine the corrosion products.

Chapter 4 deals with the results and their interpretation and is divided into three sections. The first section describes the corrosion behaviour of the Model 25Cr-35Ni-Fe alloy, HP40Nb, AISI 314 and HP40Al alloys in the sulphur-free gas and the gas containing a low level of sulphur (0.2 % H_2S) at 800°C. In both these gases the primary process was oxidation with in the latter case the presence of sulphur leading to breakaway on some alloys. The second section describes the corrosion processes for the Model 25Cr-35Ni-Fe alloy, HP40Nb and HP40Al in an environment containing a high level of sulphur (0.6 % H_2S) at 800°C. In this gas sulphidation processes dominated and therefore demonstrated what happens should breakaway occur. The third section gives the results of additional studies on Alloy 800H.

The corrosion mechanisms for the Model 25Cr-35Ni-Fe alloy and the role different alloying additions have on these mechanisms are discussed in

chapter 5. The factors which can lead to breakaway corrosion are defined and recommendations for technological applications are made.

The thesis is completed with a summary of the main conclusions of the study and suggestions are made for future work.

2. REVIEW OF THE RELEVANT LITERATURE

2.1. TECHNOLOGICAL REQUIREMENTS

Electricity can be obtained from burning fossil fuels (such as oil, coal and gas), nuclear energy or from so called renewable energy sources e.g. solar, wind, waves, tidal, geothermal etc. Unfortunately each of these options has certain technological and political limitations.

The world possesses finite reserves of fossil fuels, just how long these will last is a matter of considerable debate. It appears that oil reserves are the most limited with a considerable proportion of them being situated in politically sensitive regions. This means that in the short-term future the supply and price of oil may fluctuate dramatically as was demonstrated by the rapid increase in oil prices as a result of the OPEC embargo in the mid 1970's ⁽¹⁾, figure 2.1. In the long-term future the price of oil will increase as supplies dwindle. This may result in oil becoming too valuable for use in power generation and it being reserved exclusively for use as a chemical feedstock. Another possibility is to produce power from natural gas, but due to its convenience as a user fuel it is unlikely that it will play an important role in the generation of electricity. Coal, on the other hand, is much more plentiful and relatively easily accessible. However in recent years there has been mounting concern over environmental pollution, particularly acid rain produced from SO_x and NO_x emissions from coal-fired power stations. For example the Drax A and B, Ferrybridge and Eggborough power stations, providing 20 % of the U.K.'s electricity, will emit 600,000 tonnes of sulphur dioxide and 200,000 tonnes of nitrogen oxide annually ⁽²⁾. The cost of installing equipment to remove these pollutants from the flue gases would be considerable (approximately £ 150 million per power station).

In the 1950's and 1960's nuclear power was hailed as the major solution to the worlds energy problems providing a very clean, efficient and cheap method of producing electricity. Unfortunately the expense of having to satisfy numerous safety standards and extended construction times of power stations has led to it costing much more than anticipated. In addition to this, accidents and problems in disposing of

radioactive waste materials has turned public opinion against nuclear power. It now appears that the proportion of electricity produced in this way may be reduced in the future and in some countries e.g. Sweden, phased out altogether.

The long-term solution would appear to lie with renewable energy sources, but although these work very well on a small scale there are many complex technological problems associated with building such schemes on a commercial scale. For example 2000 windmills would be needed to replace one conventional coal fired power station. In addition to the considerable design, development and building costs, large schemes such as the Severn barrage, could dramatically change the social, economic and ecological structure of the areas in which they are set up.

Clearly there is no ideal solution to the problem. In the short to medium-term (next 100 years) the plentiful reserves of coal and problems associated with oil, nuclear and renewable energy sources mean that the generation of electricity from coal has a major role to play. However processes will have to be developed to satisfy environmental controls and operate more efficiently. Two coal conversion processes which have been proposed to do this involve either the gasification or combustion of coal. In general terms the efficiency of these processes can be improved by increasing the operating temperature. However this is limited by the high temperature properties of the construction materials. Mac Nab, Schulz and Black ⁽³⁾ listed these in order of importance as corrosion resistance, high temperature strength and erosion resistance. Before considering materials properties any further it is important to gain an understanding of how these processes work and where the potential materials problems lie.

Coal gasification

One method of using coal efficiently and satisfying environmental requirements is to convert it to a gas and subsequently remove the impurities from the gas prior to combustion in a gas turbine. The advantages of this are that the species which are removed such as

ammonia and hydrogen sulphide are relatively easy to extract at low temperatures with the waste products being acceptable to dispose of. Water-quenching is often used for the clean-up process. The problems associated with gasification are those of obtaining good efficiency, dealing with a large range of coals and slagging of the ash. In general, the high temperature corrosion problems are in the early part of the gasification system rather than in the coolers and clean-up systems.

There are three main types of gasifiers: -

- (a) Fixed bed gasifiers
- (b) Fluidised bed gasifiers
- (c) Entrained gasifiers

Extensive reviews of these have been published elsewhere. (4 - 7)

Figure 2.2 illustrates the processes schematically and indicates the temperatures at which they operate (7).

In fixed-bed gasifiers of which the Lurgi/British Gas slagging gasifier is an example, coal is fed in at the top of the vessel. In the bottom of the gasifier is a combustion zone where air or oxygen and steam is blown in. The gas produced during combustion gasifies the rest of the char in a zone immediately above the combustion zone. As the gas rises it dries the uncombusted coal. After this the gas has an outlet temperature of approximately 500°C and the energy is not really worth recovering.

Fluidised bed gasifiers e.g. Winkler, Synthane and Westinghouse gasifiers are similar to fluidised bed combustors (to be described later) except that they are blown with a mixture of steam and oxidant at a highly sub-stoichiometric ratio i.e. deficient in one of the species. The temperatures of the bed and the off-gas are about 900°C.

Finally in entrained gasifiers there is no bed. Pulverised coal is blown in either as a dry-feed (Shell-Koppers) or as a water-slurry (Texaco) and burnt immediately with oxygen, air and steam in the gas phase resulting in very high exit gas temperatures e.g. 1500°C.

Natesan (8) has reviewed the compositions of the gaseous atmospheres found in several medium and low Btu gasifiers. Table 2.1. gives the characteristics of five medium-Btu commercial gasifiers. From this

table it is clear that the process gas consists predominantly of H_2 , H_2O , CO , CO_2 , CH_4 and H_2S species. These compositions when characterised in terms of the major reactant activities, i.e. pO_2 and pS_2 and plotted against temperature are shown in figure 2.3. In general terms the atmospheres have typically very low partial pressures of oxygen and high partial pressures of sulphur. Of course the characteristics of the gases also depend on the type of coal used. Natesan demonstrated this in table 2.2. It is also worth comparing these values with those given by Holmes and Stringer ⁽⁶⁾ (table 2.3). From both tables 2.2 and 2.3 it is evident that not only must the partial pressures of sulphur and oxygen be taken into account but also that these gases may have a significant carbon activity.

In all these gasifiers the high temperature surfaces within the gasifier will be refractory lined. Minor components such as thermowells will be made from high temperature alloys and other components such as valves, inlet ducts, stirrers, tuyers and slag taps will also be metallic but water-cooled wherever possible. Although the product gas from the fixed bed systems is quenched to remove impurities, in the case of the fluidised bed and entrained systems, heat must be extracted prior to cleaning. Thus heat exchangers must be used which, being metallic, provide the major corrosion problem. It is clear, therefore, that there is a real need to develop and assess alloys for operation in such systems at temperatures within the approximate range 250° - $700^{\circ}C$ or even higher, which must show good resistance to the aggressive atmospheres likely to be encountered in gasification plant.

Coal combustion

Another method of converting coal to electricity efficiently, whilst satisfying environmental pollution controls, is to burn it in a fluidised bed combustor (F.B.C.). The advantages of F.B.C.'s are that excellent heat transfer from burning particles can be obtained. This means that the process can operate very efficiently at low temperatures which in turn results in a very low formation of oxides of nitrogen. Since the operating temperature remains below $950^{\circ}C$, the coal ash does

not melt eliminating slagging and fouling of components. SO_x emissions can be reduced by adding CaO to the bed to react with sulphur to form CaSO_4 . Thus no further cleaning of the waste gases is required.

Reviews of fluidised bed combustion have been carried out by Stringer⁽⁴⁾, Meadowcroft⁽⁵⁾ and Hoy⁽⁹⁾. In simple terms, the fluidised bed consists of granular materials such as ash and sand, figure 2.4. Air is blown through this mixture until the correct fluidising velocity is reached, the bed is then heated to about 500°C by gas burners. Coal is fed into the bed where it ignites, further raising the temperature. When a high enough temperature has been reached the gas burners are shut down. Normally atmospheric fluidised bed combustors (A.F.B.C) operate between 750 and 850°C . The temperature is prevented from increasing by an in-bed heat exchanger. The heat removed from the bed and that obtained from the flue gases by means of a heat exchanger in the free-board is used to evaporate the boiler water, converting it to superheated steam and in turn producing electricity. Coal and limestone are fed in and bed ash tapped off from time to time. Any fly-ash is removed in the cyclones.

A recent development of the A.F.B.C. is the pressurised fluidised bed combustor (P.F.B.C.). Increasing the pressure means that more air is contained in a given cubic capacity, hence an increased amount of oxygen can pass through the bed to support combustion and, in turn, the thermal output increased. Another advantage of the P.F.B.C. is that the exhaust gases from combustion can be expanded through a gas turbine and so increase the amount of electricity generated. P.F.B.C.'s are relatively new technology, whether they will provide a better alternative to A.F.B.C.'s in the future remains to be seen.

As in the case of coal gasification, the major materials problems are associated with the heat exchangers. Due to the nature of the process, not only does the material have to have good corrosion resistance but it must also be resistant to erosion. However whereas the analysis of the various gaseous species and their subsequent characterisation has been well documented for coal gasification, the situation for F.B.C.'s is not as clear. The reason for this would appear to be the fluctuating

nature of the conditions within the bed. Nagarajan et al⁽¹⁰⁾ measured the oxygen partial pressure within the bed using a solid state probe and found that values of $pO_2=10^{-1}$ atm to 10^{-15} atm occurred, figure 2.5. This fluctuation is due to the bed consisting of two types of phase, gas bubbles and dense solid particles. Minchener et al⁽¹¹⁾ estimated values at 850°C of $pO_2=10^{-2}$ atm. and $pS_2=10^{-27}$ atm. in the gas bubble phase and $pO_2=10^{-13}$ atm. and $pS_2=10^{-6}$ atm. in the dense phase, figure 2.6. Rademakers⁽¹²⁾ analysed the flue gases from an A.F.B.C. as containing N_2 , CO_2 and O_2 , with small amounts of CO , SO_2 and NO_x . Rademakers and Kolster⁽¹³⁾ using the data of Minchener et al⁽¹⁴⁾ produced a very useful summary figure showing that characterisation of the flue gas at 850°C is $pO_2=10^{-2}$ atm. and $pS_2 = 10^{-27}$ atm., figure 2.7. Finally it is important to note that in F.B.C's the metallic components are covered with $CaSO_4$ deposits. It has been proposed by Saunders and Spencer⁽¹⁵⁾ that these can significantly reduce pO_2 values and increase pS_2 values at the metallic surfaces bringing them closer to the conditions found in gasification environments.

Materials issues in coal conversion processes

It is clear then that in both the gasification and combustion processes, components, particularly heat exchangers, made from metallic materials will have to operate in aggressive environments at high temperatures. These atmospheres typically contain high pS_2 levels and low pO_2 levels and have a significant carbon activity. The present generation of Fe, Ni and Co-based high-temperature alloys were designed to resist corrosion in atmospheres of comparatively high oxygen activity ($pO_2 > 10^{-1}$ atm). Most of these alloys obtain their corrosion resistance from the presence of chromium which is oxidised selectively to form a compact adherent oxide scale which protects the underlying metal from attack by other reactants such as C, S and N. In some cases aluminium is used as the active element to form a protective alumina scale. In addition to Cr and/or Al, other elements such as Mo, W, Ti, Nb, Ta, V, Si and Mn are often added to control the mechanical properties of the alloy. The question now is, are these materials going to be suitable to operate in the conditions found in coal conversion processes ?

Barton, Hill and Yurkewycz⁽¹⁶⁾ reported the behaviour of test coupons exposed in 5 pilot plant gasifiers for periods of between 181 and 2909 hours. They concluded that conventional high-temperature alloys offered adequate corrosion resistance in many, but not all, gasifier locations. Danyluk and Diercks⁽¹⁷⁾ surveyed the results of 46 failure analyses carried out on components from 8 coal gasification pilot plants and concluded that corrosive attack and abnormal operating conditions were the most common causes of failure. Excessive sulphidation and/or oxidation was a common occurrence.

During the last 10 years a considerable amount of research has been undertaken to determine the behaviour of many alloys in environments typical of coal conversion processes. But before reviewing this complex situation, it is necessary to gain an understanding of the processes by which materials corrode in single-reactant atmospheres, i.e. by oxidation, sulphidation or carburization and also the thermodynamic principles associated with such processes.

Gasifier	Symbol	Bed Type	Pressure (atm)	Temp. (°C)	Room-Temperature Gas Composition (vol. %)							
					CO	CO ₂	H ₂	CH ₄	H ₂ O	H ₂ S	NH ₃	N ₂
U-Gas	■	Fluidized (Agglomerating ash)	30	1040	24.9	14.2	26.2	3.5	33.2	0.79	0.02	0.57
Westinghouse	▲	Fluidized (Agglomerating ash)	30	1000	38.9	11.9	24.2	9.3	13.0	1.36	0.75	-
Texaco	◆	Entrained	30	1550	35.6	12.8	24.8	0.07	26.2	0.11	-	0.28
Slagging Lurgi	▼	Fixed Bed	30	~1550	54.9	3.4	28.9	7.1	-	0.5	-	4.4
Shell Koppers	◆	Entrained	30	1900	71.0	1.6	27.0	<0.1	-	0.4	-	-

Table 2.1
Medium - Btu gasifier characteristics (8).

Feedstock Type	Temp. (K)	Reaction Potentials		
		PO ₂ (atm)	PS ₂ (atm)	a _C
Low-S Coal	773	1.9×10^{-26}	1.1×10^{-10}	0.143
	973	5.4×10^{-21}	2.2×10^{-9}	0.063
	1173	3.5×10^{-17}	2.2×10^{-8}	~0.002
High-S Coal	773	1.4×10^{-26}	1.5×10^{-8}	0.290
	973	4.1×10^{-21}	3.0×10^{-7}	0.223
	1173	8.9×10^{-18}	2.9×10^{-6}	0.031
SRC Product	773	1.5×10^{-26}	$<10^{-10}$	0.317
	973	4.5×10^{-21}	↓	0.249
	1173	9.5×10^{-18}	↓	0.038
H-Coal Resid (Illinois No. 6 Coal)	773	1.4×10^{-26}	1.7×10^{-9}	0.292
	973	4.1×10^{-21}	3.5×10^{-8}	0.225
	1173	9.0×10^{-18}	3.3×10^{-7}	0.031
Vacuum Resid	773	1.2×10^{-26}	8.7×10^{-9}	0.269
	973	3.6×10^{-21}	1.7×10^{-7}	0.206
	1173	7.5×10^{-18}	1.7×10^{-6}	0.028

Table 2.2

Effect of feedstock variation on oxygen and sulphur partial pressure and carbon activity in the raw product gas from oxygen-blown Texaco process at 30 atm (8).

Gasifier system	Temp. (°C)	Equilibrium Partial Pressures (bars)/ carbon activity		
		p_{O_2}	p_{S_2}	a_c
British Gas (2.3 MPa)	649	2.5×10^{-22}	1.4×10^{-7}	1.07
	816	4.0×10^{-18}	9.5×10^{-7}	1.04
	982	3.6×10^{-17}	5.0×10^{-6}	1.02
Texaco (4.2 MPa)	649	5.6×10^{-22}	1.5×10^{-7}	1.07
	816	1.0×10^{-18}	9.3×10^{-7}	1.07
	982	4.2×10^{-16}	4.7×10^{-6}	0.43

Table 2.3

Characterisation of raw exit gases from coal gasifiers (6).

THE EVOLUTION OF INTERNATIONAL OIL PRICES

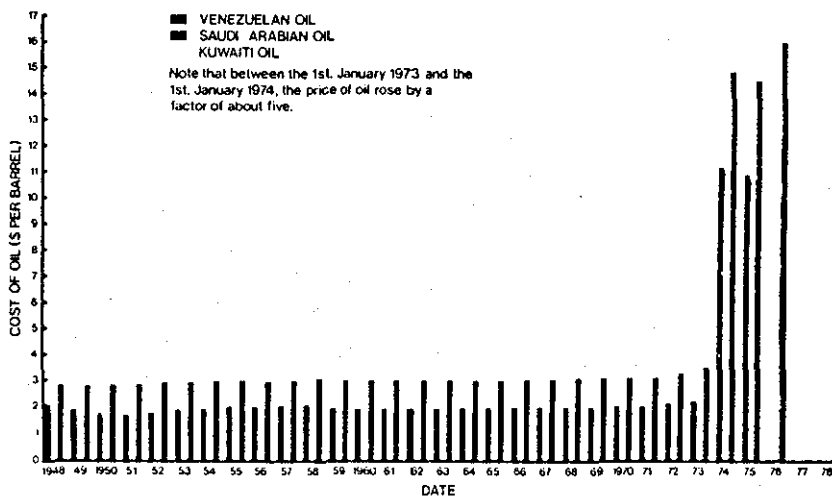


Figure 2.1

The evolution of international oil prices (1948-1976) (1).

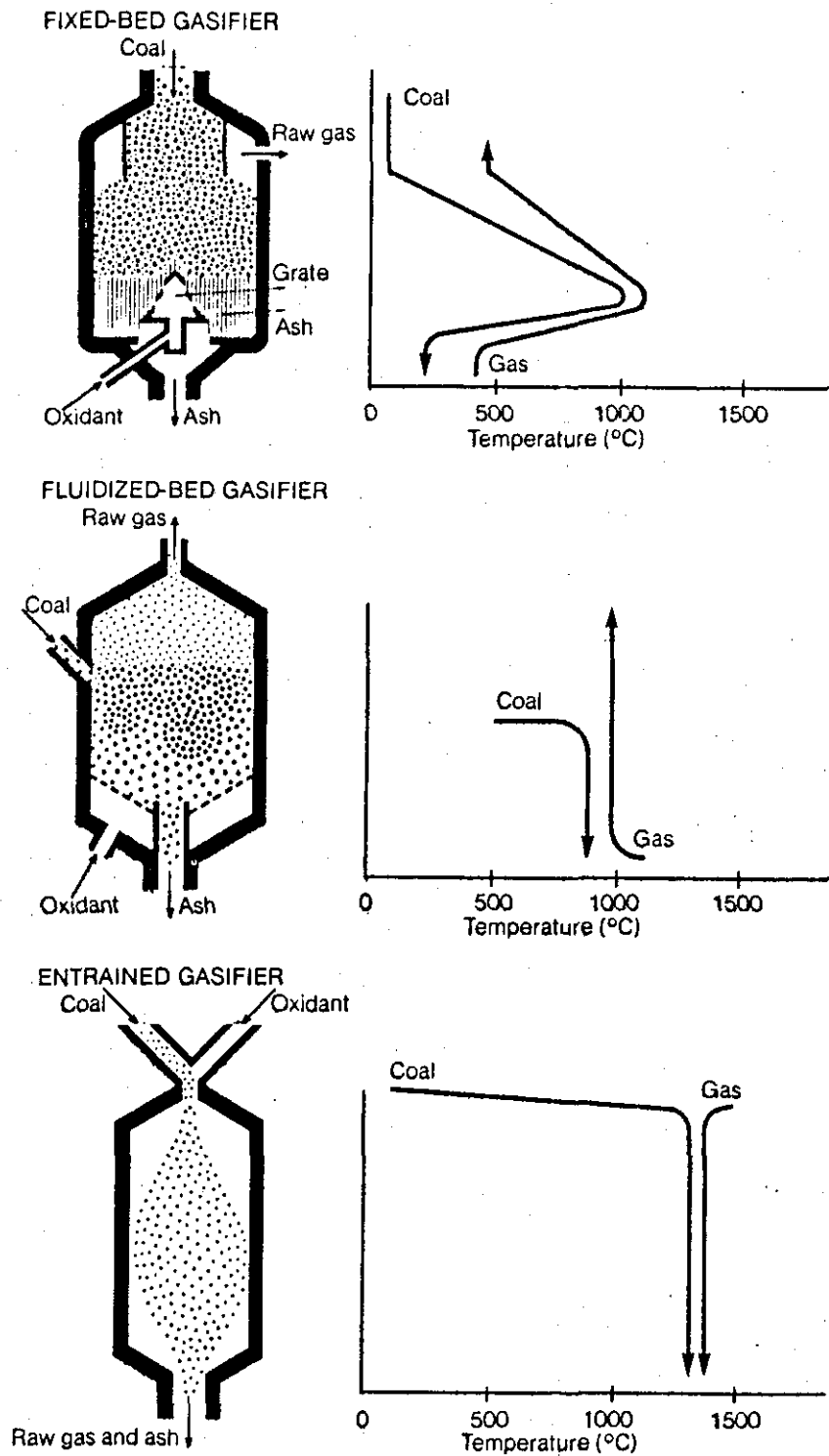


Figure 2.2
Different types of coal gasifiers and their operating temperatures (7).

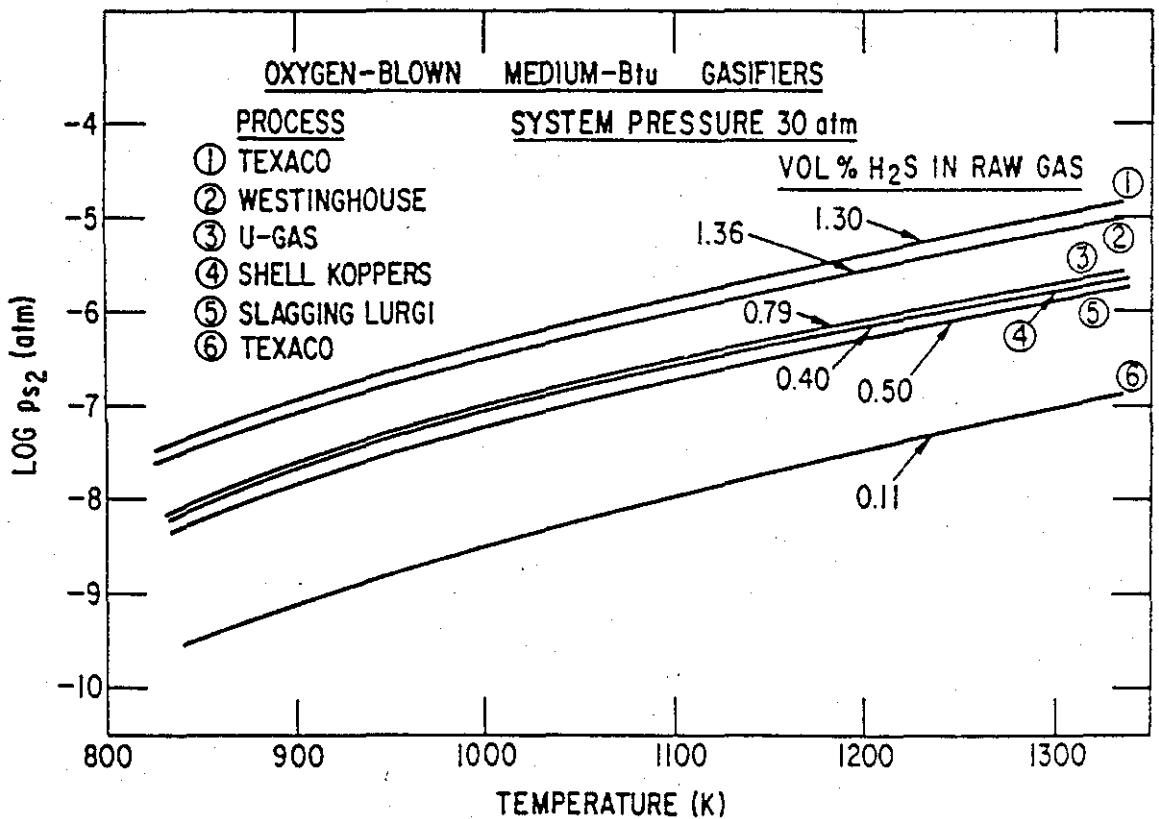
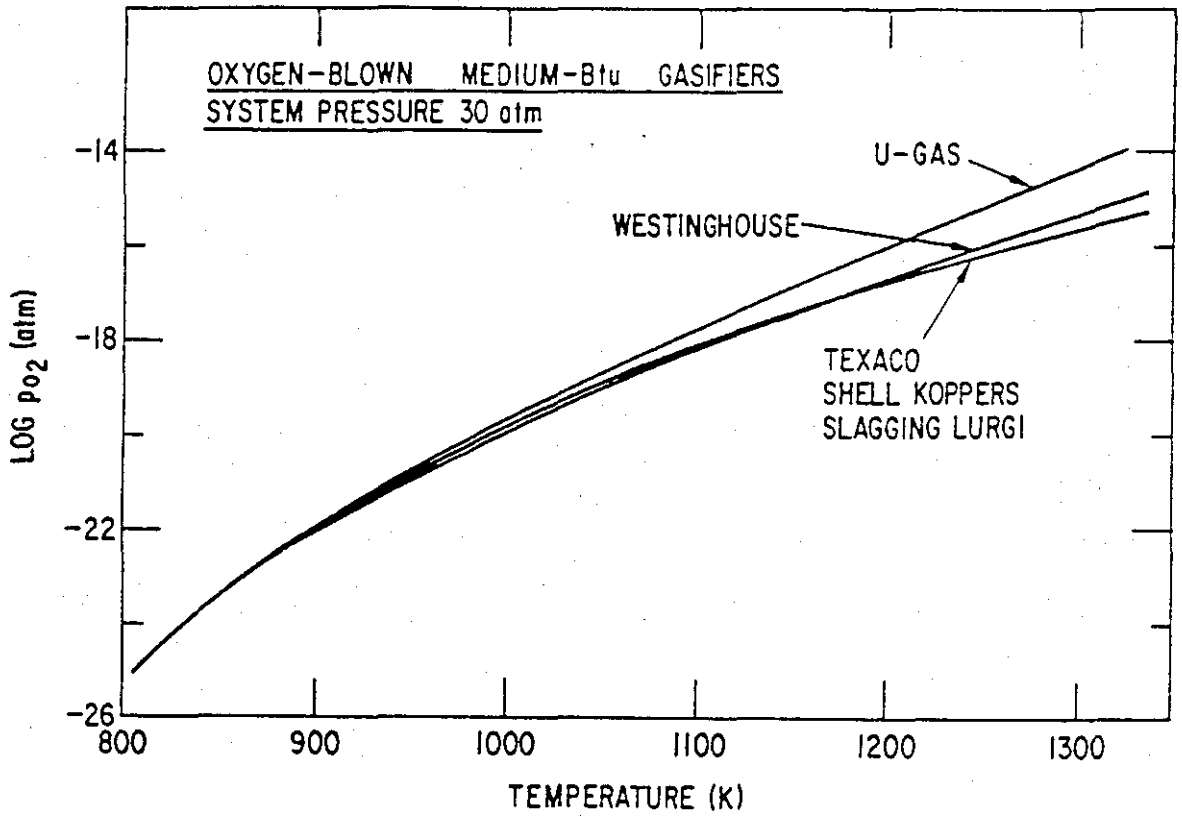


Figure 2.3

Oxygen and sulphur partial pressures as functions of temperature for several medium-Btu gasifiers (8).

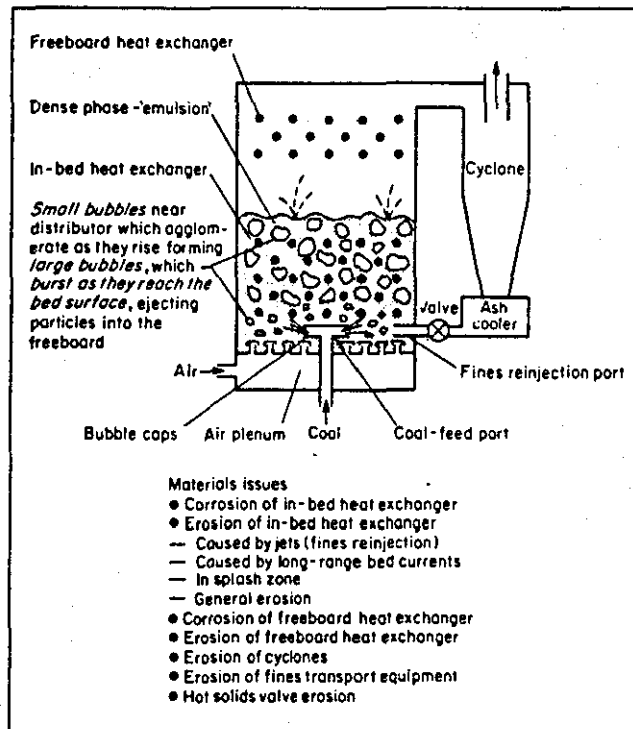


Figure 2.4

A schematic diagram of an atmospheric fluidized bed combustor, and some of the materials issues (4).

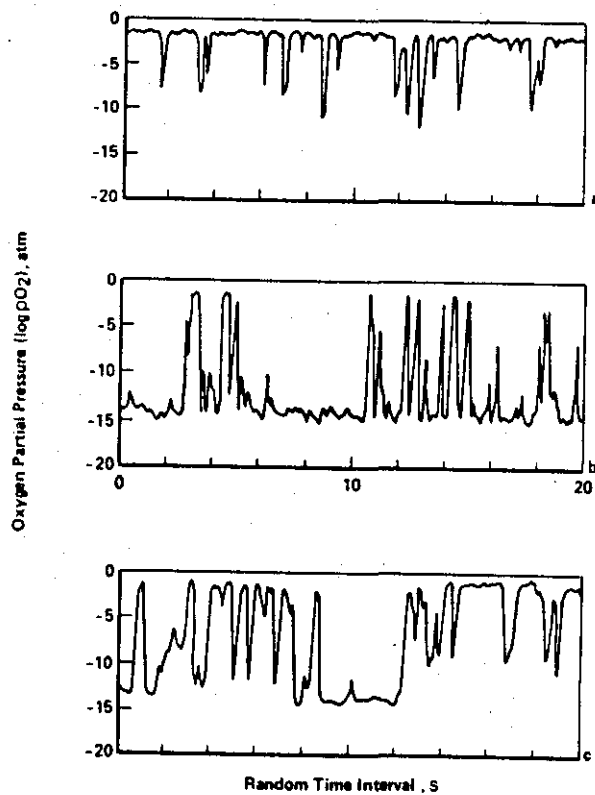


Figure 2.5

Variation of the oxygen partial pressure as a function of time in a 0.6m diameter fluidized bed combustor.

- a) Middle -bed location
- b) Bottom-bed location
- c) Near the wall location (10).

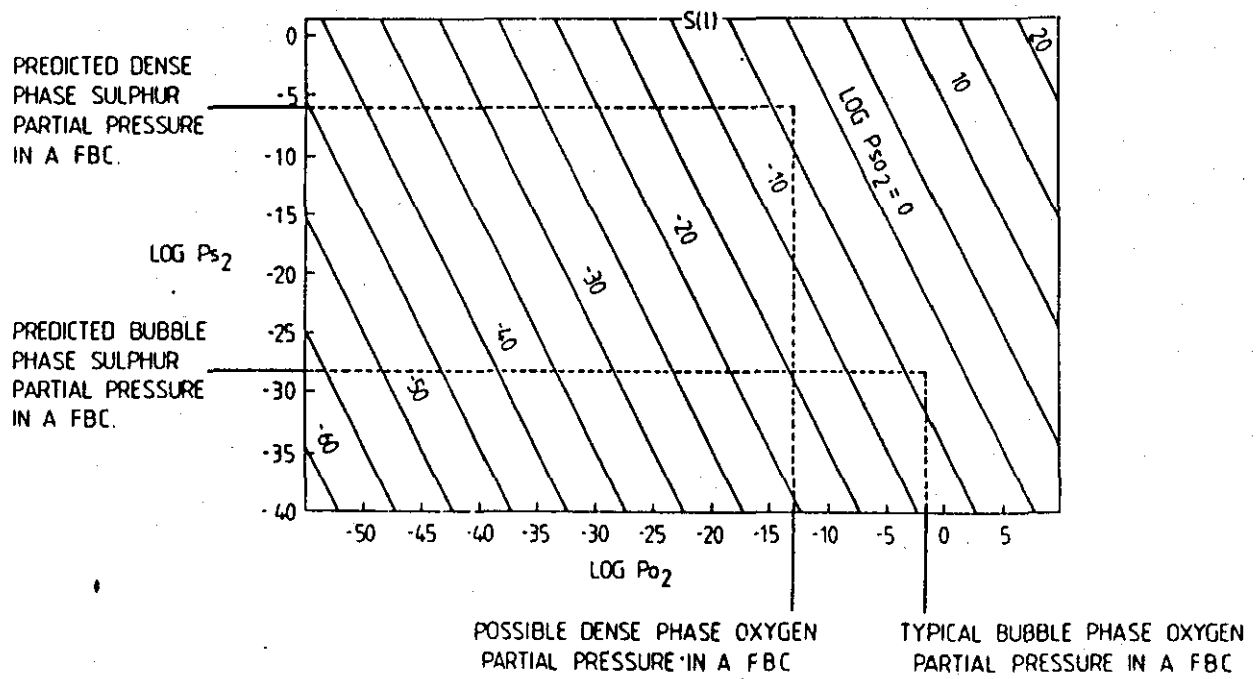


Figure 2.6
 $S_2-O_2-SO_2$ equilibria in a fluidized bed combustor at 850°C (11).

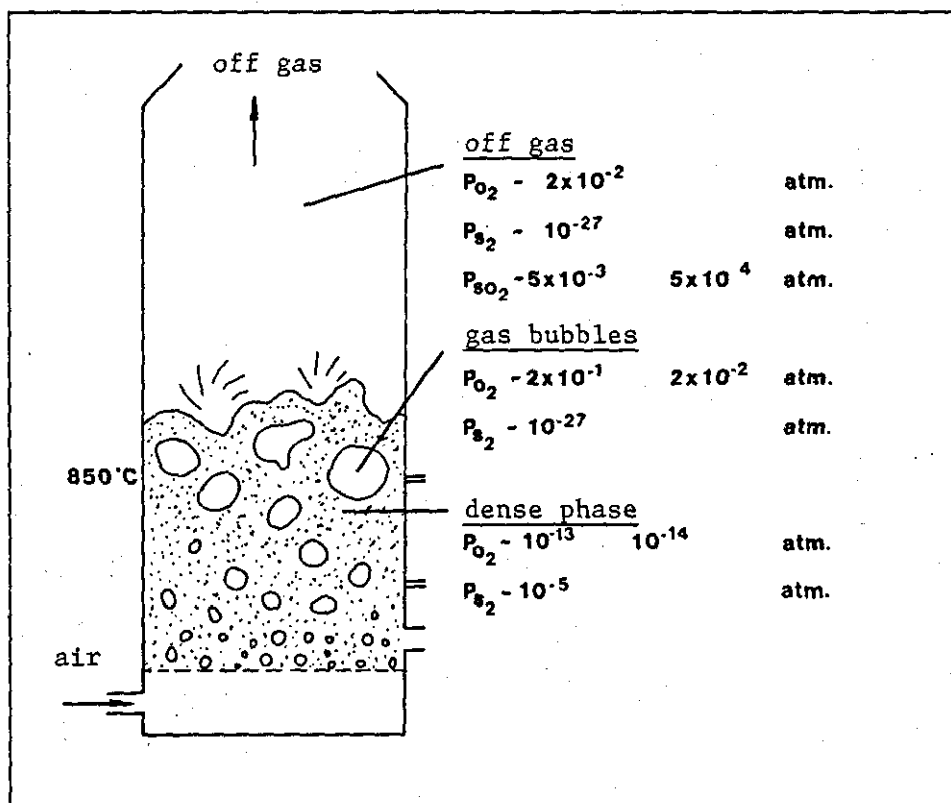


Figure 2.7

Schematic drawing of a fluidized bed combustor showing characterisation of the active species in different positions (13).

2.2. CORROSION PROCESSES IN SINGLE REACTANT GASEOUS ENVIRONMENTS

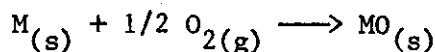
Complex environments of the type encountered in advanced coal conversion processes such as gasifiers and fluidised bed combustors can be very aggressive to metallic materials. In the previous section it was shown that these environments typically contain low oxygen levels and high levels of sulphur-containing species, in addition to carburising species. It is therefore possible for oxidation, sulphidation and carburisation to occur either independently or in association with each other. Whereas oxidation need not always be detrimental, due to the formation of protective scales under certain conditions, sulphidation can lead to rapid corrosive attack with the possible catastrophic failure of components. Carburisation is thought to be less serious but, even so, can aggravate the situation by affecting the formation and growth of oxide scales and by assisting the sulphidation process. In order to understand the behaviour of materials in these complex environments it is essential to have a clear, in-depth, understanding of the fundamental corrosion processes in terms of both the reaction kinetics and mechanisms by which materials degrade, e.g. why are oxides protective compared with sulphides? In this section a review of the oxidation, sulphidation and carburisation processes will be given with emphasis being placed on the nature, structure and composition of the various corrosion products of particular relevance to these studies.

2.2.1. Oxidation

An alloy can resist continuing attack by corrosive species if it has the potential to form a complete adherent defect-free oxide scale. In most conventional high temperature alloys this is usually achieved by the formation of a thin chromia (Cr_2O_3) layer; other oxides such as Al_2O_3 or SiO_2 are also beneficial. In general terms the main reasons why these particular elements can be relied upon to provide corrosion protection are that Cr, Al and Si each have a high affinity for oxygen and that their oxides are considered to be relatively defect-free since they do not exhibit significant deviations from stoichiometry. This, of course, confers significant benefits as it reduces ionic transport. In practice, however, oxides formed on alloys often become doped by other cations from the substrate which may result in the formation of less protective mixed oxide spinels.

Before considering the structure of potentially useful oxide systems, attention should be initially directed towards understanding conditions which are required for oxide formation to take place and secondly outlining the general stages of film formation and growth of oxide scales.

If the reaction between a pure divalent metal and a single oxidant gas such as oxygen is written :



the process of oxide formation and growth would appear to be relatively straight forward. In practice, however, the reaction may involve a number of processes and depend on a variety of factors making the oxidation mechanism much more complex than first anticipated.

The driving force for this reaction to take place is determined by the free energy changes, ΔG , and is defined as

$$\Delta G = \Sigma G \text{ products} - \Sigma G \text{ reactants} \quad (2.1)$$

If the value of ΔG is negative the reaction is likely to take place; if it is positive the reverse reaction can occur and if it is zero a state of equilibrium exists. If the product formed is the result of a reaction between a pure metal and pure oxygen, in their standard states at 1 atmosphere, the free energy change per mole of reaction product at any temperature is signified by ΔG° , (Gibbs free energy of formation).

The law of mass action states that the equilibrium constant K for a reaction is :

$$K = \frac{\text{activity of the products}}{\text{activity of the reactants}}$$

i.e.

$$K = \frac{a_{mo}}{a_m \times pO_2^{1/2}} \quad (2.2)$$

where a_{mo} = activity of the metal oxide

a_m = activity of the metal

pO_2 = partial pressure of oxygen (assuming $a_o \propto pO_2^{1/2}$)

This equilibrium constant can be related to the standard free energy by the Vant Hoff reaction isotherm.

$$\Delta G_T^\circ = -RT \ln K \quad (2.4)$$

where R is the gas constant.

Substituting for K in equation (3) gives

$$\Delta G_T^\circ = -RT \ln \frac{a_{mo}}{a_m \times pO_2^{1/2}} \quad (2.5)$$

Assuming that the metal is insoluble in the oxide the activities of the solids will be unity. Thus the standard free energy change for metal oxidation can be given by the following relationships.

$$\Delta G_T^\circ = -RT \ln K_p \quad (2.6)$$

$$\text{or } \Delta G_T^\circ = RT \ln (pO_2)^{1/2} \quad (2.7)$$

$$\text{or } pO_2^{1/2} = \frac{\exp. (\Delta G_T^\circ)}{RT} \quad (2.8)$$

where K_p = equilibrium constant for the gaseous species.

Since the equilibrium dissociation pressure of the metal oxide is equivalent to the value of pO_2 it can be determined at any given temperature if ΔG° is known. A more negative value of ΔG_T° implies a lower equilibrium dissociation pressure and therefore a greater affinity of the metal for oxygen.

A very useful way of summarising the affinity of different metals for oxygen was developed by Ellingham⁽¹⁸⁾ and modified by Richardson and Jeffes⁽¹⁹⁾, figure 2.8. In the Ellingham diagram the standard free energy of formation is plotted against the temperature. From the diagram it is clearly evident that aluminium has a higher affinity for oxygen than silicon which in turn has a higher affinity than chromium, etc. Thus if the temperature and level of oxygen are known it is possible to

predict which elements will form an oxide and which will remain inert. For example if pure chromium and nickel were placed in an environment with a p_{O_2} of 10^{-21} atm. at 800°C , the chromium would react with the oxygen to form Cr_2O_3 whereas nickel would remain inert. Incidentally, it is worth pointing out that even at these low oxygen activities the oxides of Mn, Si, Ti and Al are all stable.

Extensive accounts of oxide film formation and growth are given in the literature⁽²⁰⁻²⁴⁾. In simple terms the process is summarised by Kofstad⁽²⁵⁾ for a pure metal with single oxidant gases e.g. oxygen, figure 2.9. Initially the oxidant is adsorbed on the metallic surface. Nuclei of the reaction product then form and grow laterally to produce a continuous film which covers the whole surface. At the same time as this the oxidant dissolves in the metal substrate to an extent determined by the solubility and diffusivity of the oxidant in the metal. The continuous film separates the metal and the oxidant gas and further reaction is determined by the availability of the oxidant in the ambient atmosphere and the rate of transport of the reactants or electrons through the film. This takes place either through the lattice and/or along grain boundaries and other easy diffusion paths. As the scale thickness increases the length of diffusion path also increases with the result that the reaction rate decreases with time. In this case the kinetics (i.e. weight gain or scale thickness plotted against time) are parabolic, figure 2.10a.

$$\text{i.e.} \quad \frac{dx}{dt} = kp' \frac{1}{x} \quad (2.9)$$

$$\text{or} \quad x^2 = 2 Kp't + cp = Kpt + cp \quad (2.10)$$

where x = oxide thickness or weight gain per unit surface area of the metal

t = time

cp = integration constant

Kp' = parabolic rate constant

Stresses may also be built up in the scale and the metal substrate. This may result in plastic deformation or cracking of the scale. If frequent cracking takes place the scale loses its protective qualities and the

reaction rate is governed by diffusion through a thin oxide layer (of approximate constant thickness) adjacent to the metal surface. This could well be typified by linear kinetics, figure 2.10a.

$$\text{i.e.} \quad \frac{dx}{dt} = K_1 \quad (2.11)$$

$$\text{or} \quad x = K_1 t + C_1 \quad (2.12)$$

where K_1 = linear rate constant

C_1 = integration constant

Figure 3a also shows a curve illustrating logarithmic kinetics where rapid initial oxide formation is followed by a very low rate of reaction

$$\text{i.e.} \quad x = k \log (at + 1) \quad (2.13)$$

where k = logarithmic rate constant

a = dimensional factor.

Logarithmic kinetics usually occur at low temperatures : typically below 400°C. Many explanations for this type of behaviour have been proposed^(20, 26). These have been based on the adsorption of reactive species, the effects of electric fields developed across oxide layers, quantum-mechanical tunnelling of electrons through thin scales, progressive blocking of low resistance diffusion paths, non-isothermal conditions in the oxide layer and nucleation and growth processes. Clearly this particular type of oxidation is complex and perhaps not fully understood, but, as already mentioned, since it mainly applies to low temperature processes and is outside the bounds of this study, it will be not considered further.

In practice, however, several processes may take place simultaneously and the kinetics may be a function of parabolic, linear and logarithmic processes. A schematic diagram is shown in figure 2.10b where in the initial stages (OA) logarithmic kinetics predominate, followed by steady state parabolic kinetics (AB) and finally "breakaway" linear behaviour (BC).

Before considering ionic transport mechanisms through oxides, it is worthwhile outlining possible oxide defect structures. There are two main types of defect in a strongly stoichiometric ionic oxide. These are known as Schottky defects and Frenkel defects. A crystal with Schottky disorder (figure 2.11) contains equal concentrations of anion and cation vacancies (V_o and V_m). This type of disorder thus involves defects in both the anion and cation sub-lattices. In Frenkel disorder the effects are limited to either the cation or the anion lattice, so that a Frenkel defect pair consists of either a vacancy and an interstitial anion ($V_o + O_i$) or a vacancy and an interstitial cation ($V_m + M_i$), figure 2.12.

In order for the reaction to proceed, neutral atoms, or ions and electrons must migrate within the oxide. This is shown schematically in figure 2.13. If scale growth is taking place due to cation migration, scale formation will take place at the scale-gas interface (figure 2.13a). Conversely if scale growth is taking place by anion migration the scale will grow at the metal-scale interface, figure 2.13b. In order to explain simultaneous migration of ions and electrons it is necessary to assume that oxides are non-stoichiometric compounds i.e. that the metal to non-metal atom ratio is not exactly that given by the chemical formula.

If the oxide contains more metal than oxygen it can be regarded as an n-type semiconductor. There are two ways of considering this structure, either that the oxide contains an excess of metal ions or is deficient in oxygen ions. An example of the former case is zinc oxide (ZnO), figure 2.14. The excess metal is incorporated into the structure by Zn^{2+} ions occupying interstitial sites. The resulting excess of electrons allows conduction to take place. Alternatively if the anion lattice is deficient in oxygen atoms, figure 2.15, a vacancy having a double positive charge will be created with again an excess of electrons in the conductance band.

On the other hand if the oxide is deficient in metal or has an excess of non-metal it can be regarded as a p-type semiconductor. In this case conduction is obtained from the formation of vacancies in the cation lattice together with electron holes. Electron holes are formed when cations can exist in several valence states. This is typical for

transition metals elements. One example is NiO, figure 2.16. By virtue of the energetically close valence states of the cation it is relatively easy for an electron to transfer from Ni^{2+} to Ni^{3+} . The Ni^{3+} site offers a low energy position for an electron and is called an "electron hole". Figure 2.16 shows the process of NiO interacting with oxygen to form cation vacancies and electron holes. In step (b) the oxygen chemisorbs by attracting an electron from the Ni^{2+} site thus forming Ni^{3+} or hole. In step (c) the chemisorbed oxygen is fully ionised forming another hole, and Ni^{2+} goes to the surface to partner the O^{2-} resulting in a vacancy in the cation sub-lattice.

Ideal model

Having considered the basic principles of oxide film formation and growth, the mechanism by which reactants are transported through oxides can be examined in greater depth. In the ideal case, the scale is considered to be completely dense and transport takes place by lattice (volume) diffusion only. This is the basis of Wagner's theory of oxidation,⁽²⁰⁻²⁵⁾ which assumes that the lattice diffusion of the reacting ions or transport of electrons through the scale (figure 2.17a) is the rate determining process in the oxidation reaction. It also assumes that thermodynamic equilibria are established at the metal/oxide and oxide/-gas interfaces. The driving force behind the reaction is the free energy change of the reaction between the metal and the oxidant to form the reaction product. It is also possible for the migrating species to be considered in terms of lattice and electronic defects (figure 2.17b) i.e. interstitial metal ions and vacancies and electron holes and electrons. The growth of the scale in such a case is parabolic with time.

This is the ideal model, in practice not many oxide systems conform to this model. One exception is the oxidation of cobalt which has a relatively large degree of non-stoichiometry (concentration of point defects). This minimises the importance of impurity effects and the relative importance of grain boundary diffusion etc. Since Co diffusion is much faster than oxygen diffusion⁽²⁷⁾, it is this which determines the rate of the reaction.

This is also the case in other systems. There are few cases where the diffusion of oxygen throughout the entire scale is rate determining⁽²⁷⁾, although it is worth noting at this point that there is a lack of diffusion data of oxygen in oxides.

Having considered the ideal model the formation and growth characteristics of pure oxides relevant to this study, namely Cr_2O_3 , Al_2O_3 and SiO_2 , can be examined.

Oxidation of chromium

Whereas the oxidation of elements such as Co and Ni is relatively well understood the situation for Cr is not as clear. This is rather surprising in view of the extensive studies carried out on this oxide and also since most alloys rely on the formation of a Cr_2O_3 scale for protection against corrosive species. The reason for this would appear to be the complexity of the oxide and experimental difficulties in obtaining the necessary data. However, in a recent extensive review Lillerud and Kofstad⁽²⁸⁻³²⁾ summarised the present knowledge on Cr_2O_3 and carried out experiments to help clarify the growth mechanism, defect structure and transport properties under various conditions.

Cr_2O_3 is the only oxide of chromium that is thermodynamically stable as a solid phase at high temperatures. It has a corundum (Al_2O_3) type crystallographic structure and can be considered to consist of hexagonally close-packed oxygen ions where the chromium ions occupy two-thirds of the octohedral sites^(27,33), figure 2.18. The laws governing the kinetics of Cr_2O_3 -formation show a temperature-dependence. Above 700°C the kinetics are generally parabolic; rate constants obtained by various workers are summarised in figure 2.19⁽²⁸⁾. There appears to be a considerable scatter in the results, i.e. up to 4 orders of magnitude.

This is probably due to different methods of surface preparation, impurities in the Cr metal and differences in experimental procedures. Below 700°C the reaction behaviour changes. Young and Cohen⁽⁴²⁾ found that oxidation in the temperature range 300°C to 600°C involved an initial

logarithmic stage followed by parabolic oxidation. The logarithmic rate constant exhibited a positive pressure dependence while the parabolic rate constant had a negative pressure dependence i.e. this rate constant increased with decreasing oxygen pressure. Such a pressure dependence cannot be explained in terms of a reaction governed by homogeneous diffusion through the scale (e.g. Wagner mechanism). Therefore a model was put forward where it was assumed that the concentration of adsorbed oxygen species was determined by an adsorption equilibrium on the compact areas of the oxide scale, whereas most of the growth occurred at areas with thicker porous oxide.

Lillerud and Kofstad⁽²⁸⁾ studied the effect of different oxygen pressures on the oxidation of chromium in the temperature range 800-1100°C. They found that at a oxygen pressure of 10^5 Pa (1 atm.) a major change in kinetics took place between 800 and 900°C. At 800°C the initial kinetics were approximately logarithmic and at 900°C and above approximately linear, due to increases in the scale thickness promoting cracking of the oxide. When the oxygen pressure was reduced at 800°C the initial rapid oxidation period was reduced, figure 13. However after extended oxidation periods the oxidation kinetics at the low oxygen pressures tended to become almost linear. They also found that as the oxygen pressure decreased the ability of the Cr_2O_3 scale to deform plastically increased. Lillerud and Kofstad concluded that volume diffusion and transport along cracks and grain boundaries all contributed to the growth of Cr_2O_3 scales.

In a subsequent paper Kofstad and Lillerud⁽²⁹⁾ took this work further and suggested a defect structure model for Cr_2O_3 , figure 2.21. In this model two types of structure are proposed.

- (1) At near atmosphere oxygen pressures, Cr_2O_3 can be considered to be an intrinsic "p-type" electronic semiconductor i.e. the oxide can be considered deficient in metal or have an excess of oxygen with the result that current will be carried by electron holes.

- (ii) At oxygen pressures near the decomposition pressure of Cr_2O_3 the oxide has excess metal and is deficient in oxygen. The predominant point defects in this case are chromium interstitials and the minority defects are probably oxygen vacancies with the current carried by electrons ("n-type" semi-conductor).

In a scale the oxygen partial pressure will change from the decomposition pressure of Cr_2O_3 at the metal/scale interface to the oxygen partial pressure in the gas at the scale/gas interface. Thus it is quite possible for a Cr_2O_3 oxide scale to consist of an inner "n-type" region and an outer "p-type" region. It is not clear from Kofstad's and Lillerud's work⁽²⁹⁾ where the cross-over point from n to p type behaviour occurs. Young et al⁽⁴³⁾ investigated this and found that this point was approximately 10^{-8} atm. at 1300K and 5×10^{-6} atm. at 1520K. This would appear to be in relatively good agreement with the results of Matsui and Naito⁽⁴⁴⁾.

To add weight to Kofstad and Lillerud's model, Hindam and Whittle^(45,46) calculated from diffusion data that for the n type, chromium interstitial behaviour to be true at low $p\text{O}_2$'s the rate constant should be independent of $p\text{O}_2$. Experiments were carried out at low $p\text{O}_2$'s which confirmed this, figure 2.22.

Again it must be emphasised that in addition to lattice diffusion, scale growth by diffusion of both Cr and O along grain boundaries and other easy, diffusion paths cannot be neglected^(30, 39, 42, 47).

Short circuit diffusion and other factors

Atkinson⁽⁴⁸⁾ and Hughes et al.⁽⁴⁹⁾ compared the rate constants obtained by various workers with theoretical values calculated from lattice diffusion data for the oxidation of Ni (figure 2.23) and Cr (figure 2.24). In general the experimental results were higher than the theoretical ones, particularly at low temperatures. In the case of the oxidation of nickel the discrepancy between the oxidation rates has been quantitatively proved by Atkinson et al.^(51,52) to be due to grain boundary diffusion of Ni cations through NiO. Atkinson⁽⁴⁸⁾ also lists a considerable amount of supporting qualitative evidence for short circuit diffusion in NiO.

Unfortunately in the case of the oxidation of chromium there is no direct quantitative evidence to support the theory that grain boundary diffusion is rate controlling. Grain boundary diffusion data does not exist for this system, but grain boundary diffusion is thought to be faster than lattice diffusion. Diffusion rates for single crystal Cr_2O_3 have been found to be much lower than those in polycrystalline Cr_2O_3 ⁽⁵²⁾. Atkinson⁽⁴⁸⁾ lists some circumstantial evidence for diffusion along high-angle grain boundaries controlling the rate of oxidation viz.

- (i) Atkinson and Taylor⁽⁵²⁾ found that Cr diffusion via dislocations in low-angle grain boundaries is too slow to account for the observed oxidation rates.
- (ii) Caplan and Sproule⁽³⁹⁾ observed oxidation-rate anisotropy on etched Cr (figure 2.25). The polycrystalline oxide is thought to grow by fast outward, grain-boundary diffusion and the thin monocrystalline oxide by much slower outward lattice diffusion.
- (iii) Lillerud and Kofstad⁽²⁸⁾ found that in the initial stages of oxidation at 800°C and 1 atm. $p\text{O}_2$ the kinetics were logarithmic. This behaviour was related to grain growth, with in the initial stages transport along a large number of short circuit diffusion paths taking place. After subsequent grain growth the concentration of diffusion paths gradually decreased with time lowering the kinetics rate.
- (iv) Kofstad and Lillerud⁽²⁹⁾ vacuum annealed oxidised chromium specimens at 1000 and 1100°C. The resultant weight loss was thought to be due to Cr evaporation after Cr transport through the scale by lattice and short circuit diffusion. However the rate of this weight loss decreased with time and was attributed to the increased grain size reducing the number of short circuit diffusion paths. Perhaps another factor which should also be noted is that the length and complexity of the short circuit diffusion path as well as their concentration are important.
- (v) Stress generation in Cr_2O_3 scales causes wrinkling, buckling and cracking. One proposed mechanism for stress generation is that of

Rhines and Wolf⁽⁵³⁾ which requires countercurrent diffusion of ions with oxygen anions moving inwards via grain boundaries reacting with Cr cations moving outwards through the lattice. If this mechanism were proved the observation would provide evidence for the role of grain boundaries. However it seems strange that this mechanism does not take into account the possibility of Cr cations also diffusing along grain boundaries.

A variant on the theme of this last point is the mechanism proposed by Brückman⁽⁵⁴⁾ and Mrowec⁽⁵⁵⁾ and refined by Kofstad⁽²⁵⁾ for the formation of microchannels in oxide scales.

This is shown schematically in figure 2.26. In the first stage, the scale grows by outward cation diffusion resulting in voids at the scale metal interface. Grain boundary diffusion of cations is assumed to be much faster than lattice diffusion as a result of this the grain boundaries above the voids open up and gradually form a microchannel. This channel will remain open as long as the chemical potential of the oxygen is the same at the surface of the channel as in the neighbouring lattice. If this is the case oxygen can penetrate down the channel.

In a more recent paper Kofstad⁽⁵⁶⁾ describes this model as unsatisfactory because of the following stated reasons :

- (i) There are doubts about how the channels can remain open, because as O_2 molecules move down the channel the oxygen potential should increase, this combined with presumably metal atoms diffusing along the inner surface of the channel should lead to oxide formation in or close to the channel hence blocking it up. In the opinion of the author of this review this is unlikely, since if a large void remains at the bottom of the channel cation transport across it will be very difficult.
- (ii) The model assumes that grain boundary diffusion is much faster than lattice diffusion but even so the results strongly suggest that the gaseous penetration takes place through relatively thick growing scales in which lattice diffusion predominates.

- (iii) The model cannot be applied to scales growing predominantly by inward oxygen diffusion e.g. alumina or zirconia.

Kofstad proposes that the development of the porosity and channels is a result of plastic deformation and creep in the scales caused by growth stresses and attempts to relate his theory to the results and observations obtained by himself and his co-worker Lillerud for the oxidation of chromium^(28-32, 57). Regretably the considerable amount of contradiction both within and between these papers make it almost impossible to formulate any coherent theory and mechanism. There appears to be a considerable amount of speculation which is not confirmed by experimental evidence. (In fairness to Kofstad it would appear from the literature that the key reference to which he refers has not yet been published⁽⁵⁸⁾).

In summary from the literature it would appear that although the growth of oxides such as Cr_2O_3 is predominantly due to outward cation lattice diffusion, it is clear that cationic and anionic diffusion takes place simultaneously via grain boundaries and other short circuit diffusion paths. However the exact mechanisms for this even in the case of a pure metal and a single oxidant are not yet fully understood. It is extremely unlikely that one universal mechanism could be developed to cover the whole of this aspect. Obviously many factors have to be taken into account when considering short circuit diffusion, such as grain size and subsequent grain growth, temperature, oxygen partial pressure, stresses in the oxide, the ability of the oxide to deform plastically and impurity-enrichment at grain boundaries.

Chromia formation on alloys

The considerations so far have only been relevant to the structure and growth of Cr_2O_3 during the oxidation of pure Cr. It is of course important to compare Cr_2O_3 formation on alloys with that observed on the pure metal in order to establish and quantify what differences, if any, occur.

Before considering the formation of Cr_2O_3 on alloys it is worthwhile outlining the general stages of oxidation. There are three generally accepted stages in the oxidation of an alloy⁽⁵⁹⁾, figure 2.27. Initially a transient stage occurs, characterised by the simultaneous formation of the oxides of every active component. This is followed by a steady state stage coinciding with the development of a protective film and governed by the continued growth of this continuous layer. Finally "breakaway" oxidation may occur in which rapid oxidation takes place, often initiated by some mechanical influences such as scale adherence/spallation, void formation, thermal/mechanical stressing.

In-depth accounts of the transient oxidation of alloys have been given by Chattopadhyay and Wood⁽⁶⁰⁾ and Wood⁽⁶¹⁾. For the purpose of this review two examples are given to illustrate typical series of events which could take place before steady state scaling is reached.

In the first example a Ni based alloy containing 20-40 % Cr is exposed to pure oxygen at 1 atm. Initially both NiO and Cr_2O_3 nucleate on the surface figure 2.28a. The NiO nuclei then grow at a faster rate, figure 2.28b, and eventually overgrow the Cr_2O_3 , figure 2.28c. Meanwhile the Cr_2O_3 particles grow laterally to form a complete inner layer, figure 2.28d. A displacement reaction also takes place resulting in the formation of a NiCr_2O_4 layer between the outer NiO layer and the inner Cr_2O_3 layer.

In the second example a Ni based alloy containing only 5 % Cr is exposed to the same conditions. Again both NiO and Cr_2O_3 nucleate on the alloy surface (figure 2.28f) with subsequently the NiO overgrowing the Cr_2O_3 , figure 2.28h. In this case the Cr level is too low to form a complete inner Cr_2O_3 layer. Therefore Cr_2O_3 particles are formed inside the alloy by diffusion of atomic oxygen supplied by partial dissociation of NiO, figure 2.28i. As the scale thickens these are incorporated into the inner layer. Thus the steady state structure consists of predominantly NiO containing NiCr_2O_4 and Cr_2O_3 particles and internal Cr_2O_3 particles in the alloy substrate, figure 2.28j.

These two examples illustrate how the alloy composition can determine the formation of two very different oxide structure in the final steady state scale.

Wood⁽⁶¹⁾ has outlined several other factors which can also influence the final structure of the steady state scale :

- (i) The standard free energies of formation which determine which oxides form.
- (ii) The alloy interdiffusion coefficient which determines how rapidly the oxide forming element can be replenished from the alloy substrate.
- (iii) The oxygen solubility and diffusivity in the alloy which determine whether an internal or external oxide forms.
- (iv) The growth rates of the component oxides.
- (v) The oxidation conditions such as temperature and oxygen pressure.

Wood proposed that it is possible for up to eight steady state structures to develop for a simple binary alloy AB where B is the more reactive element, figure 2.29.

Hindam and Whittle⁽⁴⁵⁾ compared the kinetics of formation of Cr_2O_3 on metals and on alloys in the steady state region, figure 2.30. Two main conclusions can be made from this comparison,

- (i) the scatter band is only two orders of magnitude for alloys compared with four for pure metals and
- (ii) there is no obvious trend as to whether Cr_2O_3 forms at a faster or slower rate on alloys. The main problem with this comparison is that most of the data was obtained under different experimental conditions.

In an attempt to clarify the situation, Hindam and Whittle⁽⁴⁶⁾ carried out experiments on pure chromium and alloys under identical conditions of low $p\text{O}_2$'s at 1000°C and found that alloys tended to oxidise at a slower rate than pure chromium. This is due to the Cr activity at the alloy/oxide interface being less than unity with the result that the effective oxygen pressure there is higher than when pure Cr is the substrate. This would appear to agree with the results of Giggins and Pettit⁽⁶²⁾ who found that the rate constant tended to increase with chromium content of the alloy.

Breakaway has been demonstrated by Whittle and Wood^(62,64) and is illustrated for an iron-chromium alloy in figure 2.31. If the scale is damaged or lost due to mechanical or thermally induced spalling the gas reacts with the Cr depleted alloy substrate to form non-protective Fe-Cr spinel nodules. These nodules continue to grow until the alloy is consumed or a new chromium-rich protective layer is developed at the base of the nodule.

Stress in the oxide

As already mentioned, stresses can be generated during the oxidation process. As corrosion resistance relies not only upon the formation of a protective scale but also on the continuing presence of such an oxide, stress generation and relief in oxide films and the ability of an alloy to reform a protective scale, if stress-induced spalling or cracking occurs, are important considerations in high temperature oxidation. The subject has been discussed in reviews by Douglass⁽⁶⁵⁾, Stringer⁽⁶⁶⁾, Hancock and Hurst⁽⁶⁷⁾, and Baxter and Natesan⁽⁶⁸⁾. Stresses can be set up due to growth or by differential thermal expansion or contraction between the substrate and the scale.

There are various causes of growth stresses viz:

- (i) volume differences between the oxide and the metal substrate
- (ii) epitaxial stresses
- (iii) compositional changes in the alloy or scale
- (iv) point defect stresses
- (v) oxide formation within the scale
- (vi) recrystallisation stresses
- (vii) specimen geometry

Dealing with each of these in turn.

- (1) Volume differences between the oxide and the metal.

The volume occupied by an oxide is usually different to that which was occupied by the metal consumed in its formation. Work by Pilling and Bedworth⁽⁶⁹⁾ related the sign of the stress in the

oxide to the oxide/metal volume ratio, known as the Pilling Bedworth Ratio : P.B.R.

$$\text{P.B.R.} = \frac{V \text{ (per metal ion in oxide)}}{V \text{ (per metal atom in metal)}}$$

A list of P.B.R.'s for several oxides is given in table 2.4. If the ratio < 1 the scale is in tension and > 1 in compression. As can be seen in table 1 most oxides are usually in compression (e.g. $\text{Cr}_2\text{O}_3 = 2,07$ and $\text{Al}_2\text{O}_3 = 1,28$). In general oxides in tension are not protective. This mechanism really can only be applied to oxides growing by anion inward diffusion as scales formed at the oxide/gas interface should not develop stresses due to volume differences between the metal and the oxide.

(ii) Epitaxial stresses.

In the initial stages of oxidation the nuclei that form will have an epitaxial relationship with the substrate. Stresses will thus be caused by the metal and the oxide having different lattice parameters. As the scale thickens the epitaxial constraints reduce and hence the stress from this source.

(iii) Compositional changes in the alloy or scale.

As the scale grows the composition of the alloy substrate will change as it becomes depleted in one or more of the active species forming the oxide. The composition of the oxide itself may change due to different diffusion rates of different species, with the result that both the lattice parameters of the oxide and substrate may change resulting in stresses being set up.

(iv) Point defect stresses

It is possible for stresses to be built up in oxides having large deviations from stoichiometry due to point defect gradients and hence lattice parameter differences across the scale. The same effect can also apply for the substrate.

(v) Oxide formation within the scale.

Compressive stresses can be set up within the scale due to the inward migration of oxygen along grain boundaries resulting in the formation of oxide at sites in the scale. This mechanism has been proposed by Rhines and Wolf⁽⁵³⁾.

(vi) Recrystallisation stresses.

Jaenicke et al⁽⁷⁰⁾ have suggested that recrystallisation within the oxide scale or in the substrate can be a cause of stress. However it is probable that recrystallisation should release stresses rather than create them. Horibe and Nakayama⁽⁷¹⁾ found that grain growth in fine grained Fe-Cr alloys disrupted Cr_2O_3 scales resulting in the formation of iron rich oxides whereas oxidation of a coarse grained alloy produced a continuous layer of Cr_2O_3 .

(vii) Specimen geometry.

Perhaps one of the most important factors to take into account when considering growth-stresses is specimen geometry. Hancock and Hurst⁽⁶⁷⁾ divided the various possibilities into four categories, figure 2.32 :

- (a) cationic oxidation on convex surfaces
- (b) anionic oxidation on convex surfaces
- (c) cationic oxidation on concave surfaces and
- (d) anionic oxidation on concave surfaces.

In the first case when the oxide grows on a convex surface by cation migration, figure 2.32a, the metal retreats as the oxide forms at the scale/gas interface. If the scale remains adherent, compressive stresses are generated in the oxide as it tries to follow the metal surface. If the scale forms on a convex surface due to anion migration (figure 2.32b) the continued scale formation at the scale/metal interface can result in tensile

stress development in the outer regions of the scale. When an oxide forms on concave surfaces by cation migration, figure 2.32c, the initial oxide probably forms in compression but the geometry can result in a decrease and eventual change in sign of this stress so that at longer times, the scale at the metal oxide interface will be in tension. Finally, for oxide formation on concave surfaces by anion migration, figure 2.32d, the initial scale will form in compression and the stress increase as growth takes place.

Having considered stresses due to growth, stresses due to differences in thermal expansion coefficients between the metal and the oxide cannot be ignored. Table 2.5 gives thermal expansion coefficients for oxides and metals. In general the coefficient of thermal expansion is smaller for the oxide with the result that compressive stresses will develop during cooling. Since the bonding of the metal to the oxide is generally weaker than the cohesive bonding in either the metal or the scale, thermal stress can result in spalling of the oxide from the metal.

Oxide	Oxide-metal volume ratio
K ₂ O	0.45
MgO	0.81
Na ₂ O	0.97
Al ₂ O ₃	1.28
ThO ₂	1.30
ZrO ₂	1.56
Cu ₂ O	1.64
NiO	1.65
FeO (on α -Fe)	1.68
TiO ₂	1.70-1.78
CoO	1.86
Cr ₂ O ₃	2.07
Fe ₃ O ₄ (on α -Fe)	2.10
Fe ₂ O ₃ (on α -Fe)	2.14
Ta ₂ O ₅	2.50
Nb ₂ O ₅	2.68
V ₂ O ₅	3.19
WO ₃	3.30

Table 2.4
Oxide-metal volume ratios of some common metals (67)

System	Oxide coefficient	Metal coefficient	Ratio
Fe/FeO	12.2×10^{-6}	15.3×10^{-6}	1.25
Fe/Fe ₂ O ₃	14.9×10^{-6}	15.3×10^{-6}	1.03
Ni/NiO	17.1×10^{-6}	17.6×10^{-6}	1.03
Co/CoO	15.0×10^{-6}	14.0×10^{-6}	0.93
Cr/Cr ₂ O ₃	7.3×10^{-6}	9.5×10^{-6}	1.30
Cu/Cu ₂ O	4.3×10^{-6}	18.6×10^{-6}	4.32
Cu/CuO	9.3×10^{-6}	18.6×10^{-6}	2.00

Table 2.5
Linear coefficients of expansion of metals and oxides (67)

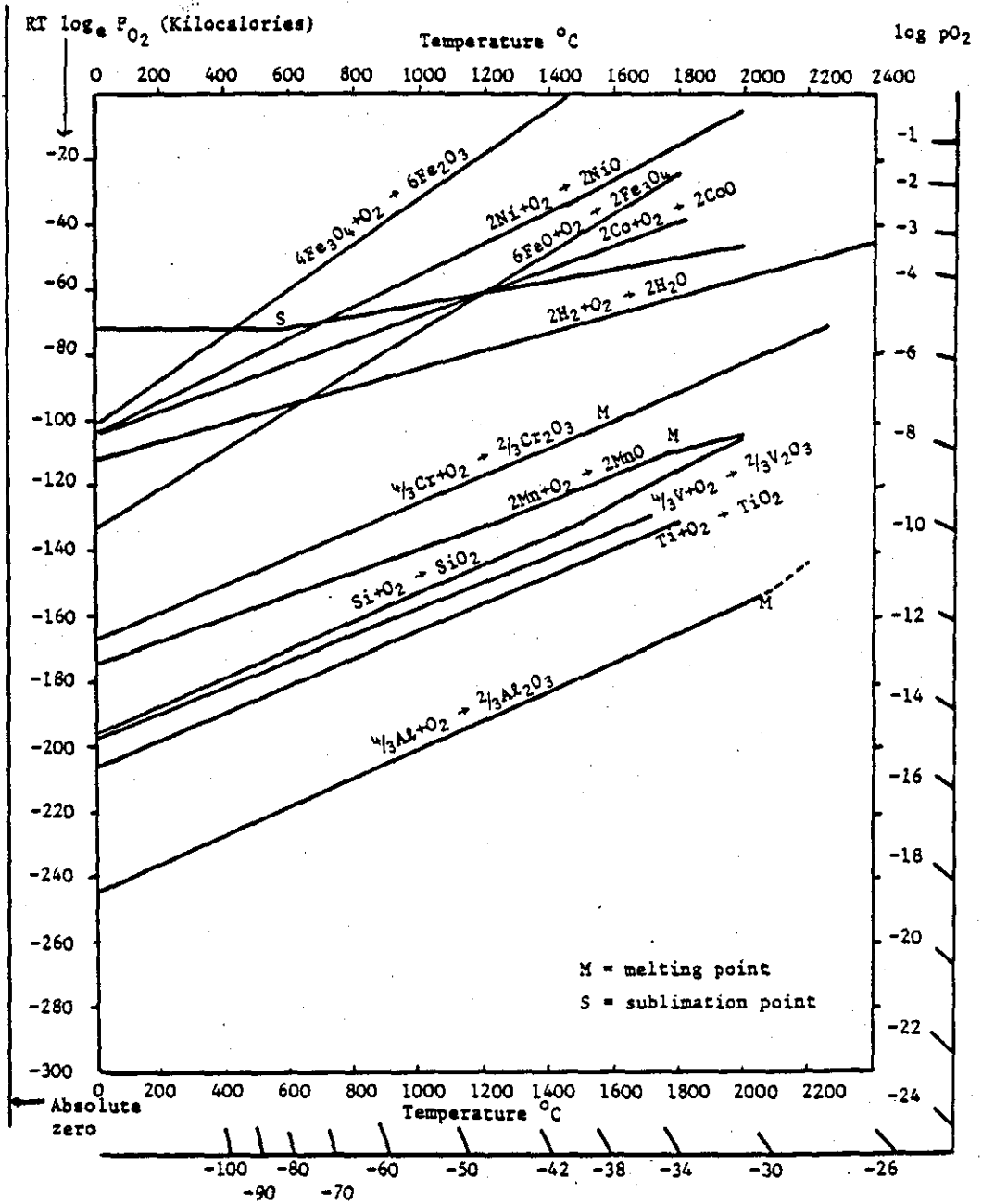


Figure 2.8

Standard free energy of formation of oxides as a function of temperature and pressure (19).

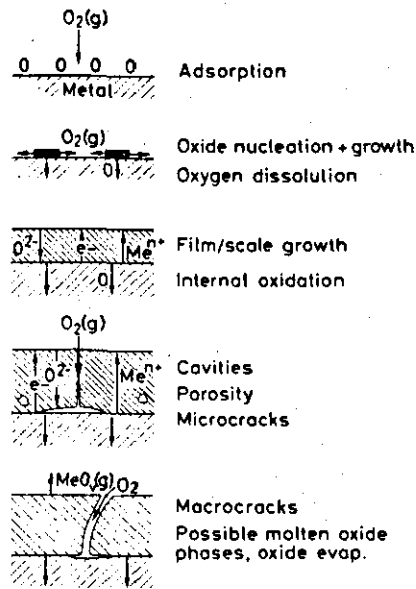


Figure 2.9

Schematic illustration of the main phenomena and part processes taking place in the reaction of metals with single oxidant gases e.g. oxygen (25).

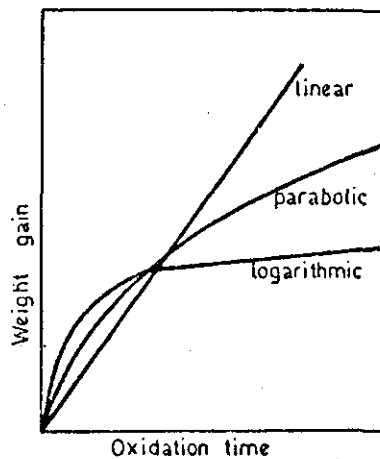


Figure 2.10a

Schematic oxidation rate curves.

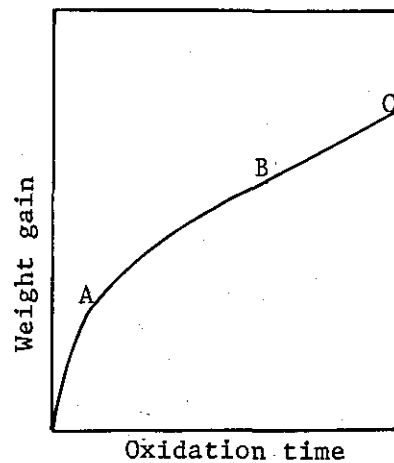


Figure 2.10b

Schematic illustration of a combination of a different rate curves.

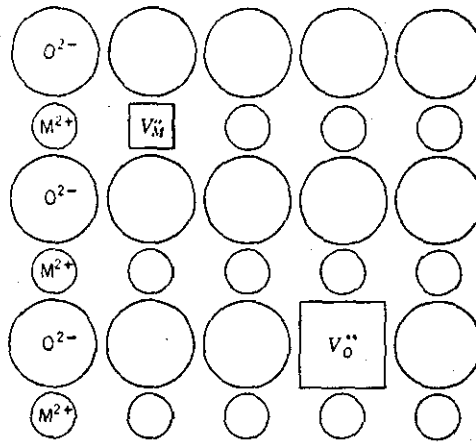


Figure 2.11
Schematic illustration of a
Schottky defect structure in MO (20)

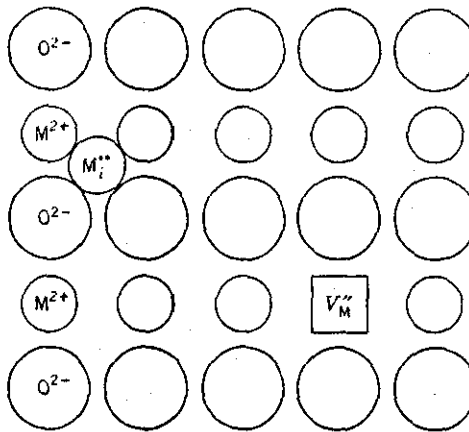


Figure 2.12
Schematic illustration of a
Frenkel defect structure in MO (20)

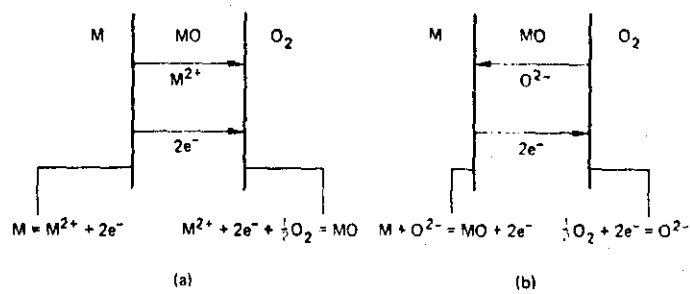


Figure 2.13
Interfacial reactions and transport processes
for high temperature oxidation mechanisms
a) cation mobile
b) anion mobile (24)

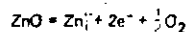
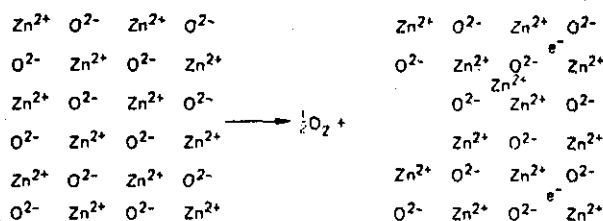


Figure 2.14
Formation of metal excess ZnO with excess electrons and interstitial zinc ions (24).

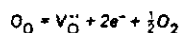
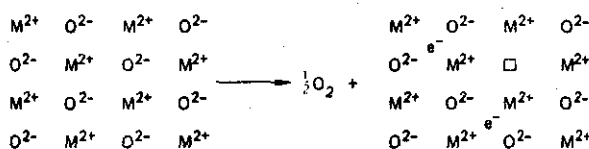
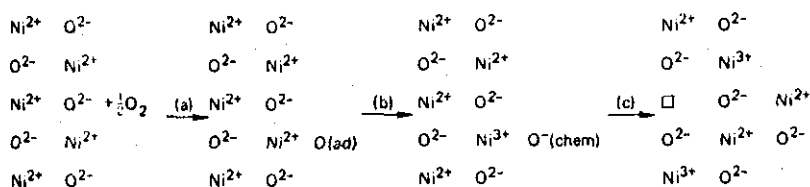


Figure 2.15
Formation of oxygen deficient MO with oxygen ion vacancies and excess electrons (24).



- (a) Adsorption: $\frac{1}{2} \text{O}_2 (\text{g}) = \text{O}(\text{ad})$
 (b) Chemisorption: $\text{O}(\text{ad}) = \text{O}^-(\text{chem}) + h^+$
 (c) Ionisation: $\text{O}^-(\text{chem}) = \text{O}_0 + \text{V}_{\text{Ni}}^{\bullet\bullet} + h^+$
 Overall reaction: $\frac{1}{2} \text{O}_2 = \text{O}_0 + \text{V}_{\text{Ni}}^{\bullet\bullet} + 2h^+$

Figure 2.16
Formation of a metal deficient p-type semiconductor with cation vacancies and electron holes by incorporation of oxygen into the perfect lattice (24).

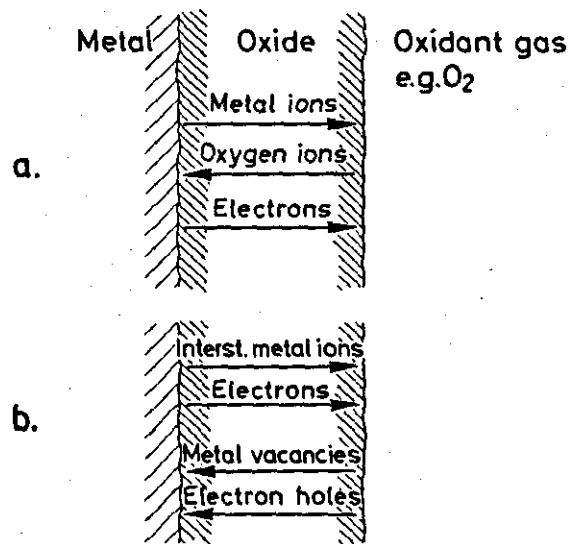


Figure 2.17
Transport processes through dense, single phase scales growing by lattice diffusion. The rate is parabolic (25).

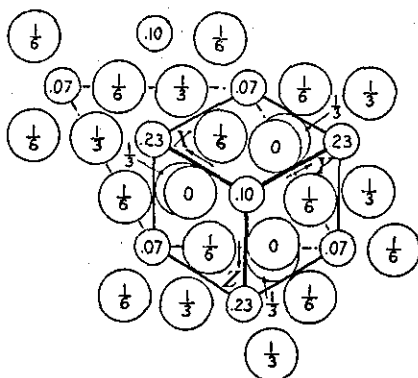


Figure 2.18a

The structure of Cr_2O_3 . A projection of the portion of the Cr_2O_3 arrangement on a plane normal to the three-fold axis and passing through the apex of the unit rhombohedron. The small circles are the metal atoms (33).

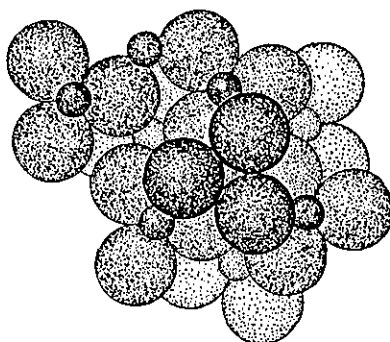


Figure 2.18b

A packing drawing of the atoms of figure 2.18a if they are given their usual atomic sizes.

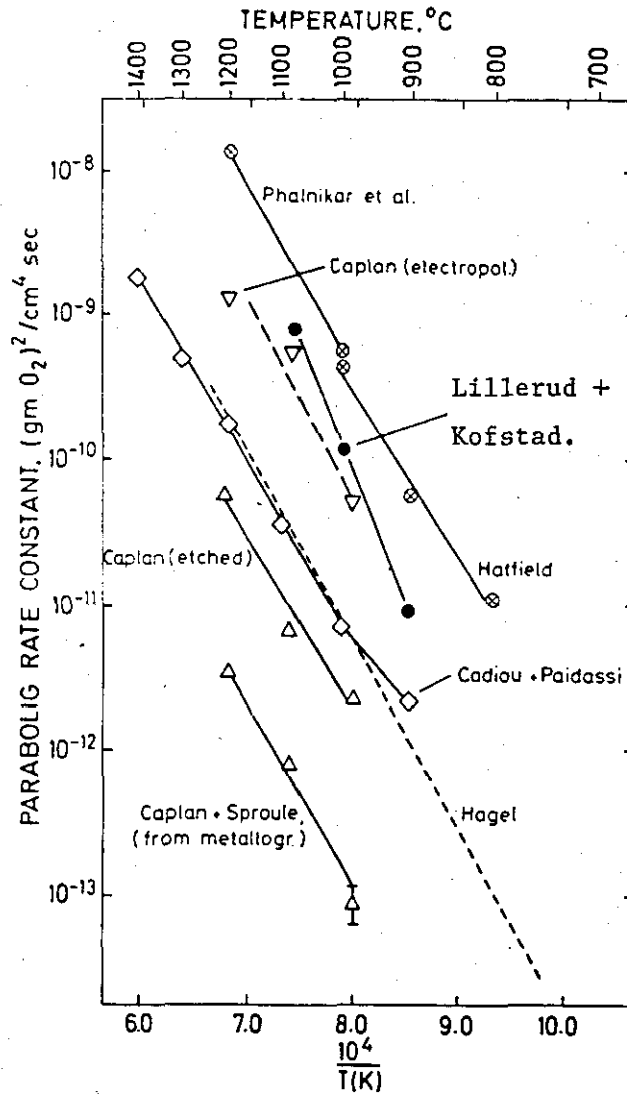


Figure 2.19

Summary of reported parabolic rate constants for the oxidation of chromium in oxygen in the temperature range 700-1400 $^{\circ}\text{C}$. Results of Hatfield (34), Phalnikar et al (35), Hagel (36), Cadiou and Paidassi (37), and Caplan and Cohen (38) and Lillerud and Kofstad (28) are included. Values of Gulbransen and Andrew (40,41) are not shown but are similar to those of Hagel (28).

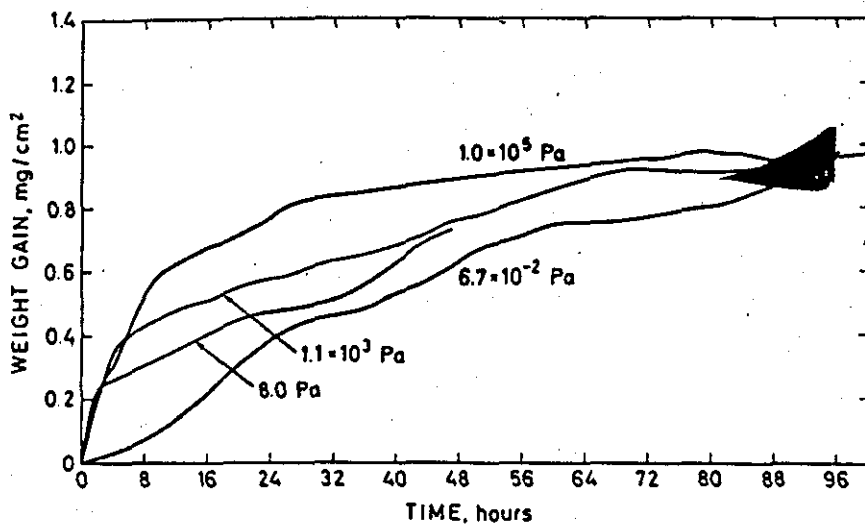


Figure 2.20
Oxidation of thermally etched chromium at 800°C and oxygen pressures ranging from 10^5 Pa (1 atm) to $6.7\text{--}7.10^{-2}$ Pa (7.10^{-7} atm) (28).

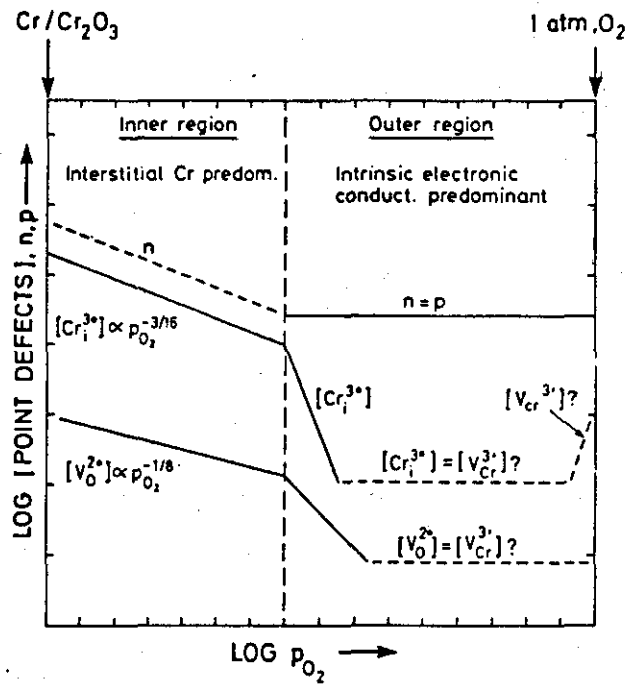


Figure 2.21
Defect structure model for Cr₂O₃ (29).

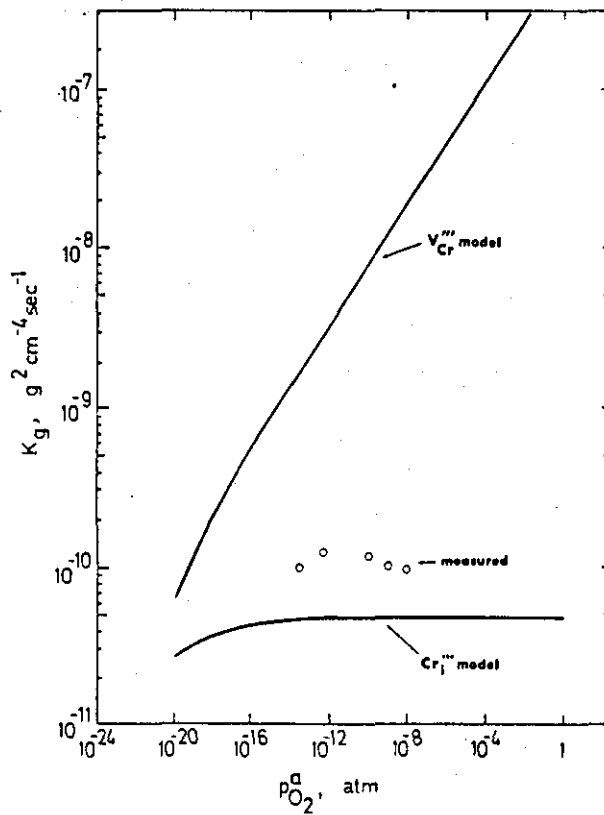


Figure 2.22
Dependence of Cr₂O₃ growth rate on P_{O₂} (45,46)

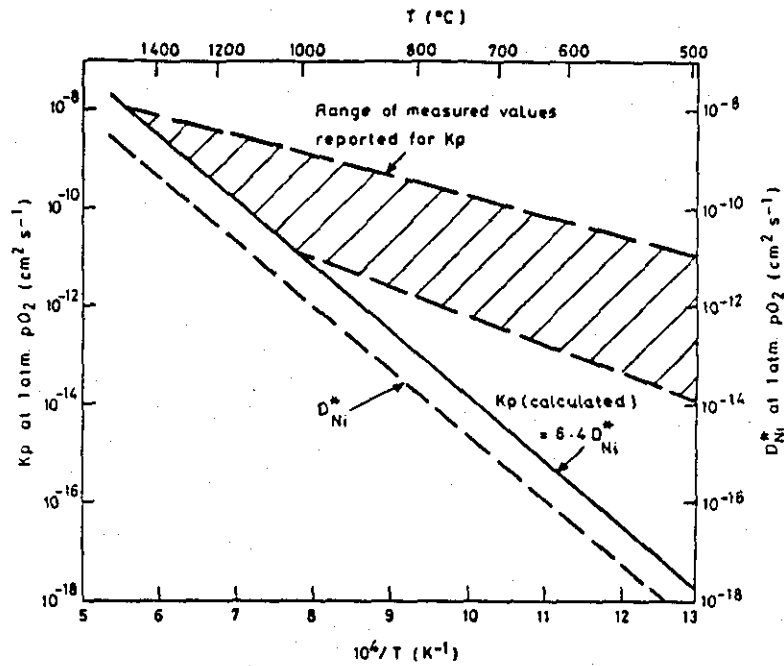


Figure 2.23

Comparison of the parabolic rate constant k_p calculated from the Wagner theory with the k_p observed for NiO growing on Ni, adapted from Hughes et al (49), D_{Ni} data from Volpe and Reddy (50) and Atkinson and Taylor (51).

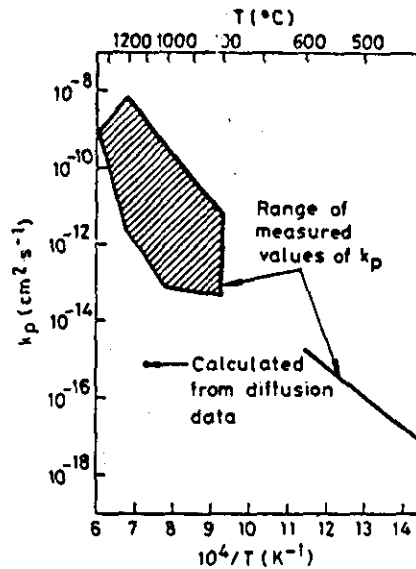


Figure 2.24

Comparison of parabolic rate constants k_p observed for the oxidation of chromium with the rate at 1100°C predicted by the Wagner theory using the diffusion coefficient for Cr in Cr₂O₃ measured by Atkinson and Taylor (52), from Hughes et al (49).

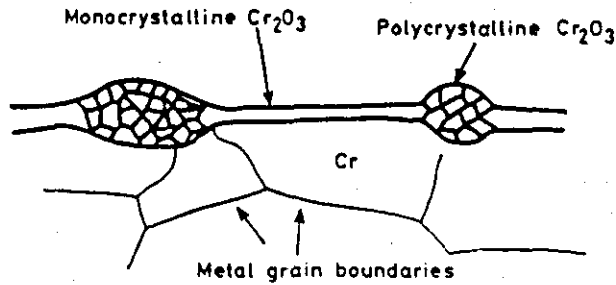


Figure 2.25
Schematic section through Cr etched and oxidized showing how some grain orientations oxidize faster than others (39).

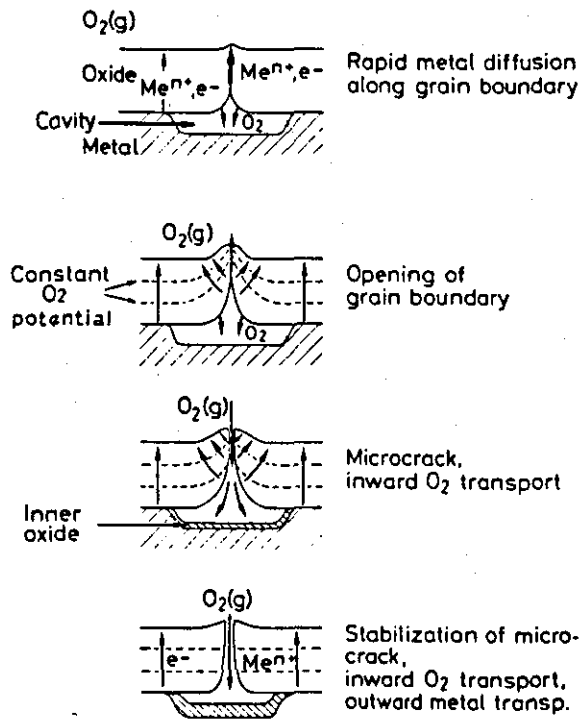
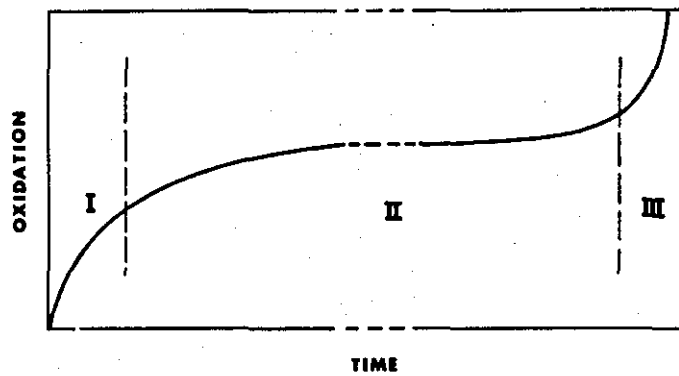


Figure 2.26
Schematic illustration of the model for formation of microchannels in oxide scales by preferential outward diffusion of metal ions along grain boundaries (25).



- | | |
|---------------------|---|
| I: TRANSIENT STAGE: | RATIO OF CATIONS IN SCALE APPROXIMATELY SAME AS THAT IN ALLOY. |
| II: STEADY STATE: | OXIDE MORPHOLOGY AND COMPOSITION DETERMINED BY DIFFUSION AND THERMODYNAMICS OF OXIDE/ALLOY SYSTEM. |
| III: BREAKAWAY: | INITIATED BY MECHANICAL FACTORS: EVENTUALLY SCALE CONTAINS ALLOYING COMPONENTS IN ORIGINAL ALLOY RATIO. |

Figure 2.27
Schematic alloy oxidation kinetics showing different stages in alloy oxidation (57).

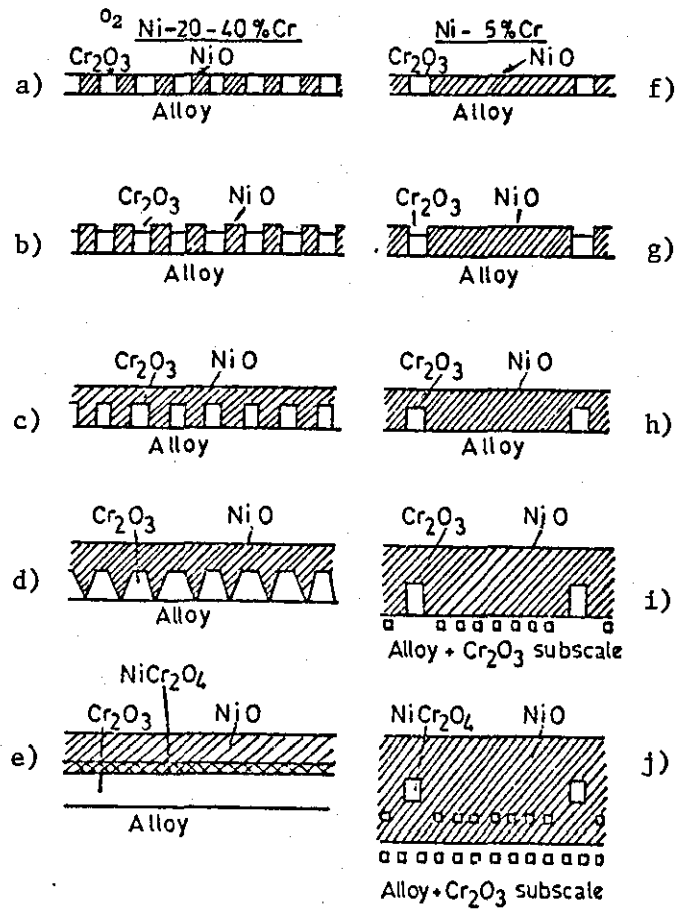


Figure 2.28
Schematic representation of approach
to steady-state scaling (61).

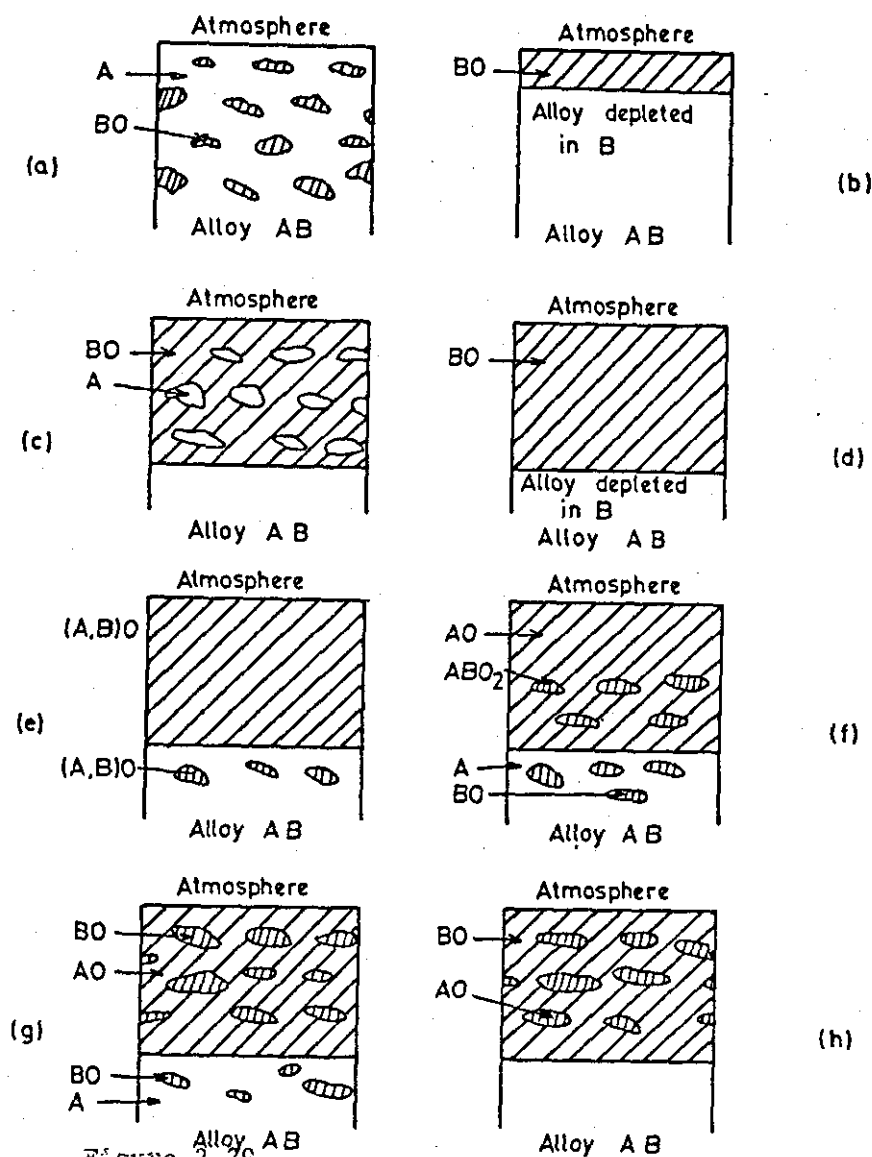


Figure 2.29

Schematic representation of modes of oxidation of alloy AB of variable composition, where B is the less noble metal.

(a) Minor element B only oxidizes, giving internal oxide BO in matrix of A. (b) Minor element B only oxidizes, giving external oxide BO above alloy depleted in B. (c) Major element B only oxidizes, giving particles of A in a matrix of BO. (d) Major element B only oxidizes, giving external oxide BO above alloy depleted in B. (e) A and B oxidize to give single solid solution or compound of variable composition, (A,B)O. (f) A and B oxidize to give compound ABO_2 dispersed in a matrix of AO. (g) A and minor component B oxidize to give insoluble oxides, with BO in a matrix of AO. (h) A and major component B oxidize to give insoluble oxides, with AO in a matrix of BO.

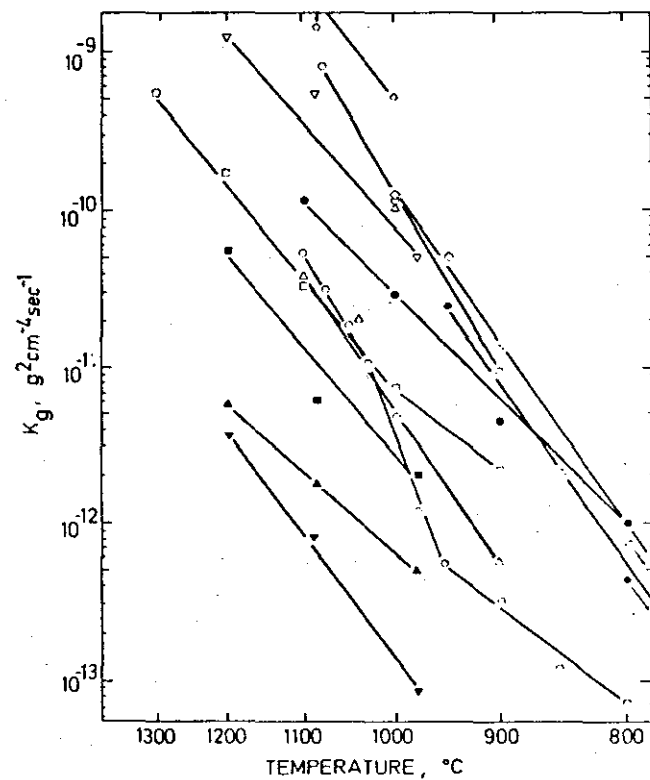


Figure 2.30a
Arrhenius plot of reported parabolic rate constants for the oxidation of pure Cr (45).

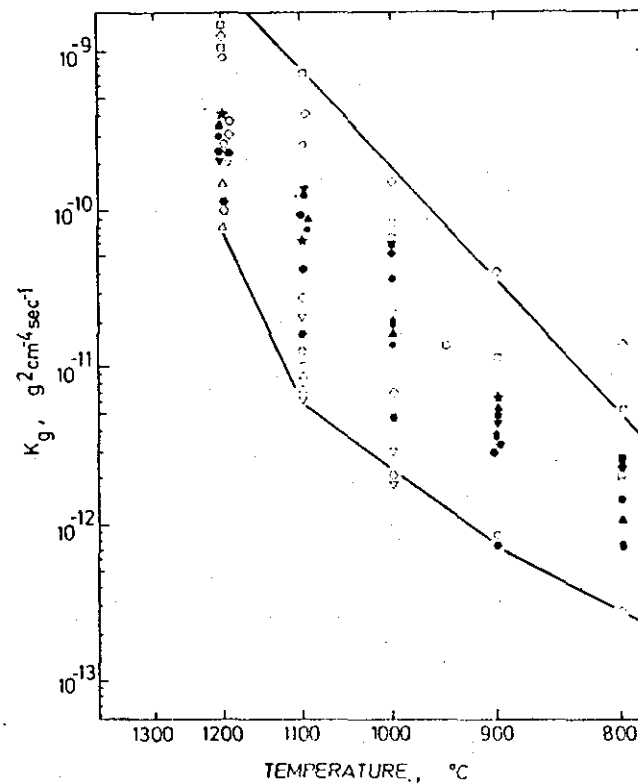


Figure 2.30b
Arrhenius plot of reported parabolic rate constants for the growth of Cr_2O_3 on binary Cr-containing alloys (45)

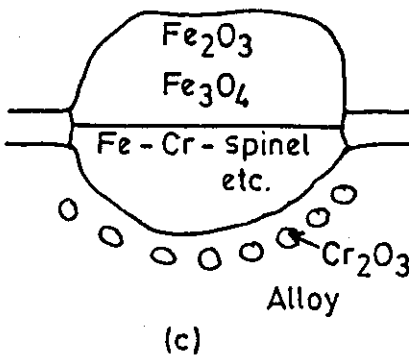
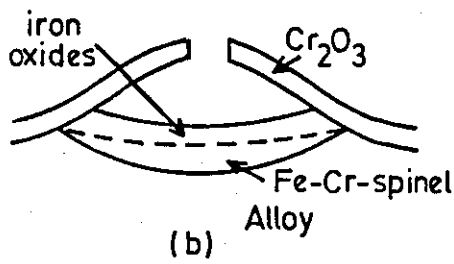
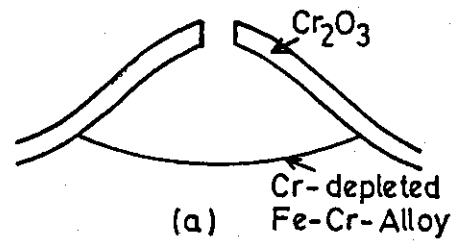


Figure 2.31

Schematic representation of breakaway oxidation on Fe-Cr alloys.

- a) Punctured ridge of Cr_2O_3 .
- b) Development of stratified scale on chromium-depleted substrate.
- c) Fully developed nodule (61).

HIGH COMPRESSIVE STRESSES DURING GROWTH AS METAL RETREATS AWAY FROM THE OXIDE



FAILURE BY:-



SHEAR IF SCALE IS ADHERENT

OR



DECOHESION WITH POSSIBLE TENSILE FAILURE AT a OR b

a)

COMPRESSIVE STRESSES GENERATED DURING OXIDE GROWTH DUE TO VOLUME CHANGES ONLY AS THE OXIDE IS FORMED AT THE METAL OXIDE INTERFACE.



FAILURE BY:-



DECOHESION AND SUBSEQUENT LAMINATION EFFECT.

OR



TENSILE CRACKING DUE TO FIRST FORMED SCALE BEING PUSHED TO LARGER CIRCUMFERENCE

b)

DURING GROWTH THE METAL RETREATS AND REDUCES COMPRESSIVE GROWTH STRESSES IN THE OXIDE



FAILURE BY:-



DETACHMENT IF ADHESIVE STRENGTH IS LOW

OR



RADIAL CRACKING IF ADHESIVE FORCES ARE STRONG

c)

VERY HIGH COMPRESSIVE STRESSES ARE INDUCED DURING GROWTH



d)

LEADING TO FAILURE BY SHEAR ONLY AND NO EVIDENCE OF LACK OF ADHESION

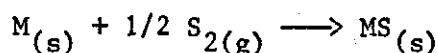


Figure 2.32

Failure of oxide scales due to growth stresses

2.2.2. Sulphidation

The reaction of metals and alloys with oxygen has been considered in depth in the previous section; the same basic thermodynamic treatment applies to their reaction with sulphur. Thus for the reaction



the standard free energy change for metal sulphidation can be given by

$$\Delta G_T^\circ = RT \ln(pS_2)^{1/2} \quad (2.14)$$

$$\text{or } pS_2^{1/2} = \exp. (\Delta G_T^\circ / RT) \quad (2.15)$$

where pS_2 is the partial pressure of sulphur.

As in the case of oxides, these data can be plotted on an Ellingham diagram as reported by Shatynski⁽⁷²⁾, figure 2.23, from which it is clear that Mn has a higher affinity for S than Cr which in turn has a higher affinity than Fe and Ni.

Whereas a large amount of knowledge has been acquired concerning the oxidation of metals and alloys, fewer systematic studies involving sulphidation have been undertaken. For example much of the basic diffusion data for many metal sulphide systems have yet to be established. One reason for this would appear to be the highly aggressive nature of sulphur containing environments making it difficult to carry out the necessary experiments.

Extensive reviews on the sulphidation of metals and alloys have been carried out by Strafford⁽⁷³⁾ and more recently, by Mrowec and coworkers⁽⁷⁴⁻⁷⁶⁾. For the purpose of this literature review the main features of sulphidation will be highlighted, but reference should be made to the above works for a more detailed account.

Sulphidation and oxidation are very similar processes. The stages of film formation i.e. adsorption, nucleation and growth by lattice diffusion and ionic transport along grain boundaries and microcracks are

the same. In general, sulphides of common metals contain the same type of cation defects as found in oxides, with the result that sulphide scales grow predominantly by outward cationic diffusion. Thus the principles of the Wagner model can equally well be applied to sulphidation and oxidation (In fact the first experimental validation of his theory was obtained by Wagner⁽⁷⁷⁾ for the sulphidation of silver). However, there are some essential differences between the two processes, notably :

- (i) Sulphides are characterised by lower thermodynamic stabilities than oxides. Table 2.6 compares the free energy of formation of some metal sulphides and oxides.
- (ii) In general sulphides have much lower melting points, table 2.7, with the consequence that molten products can form and accelerate the corrosion process. It is also possible for lower melting point metal-sulphide eutectics to form e.g. $\text{Ni-Ni}_3\text{S}_2$.
- (iii) The kinetics of sulphidation are several orders of magnitude higher than for oxidation, table 2.8.
- (iv) Sulphides have much higher deviations from stoichiometry, table 2.9, and therefore higher defect concentration.
- (v) The self-diffusion rates are several orders of magnitude higher in sulphides, table 2.10.
- (vi) Certain metal sulphides can exist over a range of compositions, e.g. Nickel can form seven stable sulphides and only one stable oxide : chromium six stable sulphides compared with one stable oxide, table 2.11.
- (vii) The solubility of sulphur in metals is much lower than that of oxygen and consequently the sulphur diffusion rate within the metal is low.

Most of these differences are related. The critical question is why, in general, are the kinetics of sulphidation several orders of magnitude greater than oxidation ?

As, has already been mentioned, sulphide and oxide scales grow predominantly by cationic diffusion, thus the kinetics can be directly related to the self-diffusion coefficients which are in turn a product of the mobility and concentration of defects. It is thus important to consider the role of each of these independently. The mobility of defects can be measured by the chemical diffusion coefficients. It is evident from figure 2.34 that the chemical diffusion coefficient for sulphides are only approximately one order of magnitude higher than those measured on the equivalent oxides. Thus it can be concluded that defect mobility does not account for the large difference in kinetic rates. A comparison of deviations from stoichiometry, however, table 2.9, shows that the concentration of defects in sulphides is several orders of magnitude higher than in oxides and it is this fact which accounts for the higher self diffusion rates and growth kinetics. This higher defect concentration is a consequence of the lower thermodynamic stability of sulphides - the more thermodynamically stable a compound is the more energy is needed to pull an atom or ion out of its crystal lattice point.

There are however some notable exceptions to these trends, viz. :

(i) Iron

FeS and FeO have large but similar deviations from stoichiometry (table 2.9), however the self diffusion coefficients of FeS and FeO differ by less than one order of magnitude, figure 2.35, compared with several orders of magnitude for other metals e.g. Ni, Cr. Thus the increased kinetic rates in FeS, figure 2.36, must be attributed in this case to the greater mobility of defects.

(ii) Manganese

Manganese is even more interesting. The mobility of defects in MnS is higher than in the oxide (figure 2.34) but the defect concentration (deviation from stoichiometry) is lower, table 2.9. Thus due to this compensation effect the self diffusion coefficient in MnS and MnO are comparable and therefore manganese corrodes at approximately the same rate in sulphur and oxygen. Although, the sulphidation rate of manganese is considerably lower

than most other common metals, it is worth emphasising that it is still several orders of magnitude greater than the oxidation rate for chromium.

(iii) Refractory Metals

The sulphidation rates of refractory metals e.g. Nb, Ta, Mo, W are exceptionally low. Niobium is particularly promising as at 1073K the sulphidation rate is comparable with the oxidation rate of Cr. However, it must be emphasised that the sulphidation rates for Ta, Mo and W are still 2 orders of magnitude higher than the rate of chromium oxidation, figure 2.37. (Direct comparison with oxidation of refractory metals is not possible as the kinetics of oxidation do not follow a parabolic law due to cracking and vaporisation of the scale).

The reason for the remarkably low rate of sulphidation of these metals is assumed to be due to the low concentration of defects in the sulphides. It is also assumed that, as refractory metal sulphide and oxide scales grow by inward diffusion of sulphur and oxygen respectively, anionic, as opposed to cationic, defects predominate, as in the case in common metal sulphides. Unfortunately little diffusion and defect data for refractory metal sulphides are available to confirm these assumptions. However the low kinetic rates have led to considerable interest in the possibility of using refractory metals or alloying additions to resist sulphidation. The reviews of Strafford^(78,79) contain much fuller details of current knowledge and possible future developments in this area.

Sulphide scale morphology

Having considered the kinetics of sulphidation and the defect structures of sulphides it is now important to establish the morphology of sulphide scales. In the ideal case, a dense compact single phase scale should form on a metal surface, when it is exposed to a sulphur containing environment. In practice however the scales formed contain cracks, voids and are poorly adherent to the metal surface. In addition to this, double layered scales of the same composition form under certain conditions

and/or multilayered scales having different compositions e.g. FeS and FeS₂ can form during the sulphidation process. Two theories have been proposed for the formation of duplex scales of the same composition.

The first theory was proposed by Geld and Krasovskaya^(80,81) for the sulphidation of iron and involved the counter diffusion of sulphur and iron, the outer layer of the scale forming due to the outward diffusion of cations and the inner layer due to the inward transport of anions. Since there are essentially no anionic defects in the scale the diffusion of sulphur must occur by a mechanism other than lattice diffusion e.g. atomic or molecular transport along grain boundaries. However Pfeiffer and Ilschener⁽⁸²⁾ investigated the sulphidation of iron using radio-active sulphur and came to the conclusion that normal ionic diffusion of sulphur can take place in FeS. According to these workers FeS contained anionic defects in addition to the cationic defects, a consequence of special thermodynamic conditions at the metal/scale interface.

Arkharov and Blankova⁽⁸³⁾ and Jesin and Geld⁽⁸⁴⁾ considered the possibility of the diffusion of sulphur via cation vacancies. They suggested that the anions became strongly polarised in the vicinity of the cation vacancies and attained a quasi-atomic state and as a result of this the anions could migrate through the cationic defects in the scale.

The second theory to explain the growth of double-layered scales was proposed by Bruckman⁽⁵⁴⁾, Bruckman and Romanski⁽⁸⁵⁾ and Mrowec^(55,86) and involves dissociation of the scale. Strafford⁽⁸⁷⁾ has summarised this mechanism using the sulphidation of chromium as an example, figure 2.38. In stage 1 a single layer of scale grows on a flat surface by normal lattice diffusion and the volume of metal consumed is compensated for by plastic flow of the scale. When the scale reaches a particular critical thickness, determined by the size of the flat surface, reaction temperature and plasticity of the scale, voids start to form in the substrate due to the injection of vacancies (stage 2). As a result of the formation of these voids the rate of transport of metal ions to the scale decreases. However, because of the chemical potential gradient of

sulphur in the scale and the defect concentration gradient, transport can still take place and leads to a disturbance of equilibrium of the metal/scale interface. The inner surface of the scale is now no longer saturated with metal ions, since the transfer of metal ions to the scale becomes so slow that it becomes the rate determining step in the overall reaction. Thus, the chemical potential of the sulphur at the interface begins to rise and the concentration gradient of the defects begins to decrease due to the tendency of the scale/sulphur system to reach equilibrium with the sulphur. The conditions which are created in this manner in the voids between the metal and the scale can allow the dissociation of the scale, stage 3, and the formation of further corrosion product by reaction of the liberated sulphur with the metal substrate, stage 4. Thus the inner porous layer grows by gradual decomposition (dissociation) of the previously formed compact outer scale, stage 5. The dissociation of the outer layer may lead to the direct supply of sulphur from the surrounding atmosphere, since the dissociation of the polycrystalline scale after void formation proceeds mainly along grain boundaries and consequently fissures can be formed between individual crystals across the entire scale, stage 6.

In order to determine the reason for the formation of multilayered scales having different compositions Bastow and Wood⁽⁸⁸⁾ studied the reaction of pure nickel with sulphur vapour over the temperature range 380-475°C. The scale was found to consist of four layers, figure 2.39. The three outer layers with preferred orientation grew according to a parabolic law while the innermost layer with random orientation grew only during the early stages of sulphidation after which time the thickness remained approximately constant. Bastow and Wood explained the formation of the multilayered scale in terms of diffusion controlled processes and different diffusion rates in the various layers.

Sulphidation of alloys

As in the case of alloy oxidation, the sulphidation of alloys is much more complex than that for pure metals. The composition of sulphide formed depends on both alloy composition and the ability of the

sulphides of the alloy components to form solid solutions or spinel structures. According to Mrowec⁽⁷⁵⁾ there are three possibilities for the sulphidation of binary alloys.

(i) Fe-Ni type alloys.

In this case both alloy components form solid solutions over the whole composition range. This results in the formation of a compact monophase scale irrespective of alloy composition. The scale grows by outward diffusion of both alloy components with the kinetics following a parabolic law which varies according to alloy composition, figure 2.40. Under certain conditions an inner porous layer can form according to the mechanism discussed for the sulphidation of pure metals.

(ii) Fe-Cr, Ni-Cr and Co-Cr alloys.

When both alloy components only form solid solutions over a limited composition range the situation is more complex. Figure 2.41 shows the sulphidation rate of iron-chromium, nickel-chromium and cobalt-chromium alloys as a function of alloy composition. This graph can be split into 3 regions, figure 2.42.

In the first region, up to 2% Cr, the sulphidation rate is comparable with or higher than that of the base metal, the scale is a single phase and consists of base-metal sulphide doped with chromium which produces a higher concentration of cation vacancies in the scale.

In the second region (2-40% Cr) a duplex scale is formed, figure 2.43. The outer layer consists of a sulphide of the more noble metal A (e.g. Ni in Ni-Cr alloys) and the inner layer a solid solution of the sulphides of both alloy components, or a mixed spinel of the general formula : $A_{1-x}B_xS_4$. Both scale layers are compact and show an ordered growth texture characteristic of the outward diffusion of cations. After longer exposure times and at edges, an inner porous layer can also form as seen in the

sulphidation of pure metals. This layer is a result of scale dissociation which gradually results in the formation of a fourth intermediate scale layer (dissociation zone) formed by partially dissociated portions of the primary compact inner layer, figure 2.44. As can be seen from figure 2.42 the rate of sulphidation in range II decreases as the chromium content increases. This is due to the inner compact $A_{1-x}B_xS$ acting as a barrier layer in which the mobility of cations of both alloy components is smaller than that of the pure sulphide of the base metal, i.e. the rate of sulphidation is controlled by this layer. As the chromium content of this layer increases, the rate approaches that of the rate of chromium sulphidation.

In range III the scale on the alloys is again single phase and consists of chromium sulphide doped with noble metal A. The reaction rate steadily decreases reaching a minimum at about 80% Cr and then increases again. This is due to the bivalent ions of the noble metal A reducing the concentration of cation vacancies in the scale to below that of chromium sulphide.

Whereas most of the results shown in figure 2.41 are for very high sulphur partial pressures it is worthwhile considering the trend at low sulphur partial pressures. Nartia et al.⁽⁸⁹⁾ found that at 800°C and a $pS_2 = 10^{-10}$ atm. the sulphidation rate was 2-3 orders of magnitude lower than at high sulphur pressures. This is not surprising as chromium sulphide is the only stable sulphide in this environment and hence Fe and Ni-containing sulphides will not form. The sulphidation rate also increased with chromium content due to the rate of reaction being now determined by diffusion in the metal phase as opposed to the sulphide scale. This trend would appear to be in good agreement with the results of Strafford et al.⁽⁹⁰⁾, Chan et al.⁽⁹¹⁾ for the sulphidation of ternary Fe-Cr-Ni alloys at $pS_2 = 10^{-11}$ atm. at 825°C.

(iii) Cu-Zn type alloys

In this case the sulphides of the two alloy components are practically immiscible in the solid state and do not form mixed spinels. This results in the formation of a heterophasic double-layered scale, figure 2.45. The outer scale layer is compact and consists of the pure sulphide of base metal A and grows by outward diffusion of the metal. The inner layer is a heterophasic mixture of sulphides of both alloy components AS and BS, it has no defined orientation and is porous. This layer grows by inward diffusion of sulphur molecules through dissociative microcracks formed along the grain boundaries of the outer layer. The contribution of inward diffusion of sulphur to the formation of double-layer heterophasic scales on Cu-Zn type alloys may be considered similar to the secondary processes which give rise to the deterioration of scale compactness near the edges or curvatures of pure metal or Fe-Ni and Ni-Cr type alloy specimens. In all cases scale porosity appears to be a consequence of the loss of contact between the scale and the metallic phase. However in the case of Cu-Zn alloys, this loss of contact is not a consequence of scale rigidity (resulting from the geometry of the reacting system) but of the formation of a third dispersed BS phase on the alloy/scale interface which obstructs plastic flow of the scale.

Ternary alloys

Small amounts of a third element e.g. Al, Si or Mn into Fe-Ni or Ni-Cr alloys lead to the formation of an additional inward growing scale. Studies carried out with radioactive sulphur have confirmed that this heterophasic porous layer is formed by the inward diffusion of sulphur by the sulphidation mechanism described for Cu-Zn alloys. Figure 2.46 summarises the scale morphology on Fe-Cr-Al alloys⁽⁷⁵⁾. The outer layer (I) consists of ferrous sulphide doped with Al. The inner layer II of the mixed spinel $\text{Fe}(\text{Fe}_x\text{Al}_y\text{Cr}_{2-x-y})\text{S}_4$. The porous intermediate and inner layers (III and IV) also consist of this phase. As in the case of binary alloys, these ternary alloys obey a parabolic rate law.

Figure 2.47 shows that increasing the aluminium content results in a gradual improvement of the protective properties of the scale, reducing the corrosion rate by 1,5 to 2 orders of magnitude for an addition of 10% Al⁽⁷⁶⁾. However the effect is rather weak and it can be concluded that using aluminium as an alloying addition to resist sulphidation is not that promising.

It is important to note that there appears to be no information in the published literature concerned with systematic studies of the pure ternary Fe-Cr-Ni system which is the basis of many high temperature alloys.

Sulphide	ΔG°	Oxide	ΔG°	$\Delta G^\circ_{\text{(oxide)}} - \Delta G^\circ_{\text{(sulphide)}}$
FeS	-20,11	FeO	- 43,84	23,73
CoS	-16,20	CoO	- 34,90	19,70
CrS	-33,09	Cr ₂ O ₃	- 64,88	31,79
MnS	-47,83	MnO	- 70,97	23,14
Al ₂ S ₃	-47,17	Al ₂ O ₃	-103,13	55,96
ZnS	-39,16	ZnO	- 53,26	14,10
TiS	-55,91	TiO	-101,53	45,62
ZrS ₂	-58,13	ZrO ₂	-104,02	45,89
ReS ₂	- 8,60	ReO ₂	- 26,91	18,31
InS	-19,63	In ₂ O ₃	- 43,44	23,81
ThS	-63,52	ThO ₂	-119,59	56,07

Table 2.6

Free energies of formation of some metal sulphides and oxides in kcal/g-atom of oxidant at 1200°C (75).

Sulfide	Melting point (K)	Oxide	Melting point (K)
TiS	2373	TiO	2023
La ₂ S ₃	2353	La ₂ O ₃	2490
Ce ₂ S ₃	2333	Ce ₂ O ₃	1963
NbS ₂	?	NbO ₂	2353
ThS ₂	2198	ThO ₂	3323
US ₂	2123	UO ₂	3113
Y ₂ S ₃	1873	Y ₂ O ₃	2683
CrS	1823	-	-
Cr ₂ S ₃	?	Cr ₂ O ₃	2607
MoS ₂	1431	MoO ₂	2200
MnS	1598	MnO	2058
FeS	1468	FeO	1697
Cu ₂ S	1403	Cu ₂ O	1515
CoS	1373	CoO	2083
Al ₂ S ₃	1373	Al ₂ O ₃	2319
In ₂ S ₃	1326	In ₂ O ₃	2273
NiS	1083	NiO	2230
Ni ₃ S ₂	1067	-	-
InS	965	InO	1325
Mn-MnS	1513		
Cu-Cu ₂ S	1343		
Fe-FeS	1258	← Metal Sulfide eutectics	
Co-Co ₄ S ₃	1153		
Ni-Ni ₃ S ₂	918		

Table 2.7

Melting points of some sulphides oxides and metal-sulphide eutectics (74).

Metal or alloy	Sulphidation		Oxidation	
	Temp _{gr} ature °C	kp g ² cm ⁻⁴ s ⁻¹	Temp _{gr} ature °C	kp g ² cm ⁻⁴ s ⁻¹
Cu	650	$8,45 \cdot 10^{-4}$	900	$1,3 \cdot 10^{-8}$
Ni	620	$1,1 \cdot 10^{-6}$	1000	$9,1 \cdot 10^{-11}$
Co	720	$6,67 \cdot 10^{-6}$	950	$1,6 \cdot 10^{-9}$
Fe	800	$8,1 \cdot 10^{-6}$	800	$5,5 \cdot 10^{-8}$
Al	800	$1,0 \cdot 10^{-9}$	1000	$1,0 \cdot 10^{-14}$
Zn	600	$2,0 \cdot 10^{-8}$	800	$6,4 \cdot 10^{-10}$
Cr	1000	$8,0 \cdot 10^{-7}$	1000	$4,5 \cdot 10^{-12}$
Fe-20Cr	1000	$9,8 \cdot 10^{-6}$	1000	$2,0 \cdot 10^{-11}$
Fe-20Cr	900	$1,8 \cdot 10^{-6}$	900	$1,7 \cdot 10^{-12}$
Ni-20Cr	1000	$8,8 \cdot 10^{-6}$	1000	$5,0 \cdot 10^{-11}$
Co-20Cr	800	$2,7 \cdot 10^{-7}$	800	$8,3 \cdot 10^{-13}$
Fe-25Cr-5Al	1000	$1,1 \cdot 10^{-6}$	1000	$2,7 \cdot 10^{-13}$
Ni-20Cr	800	$1,0 \cdot 10^{-7}$	800	$2,0 \cdot 10^{-12}$
Mn	1000	10^{-8}	1000	10^{-8}

Table 2.8

Parabolic rate constants for the sulphidation and oxidation of some metals and alloys. Pressures of oxygen and sulphur 1 atm (75). Values for Mn from (76).

Sulphide	Temperature °C	Deviation from stoichiometry y	Oxide	Temperature °C	Deviations from stoichiometry y
Cu _{1,75} S	650	0,250	Cu _{1,997} O	1000	0,003
Ni _{0,92} S	700	0,080	Ni _{0,9999} O	1000	0,0001
Co _{0,85} S	720	0,150	Co _{0,99} O	1000	0,010
Fe _{0,80} S	800	0,200	Fe _{0,89} O	800	0,110
Cr _{2,08} S ₃	700	0,080	Cr _{1,999} O ₃	600	0,001
Al _{2,01} S ₃	950	0,010	Al _{2,0001} O ₃	1000	0,0001
Mn _{0.998} S	1000	0.002	Mn _{0.9880} O	1000	0.012

Table 2.9

Maximum deviations from stoichiometry for some metal sulphides and oxides (75).
Values for Mn from (76).

Sulphide	Temperature °C	D _{Me} cm ² /s	Oxide	Temperature °C	D _{Me} cm ² /s
Cu _{2-y} S	650	5,15 · 10 ⁻⁵	Cu _{2-y} O	1000	1,7 · 10 ⁻⁸
Co _{1-y} S	720	7,0 · 10 ⁻⁷	Co _{1-y} O	1000	1,9 · 10 ⁻⁹
Ni _{1-y} S	800	1,4 · 10 ⁻⁸	Ni _{1-y} O	1000	1,0 · 10 ⁻¹¹
Cr ₂ S ₃	1000	1,0 · 10 ⁻⁷	Cr ₂ O ₃	1000	1,0 · 10 ⁻¹²
Fe _{1-y} S	800	3,5 · 10 ⁻⁷	Fe _{1-y} O	800	1,3 · 10 ⁻⁸
Al ₂ S ₃	600	1,0 · 10 ⁻¹³	Al ₂ O ₃	1000	1,0 · 10 ⁻¹⁵
Mn _{1-y} S	1000	1.0 · 10 ⁻⁹	Mn _{1-y} O	1000	1.0 · 10 ⁻⁹

Table 2.10

Self-diffusion coefficients D_{Me} in some metal sulphides and oxides (75).
Values for Mn from (76).

Formula	Stability Range [K]		Crystal structure
α -Ni _{1-y} S	555 - 1265	(b)	Hexagonal
β -Ni _{1-y} S	RT - 652	(c)	Hexagonal
α -Ni ₇ S ₆	673 - 846	(d)	Orthorhombic
β -Ni ₇ S ₆	RT - 673	(c)	Hexagonal
Ni ₃ S ₄	RT - 629	(a)	Cubic
NiS ₂	RT - 1280	(b)	Cubic
Ni ₃ S ₂	RT - 835	(c)	Rhombohedral
Ni _{3±x} S ₂	797 - 1079	(b)	Cubic
NiO	RT - 2263	(b)	Cubic
Cr _{1-y} S	RT - 1823	(b)	Monoclinic
Cr ₇ S ₈	RT - 800	(b)	Trigonal
Cr ₅ S ₆	RT - 730	(b)	Trigonal
Cr ₃ S ₄	RT - 1190	(c)	Monoclinic
Cr ₂ S ₃ (tr)	RT - ~ 1670		Trigonal
Cr ₂ S ₃ (rh)	RT - ~ 1670		Rhombohedral
Cr ₂ O ₃	RT - 2708	(b)	Hexagonal
R.T. = Room Temperature (a) = Disproportionation (b) = Melting point (c) = Transition (d) = Transition to Disproportionation			

Table 2.11

Properties of the sulphides and oxides chromium and nickel (74).

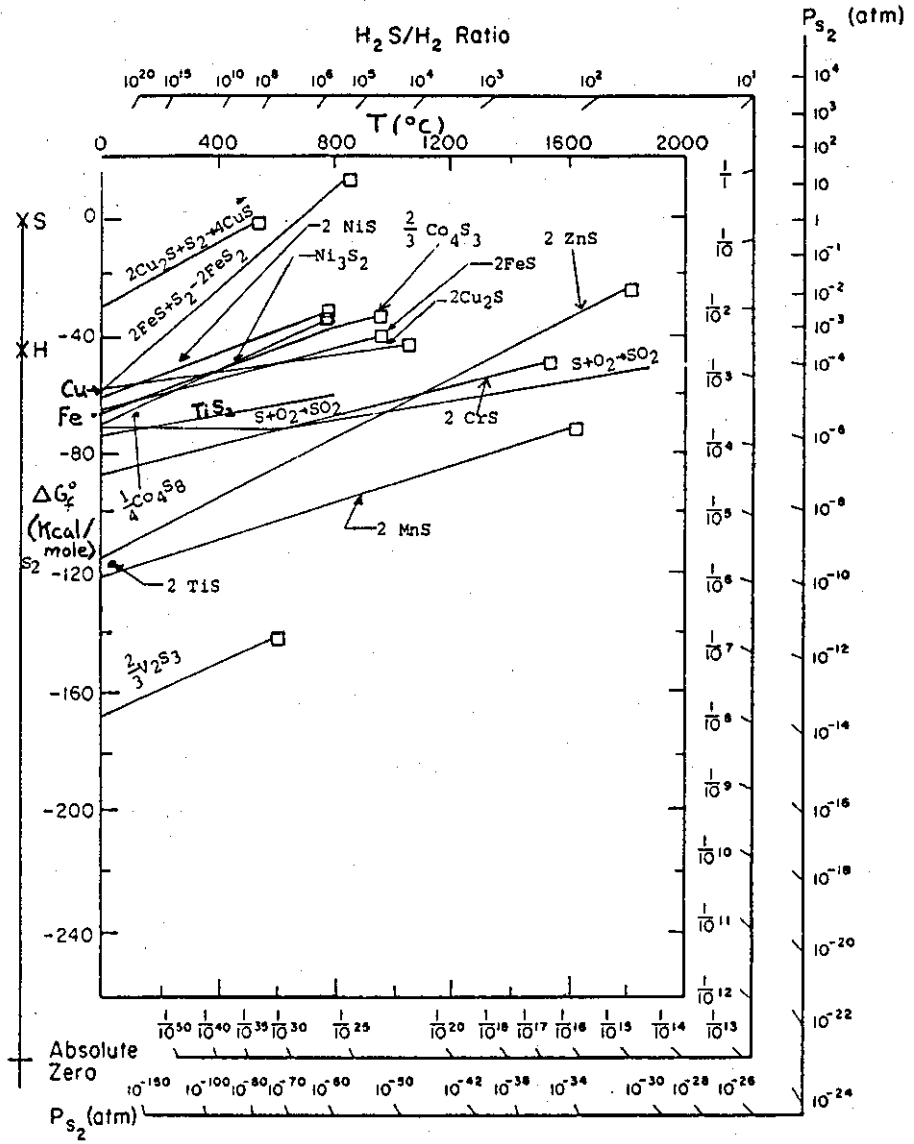


Figure 2.33

Standard free energy of formation of sulphides as a function of temperature and pressure (72).

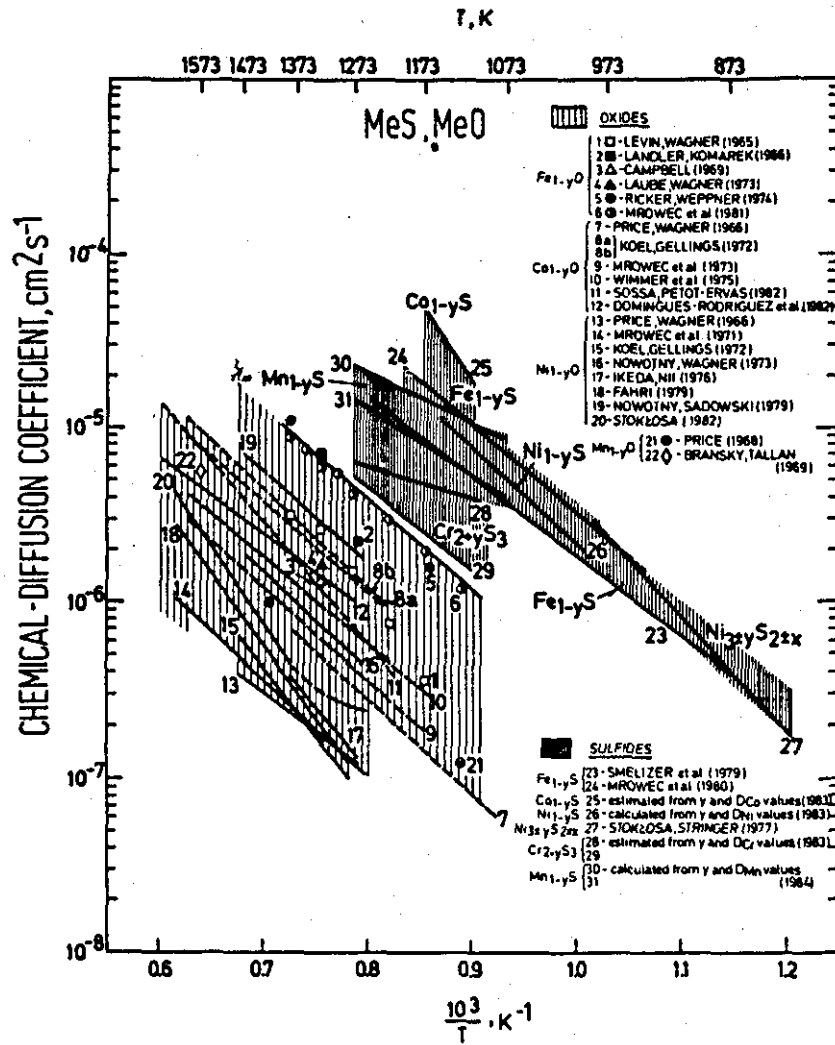


Figure 2.34
Collective plot of chemical diffusion coefficients in some metal sulphides and oxides (76).

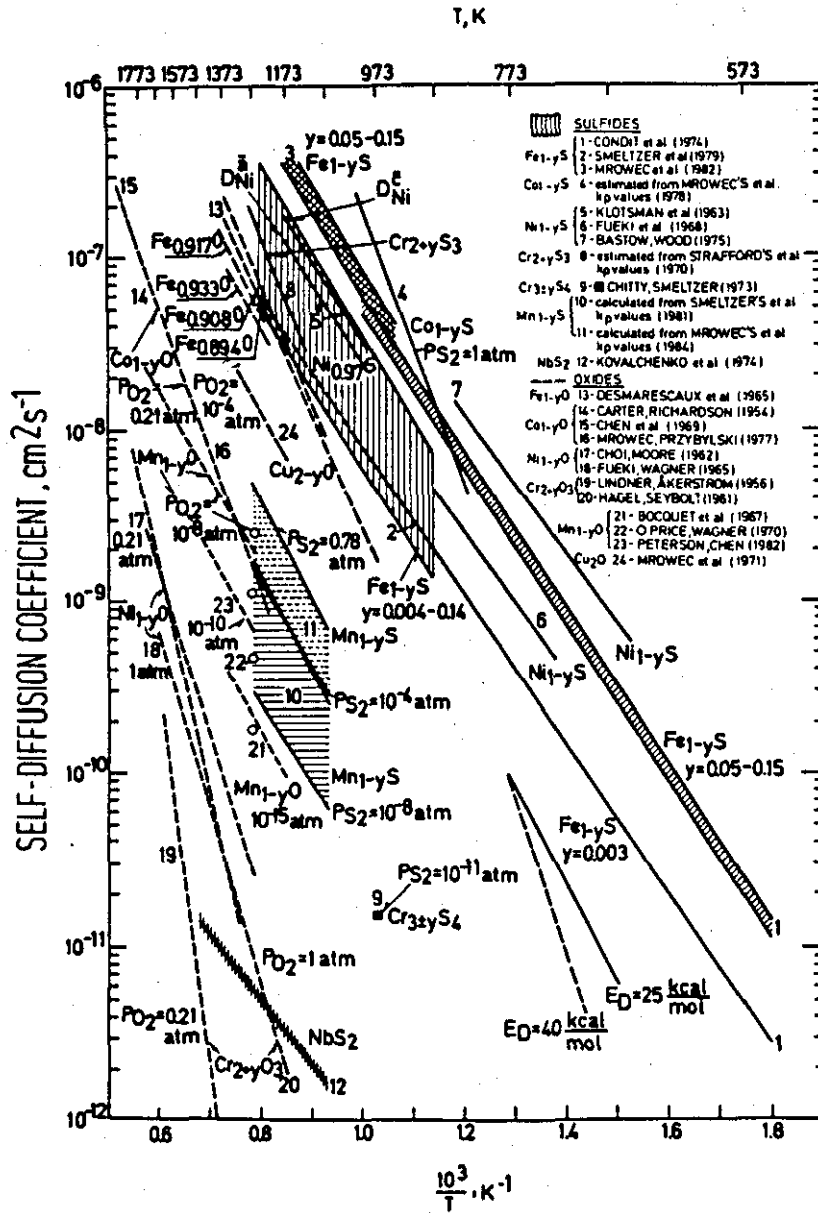


Figure 2.35
Collective plot of self-diffusion coefficients in
some metal sulphides and oxides (76).

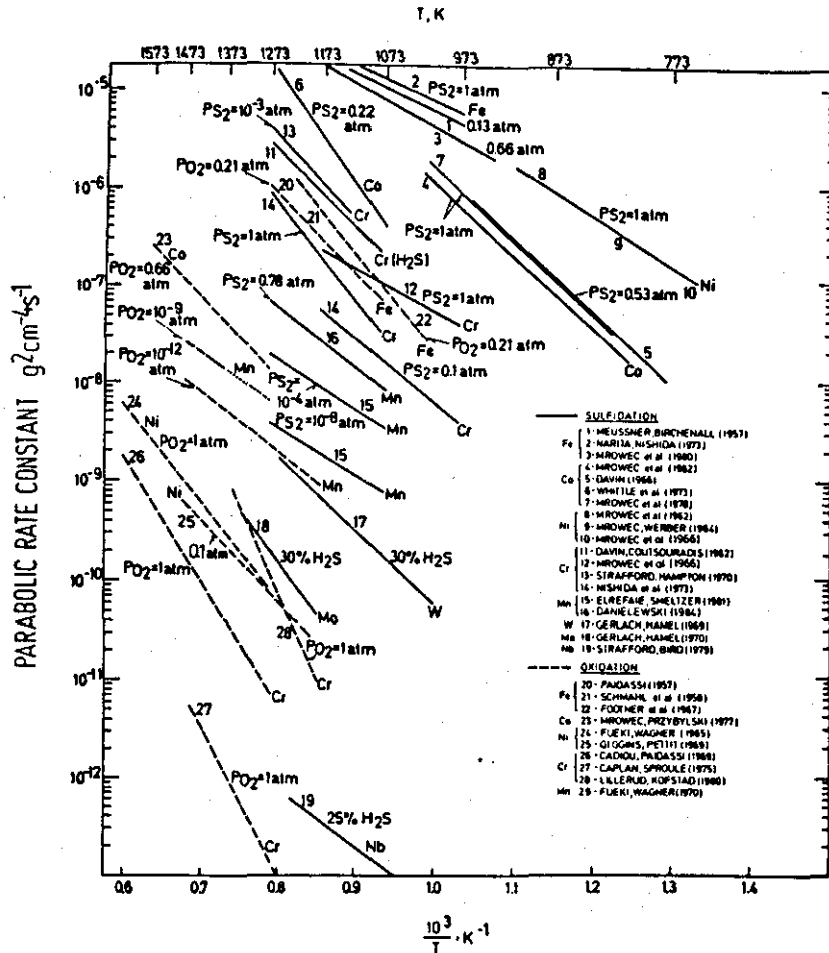


Figure 2.36
Collective plot of the temperature dependence of
sulphidation and oxidation rates of pure metals (76).

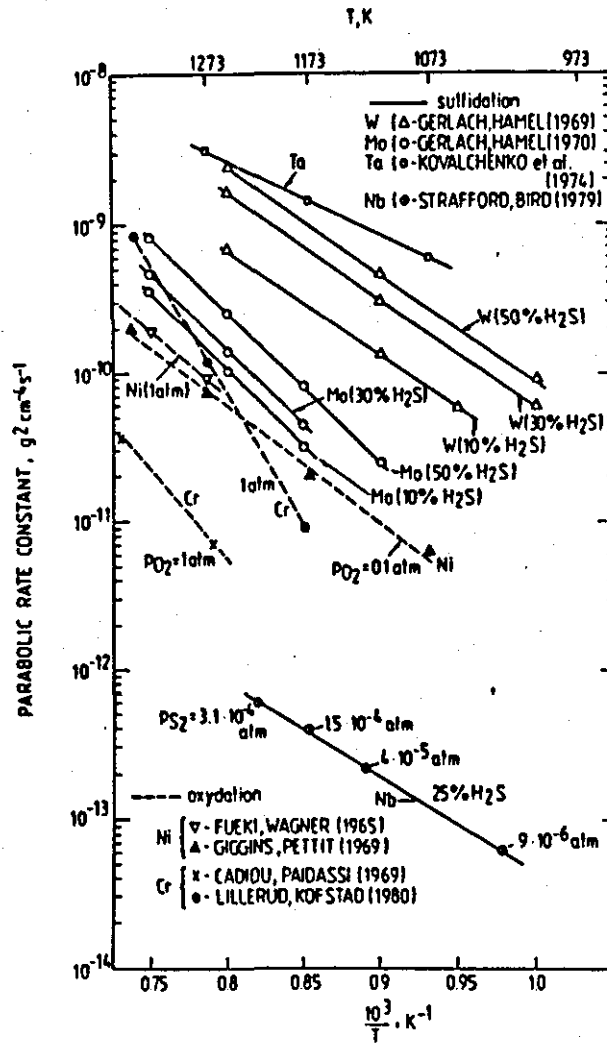


Figure 2.37

Collective plot of the temperature dependence of the parabolic rate constant of sulphidation of some refractory metals, compared with chromium and nickel oxidation rates (74).

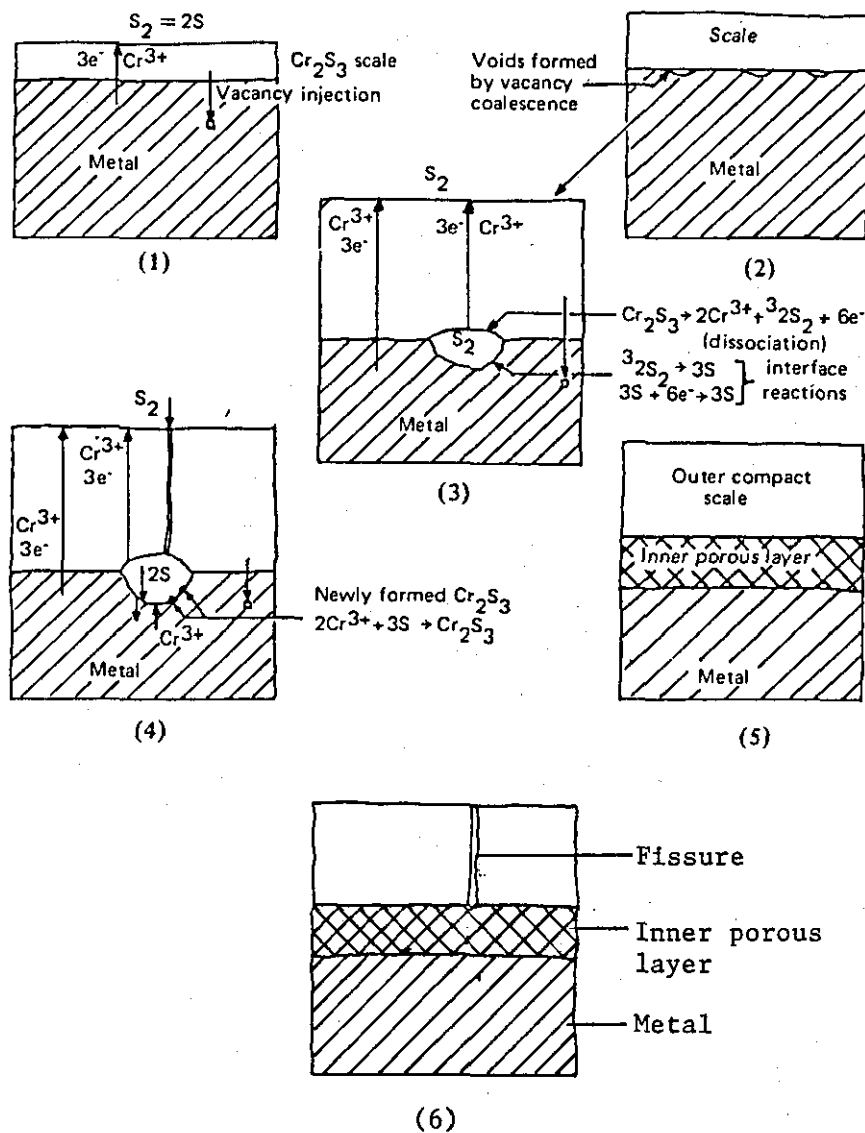


Figure 2.38
Schematic diagram illustrating duplex sulphide formation on chromium, adapted from (87).

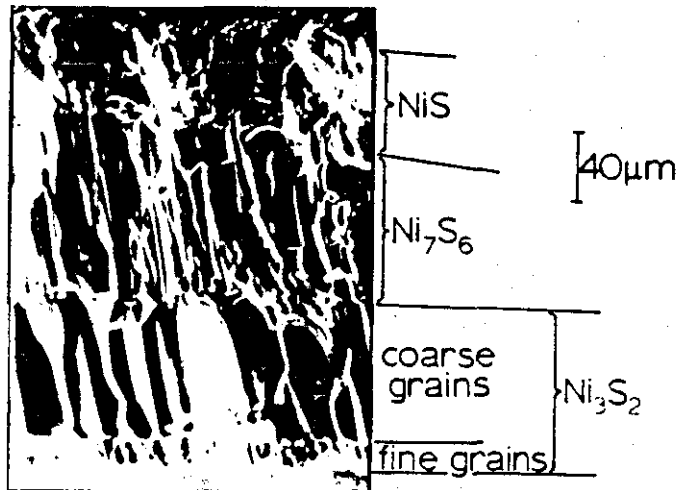


Figure 2.39
Fractograph of scale formed by the sulphidation of pure nickel at 445°C after 30 mins. (88).

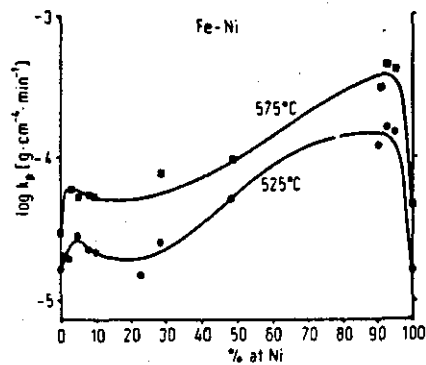


Figure 2.40
Dependence of sulphidation rate of Fe-Ni alloys on their composition at two temperatures (75).

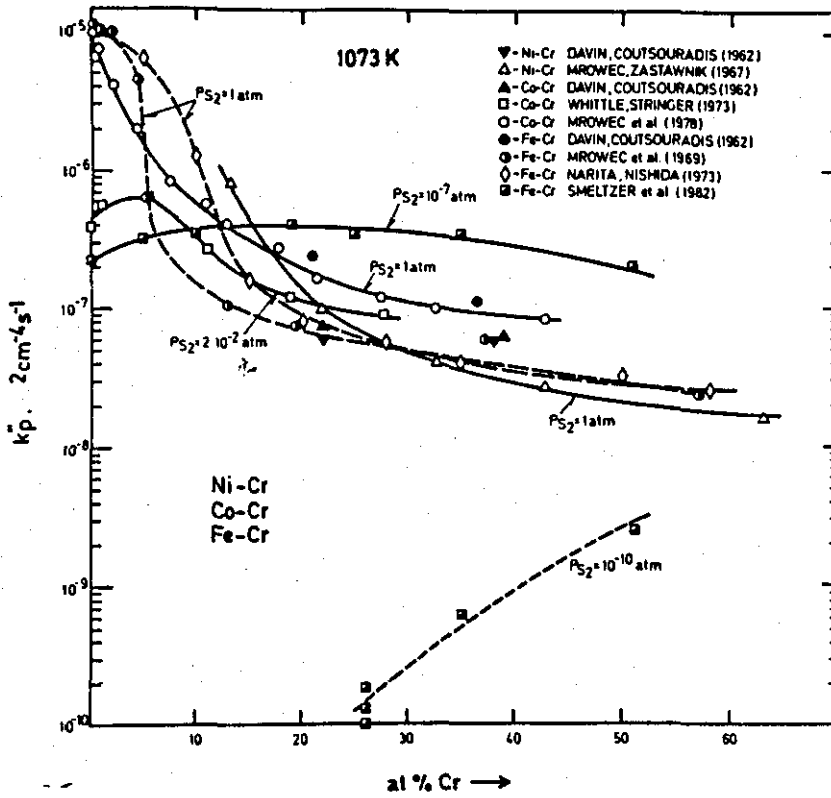


Figure 2.41

Collective plot of the dependence of the sulphidation rate of Fe-Cr, Ni-Cr and Co-Cr alloys on composition at 1073 K (76).

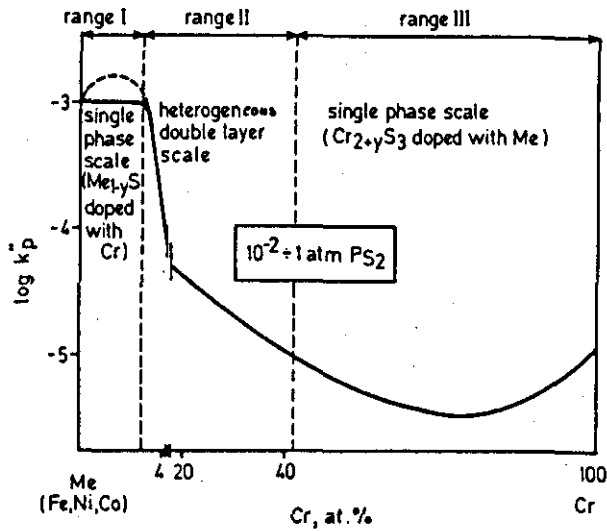


Figure 2.42

Schematic drawing of the dependence of sulphidation rate on composition for Fe-Cr, Ni-Cr and Co-Cr alloys (76).

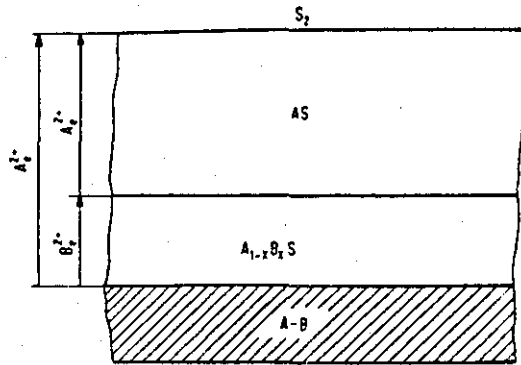


Figure 2.43
Schematic representation of the growth mechanism of a compact double-layer sulphide scale on Ni-Cr type alloys (75).

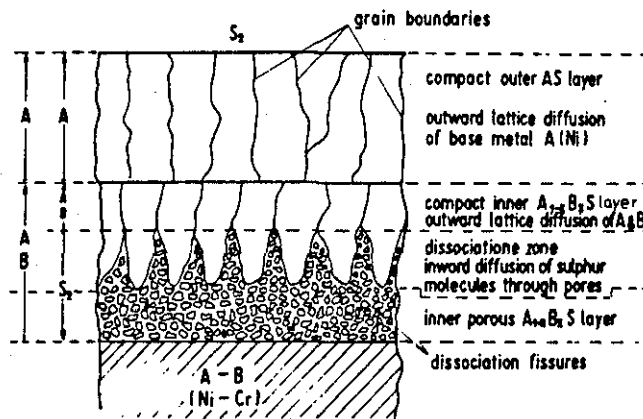


Figure 2.44
Schematic representation of the growth mechanism of a four layer sulphide scale on Ni-Cr type alloys (75).

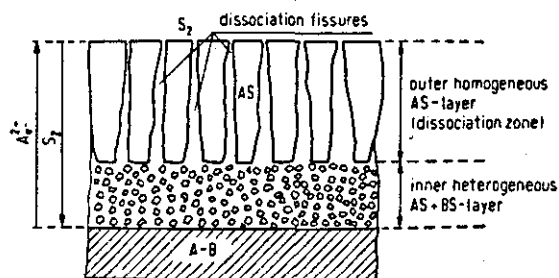


Figure 2.45
Schematic representation of the growth mechanism of heterophasic sulphide scale on Cu-Zn type alloys (75).

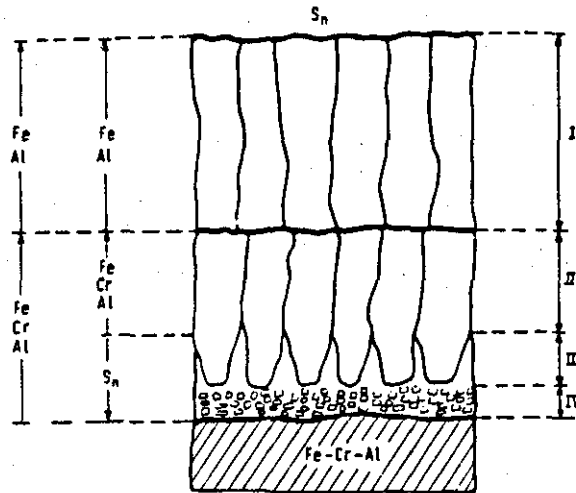


Figure 2.46

Schematic representation of the growth mechanism of a four layer sulphide scale on Fe-Cr-Al alloys.

- I compact outer layer
- II compact intermediate layer
- III porous intermediate layer
- IV porous inner layer (75).

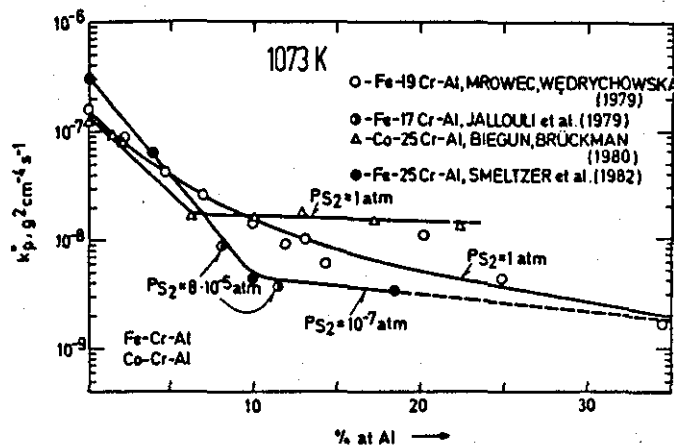


Figure 2.47

The effect of aluminium content in Fe-Cr-Ni alloys on the sulphidation rate at 1073K for various sulphur pressures (76).

2.2.3. Carburization

The degradation of metallic materials in carburizing environments can generally be considered to take one of two forms, namely the more common simple carburization of the alloy surface and substrate or a more catastrophic form known as metal dusting.

In the carburization process carbon diffuses into the alloy and reacts with elements having a high affinity for carbon such as Cr, W, Ti, etc. to form carbide precipitates. This results in internal stresses being built up in the material and can cause a deterioration in its mechanical properties such as ductility. It should be made clear, however, that carburization need not always be detrimental. For instance engineering components such as gears made from low carbon, low alloy steels are often case hardened by carburization to give a hard wear resistant surface whilst maintaining the tough impact resistant properties of the material in the core of the component⁽⁹²⁾.

Metal dusting is a very severe form of carburization. According to Hochman⁽⁹³⁾ significant dissolution and diffusion of carbon into the material does not occur. Instead there is a continuous build up of carbon atoms in solid solution a few hundred angstroms into the metal surface. When the surface layer becomes saturated with carbon a stable carbide, a meta-stable carbide or activated carbon complex forms which then grows until it reaches a level of thermodynamic instability where it decomposes to metal and carbon. These decomposition products are usually in the form of a powder or "dust". "Metal dusting" often occurs locally in the form of pits and continued attack can result in severe metal losses and lead to catastrophic failure of components. Perkins et al.⁽⁹⁴⁾ have proposed that severe metal losses can also occur in environments with low oxygen activities and with a carbon activity (a_c) > 1. Under these conditions chromium carbides and oxides form, but carbon continues to absorb in the chromium depleted matrix until eventually graphite and rejected metallic particles form.

It appears from the literature that the reasons are unclear as to why carburization can occur under one set of circumstances and metal dusting another. However Koszman⁽⁹⁵⁾ has proposed that when the carburizing

potential and the rate at which carbon penetrates the metal-gas interface are very high, steep density gradients can be set up in the metal. If the forces created by these density gradients cannot be absorbed by the specimen, due to lack of ductility, the carburized layer will crumble resulting in severe metal dusting. If, however, the carbon penetration rate is moderate and the metal has sufficient ductility, it will have time to deform and absorb the changes in density, with the result that normal carburization will occur.

As this study is only concerned with relatively low carburizing potentials, where metal dusting does not occur, this review will be restricted to the more normal form of this phenomenon. The main points of the mechanism will be highlighted but for a more detailed description reference should be made to the in depth reviews of Barnes⁽⁹⁶⁾, Smith⁽⁹⁷⁾ and Perkins⁽⁹⁸⁾.

The carburization mechanism of Fe-Cr-Ni alloys has been established by Schnaas and Grabke⁽⁹⁹⁾, Harrison et al.⁽¹⁰⁰⁾ and Norton et al.⁽¹⁰¹⁾.

In the ideal case the process involves the following steps, outlined by Norton⁽¹⁰²⁾ in figure 2.48.

- (i) Dissociation of methane at temperature resulting in the deposition of atomic carbon on the alloy surface.
- (ii) Adsorption of carbon on the alloy surface.
- (iii) Reaction of carbon with the alloy surface to form a discontinuous M_7C_3 carbide layer.
- (iv) Inward diffusion of carbon along grain boundaries and through the bulk of the material. This occurs by an interstitial mechanism at a rate determined by the composition and structure of the matrix. This results in a carbon activity gradient in the alloy.
- (v) Precipitation of $M_{23}C_6$ carbides. Initially these are rich in Cr. Fe (and Ni) are incorporated as the carbon activity in the alloys increases.

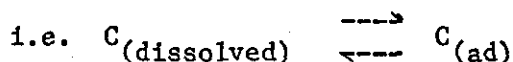
- (vi) Transformation of $M_{23}C_6$ to Cr-rich M_7C_3 with Fe and Ni rejected as metallic particles. The M_7C_3 then incorporates Fe (and Ni) as the carbon activity increases.

In the real case, however, Smith et al.⁽¹⁰³⁾ showed that transient Cr_2O_3 layers develop during the heating cycle. Following an incubation period at temperature these transient Cr_2O_3 layers convert to Cr_7C_3 as shown in figure 2.49. Carburization then proceeds according to the ideal mechanism.

The six steps outlined can be considered from the point of view of processes occurring on the alloy surface (steps i-iii) and processes within the alloy (steps iv-vi).

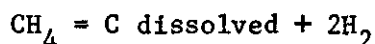
Processes on the alloy surface

According to Grabke⁽¹⁰⁴⁾ the adsorption of carbon on metal surfaces when exposed to gas mixtures such as CH_4-H_2 or CO_2-CO cannot be studied because the techniques available such as low energy electron diffraction (LEED), Auger electron spectroscopy (AES), secondary ion mass spectroscopy (SIMS) and electron spectroscopy for chemical analysis (ESCA) can only be used in ultra-high vacuum conditions. However information on adsorption can be obtained by studying surface segregation equilibria from the bulk of the material where the same adsorption states occur.



where C_{ad} = carbon adsorbed.

Grabke⁽¹⁰⁴⁾ investigated the carburization and decarburization of iron by using gravimetric and resistometric relaxation methods in the temperature range 500-900°C. The rate law for the reaction



was found to be.

$$v = \frac{dn_c}{A dt} = \frac{k p_{CH_4}}{p_{H_2}^{1/2}} - k' a_c p_{H_2}^{3/2} \quad (2.16)$$

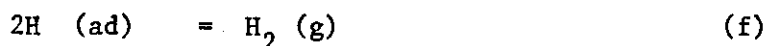
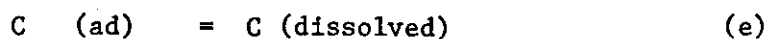
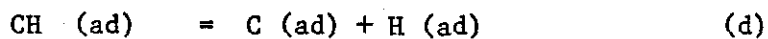
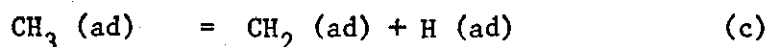
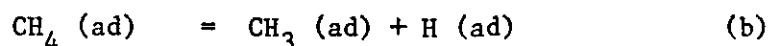
where A is the area of the sample

k and k' are rate constants of the forward and backward reactions respectively

p_{CH_4} and p_{H_2} are the partial pressures of CH_4 and H_2

and a_c is the thermodynamic activity of carbon in the metal.

The chemical surface reaction is thought to occur in steps, because it is improbable that four hydrogen atoms are released in a single elementary step. The following reaction sequence has been proposed.



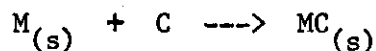
Grabke⁽¹⁰⁵⁾ attributed the rate law to the reaction step (c) which is therefore rate determining.

Grabke showed that during the carburization process the forward reaction rate did not change, in spite of increasing bulk and surface concentrations of carbon. Thus it was concluded that the occupancy of $(1/2 \ 1/2)$ sites on the (100) face by carbon (figure 2.50) did not retard the rate of reaction and therefore the rate determining step must be determined by sites not occupied by carbon atoms such as the top of two adjacent iron atoms.

Processes in the alloy

This process involves the inward diffusion of carbon into the alloy. The process is shown schematically in figure 2.51. Initially the carbon activity (a_c) in the environment is higher than in the alloy, figure 2.51a. This difference in a_c may cause a transfer of carbon from the environment to the metal surface by adsorption, figure 2.51b. Concurrent with this increase in surface carbon content is the development of a carbon activity gradient in the alloy extending inwards from the surface to the interior. This gradient which is a function of temperature, alloy composition and time provides the driving force for the diffusion of carbon into the matrix, figure 2.51c. This occurs by an interstitial mechanism and also along paths having low activation energies such as grain boundaries. Diffusion will continue until equilibrium with the environment is achieved throughout the metal, figure 2.51d.

If the alloy contains elements which have a high affinity for C, they will react with C to form carbide precipitates.



The standard free energy change for this reaction is given by

$$\Delta G_T^\circ = RT \ln a_c \quad (2.17)$$

$$\text{or } a_c = \exp (\Delta G_T^\circ / RT) \quad (2.18)$$

where a_c = carbon activity in the metal.

As in the case of oxides and sulphides, data for different carbides can be plotted on an Ellingham diagram, figure 2.52. The diagram, constructed by Shatynski⁽¹⁰⁶⁾, shows that elements such as Ti and Nb form carbides at very low carbon activities. Other points worth noting are that Ni forms no carbides and that some elements such as Cr can form several carbides such as $Cr_{23}C_6$, Cr_7C_3 and Cr_3C_2 . It is important to note that in plotting the positions of these chromium carbides Shatynski has used data from the formation of carbides from carbon and

other carbides and not from Cr and C. This gives the false impression that Cr_7C_3 will form at a lower carbon activity than Cr_{23}C_6 . In fact, as shown in other literature^(107,108,109) Cr_{23}C_6 is the first carbide to form followed by Cr_7C_3 and Cr_3C_2 as the carbon activity is increased.

A study of the carburization mechanism of a commercial 20Cr-32Ni-Fe alloy (Incoloy 800) in $\text{H}_2\text{-CH}_4$ environments between 900 and 1100°C with a carbon activity of 1 has been carried out by Schnaas and Grabke⁽⁹⁹⁾. The results of this are shown schematically in figure 2.53. After an initial incubation period, attributed by Smith⁽⁹⁷⁾ to be due to the time taken to reduce transient oxide layers, carbon diffuses into the alloy, figure 2.53a. The carbon activity in the alloy increases until it is thermodynamically favourable for M_{23}C_6 precipitates to form, figure 2.53b. Initially these are rich in chromium but with further increase in carbon activity, Fe (and Ni to a lesser extent) are also incorporated into the carbides. As more carbon diffuses into the alloy the carbide precipitation front is driven deeper into the alloy and the carbon activity increases until it becomes thermodynamically favourable for the M_{23}C_6 precipitates to transform to M_7C_3 , figure 2.53c. The M_7C_3 carbides are rich in chromium and thus it is assumed that the Fe and Ni which had been present in the M_{23}C_6 precipitates are rejected as metallic particles. Further increase in a_c results in the M_7C_3 carbides growing and becoming richer in Fe and Ni. The process continues until a_c throughout the alloy reaches the level in the gas, resulting in a uniform distribution of M_7C_3 precipitates, figure 2.53d.

Very similar results to these have been reported by Norton and Barnes⁽¹¹⁰⁾ for 25Cr-20Ni-Fe, 25Cr-35Ni-Fe and 20Cr-32Ni-Fe alloys exposed to gaseous environments with carbon activities of 0,8 and 0,3 at 825°C and 1050°C.

The kinetics of the carburization process are parabolic with both Schnaas and Grabke⁽⁹⁹⁾ and Norton and Barnes⁽¹¹⁰⁾ attributing the rate determining process to the diffusion of carbon through the base metal in the carbide precipitate zone. The components of the alloy which form the carbides are virtually immovable compared to the inward diffusion of carbon. The depth of the carbide zone (ξ) can therefore be written

$$\xi^2 = \frac{2\varepsilon D_c C_c}{v C_M} = 2k't \quad (2.19)$$

where D_c is the diffusivity of carbon in an Fe-Ni matrix

C_c is the solubility of carbon in the Fe-Ni matrix at the surface after precipitation of the carbides

v is the stoichiometric ratio = C/M in the carbides MC_v , an average value of which may be calculated

and C_M is the concentration of the metal elements precipitating in the carbide formation i.e. mainly chromium concentration.

A labyrinth factor (ε) must be introduced since the diffusion path is partially blocked by carbide particles. It must be noted that the values of ε , D_c , C_c , C_M and v are changing with time and distance from the surface, and therefore the equation is only an approximation. The temperature dependence of the internal carbide formation which is caused mainly by the temperature dependence of the solubility and diffusivity is given by :

$$\frac{\delta \ln K}{\delta 1/T} = \delta \ln D_c / \delta 1/T + \delta \ln C_c / \delta 1/T \quad (2.20)$$

which gives

$$Q = Q_D + \overline{\Delta H_C} \quad (2.21)$$

Thus, the effective activation energy of the internal carbide formation (Q) should be given approximately by the sum of the activation energy for carbon diffusion (Q_D) and the partial molar enthalpy of solution of carbon ($\overline{\Delta H_C}$).

This was confirmed by Schnaas and Grabke⁽⁹⁹⁾ who found good agreement between their experimentally determined value of $Q = 167$ KJ/mole for Incoloy 800 and the sum of $Q_D = 109$ KJ/mole⁽¹¹²⁾ and $\overline{\Delta H_C} = 63$ KJ/mole⁽¹¹²⁾.

Figure 2.54 summarises the carburization kinetics for 25Cr-35Ni-Fe alloys. It is clear from this figure that increasing the temperature from 825°C to 1050°C dramatically increases the rate of the process, with the rate constant approximately doubling for every 50°C incremental increase. Increasing the carbon activity in the gas also significantly increases the rate of diffusion particularly at the higher temperatures.

Other factors influencing Carburization

Van der Biest⁽¹¹³⁾ et al. and Demel and Degischer⁽¹¹⁴⁾ have indicated that the presence of surface carbides can reduce the amount of carburization. However because of the high solubility and diffusivity of carbon in the matrix it is unlikely that surface carbide layers offer any long term protection against carbon ingress.

Gravernhorst and Steinkusch⁽¹¹⁵⁾ and Grabke et al.⁽¹¹⁶⁾ showed that carburization can be retarded by increasing the nickel content of the alloys. The optimum composition appears to be an alloy with a Ni:Fe ratio of approximately 4:1. This is due to the low solubility of C in Ni. Wada et al.⁽¹¹²⁾ have shown that in the case of an Ni-Fe alloy the solubility of C is at a minimum value of about 70 % Ni and hint that this is due to the existence of two electronic states of Fe atoms in the alloy.

The addition of Si to the alloy can also retard carburization by reducing the solubility and diffusivity of carbon in the matrix as has been shown by Roy et al.⁽¹¹⁷⁾ and Smith⁽¹¹⁸⁾. However this is relatively minor compared to the beneficial effect of an SiO₂ barrier layer which can form at very low values pO₂ in oxidising/carburizing environments, as shown by Van der Biest et al.⁽¹¹³⁾.

Smith et al.⁽¹¹⁹⁾ have studied the effect of other minor alloying elements such as Nb, Ti and Al on carburization. It was found that Nb and Ti which are strong carbide forming elements reduce carburization by the NbC and TiC carbides precipitates blocking some of the carbon diffusion paths. Aluminium was also beneficial. It was assumed that this is due to Al reducing the solubility of C in the matrix as in the case of Ni and Si. However there appears to be no scientific evidence

available to confirm this. Again this would appear to be relatively minor compared to the beneficial effect of an Al_2O_3 layer as shown by Perkins and Goldberg⁽¹²⁰⁾.

Finally it is worthwhile mentioning the effect of surface condition and metallurgical form on carburization. It is clear from the work of Harrison et al.⁽¹⁰⁰⁾ that surface working has no effect on the carburization behaviour of ternary Fe-Ni-Cr alloys, however when other elements are added to the alloy such as Si and Mn, surface working significantly reduces the extent of carburization. This would appear to be due to the formation of a SiO_2 layer, as demonstrated by Van der Biest et al.⁽¹¹³⁾, under slightly oxidising conditions, with the surface working aiding the diffusion of Si to the surface. It is unclear from the literature as to whether there is any effect due to surface working under purely carburizing conditions.

Swales⁽¹²¹⁾ has indicated that metallurgical form can influence the amount of carburization, with alloys with a small grain size and thus a higher number of grain boundaries being more susceptible to carbon ingress.

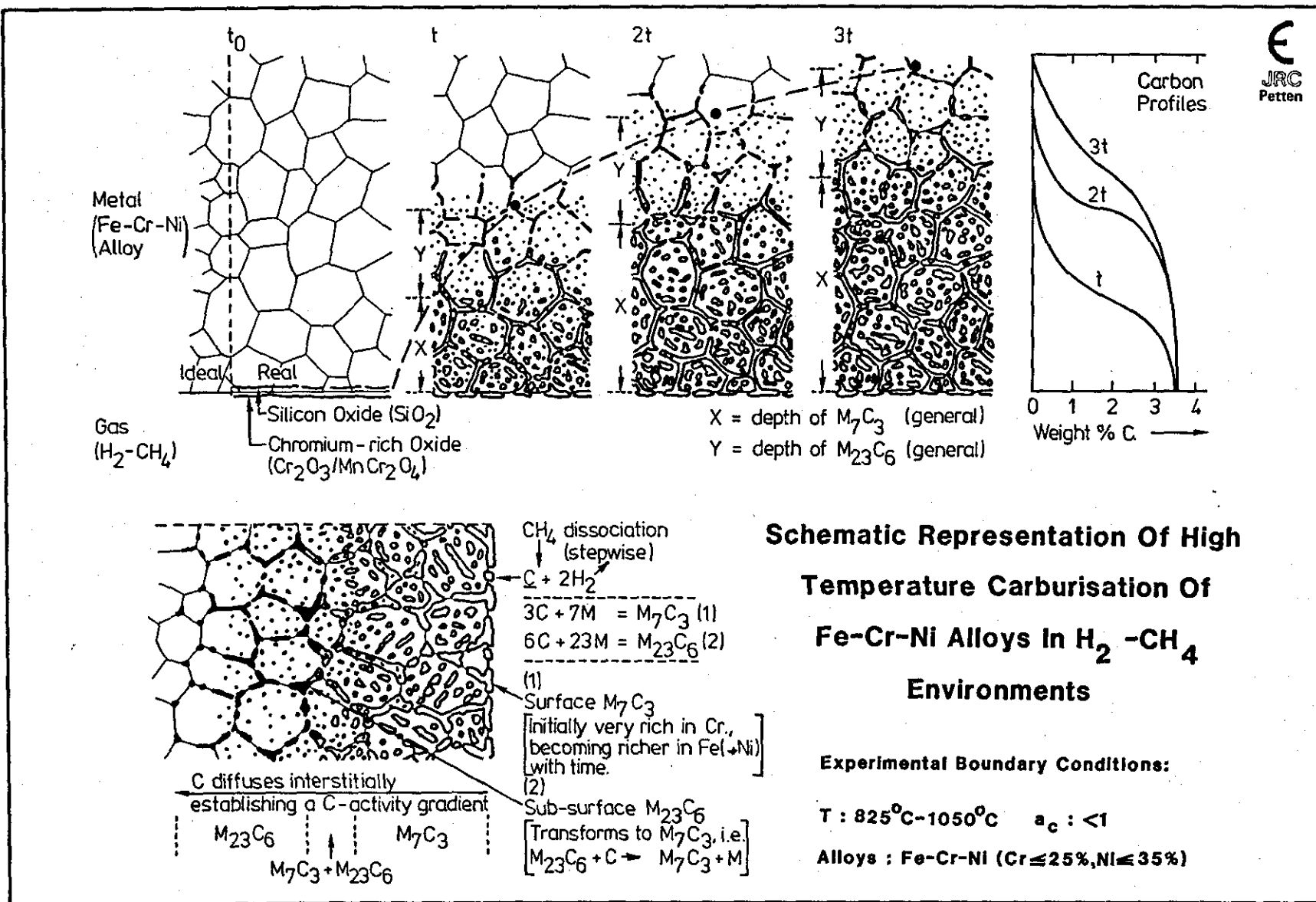


Figure 2.48

Schematic representation of high temperature carburization of Fe-Cr-Ni alloys in H_2-CH_4 environments (102).

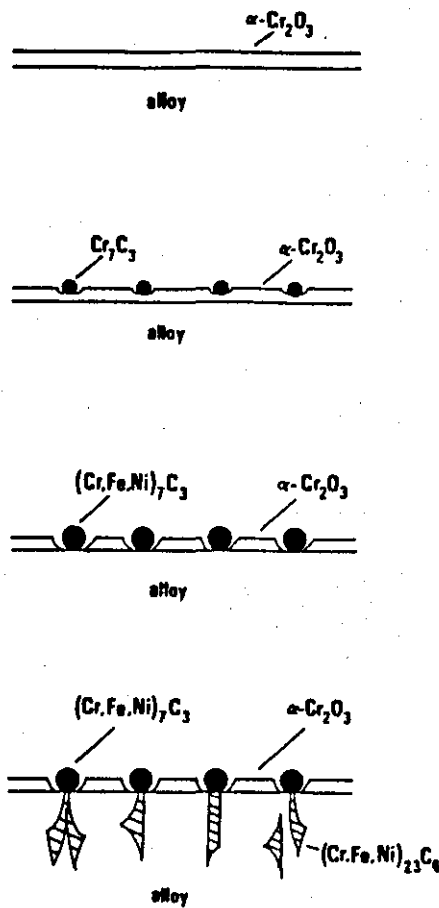


Figure 2.49

Schematic illustration of the early stages in the formation and growth of carbides in the surface regions of the alloys (103).

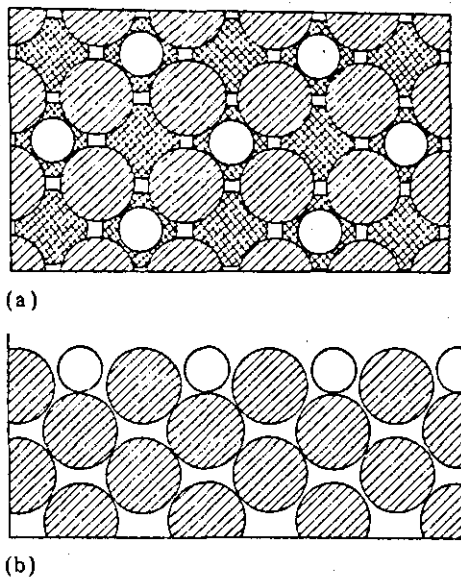


Figure 2.50

An atomic model of the adsorption of carbon on a (100) Fe surface:

a) The top view.

b) The cross section in the 110 direction (104).

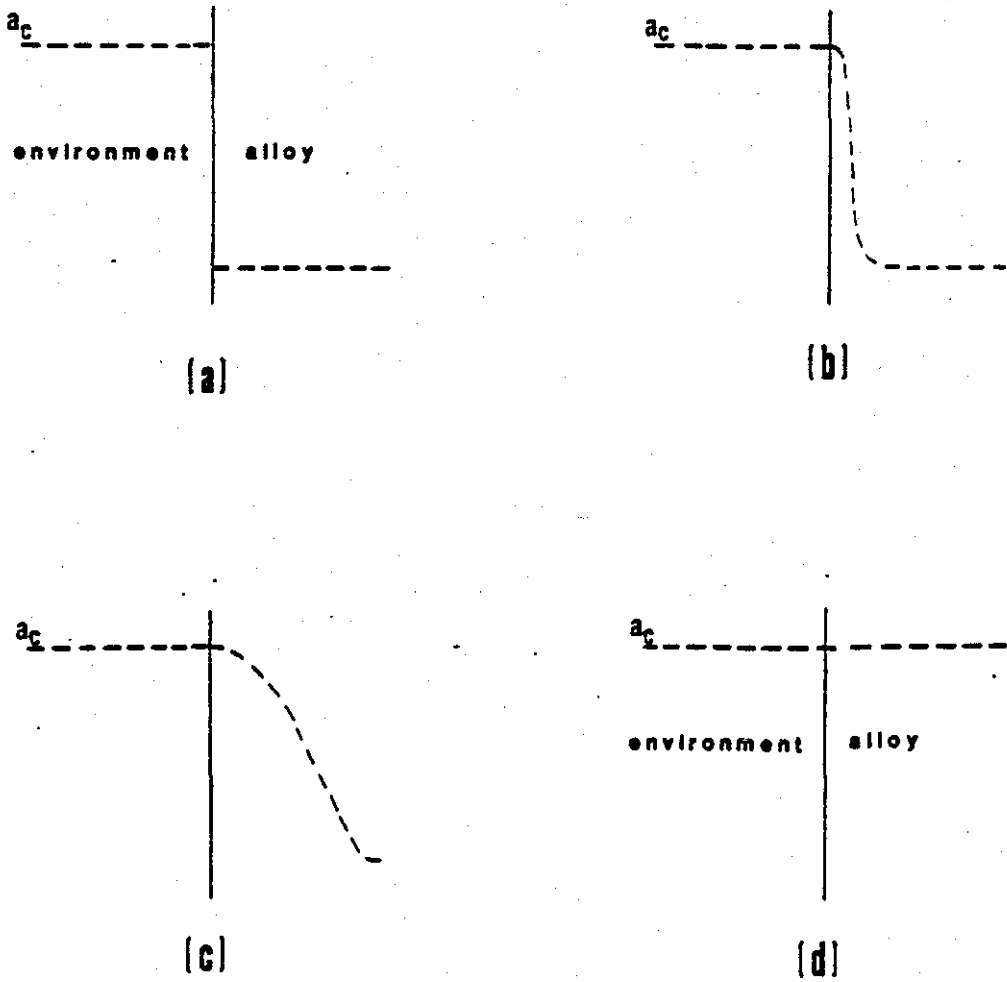


Figure 2.51

Schematic representation of the various stages of carburization of an alloy when carbide formation does not occur:

- a) Initial situation.
- b) Equilibrium of alloy surface with environment.
- c) Inward diffusion of carbon.
- d) Final situation (97).

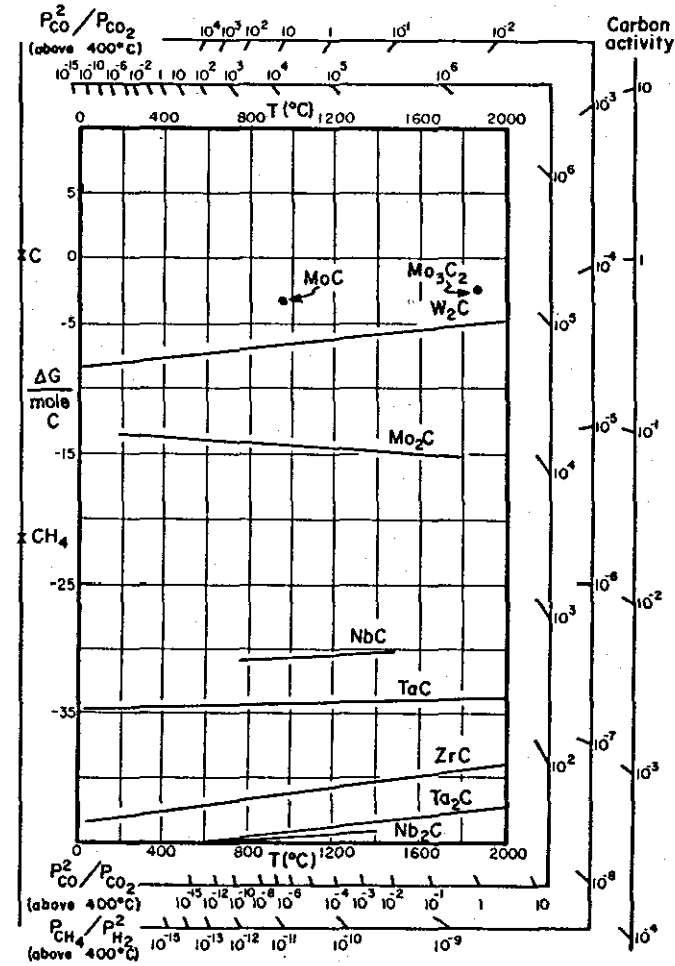
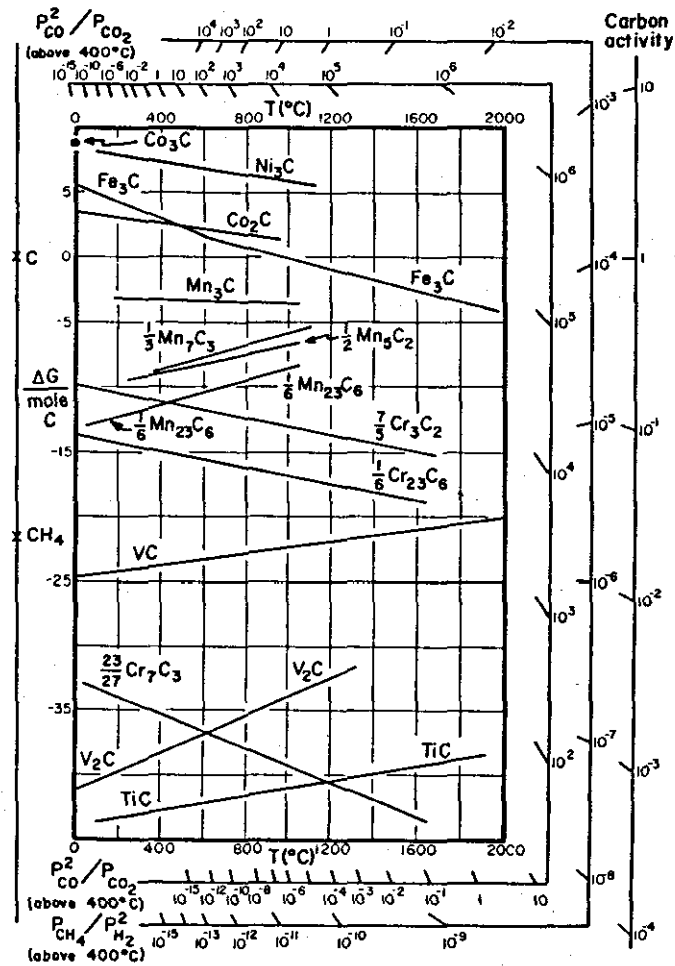


Figure 2.52
Ellingham diagrams for metal carbides (106).

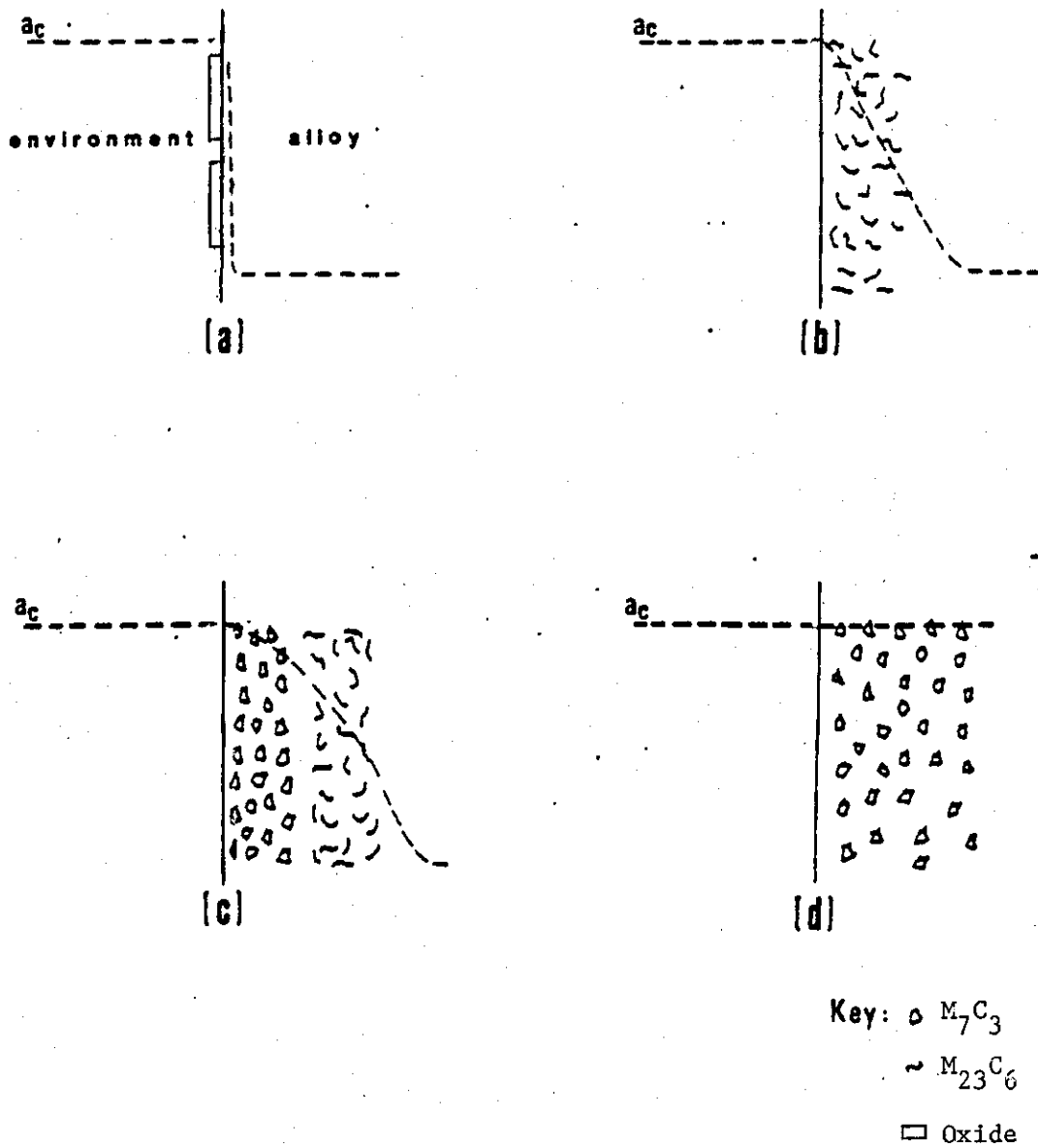


Figure 2.53

Schematic illustration showing the sequence of events involved in the carburization of an austenitic stainless steel (97).

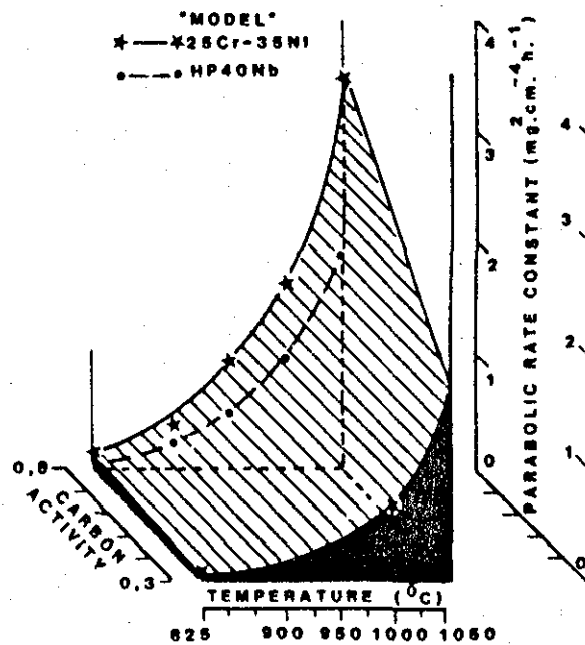


Figure 2.54
Conjoint influence of temperature and carbon activity upon corrosion kinetics of 25Cr-35Ni-Fe alloys (110).

2.3. CORROSION PROCESSES IN MULTI-REACTANT GASEOUS ENVIRONMENTS

2.3.1. Thermodynamic considerations

Earlier in this literature review in-depth consideration was given to the reaction of metals and alloys with single-reactant environments containing oxygen, sulphur or carbon. It was clear that a stable oxide, sulphide or carbide could form if the activity of the species in the atmosphere, expressed in terms of pO_2 , pS_2 or a_c , exceeded a critical value determined by the free energy change for the reaction at a given temperature. The Ellingham diagram was shown to be not only an extremely useful means of presenting these thermodynamic data, but also enabled the relative stabilities of different metal oxides, sulphides and carbides to be easily compared.

In order to aid in understanding the situation which develops in the more complex multi-reactant atmospheres, it is necessary to develop these thermodynamic considerations further in order to establish what will happen when a metal or alloy is subjected to a gaseous environment containing several reactants. Such environments can be characterised at elevated temperatures in terms of the reactant activities according to the method described in appendix 1.

Metals exposed to environments containing more than one reactant

If the reaction between a metal and two gaseous reactants is considered, the regions of stability of the various phases can be predicted from thermodynamic considerations and depicted in the form of phase stability diagrams. Figure 2.55 gives a schematic representation of one of these diagrams involving the reaction of a metal (M) with two reactants, in this example selected as sulphur (S) and oxygen (O). (In the interests of brevity the method of construction of such a diagram is described in detail elsewhere, appendix 2).

If the metal is exposed to a gas of composition A at temperature T (i.e. $pO_2 < x$ and $pS_2 < y$) it will remain inert. If however the value of $pO_2 > x$ (position B) it is possible for metal oxide to be in stable equilibrium with the gas and thus a MO surface scale can form. Likewise if the $pS_2 > y$ (position C) MS can form. At positions D and E where

$pO_2 > x$ and $pS_2 > y$ it is thermodynamically possible for both the sulphide and oxide to form. However unless the composition of the gas is actually on the upper diagonal boundary that defines the equilibrium between MS and MO, it is only possible for one phase to come to stable equilibrium with the gas. Thus, to the right of this line (position D) MO is in equilibrium with the gas phase, but MS can exist at the metal/scale interface, where the equilibrium oxygen pressure is lower. Likewise to the left of the diagonal boundary (position E) MS is in equilibrium with the gas phase but MO can exist at the metal/scale interface.

Many workers such as Hemmings and Perkins⁽¹²²⁾, Natesan⁽¹²³⁾ and Gulbransen and Jansson⁽¹²⁴⁾ have constructed phase stability diagrams for a number of M-O-S systems at various temperatures. A large number of similar diagrams for M-O-C systems have been constructed by Bresselers et al.⁽¹⁰⁷⁾ and Grabke and Schnaas⁽¹⁰⁸⁾ and M-S-C systems by Barnes et al.⁽¹²⁵⁾. Such diagrams for Cr-O-S, Cr-O-C and Cr-S-C at 800°C which apply to this study are shown in figure 2.56.

It is sometimes possible for a metal to form more than one sulphide, carbide or even oxide. If this is the case the regions of stability of these reaction products can also be marked on the diagrams. For example, from figure 2.56 it is clear that if chromium is exposed to an environment containing a $pS_2 > 10^{-4}$ atm. it is possible for a sulphide with a higher S to Cr ratio (Cr_7S_8) to exist. Similarly as the carbon activity is increased carbides with higher C to M ratios can exist, e.g. $Cr_{23}C_6 < Cr_7C_3 < Cr_3C_2$.

If the situation is now considered where a metal is exposed to an environment containing all three reactants O, S and C, problems arise in using the binary M-O-S, M-O-C and M-S-C phase stability diagrams. For example if chromium is exposed to gas having the activities $pO_2 = 10^{-21}$ atm., $pS_2 = 10^{-9}$ atm. and $a_c = 0,4$ at 800°C (position A on figure 2.56a) it is impossible to determine whether Cr_2O_3 (figures 2.56a and b) or CrS (figure 2.56c) will be in equilibrium with the gas. To overcome this problem Wang and Douglass⁽¹⁰⁹⁾ constructed a 3-dimensional metal stability diagram for the Cr-O-S-C system, figure 2.57. Thus by taking a

section through this diagram at the given carbon activity (0.4), figure 2.58, it becomes clear that Cr_2O_3 and not CrS will form at the scale/gas interface.

Alloys exposed to environments containing more than one reactant

In considering the behaviour of alloys in multi-reactant gas mixtures it has become common practice to superimpose several binary diagrams of the major metallic elements in order to obtain information on the stability of surface phases. Figure 2.59a gives an example where the binary Cr-O-S and Ni-O-S have been drawn on one diagram⁽¹²⁶⁾. However these diagrams only indicate which phase will be in equilibrium with a gas of given composition, i.e. the situation at the scale/gas interface.

If a typical scale formed on an alloy is considered in cross section (figure 2.59b) the activity of the reactants will decrease from a maximum value at the scale/gas interface to a minimum in the alloy, whilst the activity of the metallic elements increases. This is the basis of "the reaction path" concept which was introduced by Stringer and Whittle⁽¹²⁷⁾ and used to explain why certain phases occur in certain places. For example the scale morphology shown in cross section in figure 2.59b can be explained by following the broken line from position A to position D on the phase stability diagram.

At the gas/scale interface (A) NiS is in equilibrium with the gas. As the local values of $p\text{O}_2$ and $p\text{S}_2$ decrease through the scale a point (B) is reached where the value of $p\text{S}_2$ is below the Ni/NiS boundary but the value of $p\text{O}_2$ is still sufficiently high for Cr_2O_3 to form and this explains the presence of the Cr_2O_3 layer beneath the NiS layer. At position C the $p\text{O}_2$ value has become too low for Cr_2O_3 to be stable but the $p\text{S}_2$ is still sufficient for CrS to form, hence explaining the presence of CrS precipitates in the alloy. Finally position D is reached where only the alloy is stable.

It therefore appears that the use of superimposed thermodynamic phase stability diagrams to explain the occurrence of the various corrosion products is relatively straight-forward. Unfortunately there are a number of limitations to these diagrams which are not always realised.

- (i) The lines on the diagrams are for unit metal activity, both in the alloy and in the corrosion product.
- (ii) The diagrams are sometimes calculated without considering any interactions between metallic phases to form reaction products containing both metals e.g. NiCr_2O_4 .
- (iii) Phases are sometimes identified on the diagrams although they do not form. For example for the gas composition E in figure 2.59a both NiO and Cr_2O_3 are stable but perhaps, due to kinetic reasons or the relative concentrations of each element in the alloy, only one oxide forms.

A number of modifications have been proposed to overcome these limitations.

Firstly, lines indicating the position of boundaries for metal activities of less than one in the alloy can be marked on the diagrams. For example the broken line on figure 2.60 indicates the position of the Cr/CrS and $\text{Cr/Cr}_2\text{O}_3$ boundaries for an alloy in which the activity of chromium $a_{\text{Cr}} = 0.1$ at 800°C . Whereas a $p_{\text{S}_2} > 10^{-14}$ atm. is required to convert pure Cr to CrS, in the case of the alloy the p_{S_2} must be increased by two orders of magnitude to 10^{-12} atm. before the sulphide can form. Similarly for the oxide to form on the alloy the p_{O_2} must be increased by approximately 1.9 orders of magnitude.

Very interesting diagrams illustrating the effect of metal activity on metal/ metal oxide (figure 2.61) and metal/metal carbide (figure 2.62) phase stability boundaries have been constructed by Bresseleers et al. (107) Figure 2.61 shows that with the exception of Nb no cross-over of the lines occurs for oxide systems at 1098K within the range $a_{\text{M}} = 1$ to 0.01, i.e. it will always be possible for Cr_2O_3 to form at a lower p_{O_2} than FeO regardless of the activity of the elements in the alloy. Conversely figure 2.62 indicates considerable crossing of the lines for carbides. For example in the chromium carbide system the stability sequence changes from $\text{Cr/Cr}_{23}\text{C}_6/\text{Cr}_7\text{C}_3/\text{Cr}_3\text{C}_2$ at unit activity to $\text{Cr/Cr}_7\text{C}_3/\text{Cr}_{23}\text{C}_6/\text{Cr}_3\text{C}_2$ at $a_{\text{Cr}} = 0.7$ and subsequently to $\text{Cr/Cr}_7\text{C}_3/\text{Cr}_3\text{C}_2/\text{Cr}_{23}\text{C}_6$ at $a_{\text{Cr}} = 0.3$ and $\text{Cr/Cr}_3\text{C}_2/\text{Cr}_7\text{C}_3/\text{Cr}_{23}\text{C}_6$ at

$a_{\text{Cr}} = 0.1$. This point is often not appreciated or taken account of in thermodynamic phase stability considerations. Such diagrams for sulphides are, at present, not available in the literature.

Perhaps at this stage it is worthwhile examining typical activity values for the metallic constituents in the alloys relevant to this study.

A systematic study of the activity of Cr (a_{Cr}) in Fe-Cr, Ni-Cr and Fe-Ni-Cr alloys has been carried out by Mazandarany and Pehlke⁽¹²⁸⁾, the results of which showed that a_{Cr} is not directly related simply to the atomic fraction of Cr in the alloy, as indicated by the straight line on figure 2.63. Due to interactive influence of the other alloying element(s) the chromium activity was considerably higher than expected. For example figure 2.63 shows that a Fe-Cr alloy containing 20 at% Cr at 1000°C had a chromium activity of approximately 0.35 and that lowering the temperature by 100°C to 900°C increased a_{Cr} to 0.4. In ternary alloys the presence of Ni was found to significantly increase a_{Cr} . For example a 20Cr-35Ni-Fe alloy had a chromium activity of approximately 0.5 at 1000°C, figure 2.64. Whilst considering this figure it is worth pointing out that if during the corrosion process the alloy became depleted in chromium to a value of say 9 at.%, a_{Cr} would be more than halved to 0.22.

Therefore in general terms typical a_{Cr} values of 0.2 to 0.6 occur in FeCrNi alloys in the temperature range 800-1000°C. When related back to the Cr-O-S phase stability diagram (figure 2.60) this results in a 1-2 orders of magnitude positive shift in the Cr/CrS and Cr/Cr₂O₃ boundaries. In the case of the chromium carbide system it is perhaps better not to generalise at this stage due to the change in relative stabilities of the carbides with metal activity.

Having considered the activity of the metallic constituents in the alloy it is now possible to consider the activity of these constituents in the reaction products. This can be done by examining the three-dimensional metal stability model for Ni-Cr-O-S system, figure 2.65, constructed by Giggins and Pettit⁽¹²⁹⁾.

In the model, the binary phase stability diagrams for the Cr and Ni systems are used to form the vertical front and back planes respectively, with $\log pO_2$ and $\log pS_2$ as variables. The space created between them is used to indicate which phase can be stable for given activities of Cr or Ni in the reaction product; i.e. the vertical side plane consists of the stability diagram for the Ni-Cr-O system (figure 2.65d) with a_{Cr} and $\log pO_2$ as variables and the horizontal plane consisting of the Ni-Cr-S stability diagram with a_{Cr} and pS_2 as variables. The Ni-Cr-S and Ni-Cr-O diagrams were constructed from thermodynamic data⁽¹³⁰⁾. Thus, if a gas composition of fixed pO_2 and pS_2 , marked by the rod on the diagrams is considered, it is clear that when the activity of Cr in the reaction product is unity (right hand side of figure 2.65b) Cr_2O_3 will be in stable equilibrium with the gas. But as the activity of Cr in the reaction product is reduced, a solution of CrS , $NiCr_2S_4$ and NiS can be in stable equilibrium with the gas.

The 3-dimensional phase stability diagram can also be used to explain the previously mentioned limitations of 2-dimensional phase stability diagrams. For instance it is now easy to see that the reaction products containing both metals e.g. $NiCr_2O_4$ are absent from the 2-dimensional diagram because they occur in the space created between the primary planes of the chromium and nickel systems. It is now also obvious why only one corrosion product occurs when it appears that two are stable on the 2-dimensional diagram. For example gas composition E on figure 2.59a indicated that both NiO and Cr_2O_3 were stable. However if the activity of Cr in the corrosion product is significant it will fall in the right hand side of figure 2.65b and hence Cr_2O_3 and not NiO will form.

Similar diagrams for the Fe-Cr-O-S system at $1000^\circ C$ have been constructed by Tellez⁽¹³¹⁾. Although such diagrams are very useful for identifying the limitations of superimposed binary metal stability diagrams, they are extremely complicated and tedious to construct and often the thermodynamic data for all the intermediate compounds e.g. $MnCr_2O_4$ do not exist. Four component systems can be considered but the diagrams obviously cannot be constructed for ternary or more complex alloys.

In summary it has been seen that thermodynamics provide a very useful guide as to which corrosion products may form when a metal or alloy is exposed to a multicomponent gaseous environment at a given temperature. However many other factors such as kinetic rates of formation, activities of the various components in both the alloy and the reaction product can result in different behaviour in practice to that predicted from theory. Thus it is necessary to examine the specific experimental findings of various research workers.

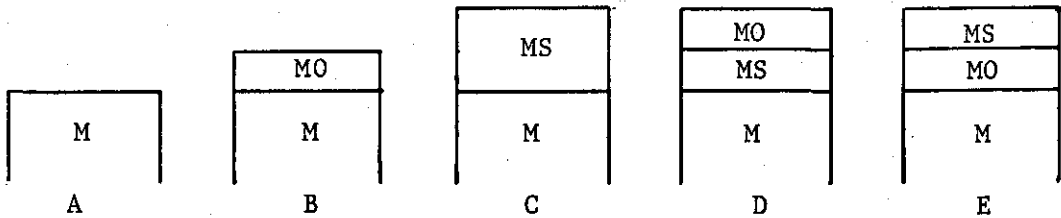
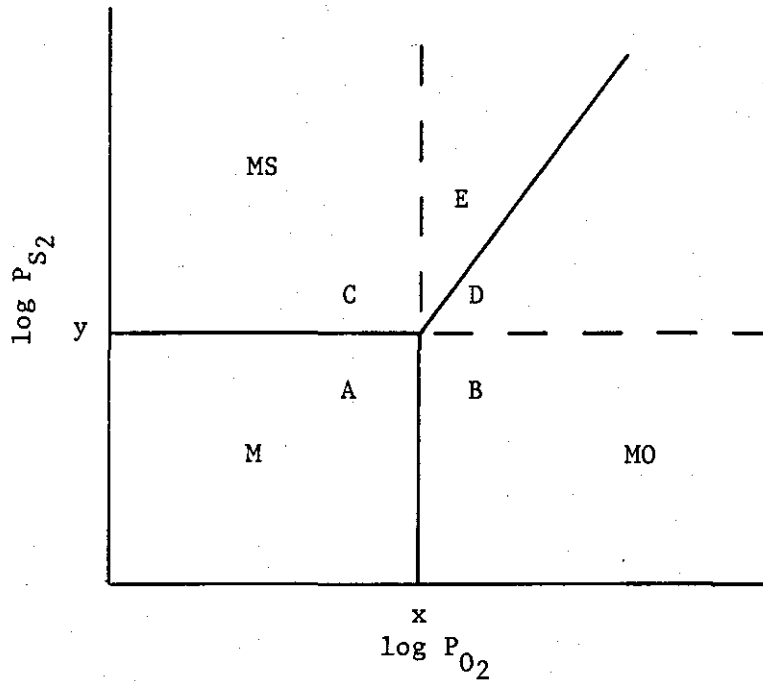


Figure 2.55
Schematic metal stability diagram for the M-O-S system at temperature T, showing the possible reaction products that can form when a pure metal is exposed to an environment containing the reactants O and S.

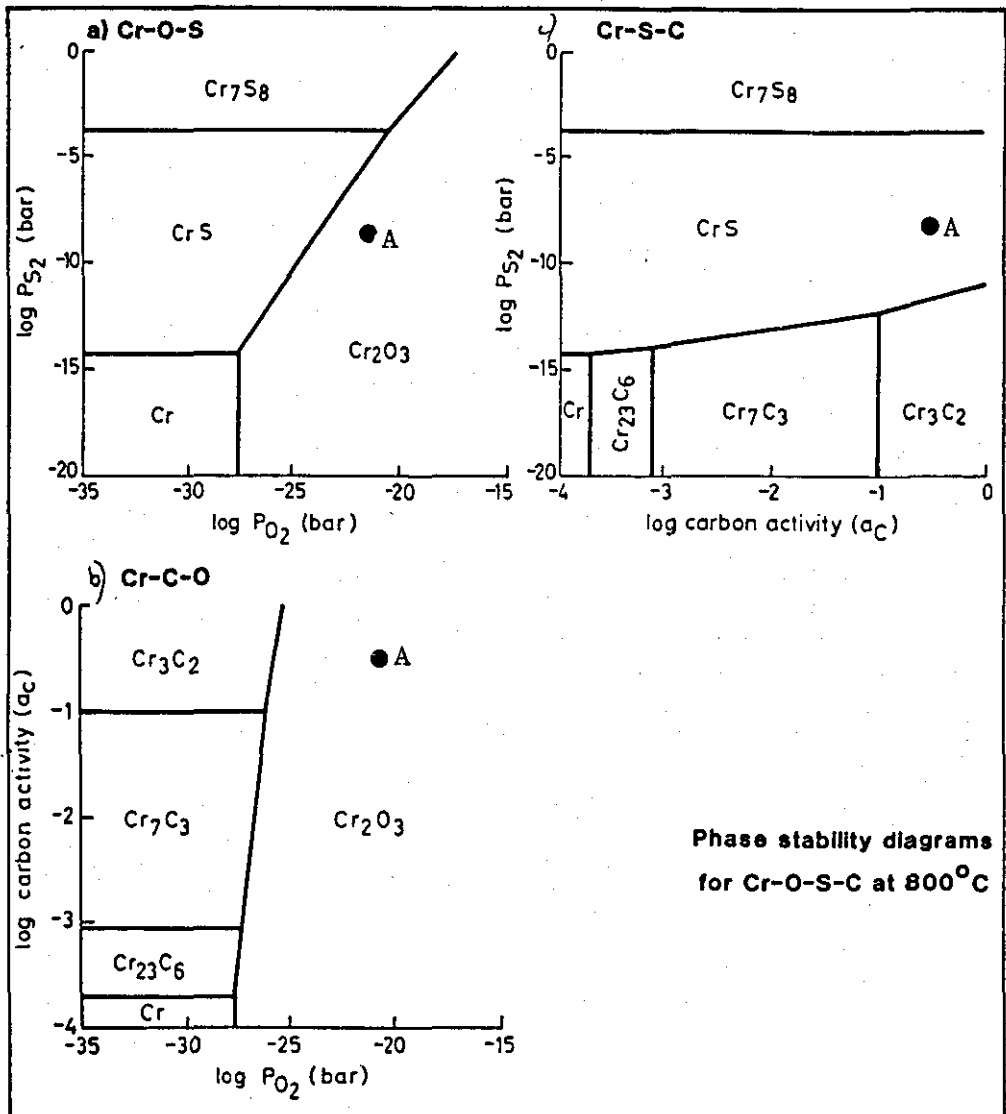


Figure 2.56
Phase stability diagrams for Cr-O-S-C at 800°C.

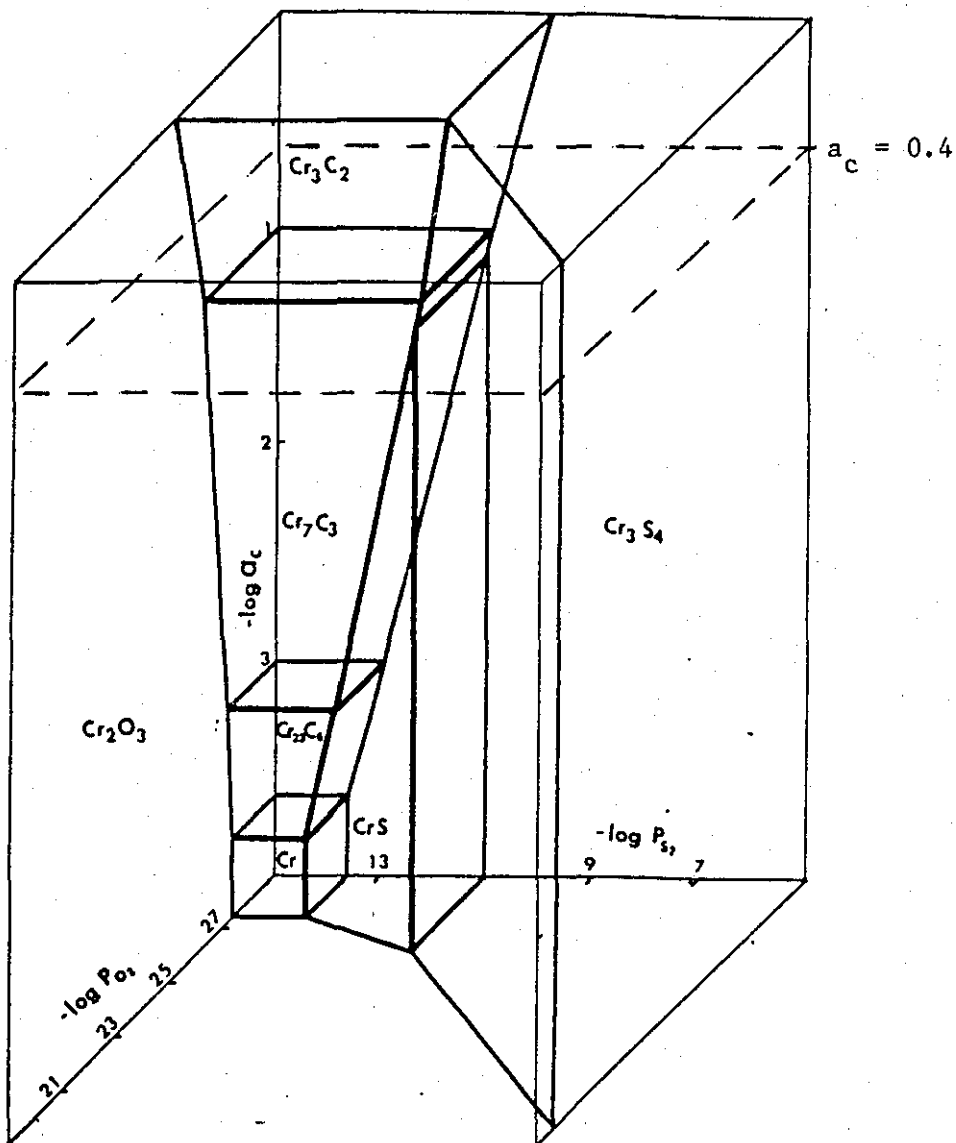


Figure 2.57
Three-dimensional metal stability diagram for the system Cr-O-S-C at 800°C, showing the position of the section taken for a fixed carbon activity of 0.4 (109).

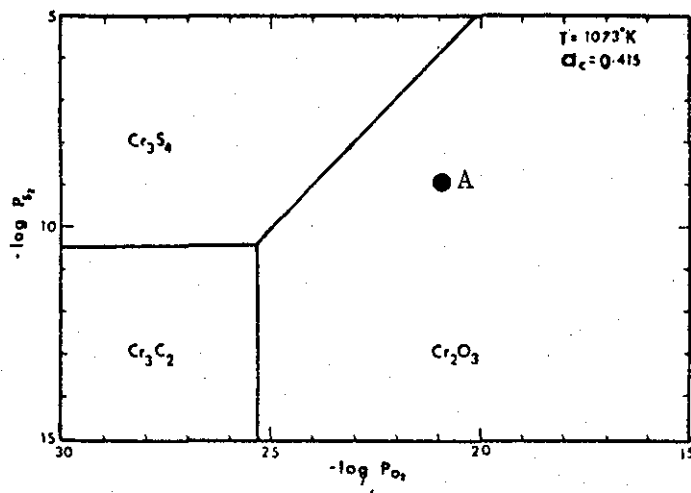


Figure 2.58

Cross-section taken from figure 2.57 for the Cr-S-O system at a fixed carbon activity of 0.4 at 800°C (109).

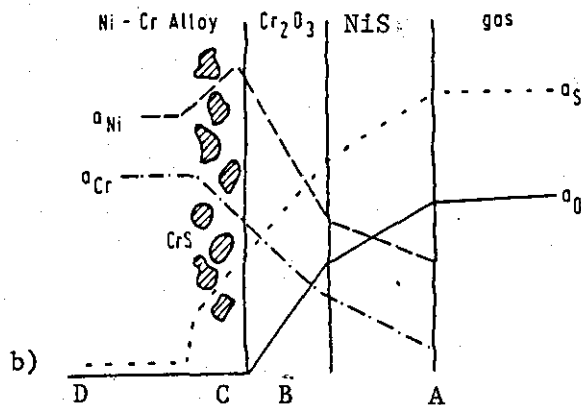
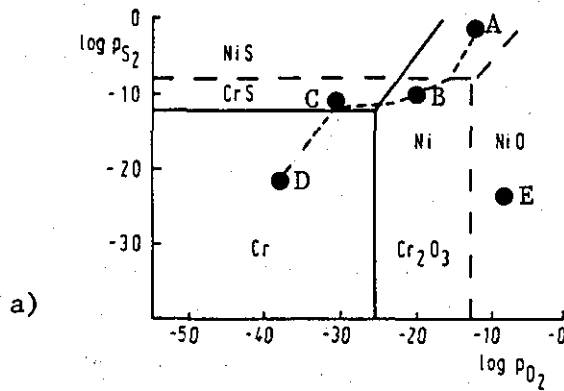


Figure 2.59a

Superimposed phase stability diagram and reaction path depicting the change of sulphur and oxygen activities in the reaction products when a Ni-Cr alloy is exposed to a gaseous environment containing the reactants O and S.

Figure 2.59b

Cross-section taken through the scale and alloy giving the sequence of the reaction products and changes in element activities (adapted from Grabke 126).

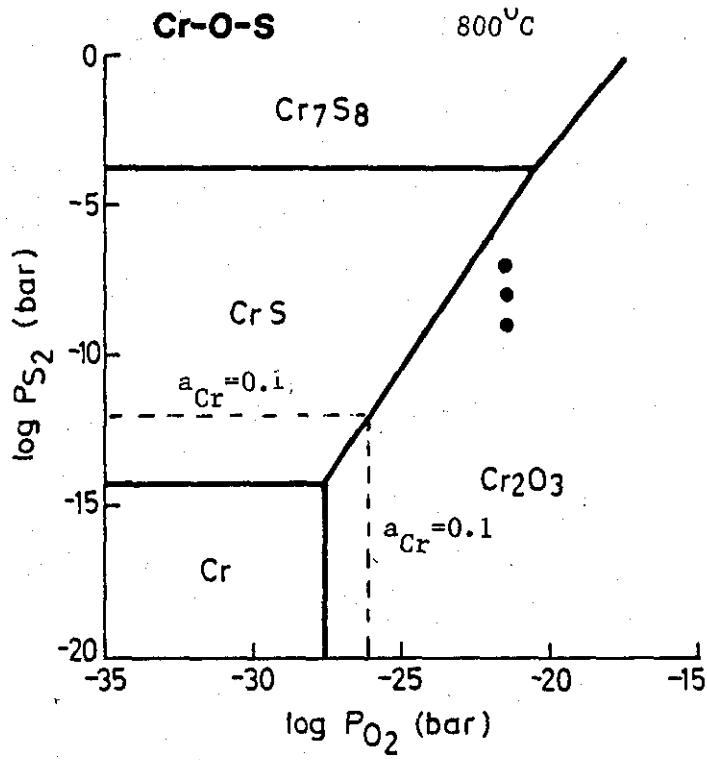


Figure 2.60
Effect of decreasing the activity of Chromium in the alloy on the Cr/Cr_2O_3 and Cr/CrS boundaries.

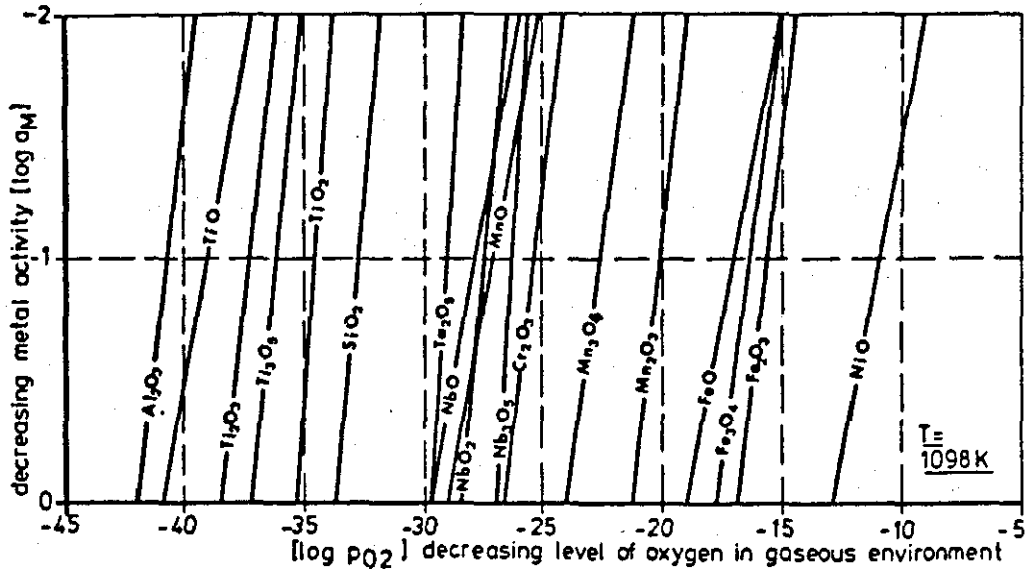


Figure 2.61

Effect of oxygen level (P_{O_2}) and metal activity (a_m) on reaction of metals to form stable oxides (107).

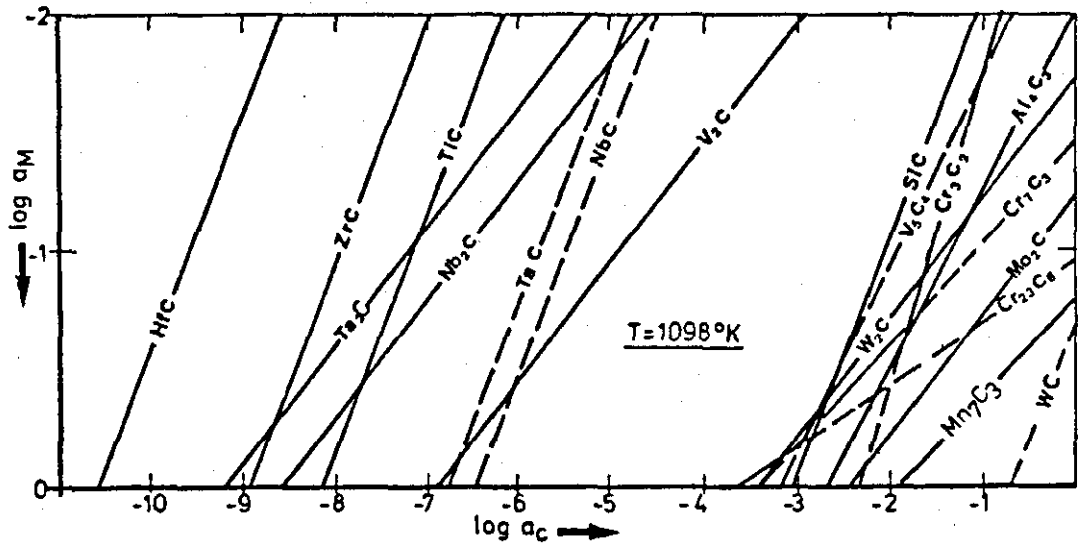


Figure 2.62

Effect of carbon activity (a_c) and metal activity (a_m) on reaction of metals to form stable carbides (107).

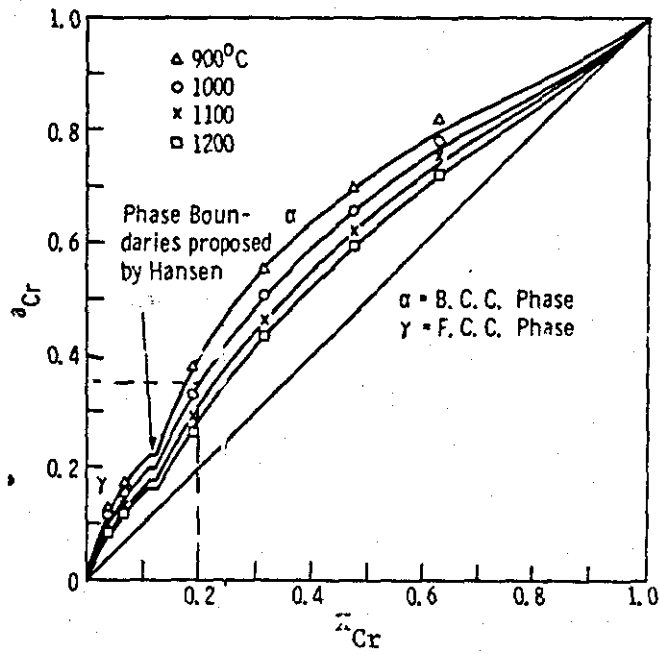


Figure 2.63
Thermodynamic activity of chromium in the solid Fe-Cr system referred to pure Cr (128).
(X = atomic fraction)

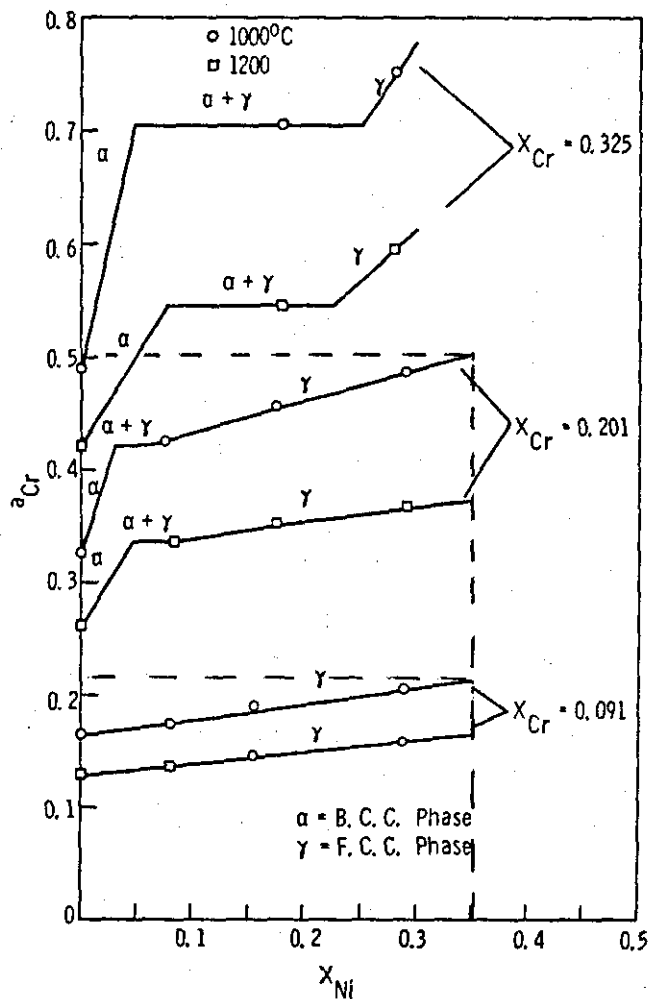


Figure 2.64
Thermodynamic activity of chromium in the solid Fe-Ni-Cr system referred to solid pure Cr; effect of Ni at constant Cr contents (128).

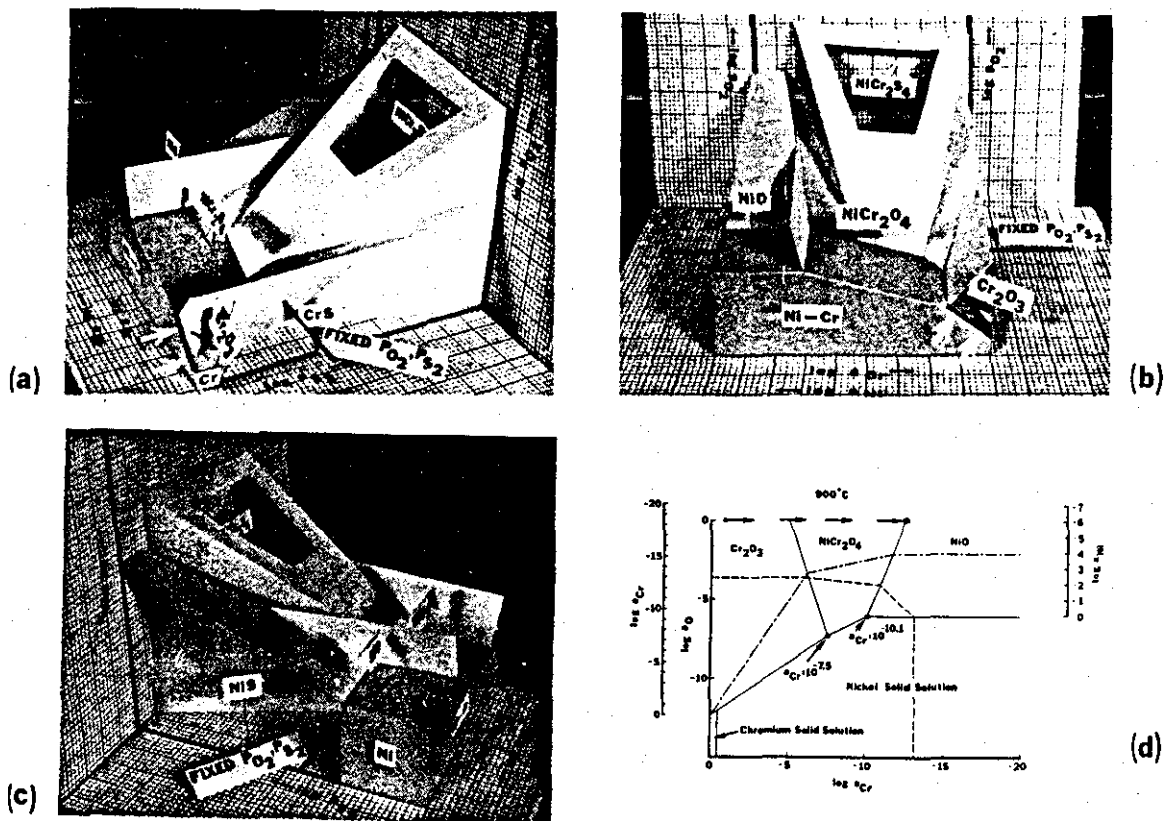


Figure 2.65

Three views (a,b,c) of a schematic three-dimensional stability diagram for the Ni-Cr-O-S system. The rod extending through the diagram shows the phases which are stable in a fixed gas composition. (d) Stability diagram for the Ni-Cr-O system with isoactivity lines for Cr (---) and Ni (- - -). (129).

2.3.2. Carburization/Oxidation

A considerable amount of research has taken place in environments containing the reactants (C) and (O). For the purpose of this literature review the findings of various workers will be reviewed in a systematic manner by considering the changes resulting from a progressive increase in oxygen activity of these environments, figure 2.66. From basic thermodynamic considerations this figure can be divided into the following regions:

- (a) Carbides could be in stable equilibrium with the gas but no oxides could be thermodynamically stable.
- (b) Carbides could be in stable equilibrium with the gas and the oxygen partial pressure could be sufficient for SiO_2 to form at the scale/alloy interface.
- (c) Carbides and SiO_2 could be in equilibrium with the gas.
- (d) Carbides and SiO_2 could be stable with the gas and the oxygen partial pressure could be sufficient for Cr_2O_3 to form at the scale/alloy interface.
- (e) Carbides, SiO_2 , Cr_2O_3 could be stable in the gas.
- (f) Carbides, SiO_2 , Cr_2O_3 and oxides of Fe and Ni could be stable in the gas.
- (a) Carbides could be in stable equilibrium with the gas but no oxides could be thermodynamically stable.

This region corresponds to the case of pure carburization. A typical cross-sectional morphology consisting of M_7C_3 surface carbides and internal M_7C_3 (outer zone) and M_{23}C_6 (inner zone) precipitates is shown in figure 2.66a. The carburization mechanism resulting in this morphology was described in detail earlier in this review.

The effect of Silicon

Several studies have been carried out in environments where SiO_2 can form viz. Harrison et al.⁽¹⁰⁰⁾, Norton et al.⁽¹⁰¹⁾ and Van der Biest et al.⁽¹¹³⁾ with $a_c = 0.3$ and 0.8 at 825°C ; Kane⁽¹³²⁾ with $a_c = 1$ at 1366K (1093°C); Ramanarayanan and Petkovic-Luton⁽¹³³⁾ at 1150°C and Tomas et al.⁽¹³⁴⁾ with $a_c = 1$ at 1000°C . With the exception of Tomas et al. the results are in very good agreement with each other. The corrosion behaviour in this regime can best be described by considering the results of Kane⁽¹³²⁾ who made the most systematic study.

Kane systematically varied the water level and hence the oxygen level in the gas. The findings can be divided into 2 regions.

- (b) Values of $p\text{O}_2$ below the SiC/SiO_2 boundary
 - (c) Values of $p\text{O}_2$ above the SiC/SiO_2 boundary
- (b) $p\text{O}_2$ below the SiC/SiO_2 boundary

At these low oxygen levels carburization was extensive. The morphology and extent of the carbides was the same as in the purely carburizing regime, figures 2.66 a and b. Kane indicates that there was some evidence of Si rich oxides in pores but it is rather unclear as to whether this was due to exposure to the gas or that the oxides existed prior to exposure.

The Si level in the alloys did not significantly affect the level of C injected into the alloy, figure 2.67.

- (c) $p\text{O}_2$ above the SiC/SiO_2 boundary

At higher oxygen levels the behaviour depended significantly on the Si level in the alloy, the oxygen level and the amount of surface working, figure 2.66c. At oxygen levels just above the SiC/SiO_2 boundary a Si content of $> 2\%$ was required to form a complete SiO_2 layer and hence a barrier to carbon ingress, figure 2.68. At levels of Si below this, SiO_2 formed at the scale/gas interface but the layer was not complete and a significant amount of carbon ingress occurred. At higher oxygen levels

only 1.66 % Si was required to form the complete SiO_2 layer (figure 2.69) and 1.55 % Si reduced carbon ingress but did not form a complete SiO_2 layer.

The work Van der Biest et al.⁽¹¹³⁾ and Norton et al.⁽¹⁰¹⁾ shows that the formation of a complete SiO_2 layer can be aided by surface working due to the point defects and fine grain structure providing easy diffusion paths for Si to the surface and perhaps increasing the number of nucleation sites at the surface.

Finally it is important to emphasize that although a complete SiO_2 layer drastically reduces the amount of C ingress into the alloy it does not totally prevent it.

- (d) SiO_2 and carbides stable at the scale/gas interface but Cr_2O_3 could form at the scale/alloy interface

In this region Kane⁽¹³²⁾ detected no Cr_2O_3 . The behaviour of the alloys was as in the case of the previous regime, figure 2.66. The oxygen level was sufficient for a complete SiO_2 layer to form with a Si level of only 1.55 % with 1.27 % Si significantly reducing carbon ingress, figure 2.70.

- (e) Cr_2O_3 stable at the scale/gas interface but carbides can form at the scale/alloy interface

Crossing the $\text{Cr}_2\text{O}_3/\text{Cr}_x\text{C}_y$ thermodynamic boundary resulted in significantly different morphologies. A systematic study illustrating the behaviour of alloys in this region has been carried out by Meier et al.⁽¹³⁵⁾ at 850°C for 48 hour exposure periods.

Three environments were investigated, figure 2.66e.

- (i) At a carbon activity where no carbides are stable, position (i), on figure 2.66.
- (ii) At a carbon activity where some carbides are stable, position (ii), on figure 2.66.

(iii) At a carbon activity where all carbides are stable, position (iii) on figure 2.66.

The scale morphologies formed on preoxidised and ground specimens were very similar and are shown schematically in figure 2.66e. The scale in general consisted of three layers: an outer MnCr_2O_4 spinel, an intermediate Cr_2O_3 layer and an inner Si rich layer. In all cases these oxides provided good resistance to carburization. No evidence of internal carbides in pre-oxidised and ground specimens was found. However it should be pointed out that this was after a very short exposure time (48 hours).

Guttman et al.⁽¹³⁶⁾ carried out much longer testing (2000 hours) of commercial and model Fe-Cr-Ni alloys at 1000°C in an environment corresponding to position (ii) on figure 2.66. Internal carbides were found in the commercial alloys but no carbides in the model alloy. This difference was attributed to the model alloy forming a complete Cr_2O_3 layer whereas the commercial alloys formed additional M_3O_4 spinels, which did not provide such a good barrier to carbon ingress, figure 2.66e.

To help clarify the situation Wolf and Grabke⁽¹³⁷⁾ used radioactive carbon tracer techniques to investigate the mechanism of carbon transport through oxide scales. Samples of Fe-Cr alloys of varying Cr contents were preoxidised in H_2 - H_2O gas mixtures at 900°C for 100 hours. They were then exposed to H_2 - H_2O -CO-CO₂ atmospheres ($p_{\text{O}_2} = 10^{-20}$ atm., $a_c = 0.2$) at 900°C for up to ≈ 700 hours. Alloys with low Cr contents (< 5 %) contained insufficient Cr to form a complete Cr_2O_3 layer and thus were unable to provide a barrier to carburization, figure 2.71. When the Cr level was increased to 12.5 % Cr a continuous oxide formed which contained very few pores and provided a very good barrier to carburization. The number of pores in the oxide increased with higher Cr-contents, leading to greater amounts of carbides within the alloy adjacent to the oxide layer, figure 2.71. No reason is given as to why the porosity increases with increasing Cr-content.

Wolf and Grabke also showed that surface working reduced the amount of carbon ingress, figure 2.72. This is due to surface working aiding diffusion of Cr to the surface by the formation of short circuit diffusion paths. The porosity of the oxide decreased as the amount of

cold work increased and thus reduced the carbon ingress. It is interesting to note that the porosity was found to be much greater at the scale/gas interface than at the scale/alloy interface.

Wolf and Grabke concluded from their findings that carbon penetrated oxide scales by the migration of C-bearing molecules through pores and cracks in the oxide.

Before leaving this regime it is worthwhile considering further work of Meier et al.⁽¹³³⁾ who found that carburization took place on pickled and pre-corroded specimens even in environments in which the carbon activity was not sufficient for carbides to form (position (i) on figure 2.66). It was proposed that CO_2 molecules penetrated pores and voids in the Fe containing oxide scale. The CO_2 then reacted with the metal to form more oxide, reducing the local oxygen partial pressure but increasing the local carbon activity to a level where carbide formation could take place.

(f) All oxides (including oxides of Fe and Ni) are stable

The behaviour in this region is nicely illustrated by the work of Waher⁽¹³⁸⁾. Specimens of a 20Cr-30Ni-Fe alloy with and without 0.5 % Si were exposed for 24 hours in CO . This corresponds to region (e) on figure 2.66. A Cr_2O_3 layer formed on the Si free alloy and a duplex Cr_2O_3 (outer) and SiO_2 (inner) scale, on the silicon containing alloy. The specimens were then exposed in CO_2 in which oxides of iron can be stable, region (f) on figure 2.66. This resulted in Fe diffusing through the Cr_2O_3 layer to form $\text{FeFe}_{(2-x)}\text{Cr}_x\text{O}_4$ spinel nodules on the outer surface with internal oxidation of Cr also occurring, figure 2.66f. This process was much slower for the Si containing alloy indicating the SiO_2 layer acted as a barrier to the outward diffusion of Fe. Interestingly the lattice parameter of Cr_2O_3 did not change indicating that little Fe was taken into solution. However the parameter of the spinel increased with time as it became enriched in Fe. Some decarburization took place in the CO_2 environments.

When the specimens were placed back in the CO environment the spinel was reduced with the result that significant carburization took place. Once breakdown had started it did not cease.

General comments on carburization/oxidation

In general terms it is clear that the formation of complete Cr_2O_3 and/or SiO_2 scales on alloy surfaces dramatically reduces the amount of carburization. However the following points should be emphasised.

- (i) Most of the experimental work carried out in this area has been short term, typically of the order of 100 hours, maximum 2000 hours.
- (ii) Little attention has been given to the development sequence of the various corrosion morphologies.
- (iii) There must be some doubt as to whether some of the gaseous environments used were in equilibrium. Particularly in cases where carbon deposition occurred, see for example Meier et al.⁽¹³⁵⁾.
- (iv) Even when a complete oxide layer forms, a small amount of carbon ingress can take place. Although this may be of no practical significance mechanistically it could be extremely important, particularly in environments containing additional reactants such as sulphur.
- (v) With prolonged exposure the protective oxides may be disrupted or breakdown, resulting in extensive carburization. It is worthwhile considering this in more detail.

Breakdown and penetration of carbon through oxide layers

There have been several theories put forward for the breakdown and penetration of carbon through oxide scales in oxidising/carburizing environments.

- (i) Mechanical cracking and disruption of the oxide,
- (ii) Conversion of iron rich oxides formed in high pO_2 environments to carbides in low pO_2 environments,
- (iii) Deposition of graphite in the oxide,
- (iv) Diffusion of C through the oxide,
- (v) Transport of carbon containing molecules through pores in the oxide.

(i) Mechanical cracking and disruption of the oxide

Schnaas and Grabke^(99,108) investigated the effect of applied stress on the corrosion behaviour in oxidising/carburizing environments where an oxide layer forms. They found that at low strain rates grain boundary sliding led to repeated cracking of the oxide layer over the grain boundaries. This enabled carbon to penetrate down the crack before the oxide layer was restored, resulting in carbide precipitation at grain boundaries and chromium depletion in the matrix in the vicinity of the grain boundary. Eventually this became so severe that no protective oxide layer could form over the grain boundary and the carbide was able to transform to oxide. The resulting lack of cohesion led to cracks opening from the surface into the grain boundaries. At high strain rates this form of attack was not limited to grain boundaries but occurred throughout the specimen.

Similar findings to these have also been found by Schutze and Rahmel⁽¹³⁹⁾ and Guttman and Beck⁽¹⁴⁰⁾. However in these cases it was proposed that oxide formation in cracks and crevices led to an oxygen depletion in the gaseous atmosphere in the cracks and crevices resulting in carburization in the neighbourhood of the crevices.

As already indicated in this review there are many other sources of stress in oxides which can result in the formation of cracks. Although these have not been investigated in carburizing/oxidising environments, they could be very important, particularly when long term testing is carried out and specimens are frequently thermally cycled.

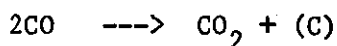
(ii) Conversion of oxides formed in high pO_2 environments to carbides in low pO_2 environments

This is illustrated by the work of Ledjeff et al.^(141,142). Specimens were oxidised in air to form chromium and iron rich oxides. When these specimens were subsequently subjected to CO-CO₂ environments, where oxides of iron are not stable, the iron containing oxides were reduced to either carbides or metal and the protective oxide was destroyed.

(iii) Deposition of graphite in the oxide

Ledjeff et al.⁽¹⁴²⁾ also showed that graphite deposited in cracks and pores can grow and set up stresses in the oxide. This led to spalling and cracking of the scale and subsequent degradation of the material by carburization.

The deposition of graphite in the scale often appears to be delayed for long periods of time. Gibbs⁽¹⁴³⁾ proposed that this delay was due to the formation of a catalyst for the Boudouard reaction at the scale/metal interface.



P.C. Rowlands⁽¹⁴⁴⁾ suggested that carbon was not deposited initially as the alloy acted as a sink for carbon. Only when the alloy had become saturated with carbon could the carbon activity reach a high enough value for carbon deposition to occur at the scale-alloy interface.

(iv) Diffusion of carbon through the oxide

A recent study by Wolf and Grabke⁽¹⁴⁵⁾ has been carried out to measure the solubility of C in FeO, Fe₃O₄, MnO, MgO, Cr₂O₃ and Al₂O₃ at 1000°C using a radiocarbon technique. In all cases no carbon (< 0,01 ppm) was detected in the lattice or grain boundaries of the oxides. It was therefore concluded that carbon does not penetrate oxides by diffusion through the lattice or grain boundaries.

(v) Transport of carbon containing molecules through pores in the oxide

Wolf and Grabke⁽¹⁴⁵⁾ did however detect radioactive carbon in voids and pores in the oxides. This together with the previously discussed observations of Wolf and Grabke⁽¹³⁷⁾ on the amount of carburization being related to the porosity in the oxide, would appear to prove the theory that carbon can be transported through oxide scales by carbon containing molecules such as CH_4 , CO and CO_2 .

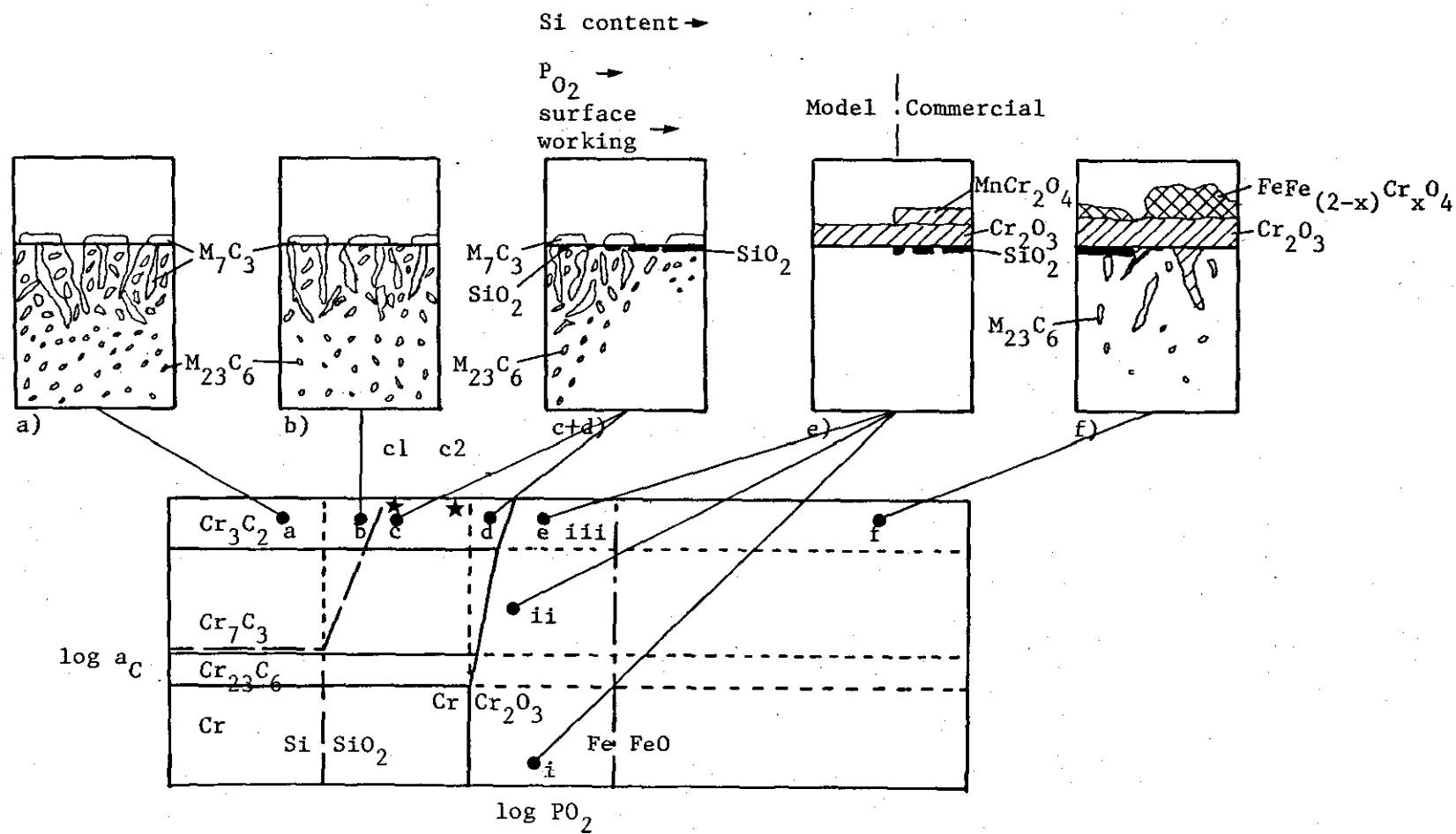


Figure 2.66

Schematic representation of corrosion morphologies obtained in carburizing/oxidizing environments at a set time t and temperature T .

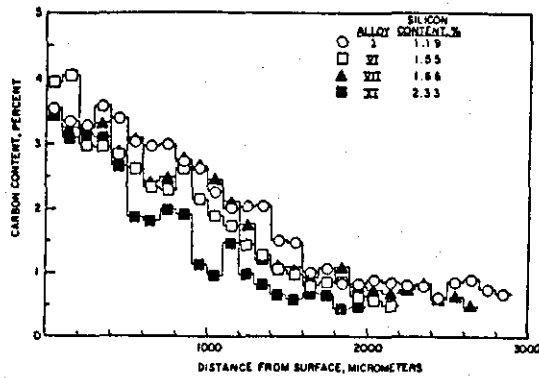


Figure 2.67
Carbon concentration profiles in alloys with different Si levels exposed to gas (b) in figure 2.66 (132).

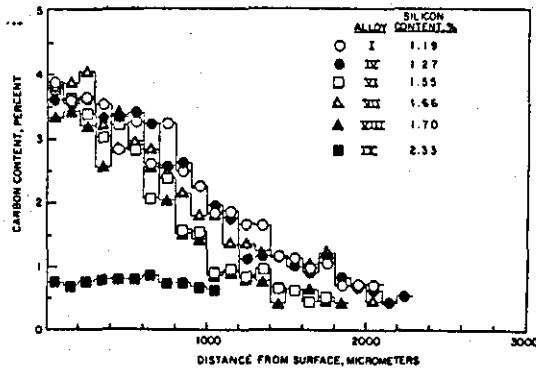


Figure 2.68
Carbon concentration profiles in alloys with different Si levels exposed to gas (c1) in figure 2.66 (132).

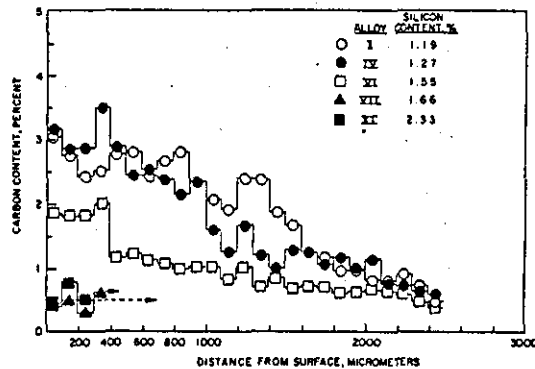


Figure 2.69
Carbon concentration profiles in alloys with different Si levels exposed to gas (c2) in figure 2.66 (132).

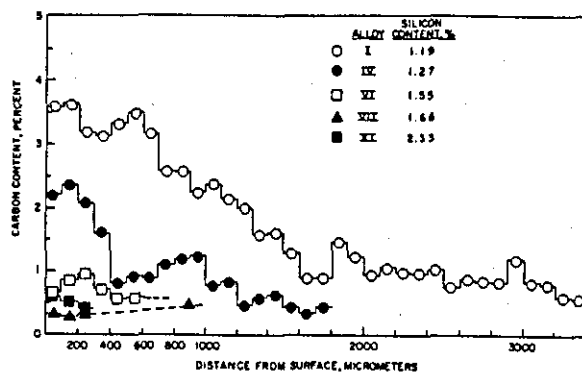


Figure 2.70
Carbon concentration profiles in alloys with different Si levels exposed to gas (d) in figure 2.66 (132).

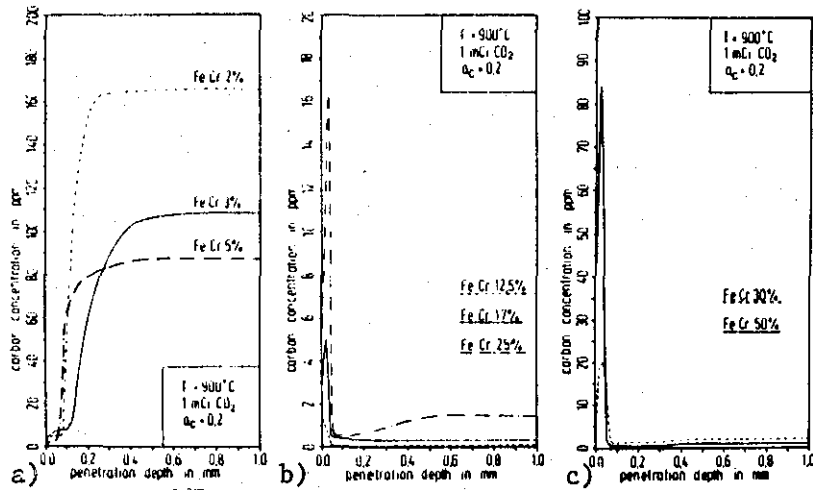


Figure 2.71
Depth profiles of ^{14}C for different Fe-Cr alloys. (The maxima in b) and c) correspond to an area in the alloy immediately below the oxide/alloy interface) (137).

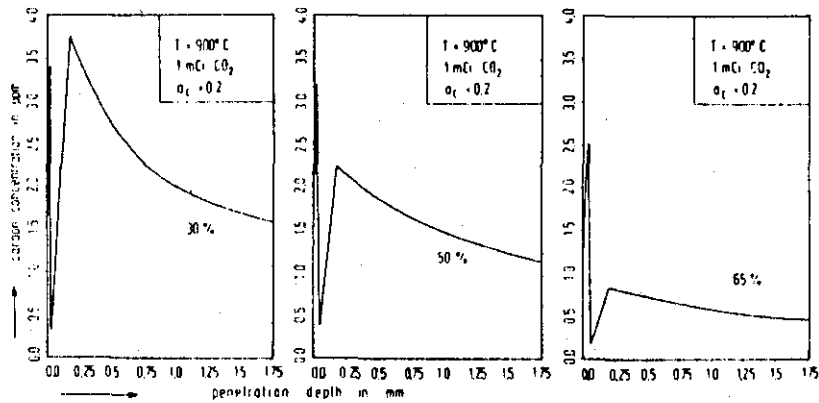


Figure 2.72
Depth profiles of ^{14}C for Incoloy 800 with different degrees of cold work (137).

2.3.3. Carburization/Sulphidation

Earlier in this review it was shown that the carburization process was controlled by the diffusion of carbon through the metallic matrix in the carbide precipitate containing zone of the alloy. However it has been known for many years that the presence of low levels of sulphur in the gaseous environment can lead to the formation of an adsorbed layer of sulphur on the alloy surface which inhibits the uptake of carbon to such an extent that the adsorption process becomes the rate determining step. This phenomenon has been studied by Grabke et al.⁽¹⁴⁶⁾, Fruehan⁽¹⁴⁷⁾ and Barnes et al.^(148,125).

Grabke et al.⁽¹⁴⁶⁾ investigated the carburization behaviour of Alloy 800 in H_2 - CH_4 - H_2S atmospheres at $1000^\circ C$ with a carbon activity = 1. The kinetics (figure 2.73) and amount of carbon ingress (figure 2.74a) decreased rapidly with increasing H_2S ratio, reaching a minimum value at a H_2S/H_2 ratio of 10^{-4} , figure 2.73. This corresponds to the position of the Cr/CrS phase stability boundary at $1000^\circ C$. Once this value of H_2S/H_2 was exceeded CrS became thermodynamically stable with its formation accounting for the increase in kinetics, figure 2.73. The amount of carbon ingress also increased again but the level did not reach that which occurred in purely carburizing environments, figure 2.74a. There was also a considerable amount of internal sulphidation, figure 2.74b.

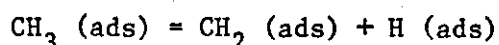
Similar trends to these occurred at lower temperatures (figure 2.73), with the minimum amount of corrosion occurring at lower $H_2S : H_2$ ratios due to the Cr/CrS thermodynamic boundary shifting to lower values of pS_2 as the temperature decreases. Grabke et al. also found that the presence of sulphur suppressed the deposition of graphite in gaseous environments with $a_c > 1$.

Very similar observations to Grabke et al.'s have been reported by Barnes et al.^(148,125) for a wider range of alloys; i.e. 25Cr-20Ni-Fe, 25Cr-35Ni-Fe and 20Cr-32Ni-Fe alloys exposed to a number of gaseous environments with a carbon activity of 0.8 at $1000^\circ C$. In general all the alloys exhibited similar behaviour in the sulphur containing environments. The effect of increasing the amount of sulphur on the corrosion morphologies are summarized in figure 2.75.

Figure 2.75a corresponds to the case of pure carburization with a typical cross-sectional morphology consisting of M_7C_3 surface carbides and internal M_7C_3 (outer zone) and $M_{23}C_6$ (inner zone) precipitates. The carburization mechanism resulting in this morphology was described in detail earlier in this review.

When 20 ppm of H_2S was added to the gaseous environment sulphur adsorbed on the alloy surface and significantly reduced the amount of internal carburization, figure 2.75b. Barnes et al. also found that the adsorbed sulphur layer reduced the effective carbon activity, with the result that $M_{23}C_6$ carbides developed initially on the alloy surface instead of M_7C_3 which form in purely carburizing environments. These $M_{23}C_6$ carbides subsequently transformed to M_7C_3 with time. Sulphur was also found to adsorb on the surface carbides. This retarded the growth of low angle planes in the M_7C_3 surface carbides resulting in columnar shaped particles, figure 2.75b.

The inhibition of carburization by sulphur can be explained by considering the adsorption of C and S on Fe. According to Grabke⁽¹⁰⁴⁾ the adsorption of C on the metal surface during the carburization process results in the $(1/2, 1/2)$ sites on the (100) face being occupied by carbon atoms, figure 2.76. However the reaction rate of adsorption does not reduce when all these sites are occupied. The rate controlling factor is therefore attributed to the reaction



occurring on other sites, not occupied by carbon atoms, such as the top of two adjacent metal atoms. However if sulphur is introduced into the gas it also adsorbs on the surface and occupies the $(1/2, 1/2)$ sites on the (100) face. But because the sulphur atoms are much larger than the carbon atoms and more mobile they cover up the metal sites on which the reaction takes place, thus inhibiting the amount of carbon adsorption, figure 2.77. As the level of sulphur is increased the number of sites available for carbon adsorption decreases resulting in carbon adsorption becoming slower than carbon diffusion in the alloy and hence the rate determining step with linear reaction kinetics obeyed.

The reduced amount of the internal carburization at a higher sulphur level (100 ppm) is illustrated in figure 2.75c. Although this environment contained a pS_2 in excess of the Cr/CrS thermodynamic boundary (dotted line on figure 2.75c), chromium sulphides did not form. This was because the effective thermodynamic boundary was shifted to higher values of pS_2 (broken line on figure 2.75) for the alloys having a typical a_{Cr} of 0.5. However MnS was thermodynamically stable, with the result that alloys containing Mn formed small MnS particles both on the surface and internally. The MnS particles on the surface acted as nucleation points for carbides and consequently led to the formation of a continuous carbide layer on the alloy surface.

When the pS_2 was increased to values in excess of the Cr/CrS thermodynamic boundary for the alloys, additional chromium sulphides formed on the alloy surface, figure 2.75 d and e. Initially $M_{23}C_6$ nucleated on the MnS particles. The $M_{23}C_6$ carbides then transformed to M_7C_3 with continued exposure. Eventually the M_7C_3 transformed to chromium containing sulphides. With the exception of HP40Nb, once the chromium sulphide layer was complete carbon ingress was reduced or prevented with the main form of attack due to sulphidation. The internal sulphidation front proceeded by transforming the carbides to sulphides liberating carbon which diffused into the alloy.

In the case of HP40Nb carburization increased in this regime. This agrees with the findings of Grabke et al.⁽¹⁴⁶⁾. Neither set of authors offer any explanation for their respective findings in this regime.

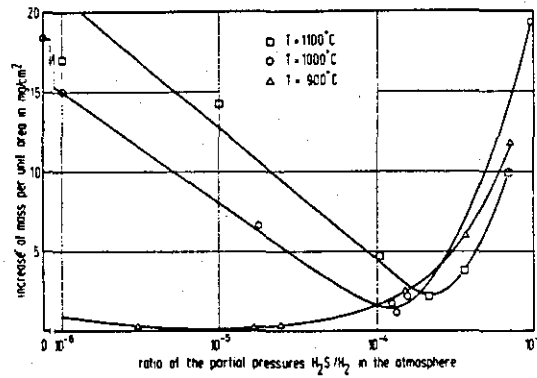


Figure 2.73
Mass increase after exposure for 100 h in $\text{CH}_4\text{-H}_2\text{-H}_2\text{S}$ gas mixtures ($a_c = 1$) at 900, 1000, and 1100°C with different $\text{H}_2\text{-H}_2\text{S}$ ratios (146).

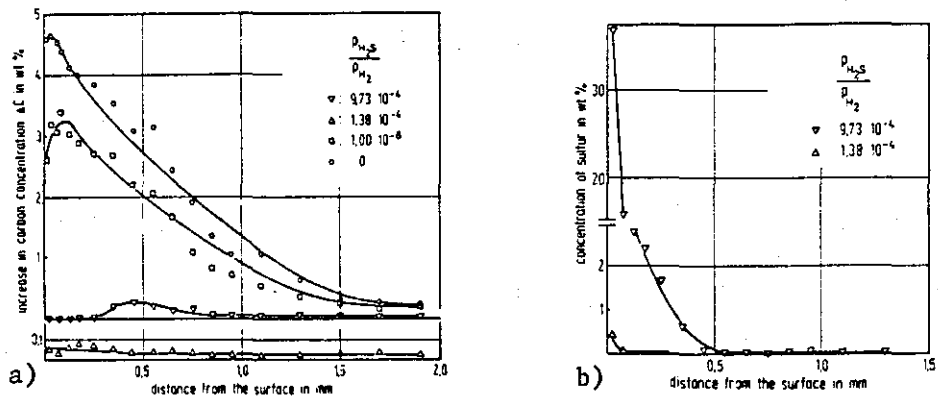


Figure 2.74
Concentration profiles for a) carbon and b) sulfur for Alloy 800 carburized at 1000°C in gases containing different $\text{H}_2\text{S/H}_2$ ratios.

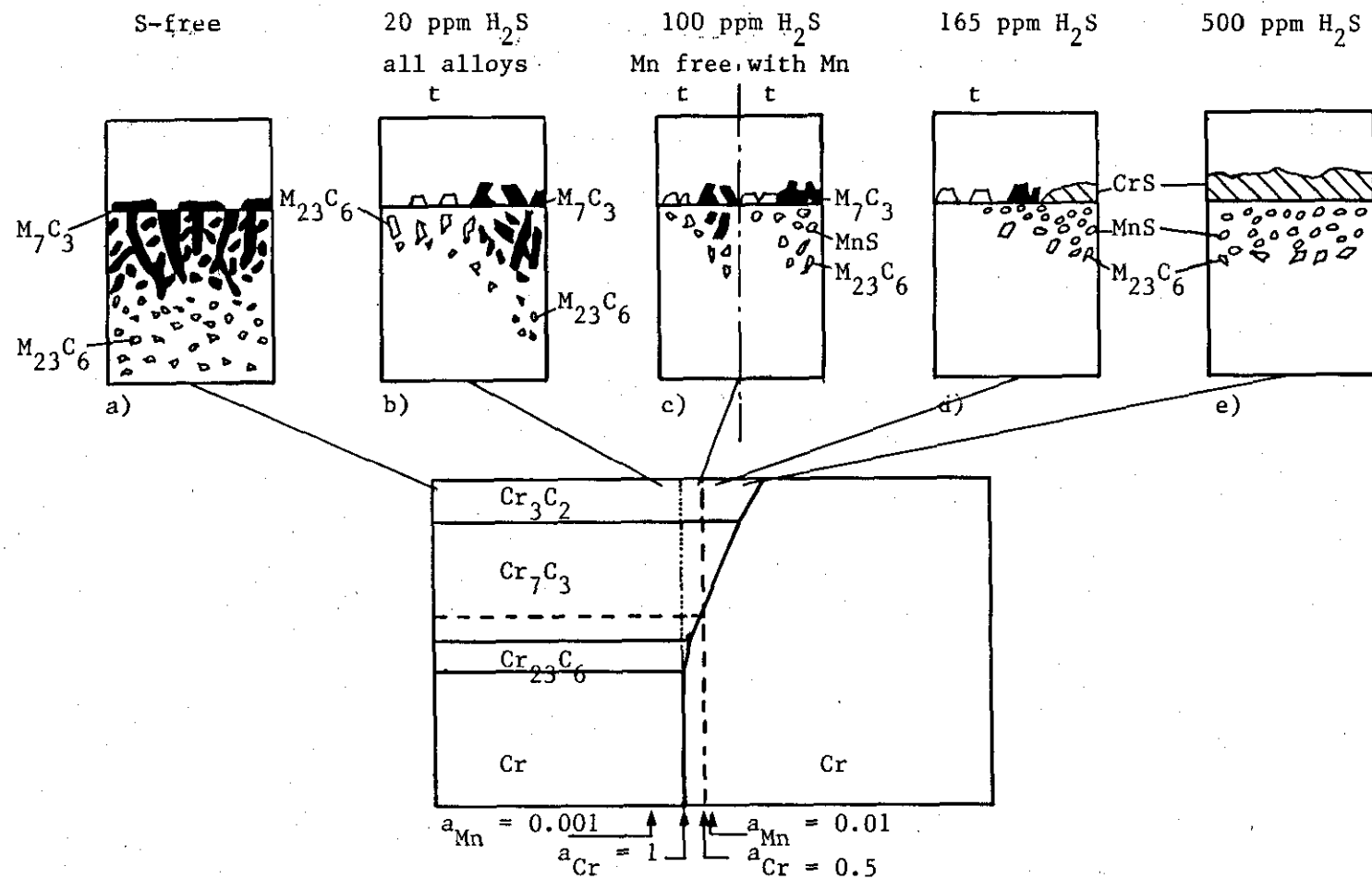
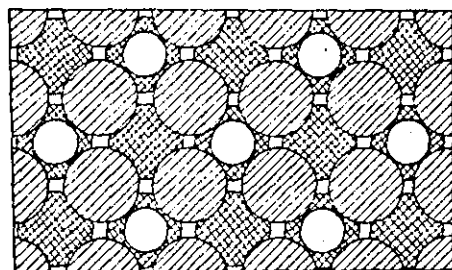
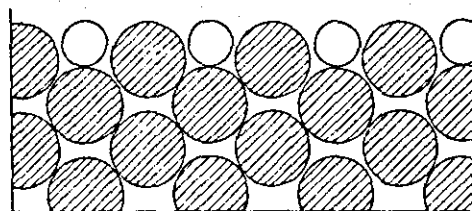


Figure 2.75

Schematic representation of corrosion morphologies obtained in Carburizing/Sulphidizing environments at 1000°C.



(a)



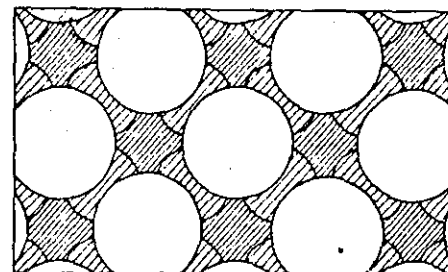
(b)

Figure 2.76

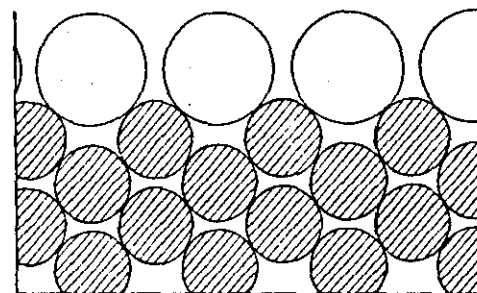
An atomic model of the adsorption of carbon on a (100) Fe surface:

a) the top view

b) the cross section in the 110 direction (104).



a)



b)

Figure 2.77

An atomic model of the adsorption of sulphur on a (100) Fe surface

a) the top view

b) the cross section in the 110 direction (104).

2.3.4. Sulphidation/Oxidation

A considerable amount of research has taken place in environments containing the reactants (S) and (O). From basic thermodynamic considerations a schematic metal stability diagram for the M-S-O system (figure 2.78) can be divided into the following regions.

- (a) Sulphides of Cr and the base metal could form.
- (b) Sulphides of Cr and the base metal could form but the oxygen partial pressure could be sufficient for Cr_2O_3 to form at the scale/alloy interface.
- (c) Cr_2O_3 could form but the partial pressure of sulphur could be sufficient for sulphides of Cr and the base metal to form at the scale/alloy interface.
- (d) Only CrS could form.
- (e) CrS could form and the oxygen partial pressure could be sufficient for Cr_2O_3 to form at the scale/alloy interface.
- (f) Cr_2O_3 could form but the partial pressure of sulphur could be sufficient for CrS to form at the scale/alloy interface.
- (g) Only Cr_2O_3 could form.

The research carried out to date in sulphidising/oxidising conditions shows that the actual corrosion behaviour is considerably different to that predicted from thermodynamics.

Natesan and Delaplane⁽¹⁴⁹⁾ determined the types of scale developed on commercial alloys such as Incoloy 800, Type 310 stainless steel, Inconel 671, RA 333 and U.S. steel Alloy 18-18-2 in oxidising/sulphidising environments at 750, 875 and 1000°C. Figure 2.79 summarises their findings for Alloy 800 (similar trends were established for the other alloys). Essentially the diagram can be divided into two regimes by a threshold or kinetic boundary (broken line on figure 2.79) with sulphidation dominant at low $p\text{O}_2$'s below the threshold and oxidation dominant at high $p\text{O}_2$'s in excess of the threshold. At these temperatures the threshold or kinetic boundary was found to be to the right of the CrS/ Cr_2O_3 thermodynamic boundary by 2 orders of magnitude at 1000°C and 3 orders of magnitude at 750°C.

Subsequent work by Tiearney and Natesan⁽¹⁵⁰⁾ showed that at a lower temperature (923K, 650°C) the threshold oxygen partial pressure was approximately 5 orders of magnitude to the right of the CrS/Cr₂O₃ thermodynamic boundary.

The position of the kinetic boundary has also been found to be dependent on the alloy composition. This is demonstrated by the work of Perkins^(151,152) who determined the position of the kinetic boundary for six different alloys in H₂-H₂O-H₂S mixtures at 1144K (871°C), figure 2.80. For a given pS₂ there was a difference in the pO₂ of 2 orders of magnitude between the best alloy (Ni-46Cr) and the worst alloy (Fe-25Cr). The positions of these boundaries did not change when the exposure period was increased from 1 hour to 48 hours. This led to the conclusion that the position of the boundary was established in the initial stages of the corrosion process, when sulphides and oxides formed and grew simultaneously. It is therefore important to consider what happens when a metal is first exposed to a gaseous environment containing more than one reactant.

Short-term exposures

Several workers such as Rahmel⁽¹⁵³⁻¹⁵⁴⁾ (Fe in N₂-O₂-SO₂ and CO-CO₂-COS gas mixtures), Flatley and Birks⁽¹⁵⁵⁾ (Fe in SO₂-Ar), Luthra and Worrell⁽¹⁵⁶⁻¹⁵⁷⁾ (Ni in SO₂-O₂-SO₃) and Gesmundo et al.⁽¹⁵⁸⁻¹⁵⁹⁾ have observed the simultaneous formation of oxides and sulphides in SO₂-containing environments. As these fall outside the scope of this study they will not be dealt with here. The reader is referred to a recent review of this area by Stroosnijder and Quadackers⁽¹⁶⁰⁾. Yurek and La Branche⁽¹⁶¹⁾ have, however, considered this question for H₂-H₂O-H₂S environments.

Yurek and La Branche⁽¹⁶¹⁾ proposed that if a gaseous environment contains a pS₂ in excess of the Cr/CrS thermodynamic boundary and a pO₂ in excess of the Cr/Cr₂O₃ thermodynamic boundary both sulphides and oxides can nucleate on the metal surface in the initial stages. It was also proposed that the relative amounts of these phases formed depend on the rate at which H₂O and H₂S molecules strike unit area of the chromium surface. This can be calculated from the Herz-Langmuir equation.

$$j_i = \alpha_i P_i (2\pi M_i kT)^{-1/2} \quad (2.22)$$

where j_i is the rate of adsorption per unit area
 α_i is the sticking coefficient
 P_i is the partial pressure in the gas phase
 M_i is the mass per molecule of species

Assuming that once H_2O and H_2S molecules adsorb on the surface they react very rapidly to form oxide and sulphide. One mole of Cr_2O_3 will be formed per three moles of H_2O and one mole of $Cr_{1-x}S$ per mole of H_2S . If it is also assumed that the sticking coefficients for H_2S and H_2O are approximately equal, the number of moles of sulphide per mole of oxide formed on chromium ρ can be expressed by

$$\rho = 3 (P_{H_2O}/P_{H_2S}) (M_{H_2O}/M_{H_2S})^{1/2} \quad (2.23)$$

where M_{H_2O} and M_{H_2S} are the molecular weights of H_2O and H_2S respectively.

To convert to the volume of sulphide formed per unit volume of oxide ρ can be multiplied by the molar volume of $Cr_{1-x}S$ and divided by the molar volume of Cr_2O_3 to give.

$$\rho = 1.29 \frac{P_{H_2S}}{P_{H_2O}} \quad (2.24)$$

If it is also assumed that the thickness of Cr_2O_3 and $Cr_{1-x}S$ formed initially are about the same, then equation 2.24 may be employed to calculate the fraction of the chromium surface which is converted to sulphide on initial exposure to the gas.

$$\text{i.e. } A_s \sim \frac{\rho}{(1 + \rho)} \quad (2.25)$$

where A_s is the area fraction of sulphide.

According to the thermodynamic considerations only one phase should come to equilibrium with the gas. However Yurek and La Branche argue that once two phases have formed in the initial stages, continued formation of a two phase scale can occur if the rate of scale growth is controlled by a phase boundary reaction or by diffusion in the gas phase. For example for a H_2 - H_2O - H_2S gas mixture simultaneous formation of Cr_2O_3 and $Cr_{1-x}S$ will involve a series of parallel reaction steps involving H_2O and H_2S . In the case of oxide formation these could be diffusion of H_2O in the gas phase, adsorption of H_2O on the surface of the scale, dissociation of adsorbed H_2O etc. Likewise formation of sulphide involves a similar parallel set of reaction steps. Of course other gaseous sulphur-containing species such as SO_2 and SO_3 could be formed at the reaction temperature but these are assumed to exist in very low concentrations.

As a consequence of these parallel processes, the net rate of corrosion will correspond to the weighted sum of the rate-limiting steps for the formation of oxides and sulphides. This can be expressed in terms of the consumption of chromium, \dot{n}_{Cr}/A (moles Cr/cm²s). For example if the rates of formation of Cr_2O_3 and $Cr_{1-x}S$ were both limited by a phase boundary reaction at the scale/gas interface the net rate of corrosion would be

$$\frac{\dot{n}_{Cr}}{A} = 2/3 v_o + (1 - x) v_s \quad (2.26)$$

where v_o and v_s are the rates per unit area (moles/cm²s) of the phase boundary reactions that control the supplies of oxygen and sulphur at the scale/gas interface. Alternatively if the rates of formation of both Cr_2O_3 and $Cr_{1-x}S$ were limited by diffusion of H_2O and H_2S in the gas phase then the net rate of corrosion would be

$$\frac{\dot{n}_{Cr}}{A} = 2/3 j_{H_2O} + (1 - x) j_{H_2S} \quad (2.27)$$

where j_{H_2O} and j_{H_2S} are the molar fluxes of H_2O and H_2S in the gas phase.

When the rate of formation of one phase in a two-phase scale is much greater than the rate of formation of the other phase the net rate of scale growth is controlled by the faster of the two parallel processes.

For example, if both oxide and sulphide formation were limited by diffusion in the gas phase and if $j_{H_2O} \gg j_{H_2S}$ then diffusion of H_2O would control the rate of corrosion i.e.

$$\frac{n_{Cr}}{A} \sim 2/3 j_{H_2O} \quad (2.28)$$

In this limiting case which would generally occur when $p_{H_2O} \gg p_{H_2S}$ oxide should form exclusively at the scale/gas interface, although a small amount of sulphide might form along with oxide on initial exposure of chromium to the gas. Propagation of the two phase scale would be inhibited because of the overwhelmingly greater supply of oxygen to the surface. The scale would therefore consist of a mixture of oxide and sulphide at the metal/scale interface overlaid by a continuous oxide layer.

To establish the conditions at which transition from a two-phase scale to a single phase Cr_2O_3 scale occurred Yurek and La Branche exposed pure Cr to various H_2 - H_2O - H_2S gas mixtures at 1 atm. and $900^\circ C$. A critical ratio of $p_{H_2O}/p_{H_2S} \sim 8$ was obtained. This is marked by the dash-dot line on figure 2.68. This would appear to correspond to the kinetic boundary established by Natesan and Delaplane⁽¹⁴⁹⁾, both research groups finding the difference between this boundary and the thermodynamic boundary to be approximately 2 orders of magnitude in this temperature range ($1000-900^\circ C$).

Thus in summary according to Yurek's and La Branche's reasoning, at ratios of $p_{H_2O}/p_{H_2S} > 8$ (to the right of the threshold boundary) a single phase Cr_2O_3 with perhaps some $Cr_{(1-x)}S$ at the metal scale interface should form and at ratios of $p_{H_2O}/p_{H_2S} < 8$ the scale should consist of both sulphides and oxides.

At this stage it is perhaps worthwhile examining the corrosion morphologies which La Branche et al.⁽¹⁶²⁾ actually found when they exposed pure Cr to H_2 - H_2O - H_2S gas mixtures.

At a $pS_2 = 10^{-14}$ atm., position (a) on figure 2.82, the scale consisted entirely of Cr_2O_3 with only slight traces of sulphur at the scale/gas interface. The presence of sulphur was attributed to adsorption occurring on the surface during the cooling to room temperature. No sulphides formed because the partial pressure of sulphur was less than that required for chromium sulphide to be stable. It is important to realise that this applies only to gases in which the pS_2 is determined from the ratio of H_2 to H_2S . In the case of a gas mixture containing bioxidant molecules such as SO_2 , sulphide formation can occur at the metal/scale interface even though the pS_2 in the gas is insufficient for sulphides to be thermodynamically stable. The reader is referred to a review of Birks⁽¹⁶³⁾ for a detailed description of this mechanism.

When the pS_2 was increased to 10^{-10} , position (b) in figure 2.82, chromium sulphide could be stable. However, La Branche et al.⁽¹⁶²⁾ detected no sulphides in or beneath the Cr_2O_3 scale. This was not really surprising if examined from the point of view of the relative amount of oxide and sulphide being controlled by the relative rates of adsorption of H_2O and H_2S on the substrate. The H_2O to H_2S ratio of the gas was 160 and thus according to equation 2.25 only 0.8 % of the surface area would be covered with sulphides.

When the pS_2 was increased to $10^{-7.5}$, position (c) on figure 2.82, the pH_2O/pH_2S ratio was reduced to 9, which lies just to the right of the threshold boundary. La Branche et al. found that after the initial exposure (2.5 mins.) 9-10 % of the surface was covered with sulphide with the rest covered with oxides. This was in good agreement with the theoretical value of 13 % obtained from equation 2.25. The amount of sulphide was also found to vary according to the orientation of the Cr with a randomly orientated grain of Cr having a higher area fraction of sulphide than a (100) orientation exposed under the same conditions.

As the H_2O/H_2S ratio was > 8 the rate of supply of oxygen was greater than the supply of sulphur and the oxides subsequently overgrew the

sulphides to form an outer Cr_2O_3 layer with chromium sulphides at the metal/scale interface. These sulphides subsequently became larger but fewer in number. The authors estimated that the overall volume of sulphides doubled between 2.5 minutes and 60 minutes exposure. They concluded that as the sulphides increased in size uniformly, inward diffusion of sulphur occurred by lattice or grain boundary transport through the oxide and not by diffusion of H_2S through cracks and pores.

Finally, when the $p\text{S}_2$ was increased to $10^{-6.5}$ atm., position (d) on figure 2.82, the ratio of $p\text{H}_2\text{O}/p\text{H}_2\text{S}$ was only 2.8 and hence the rate of supply of H_2O and H_2S to the metal surface was similar. The scale formed after 60 minutes consisted of mixed oxides and sulphides. The authors state that the rate of corrosion up to 60 mins. exposure was controlled at least partially by diffusion in the gas phase or by a chemical reaction at the scale/gas interface. However it was not possible to determine which step was rate-controlling.

Having established the kinetic or threshold boundary for pure Cr exposed to H_2 - H_2O - H_2S environments at 900°C , Yurek et al.⁽¹⁶⁴⁾ then investigated the behaviour of a Fe-25%Cr alloy under similar conditions. At low oxygen activities the kinetic boundary for the alloy followed the boundary for pure Cr, but at high oxygen activities the boundary for the alloy ran parallel to the Fe/FeS thermodynamic boundary, figure 2.83. This would appear to be due to nuclei of FeS, (FeCr)S solid solution and FeCr_2O_4 forming on the alloy surface during the initial stages of the corrosion process. The subsequent reasoning is very unclear. Having gone to a great deal of trouble of showing how oxides overgrow sulphides in the previous paper⁽¹⁶²⁾ Yurek et al.⁽¹⁶⁴⁾ now totally ignore and contradict this and suddenly propose that chromium sulphide is converted to chromium oxide when pure Cr is exposed to a gas having a composition to the right of the threshold boundary. No evidence is offered to support this. However the authors now find that the modified theory is very convenient for explaining the behaviour of the alloy. It is argued that it is very difficult for the Fe-rich sulphides (with a low a_{Cr}), which are thermodynamically stable in gases with a $p\text{S}_2$ in excess of the Fe/FeS thermodynamic boundary (such as B and E on figure 2.83), to convert to oxides. It is however thermodynamically favourable for a Cr-rich sulphide (with a higher a_{Cr}) to convert to an oxide.

The transformation of sulphides to oxides has also been proposed by Hussey et al.⁽¹⁶⁵⁾. A model Fe-32Ni-20Cr alloy was heated to 700°C in hydrogen and subsequently exposed to H_2 - H_2O - H_2S gas mixtures corresponding to the compositions marked in figure 2.84 for exposure periods in the range 2-120 minutes.

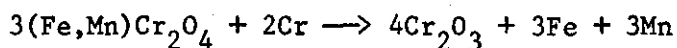
Unfortunately the results and interpretation do not tie up very well and the reader is left guessing as to what really happened. In the opinion of the author of this review Cr_2O_3 and Cr_3S_4 nucleated on the surface of the alloy in the initial stages ($FeCr_2O_4$ and $(Ni,Fe)Cr_2S_4$ could also have formed). The Cr_2O_3 and Cr_3S_4 then grew side by side with the rate of reaction being controlled by phase boundary processes. The Cr_3S_4 particles acted as short circuit diffusion paths for Cr^{3+} , Fe^{2+} and Ni^{2+} ions to the surface where they reacted with S to form the thiospinel $(Fe,Ni)Cr_2S_4$. The amount of sulphide was higher at lower oxygen pressures. Both the chromium sulphides and the thiospinel vanished after 120 hours exposure. It was speculated that the reasons for this were presumably due to the reaction process becoming controlled by diffusion in the scale resulting in the $(Ni,Fe)Cr_2S_4$ converting to an $FeCr_2O_4$ oxide (no mention is made of what happened to the Ni) and the Cr_3S_4 decomposing by dissolution of sulphur into the alloy to form CrS precipitates (no evidence is presented to support this). Finally the authors conclude that the first transient state of reaction has no great consequences for the further development of the scale.

In summary it appears that in the initial stages both oxides and sulphides nucleate and grow on the surface of a metal and alloy with the rate of reaction being controlled by either diffusion in the gas phase or phase boundary transport processes. After further exposure oxidation or sulphidation becomes dominant with either oxides overgrowing and/or transforming sulphides to the right of the kinetic boundary and sulphidation taking over to the left of the kinetic boundary. It is now possible to move or to determine what has been found for longer exposure times, firstly for conditions to the right of the kinetic boundary and secondly for conditions to the left of the kinetic boundary.

Reported corrosion behaviour in oxidizing/sulphidizing conditions to the right of the kinetic boundary

Medium term exposures
.....

Rao et al⁽¹⁶⁶⁾ investigated the behaviour of AISI 310 in a H_2 - H_2O - H_2S gas mixture corresponding to a $pO_2 = 6 \times 10^{-13} \text{ Nm}^{-2}$ ($6 \times 10^{-18} \text{ atm.}$) and a $pS_2 = 0.19 \times 10^{-2} \text{ Nm}^{-2}$ ($1.9 \times 10^{-18} \text{ atm.}$) at 1150K (877°C) up to 1200 hours exposure. A mechanism was tentatively proposed. Initially a continuous layer of $(Fe,Mn)Cr_2O_4$ formed. Corrosion proceeded by cation diffusion through this layer. As the spinel layer grew, the oxygen potential at the scale/subscale interface became less than in the gas phase. Thus the spinel phase became unstable at the scale/alloy interface and decomposed into Cr_2O_3 according to the exchange reaction



and resulted in the formation of an outer spinel layer and an inner Cr_2O_3 layer, with the Fe and Mn released diffusing outwards to form further $(Fe,Mn)Cr_2O_4$ spinel at the gas/scale interface. The authors speculated that because of this the thickness of the $(Fe,Mn)Cr_2O_4$ layer would remain either constant as time progressed or grow at a relatively slower rate than the formation of the Cr_2O_3 . It was also argued that since part of the chromium flux from the alloy to the scale/gas interface was consumed by the exchange reaction it was likely that the flux of iron diffusing to the gas/scale interface would be higher than that required to form the spinel. Since FeO was unstable at the oxygen partial pressure used, the excess iron would form sulphides. (A discontinuous FeS layer was found after prolonged exposure, 1200 hours.) Finally it was claimed that the oxidation of chromium resulted in the depletion of Cr in the alloy and the enrichment of Si in the alloy facilitating the formation of SiO_2 at the scale/alloy interface.

Cooper and Strafford⁽¹⁶⁷⁾ also found similar findings for AISI 314 exposed at 825°C with $pO_2 = 10^{-21} \text{ atm.}$ and $pS_2 = 10^{-10} \text{ atm.}$ for 302 hours. The results were interpreted in the same way as Rao et al.⁽¹⁶⁶⁾. Perhaps it should be pointed out here that both sets of

authors did not seem clear concerning the thermodynamic stability of the oxide spinels. A brief look at the stability diagram shows that a Cr_2O_3 will exist at lower $p\text{O}_2$'s than FeCr_2O_4 but MnCr_2O_4 will be relatively more stable than Cr_2O_3 . The work of Giggins and Pettit⁽¹²⁹⁾ shows that the position of these lines also changes depending on the activity of the various constituents in the reaction product. Finally both sets of authors did not carry out a systematic study of the development of the corrosion products with increasing time but simply found the final corrosion morphology and speculated how it was formed.

In the case of a model 25Cr-35Ni-Fe alloy Cooper and Strafford⁽¹⁶⁷⁾ found that relatively pure Cr_2O_3 scale containing small amount of Fe and Ni (< 0,46 wt%) formed. The growth of this scale was assumed to be due to outward Cr^{3+} diffusion.

In the case of Alloy 800H and H39W which had lower Mn contents (0,66 and 0,62 %) the Mn rich spinel formation was more localised. This time it was speculated that the levels of Mn in the bulk phase were insufficient to form the initial $(\text{Mn},\text{Fe})\text{Cr}_2\text{O}_4$ phase and that the formation of the outer spinel occurred by the outward migration of Mn^{2+} ions from the bulk alloy through the Cr_2O_3 rich scale.

Long-term exposures

Hill and co-workers⁽¹⁶⁸⁻¹⁷⁰⁾ exposed a large number of commercial high temperature alloys for periods of up to 10000 hours to coal gasification atmospheres containing 0.5 and 1 % H_2S at 899 and 982°C and system pressures of 3.45 MPa (34.5 atm.) and 6.89 MPa (88.9 atm.). Some alloys such as 6B had a low constant corrosion rate throughout the test duration, figure 2.85. In the case of other alloys the initial corrosion rate was also low but after several thousand hours a transition to much higher rates took place. No real in-depth analysis was carried out to establish why this breakaway mechanism occurred. The authors did however indicate that the time to breakaway was shorter for alloys with low chromium contents, figure 2.86. The time to breakaway was also reduced by increasing the temperature, and the system pressure, figure 2.87. These studies clearly illustrated that the breakaway phenomenon is extremely important and that life-time prediction from short-term corrosion data could be very risky.

Before leaving the studies of Hill and co-workers it is worthwhile noting that the experimental procedure involved starting up in nitrogen. The H_2S level was then slowly increased to the operating level over a period of about 10 hours. Thus the specimens were in effect preoxidised during this time.

Reported corrosion behaviour in oxidizing/sulphidizing conditions to the left of the kinetic boundary

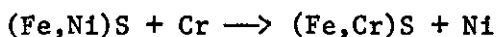
a. pS_2 in excess of the base metal sulphidation potential
..2.....

The majority of the research has taken place in this sub-regime with the result that the corrosion behaviour is relatively well understood. The corrosion mechanism for Hastalloys (Ni-Cr-Mo-Fe), Haynes alloys (Co-Cr-Ni-W), Inconels (Ni-Cr-Co-Al-Ti), oxide dispersion-strengthened alloys and commercial Fe-Cr-Ni alloys such as AISI 310 and Incoloy 800 at 923K and 1144K has been established by Tiearney and Natesan^(171,150), figure 2.88. In the initial stages the protective oxide and base metal sulphide compete for surface sites. As the reaction proceeds the fast outward growing base metal sulphide overgrows the oxide, complete coverage occurring especially quickly if the base metal sulphide is molten. The chromium in the matrix reacts with the base metal sulphide at the scale/alloy interface to form chromium sulphide, which also grows by outward cation diffusion, and the base metal ions, which in turn diffuse to the gas-scale interface to react with sulphur. Porosity and void formation accompany all of these processes and at some point in the scaling process the scale dissociates at these voids due to growth stresses and forms sulphur vapour within the voids. The sulphur in turn reacts with the remaining chromium in the matrix to form internal chromium-rich sulphide in a chromium-depleted matrix.

In general terms the mechanism was similar for all alloy systems. However high Al and Ti contents helped stabilize the oxide nuclei relative to the sulphide in the initial stages by providing a greater number of surface sites for preferential oxide formation and by increasing the thermodynamic stability of the oxide relative to pure

Cr_2O_3 . Although these additions of Al and Ti reduced the rate of corrosion attack, extensive sulphidation still occurred in this type of environment.

Another similar mechanism for corrosion in these types of environments has been proposed by Rao et al.⁽¹⁶⁵⁾. In this study AISI 310 was exposed to an H_2 - H_2O - H_2S gas mixture at 1150K (at a fixed $p_{\text{O}_2} = 6 \times 10^{-13} \text{ Nm}^{-2} \equiv 6 \times 10^{-18} \text{ atm.}$ and variable p_{S_2} from 0 to $33 \times 10^{-2} \text{ Nm}^{-2} \equiv 0-3.3 \times 10^{-6} \text{ atm.}$). When $p_{\text{S}_2} \geq 2.7 \times 10^{-2} \text{ Nm}^{-2}$ ($2.7 \times 10^{-7} \text{ atm.}$) extensive sulphidation took place. A three stage mechanism for scale formation was proposed, figure 2.89. In stage I both $(\text{Fe},\text{Mn})\text{Cr}_2\text{O}_4$ and $(\text{Fe},\text{Ni})\text{S}$ formed separate nuclei. The sulphides then overgrew the oxides due to the higher diffusivities in sulphides than in oxides, stage II. As a result of this the gas phase became separated from the alloy and oxide ceased to grow. After the formation of the continuous $(\text{Fe},\text{Ni})\text{S}$ layer an exchange reaction



took place at the scale/alloy interface, stage III. The rejected Fe and Ni diffused outwards to the scale/gas interface where they reacted with the sulphur again to form the $(\text{Fe},\text{Ni})\text{S}$ phase.

The corrosion morphologies formed, with the exception of the presence of Cr_2O_3 , were the same as those obtained by the same research group⁽¹⁷²⁻¹⁷⁴⁾ in purely sulphidising conditions. However it should be emphasised that under purely sulphidising conditions the $(\text{Fe},\text{Cr})\text{S}$ phase formed initially and the $(\text{Fe},\text{Ni})\text{S}$ formed later.

Yet another study was carried out by Wang and Douglass⁽¹⁰⁹⁾ on pure Cr and Ni-10Cr, Ni-20Cr and Ni-30Cr alloys at 1073K with a constant p_{S_2} of $1 \times 10^{-6} \text{ atm.}$ whilst the oxygen partial pressure was varied from 5×10^{-21} to $5 \times 10^{-20} \text{ atm.}$ and the carbon activity varied from 0.108 to 0.416. In the case of pure Cr, Cr_2O_3 and Cr_3S_4 nucleated on the metal surface initially, figure 2.90. Both phases were highly orientated with the Cr_2O_3 growing in the (0001) direction and the Cr_3S_4 in the (001) direction. After longer term exposures (eg. 24 hours) the morphologies

consisted of Cr_2S_3 crystals on top of a Cr_2O_3 layer with some internal chromium sulphides, figure 2.91. No explanation is given as to how this morphology developed from the initial nuclei.

In the case of the Ni-Cr alloys an additional Ni_3S_2 phase nucleated on the alloy surface and resulted in the outer layer consisting of mixed Cr_3S_4 and Ni_3S_2 , figure 2.91. Apart from this extra phase the corrosion morphologies were the same as for pure Cr. The appearance of both sulphide and oxide on the alloy surface was attributed to local variations in the gas composition that enabled the gas to become enriched locally to satisfy the thermodynamics of scale formation.

The corrosion kinetics decreased as the $p\text{O}_2$ increased and the Cr content of the alloys increased due to improved possibility of forming more Cr_2O_3 and less Ni_3S_2 . No carburisation was detected in any environment.

Chu and Rahmel⁽¹⁷⁵⁾ also found that the corrosion kinetics decreased with increased $p\text{O}_2$. In this study an Fe-20Cr alloy was exposed to H_2 - H_2O - H_2S gas mixtures at 973K, 1073K and 1223K. The $p\text{S}_2$ was kept constant (e.g. $p\text{S}_2 = 10^{-5.6}$, at 1073K) and the water level and hence the $p\text{O}_2$ varied. The decrease in kinetics due to increased $p\text{O}_2$ was attributed to the following reasons :

- (i) Displacement adsorption of H_2S by H_2O .
- (ii) Increased Cr_2O_3 particles in the inner scale thus reducing the diffusion cross-section.
- (iii) By influencing the vacancy concentration at the scale/gas interface.

Typical scales formed are shown schematically in figure 2.93 with an outer FeS layer, and intermediate (Fe,Cr)S layer and an inner (Fe,Cr)S layer with small Cr_2O_3 inclusions. The (Fe,Cr)S solid solution partially decomposed during cooling to yield a Fe-rich metal phase and FeCr_2S_4 . No short-term analysis was carried out.

Another study by Hindam and Whittle⁽¹⁷⁶⁾ was carried out on Ni-25Cr, Co-25Cr and Fe-25Cr alloys in H_2 - H_2O - H_2S atmospheres at 1300K with a constant $p\text{S}_2 = 9.5 \times 10^{-5}$ atm. and variable $p\text{O}_2$ in the range 10^{-12} to

10^{-16} bar. With the exception of Fe-25Cr at $p_{O_2} \geq 10^{-14}$ atm. which formed a protective oxide, the behaviour of the alloys fell into the sulphidation regime. This study was however different because a Cr_2O_3 film formed initially which was followed by localised growth of external base-metal sulphides and internal Cr-rich sulphides, figure 2.94a. The authors suggested that sulphides did not nucleate in the initial stages due to the initial corrosion products being directly related to the amount of H_2S to H_2O in the gas. In this case the ratio was very small and therefore oxide and not sulphide formed. Another possibility is that the overall free energy change associated with Cr_2O_3 formation is much larger than that associated with base-metal sulphide formation.

At 1200K Hindam and Whittle became very confused. A multilayered scale formed on the Ni-25Cr alloy which consisted of an external NiS layer and intermediate porous Cr_2O_3 layer and an inner CrS layer, figure 2.94b. The authors suggest that the Cr_2O_3 layer grew by reaction of Cr dissolved in the NiS with oxygen.

Nagarajan et al.⁽¹⁷⁷⁾ proposed that the corrosion mechanism shown in figure 2.95 operates. In stage 1 only Cr_2O_3 nuclei form. This results in Cr depletion of the surface of the alloy. These depleted regions in turn develop FeS nuclei, stage 2. The sulphides then overgrew the Cr_2O_3 due to the rapid diffusion rates in sulphides and some Cr was incorporated into the sulphide, stage 3. In the final stage the sulphide spread beneath the Cr_2O_3 precipitates and forced them outwards away from the metal surface. According to the authors, as the corrosion front reached the region of the alloy which was not depleted in Cr, Cr_2O_3 can nucleate and reaction sequence commenced again.

Danielewski and Natesan⁽¹⁷⁸⁾ carried out a very good systematic study of the effect of increasing Cr content in Fe-Cr-8Ni alloys exposed to oxidizing/sulphidizing/carburizing environments at 875°C and 750°C. The partial pressure of sulphur was kept constant and the p_{O_2} varied. The compositions of the gases are marked on the relevant metal-stability diagrams at 875°C, figure 2.96a. In all cases the kinetics were parabolic and, with the exception of the 22%Cr containing alloy in the highest oxygen containing gas, sulphide scales were formed, figure 2.96b. For a given p_{S_2} an increase in p_{O_2} resulted in a decrease in parabolic

rate constant, figure 2.97. The authors offer no explanation for this trend. It could be speculated that this could be due to the formation of a some Cr_2O_3 but no mention was made of this. As this trend also occurred on pure Fe where obviously no Cr_2O_3 can form, perhaps the reduction in parabolic rate constant could be attributed to an adsorbed layer of oxygen inhibiting the adsorption of sulphur on the surface of the sulphides and the alloy. No explanation is offered for the rate increasing as the Cr content was increased to 12 %. This observation appears to be contrary to work reviewed earlier for binary Fe-Cr alloys in purely sulphidizing environments.

The fact that a Cr_2O_3 layer formed on the 22%Cr-containing alloy in the environment containing the highest $p\text{O}_2$ is not surprising due to the $p\text{O}_2$ being in excess of the threshold boundary and the Cr level also being in excess of the 18 % required to form a protective Cr_2O_3 on alloys exposed to purely oxidizing conditions.

Finally carburization was found only in the 22%Cr-containing alloy in the sulphidation regime with the carbides penetrating ahead of the sulphides. The Cr_2O_3 scale offered a good barrier to carburization. Carbides did not form in the lower Cr-containing alloys due to the lack of chromium. It should be noted that the carbon activity increased as the $p\text{O}_2$ increased for the gaseous environments used.

The effect of increasing the Si content in Fe-18%Cr alloys was investigated by Nagarajan et al.⁽¹⁷⁷⁾ at 982°C ($p\text{O}_2 = 10^{-18}$ atm. and $p\text{S}_2 = 10^{-6}$ atm.). The addition of up to 2%Si did not result in the formation of a complete SiO_2 inner layer. However small isolated SiO_2 precipitates did form in the substrate which although reducing the rate of corrosion did not prevent catastrophic sulphidation.

In a parallel study Nagarajan et al.⁽¹⁷⁹⁾ investigated the effect of adding Al to Fe-18%Cr alloys in the same environments ($p\text{O}_2 = 10^{-18}$ atm., $p\text{S}_2 = 10^{-6}$ atm. at 982°C). Alloys with high Al contents (5, 7 and 10 %) underwent severe corrosion with external (Fe,Cr) sulphide scales forming along with internal Al_2O_3 precipitates, i.e. essentially the same mechanism as Fe-18Cr-Si alloys described previously. However an alloy containing only 3 % Al formed a protective oxide scale.

The reasons for this appear to be related to duplex $\text{Cr}_2\text{O}_3/\text{Al}_2\text{O}_3$ layers forming on alloys with low Al contents whereas the higher Al-containing alloys tend to form a single Al_2O_3 layer. Why the duplex oxide is more protective than the single oxide is not clear. The authors conclude that an optimum Cr/Al ratio of approximately 6 is desirable for good sulphidation resistance. Similar trends to these have also been found by Perkins and Bhat⁽¹⁸⁰⁾.

b. $p\text{S}_2$ below the base metal sulphidation potential
.....

Surprisingly little research has taken place in this area, with no growth mechanism proposed. Tiearney and Natesan⁽¹⁷¹⁾ investigated the behaviour Hastelloy C-276, Haynes 188, IN-738 and MA6000E at 1144K. In this regime chromium sulphide scales formed containing variable amounts of soluble Fe or Co. Occasionally traces of molten nickel-rich sulphide were observed even though the sulphidation potential was below the pure nickel sulphidation potential. Some internal sulphidation also took place with porous chromium sulphide subscales forming.

In another study Williams et al.⁽¹⁸¹⁾ exposed Alloy 800 for 100 hours at temperatures between 800 and 1100°C in oxidizing/sulphidizing environments at $p\text{S}_2$'s below the iron and nickel sulphidation potentials. External porous mixed iron-chromium sulphide scales containing metallic nickel/iron particles formed. The authors claimed that these particles were rejected from the sulphide as the scale grew. Internal sulphidation also took place initially at grain boundaries and subsequently throughout the grains. When the $p\text{O}_2$ was increased to values nearer the threshold boundary the rate of corrosion was reduced due to the formation of an additional discontinuous oxide layer at the scale/alloy interface. Sulphidation however remained the dominant process. In this study the threshold boundary was found to be less than two orders of magnitude in excess of the $\text{CrS}/\text{Cr}_2\text{O}_3$ thermodynamic boundary.

When identical experiments were carried out at the same $p\text{O}_2$ and $p\text{S}_2$'s but with an additional carbon activity ($a_c = 0.9$) in the gas the scale morphologies were very similar to those produced in purely oxidizing/sulphidizing environments. The only difference was that an additional zone of carburization preceded the internal sulphidation

zone. The authors proposed that carbon initially diffused into the alloy to form carbide precipitates. Subsequently sulphur also diffused into the alloy. As the sulphur activity increased the carbides were transformed to sulphides and the carbon released was driven deeper into the alloy. Interestingly, the amount of carburization was much less than in purely carburizing environments. Only 3mg/cm^2 were attributed to carbon uptake in oxidizing/sulphidizing/carburizing conditions compared with 40 mg/cm^2 under purely carburizing conditions (Schnaas and Grabke⁽⁹⁹⁾). Even though the amount of carburization was small it should be emphasised that the conversion of carbides to sulphides resulted in considerable carbon penetration depths.

Preoxidation

The formation of an oxide layer in a sulphur-free gas prior to exposure to a sulphur-containing gas has been proposed as a method of improving an alloy's resistance to sulphidation.

Unfortunately the advocates of such a theory do not always realise that :

- (i) The scale will continue to grow when it is subjected to the sulphur-containing environment.
- (ii) The scale will probably contain physical defects in the form of cracks and pores, which could form a continuous network through the oxide and allow direct access of the sulphur-containing gas to the alloy substrate.
- (iii) The composition of the oxide could be very important.

The first point is illustrated by the work of Natesan⁽¹⁸²⁾ who pre-oxidised pure Cr at a $p\text{O}_2 = 9 \times 10^{-18}$ atm. (presumably at 875°C) for 244 hours. Specimens were then exposed to $\text{CO-CO}_2\text{-CH}_4\text{-H}_2\text{-H}_2\text{S}$ gas mixtures for 120 hours, figure 2.98. In the case of gas mixtures with $p\text{O}_2$'s 2-3 orders of magnitude in excess of the thermodynamic boundary (i.e. to the right of the kinetic boundary) no S was detected either at the gas/scale interface or in pores in the scale.

In a gas mixture with the pO_2 only one order of magnitude in excess of the thermodynamic boundary (i.e. to the left of the kinetic boundary) chromium sulphide formed at the scale/gas interface but no S was detected in the preformed oxide. The same findings were observed by La Branche et al.⁽¹⁶²⁾ who preoxidised pure Cr at $pO_2 = 10^{-19}$ atm. at 900°C for 2 hours in H_2-H_2O and subsequently exposed the sample for 111 hours to $H_2-H_2O-H_2S$ atmospheres corresponding to $pS_2 = 10^{-6,5}$ atm. and $pO_2 = 10^{-19}$ atm. at 900°C (to the left of the kinetic boundary). Because little or no sulphur was detected in the pores of the preformed oxide Natesan⁽¹⁸²⁾ and La Branche⁽¹⁶²⁾ deduced that gas phase transport of H_2S through the pores was negligible and that sulphide formation at the scale/gas interface was due to Cr^{3+} diffusion through the oxide scale.

When the results of Natesan⁽¹⁸²⁾ and La Branche et al.⁽¹⁶²⁾ are considered together it really does appear that the only benefit of a preformed Cr_2O_3 layer on Cr is to overcome the initial transient sulphidation behaviour and to slow down the rate of supply of Cr ions to the scale/gas interface. In other words, for a given gas composition the end result after long term exposure, whether a sulphide scale (to the left of the threshold boundary) or an oxide scale (to the right of threshold boundary), will be the same regardless of whether the Cr was preoxidised or not.

Bearing this point in mind it is worthwhile considering the preoxidation of alloys. Natesan⁽¹⁸²⁾ preoxidised Incoloy 800 for 165 hours at 875°C ($pO_2 = 10^{-18}$ atm.). Subsequently specimens were exposed for 165 hours to H_2-H_2S or $CO-CO_2-CH_4-H_2-H_2S$ gas mixtures with a wide range of oxygen and sulphur partial pressures. The results of this study are summarised in figure 2.99. As in the case of pure Cr, subsequent exposure to gas mixtures ES, GM and IM (to the left of the threshold boundary for the virgin alloy) resulted in the formation of external sulphides, except in this case Fe and Ni were also incorporated into the scale. To the right of the kinetic boundary, gas EM on figure 2.99, a chromium oxide continued to form and some internal chromium sulphide precipitates formed at grain boundaries. The important point to emerge from this study, which incidently Natesan missed, is that sulphur penetrated a preformed chromium oxide on the alloy but did not penetrate a preformed

chromium oxide on the metal. Thus the two oxide scales must either have different compositions or physical structures.

This point is extremely important if the results of another pre-oxidation study by Stott et al. are considered⁽¹⁸³⁻¹⁸⁵⁾. A Fe-28%Cr alloy and several Fe-28%Cr alloys with additions of Al and Y, Incoloy 800 and SS310 were preoxidised for up to 20 hours either in H_2 - H_2O or air at 900°C. The temperature of the rig was then lowered to 750°C and the preoxidised specimens subjected to the H_2 - H_2O - H_2S gas mixtures marked in figure 2.100. These gases are very severe (1.5-2% H_2S) and lie to the left hand side of the threshold boundary. In other words, the virgin alloy would form a sulphide scale if subjected to the environment without being preoxidised. Although the preformed oxides remained protective for short exposure times scales on all alloys broke down in less than 300 hours, figure 2.101. Alloys containing significant Al_2O_3 additions (1-3 %) tended to form Al_2O_3 scales in the preoxidation treatment which resisted sulphidation longer than preformed Cr_2O_3 scales. A mechanism was proposed for the breakdown of both Cr_2O_3 and Al_2O_3 scales, figure 2.102. Initially sulphur penetrated the preformed oxide via localised paths and headed for the alloy/scale interface, figure 2.102a. Sulphides then formed at the alloy/scale interface, figure 2.102b. These sulphides were subsequently incorporated into the oxide scale and being relatively non-stoichiometric provided easy diffusion paths for the outward diffusion of metal cations, figure 2.102c. The reaction between these ions and the inward diffusing sulphur-containing species at the sulphide-oxide interface resulted in the development of sulphide "ducts" across the scale, figure 2.102d. These ducts provided rapid diffusion paths for metal ions from the alloy to the scale/gas interface enabling sulphides of the base metals (Cr and Fe) to form at the scale/gas interface, figure 2.102e. This process continued with the ducts enlarging to allow easier transport of metal ions outwards to form large external sulphides and sulphur inwards resulting in substantial internal sulphidation, figure 2.102f-i.

As in the case of Natesan's⁽¹⁸²⁾ work, the critical question is how does the sulphur penetrate the oxide scale in the first place? Stott indicates that if breakdown occurs very quickly, sulphur penetration

occurs by gaseous transport through cracks formed during the growth of the scale or during cooling from the preoxidation temperature. However, if breakdown is delayed sulphur penetration occurs by S diffusing down high angle grain boundaries, microchannels or other localised defects. The authors conclude that more detailed investigations are needed to determine how S penetrates oxide scales.

Perkins⁽¹⁵²⁾ proposed two modes of failure of metallic materials in coal gasification atmospheres.

- (i) Random pitting attack
- (ii) General sulphide slagging

In random pitting attack, surface defects permitted localized build up of carbon and sulphur activities. The high local carbon activity then promoted carbide formation. This depleted the alloy in Cr and resulted in the formation of a non-protective Fe-rich (Fe, Cr) oxide. This in turn allowed sulphur to enter into the alloy and attack the carbides thus releasing the carbon and causing further carburization. The cycle was repeated until the component failed.

Perkins claimed that this type of attack could be prevented by forming an oxide layer in the absence of sulphur and carbon. He proved this by pre-forming a Cr_2O_3 layer on a Ni-46Cr alloy which subsequently acted as a complete barrier to sulphur and carbon ingress on exposure to a medium BTU gas containing 1 % H_2S for 1500 hours at 871 and 982°C.

In sulphide slagging, a sulphide scale formed at the scale/gas interface. In this case Perkins claimed to form a Cr_2O_3 layer on 310SS in H_2 - H_2O . (In the opinion of the author of this review it is impossible to do this without also forming MnCr_2O_4). Fe and Mn were then transported outwards through the Cr_2O_3 layer to form an additional outer spinel layer. This process continued until the Fe activity in the oxide reached a value at which sulphides of Fe could be in equilibrium with the gas and external sulphides formed. Perkins therefore concluded that in this case pre-oxidation could only prevent failure if the sulphur level in the gas was kept below the base metal sulphidation potential.

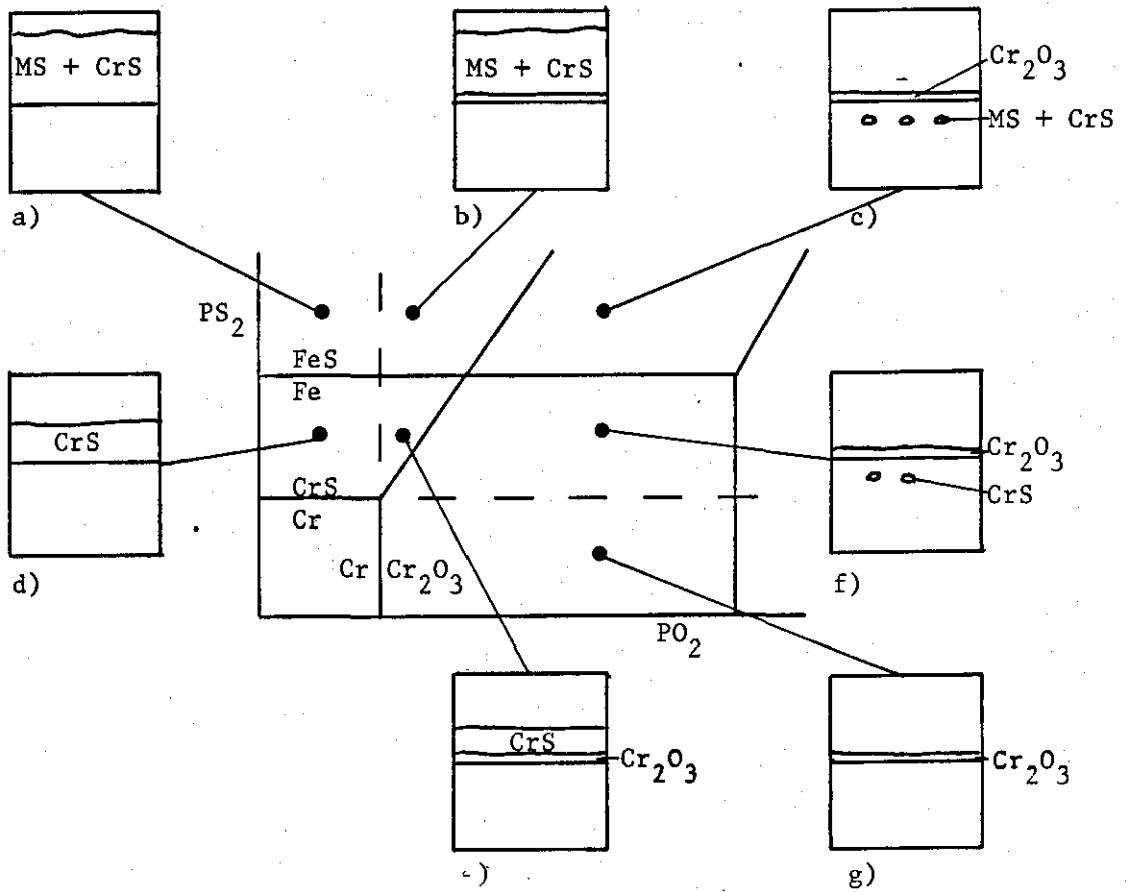


Figure 2.78
Schematic metal stability diagram for the M-S-O system and theoretical corrosion morphologies.

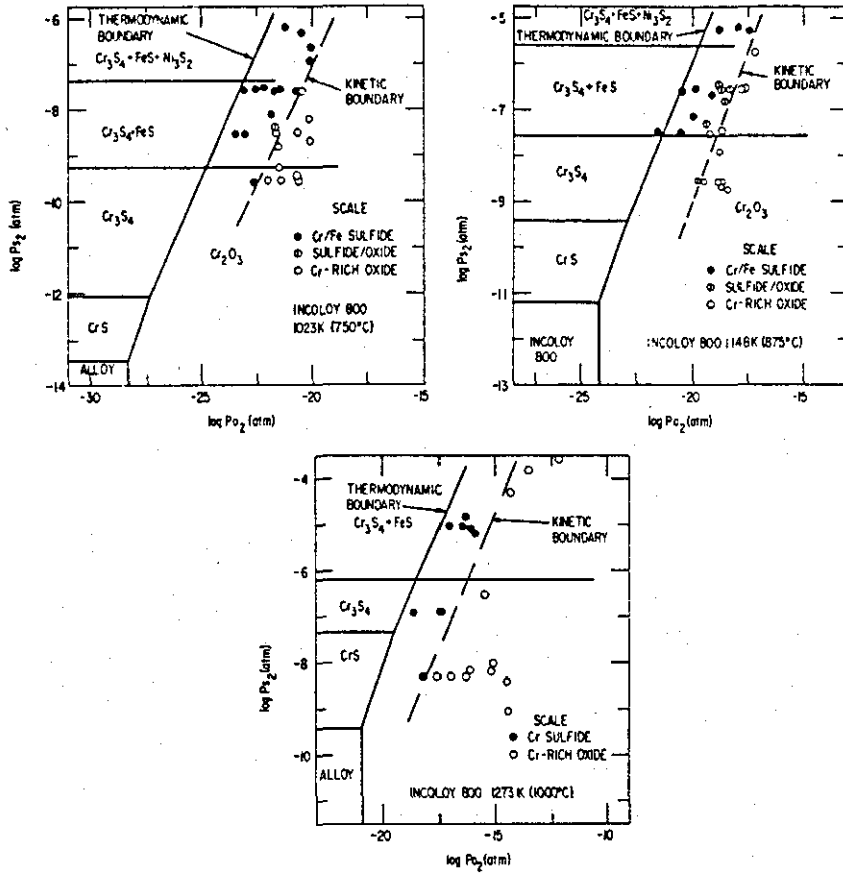


Figure 2.79

Types of scale developed on Incoloy 800 as a function of oxygen and sulphur partial pressures at temperatures 750, 875 and 1000°C (149).

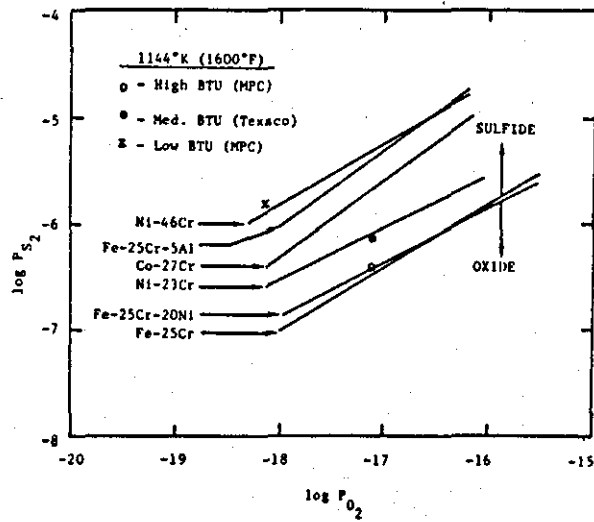


Figure 2.80
Oxide/sulphide kinetic boundaries for
the initial stage of scale formation
on Fe, Ni and Co-based alloys in
 $H_2-H_2O-H_2S$ mixtures at 1144 K (151).

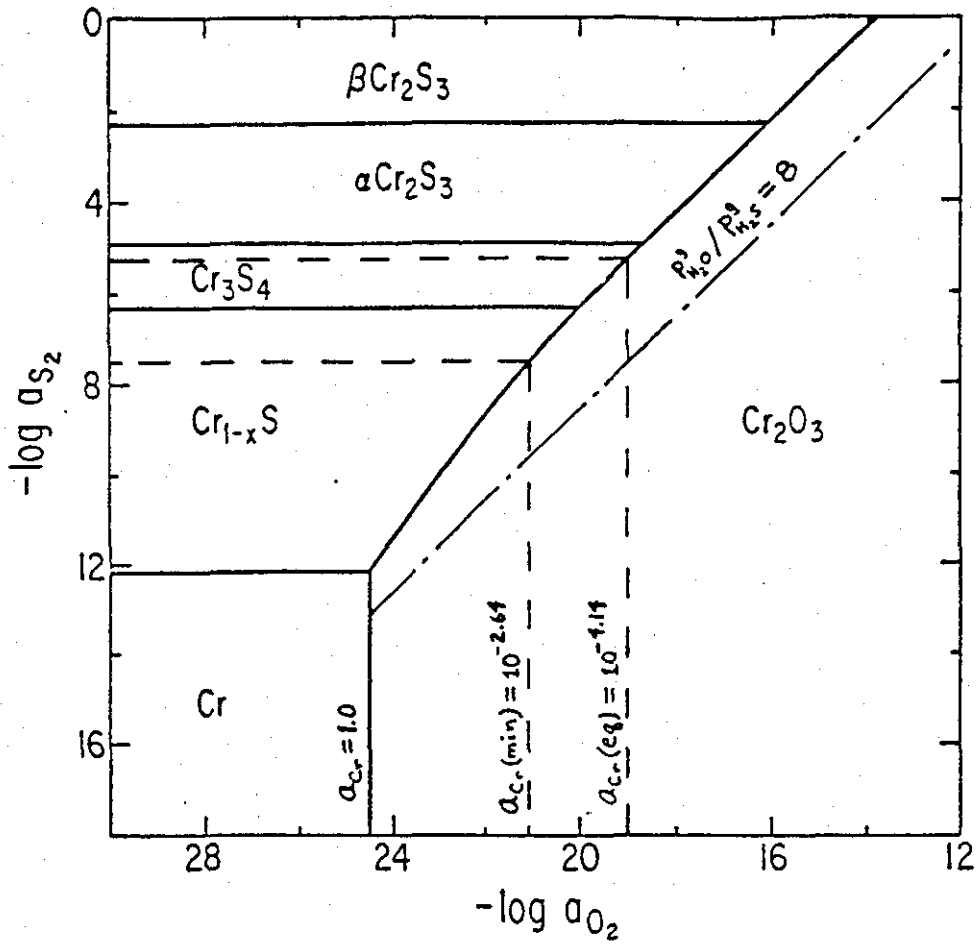


Figure 2.81

Stability diagram for the Cr-S-O system at 900°C. The dotted lines represent constant activities of Cr. The dash-dot line corresponds to a $\text{H}_2\text{O}/\text{H}_2\text{S}$ ratio of eight (161).

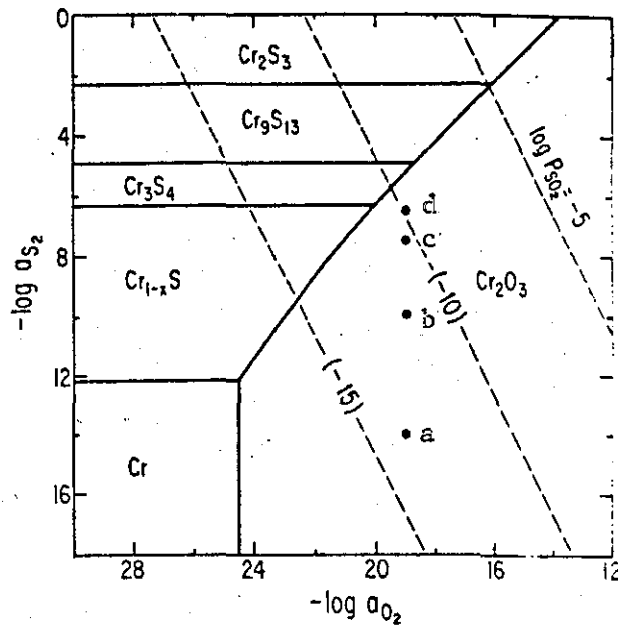


Figure 2.82

Stability diagram for the Cr-S-O system at 900°C. The filled circles indicate the gas compositions used by La Branche et al (162).

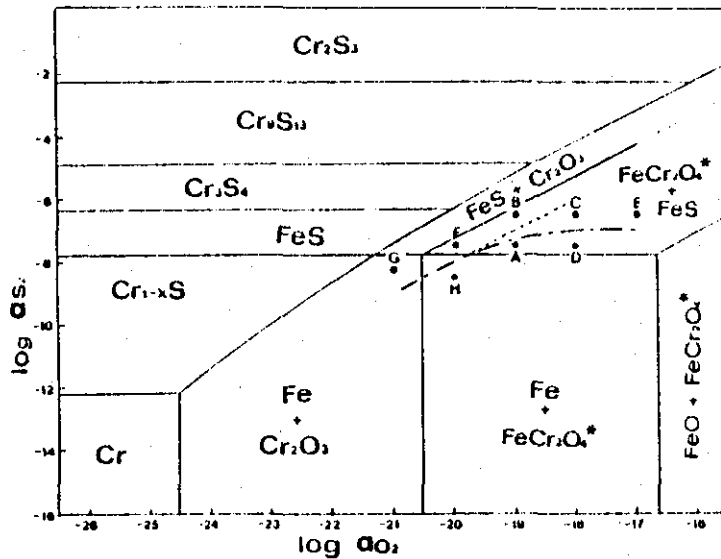


Figure 2.83

Stability diagram for the Fe-Cr-S-O system at 900°C. The dashed line is the kinetic boundary for pure chromium and the dash-dot line the boundary for Fe-25Cr (164).

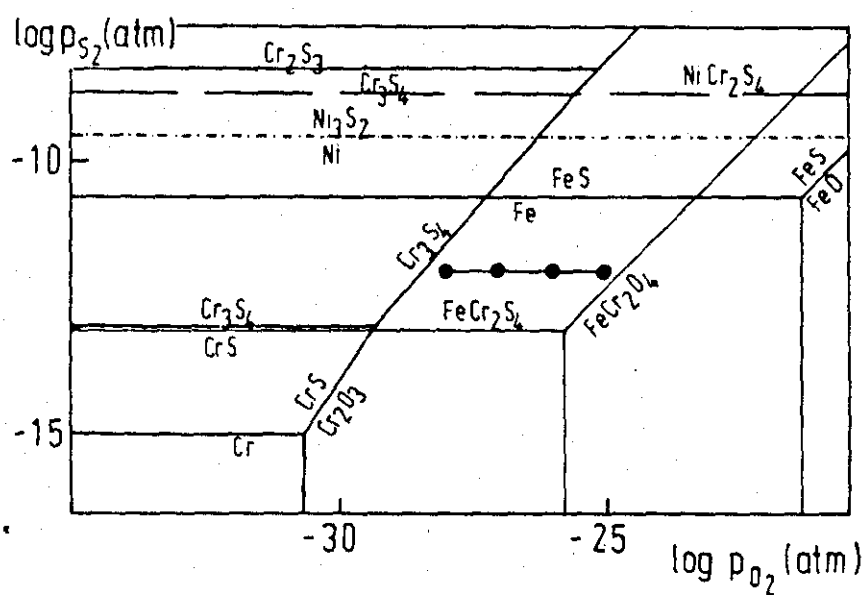


Figure 2.84

Superimposed phase stability diagram for an Fe-Cr-Ni alloy. The points indicate the composition of the gases used (165).

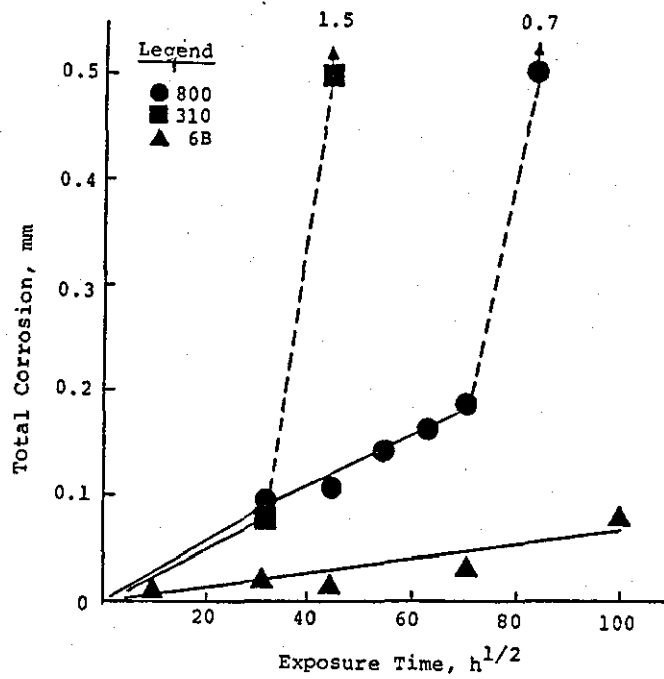


Figure 2.85

Typical corrosion behaviour of selected alloys in a simulated coal gasification atmosphere at 982°C, 0.5% H₂S, 6.89 MPa. (169).

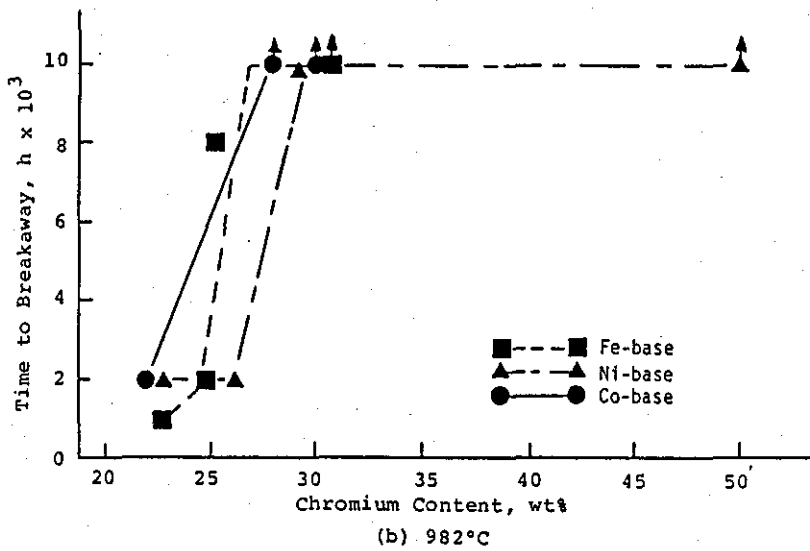
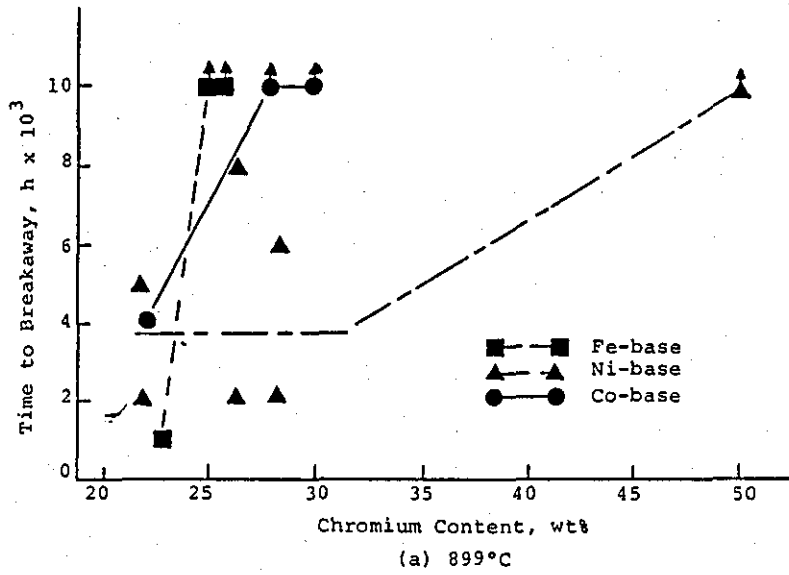


Figure 2.86

Effect of chromium content on time to breakaway in 1% H₂S, 6.89 MPa gas at 899 and 982°C (169).

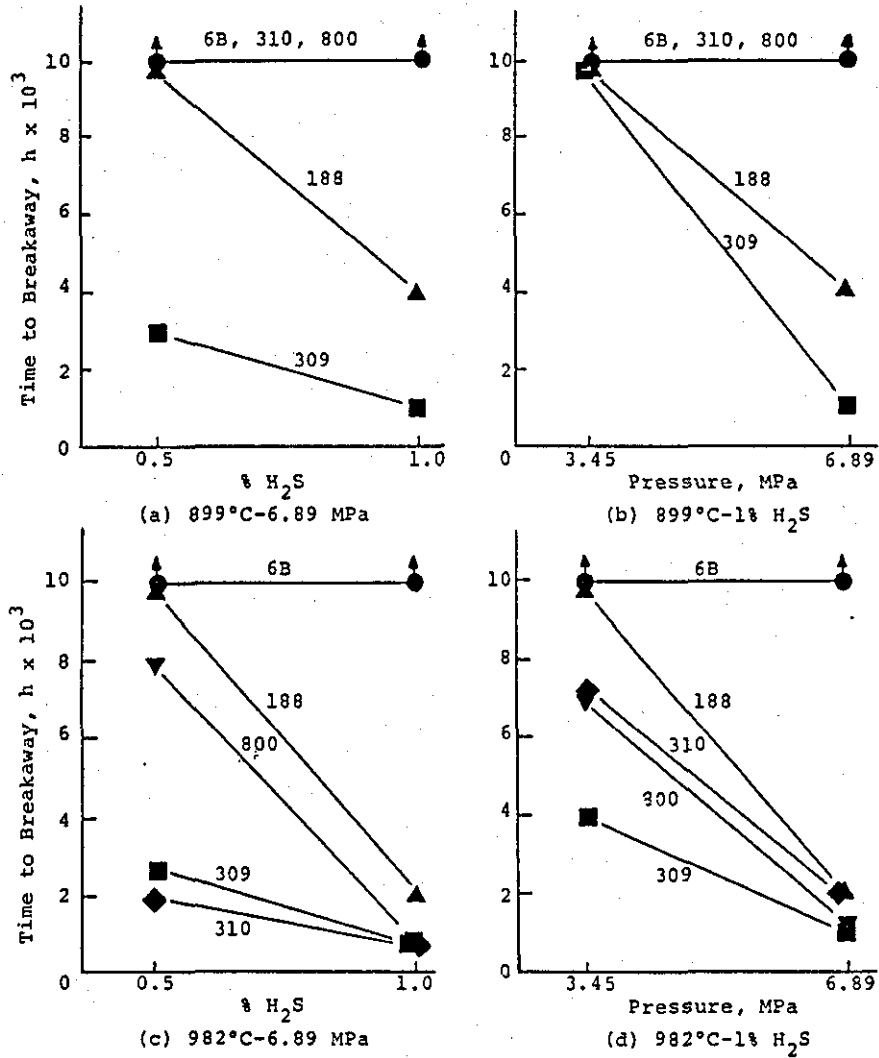
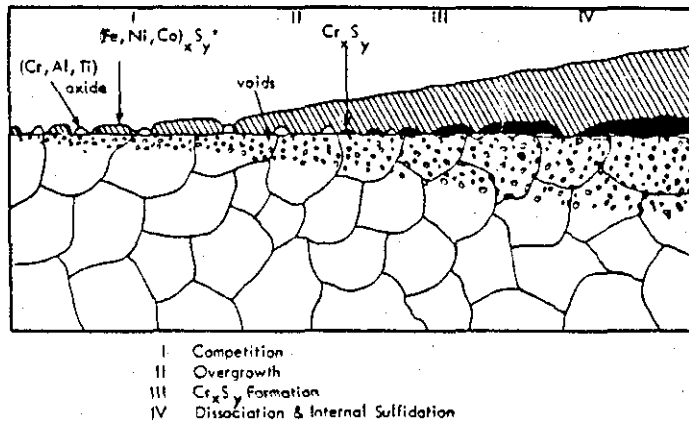


Figure 2.87

Effect of pressure and H_2S concentration on time to breakaway at 899 and 982°C (169).



*If the base metal sulfide is molten at test temperature, islands of Cr_xS_y , oxides and Cr-depleted alloy exist in the outer scale after cooling due to grain boundary attack by the liquid.

Figure 2.88
Reaction model for sulphidation-oxidation of advanced alloys in low-Btu gasifier conditions (171).

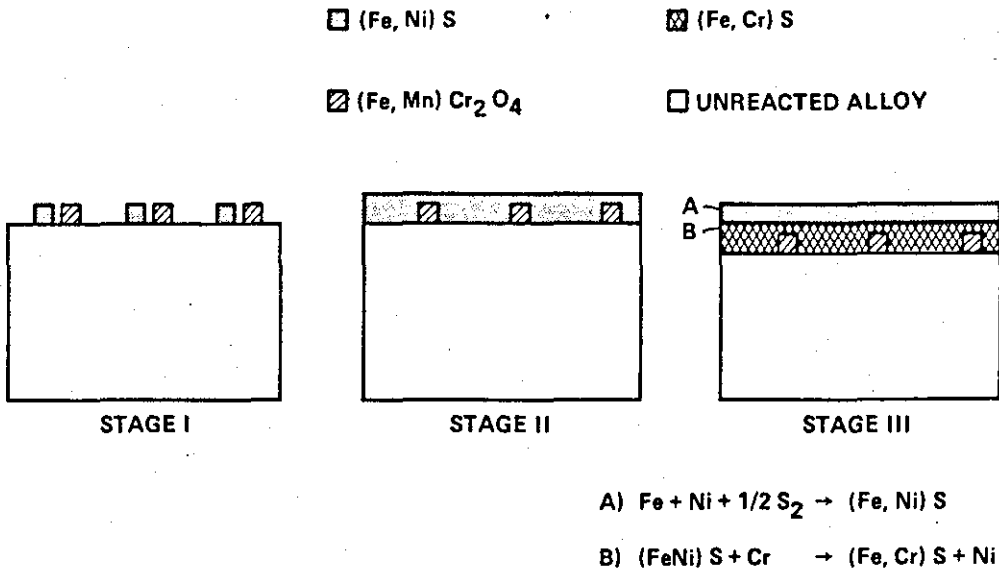


Figure 2.89
Schematic drawing of the corrosion mechanism suggested by Rao et al (160).

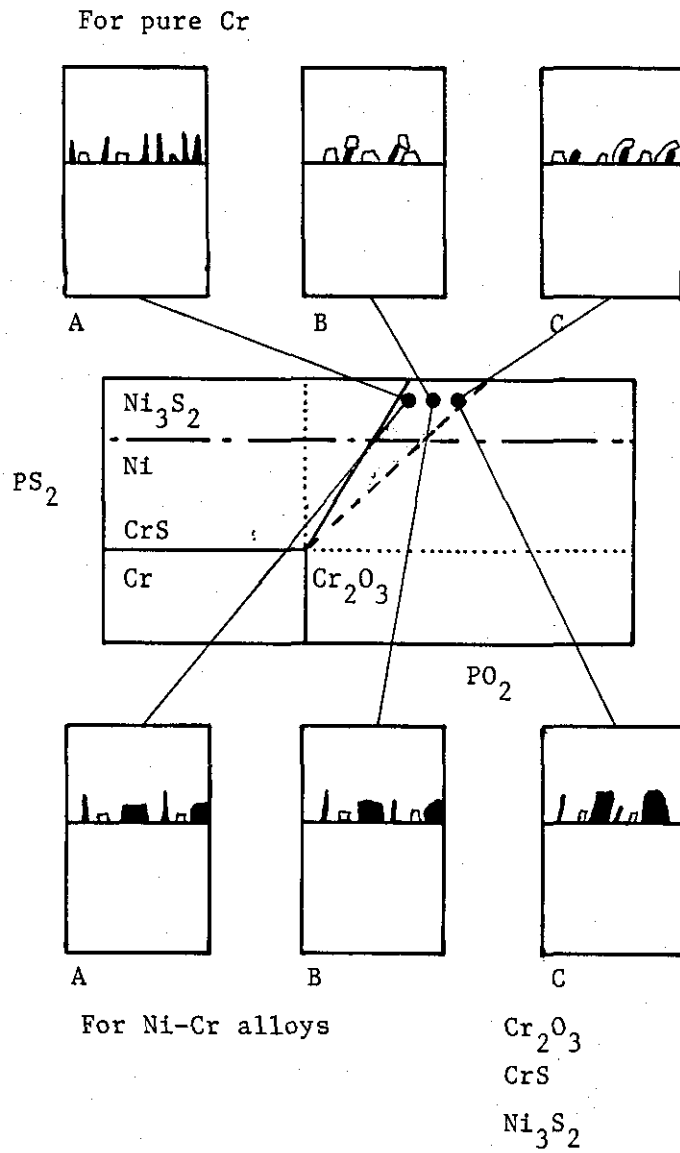


Figure 2.90

Schematic diagram showing corrosion morphologies found by Wang and Douglass (109) at 800°C and $a_c = 0.4$. Short term exposures up to 15 mins.

A) $PO_2 = 10^{-21}$, $PS_2 = 10^{-6}$ bar.
 B) $PO_2 = 10^{-21}$, $PS_2 = 10^{-6}$ bar.
 C) $PO_2 = 5 \times 10^{-20}$, $PS_2 = 10^{-6}$ bar.

The dashed line is the kinetic boundary.

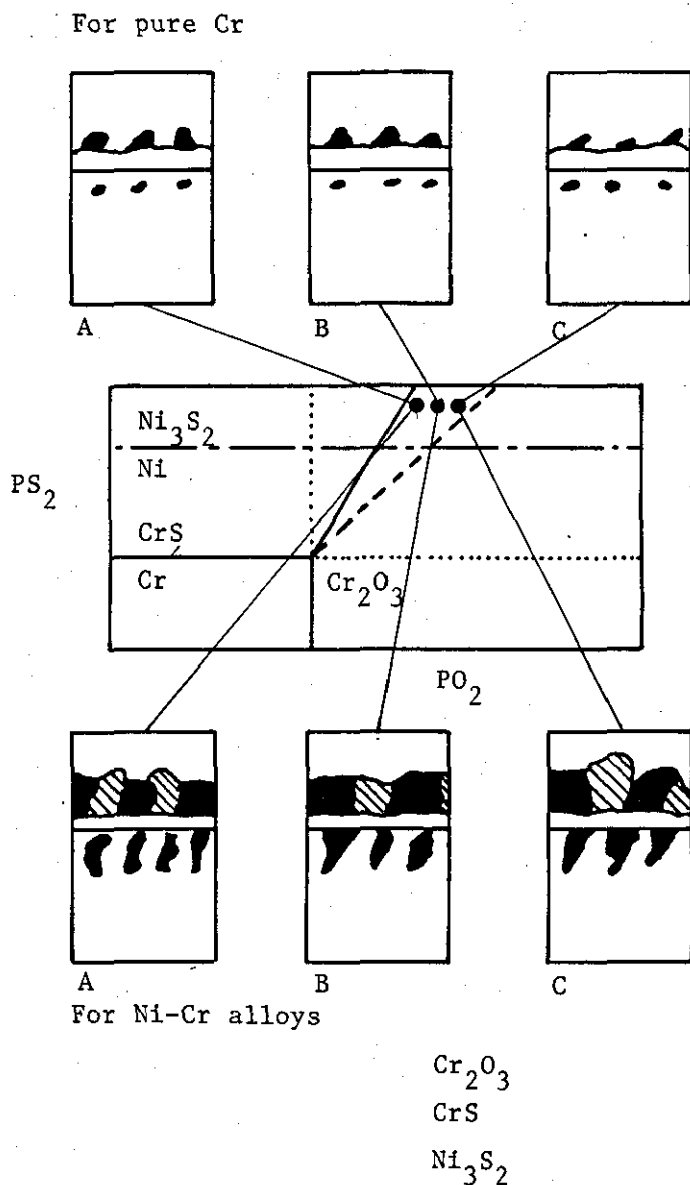


Figure 2.91

Schematic diagram showing corrosion morphologies found by Wang and Douglass (109) at 800°C and $a_c = 0.4$. Long term exposures up to 24 hours.

A) $PO_2 = 10^{-20}$, $PS_2 = 10^{-6}$ bar.
 B) $PO_2 = 10^{-20}$, $PS_2 = 10^{-6}$ bar.
 C) $PO_2 = 5 \times 10^{-20}$, $PS_2 = 10^{-6}$ bar.

The dashed line is the kinetic boundary.

FeS
(Fe,Cr)S + FeCr ₂ S ₄ + Metal
Cr ₂ O ₃
Alloy

Figure 2.92
Typical corrosion morphology
obtained by Chu & Rahmel.

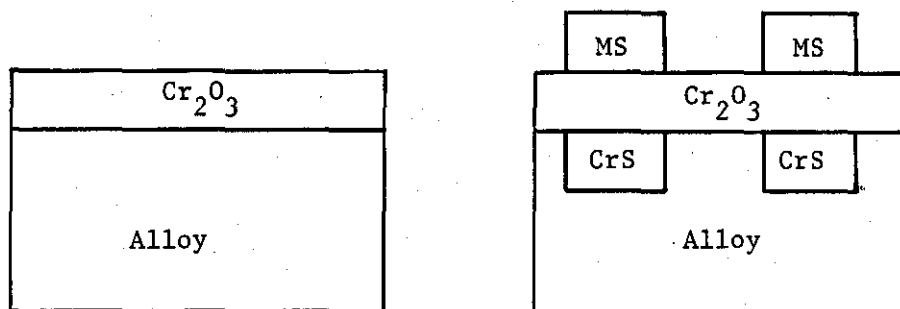


Figure 2.93

Schematic illustration of the corrosion morphology found by Hindam + Whittle for an M-25Cr alloy at 1300 K.

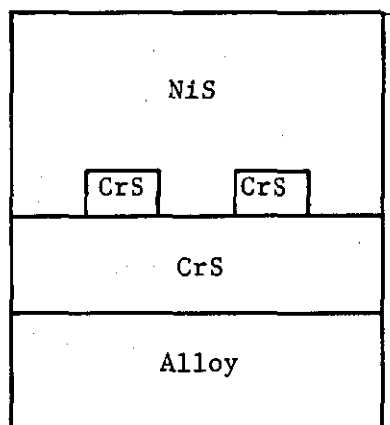


Figure 2.94

Schematic illustration of the corrosion morphology found by Hindam and Whittle at 1200 K.

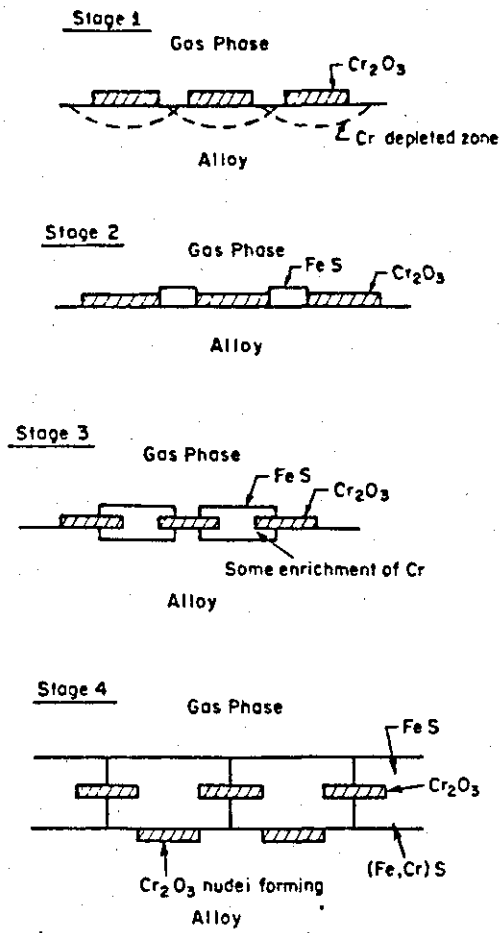


Figure 2.95
Schematic drawing of scale growth
found by Nagarajan et al. (177).

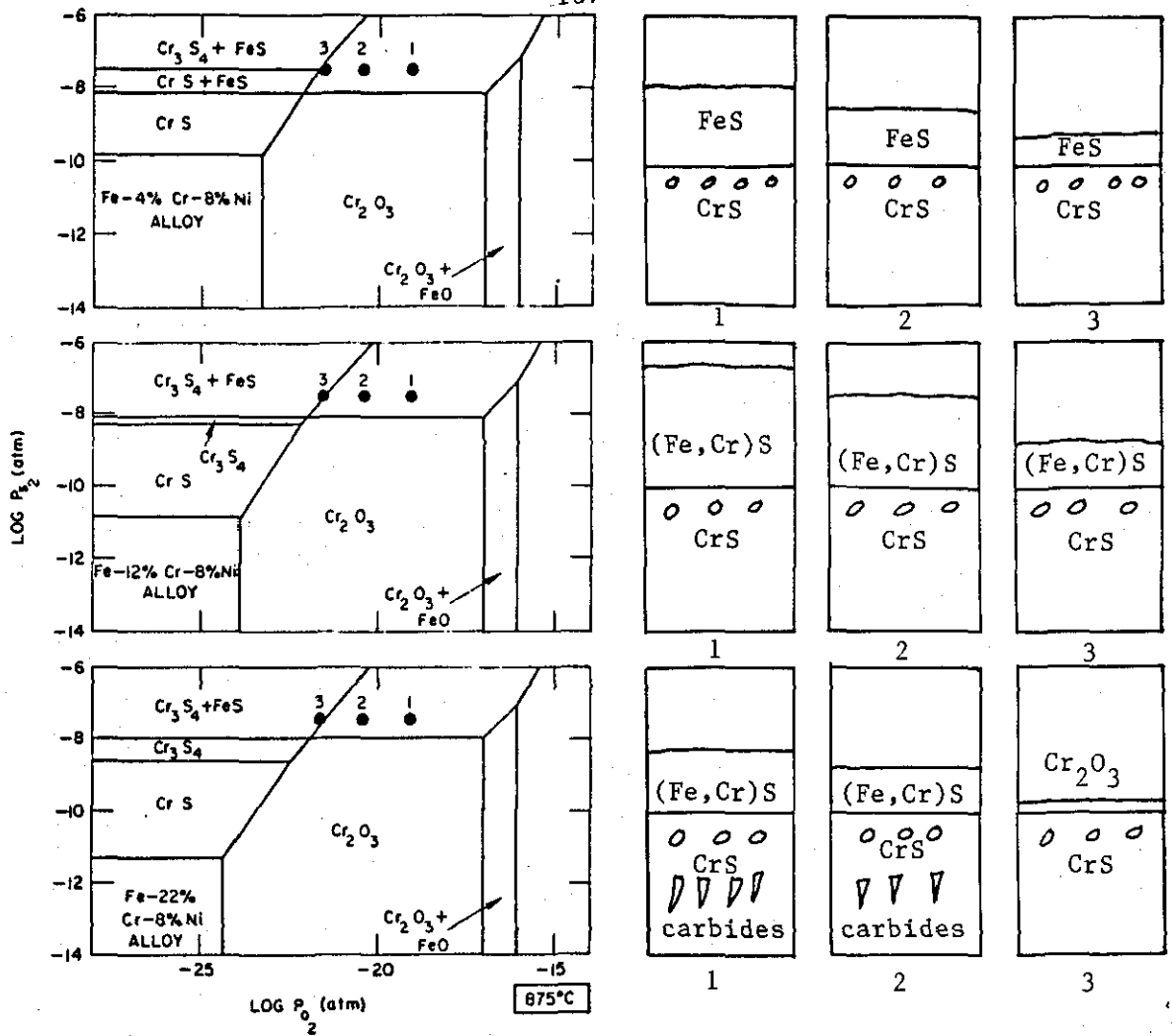


Figure 2.96

- Thermodynamic stability diagram showing the gas compositions used by Danielewski and Natesan (178).
- Schematic drawing of the corrosion morphologies obtained when Fe-Cr-Ni alloys were exposed to these gases for 25 hours.

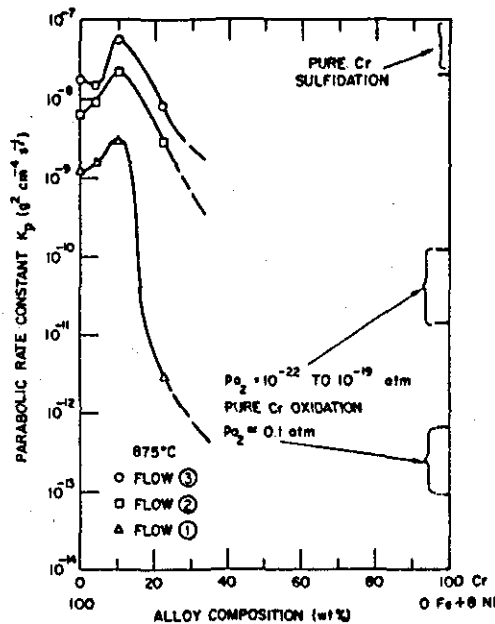


Figure 2.97

Variation of parabolic rate constant as a function of Cr content in Fe-Cr-Ni alloys (178).

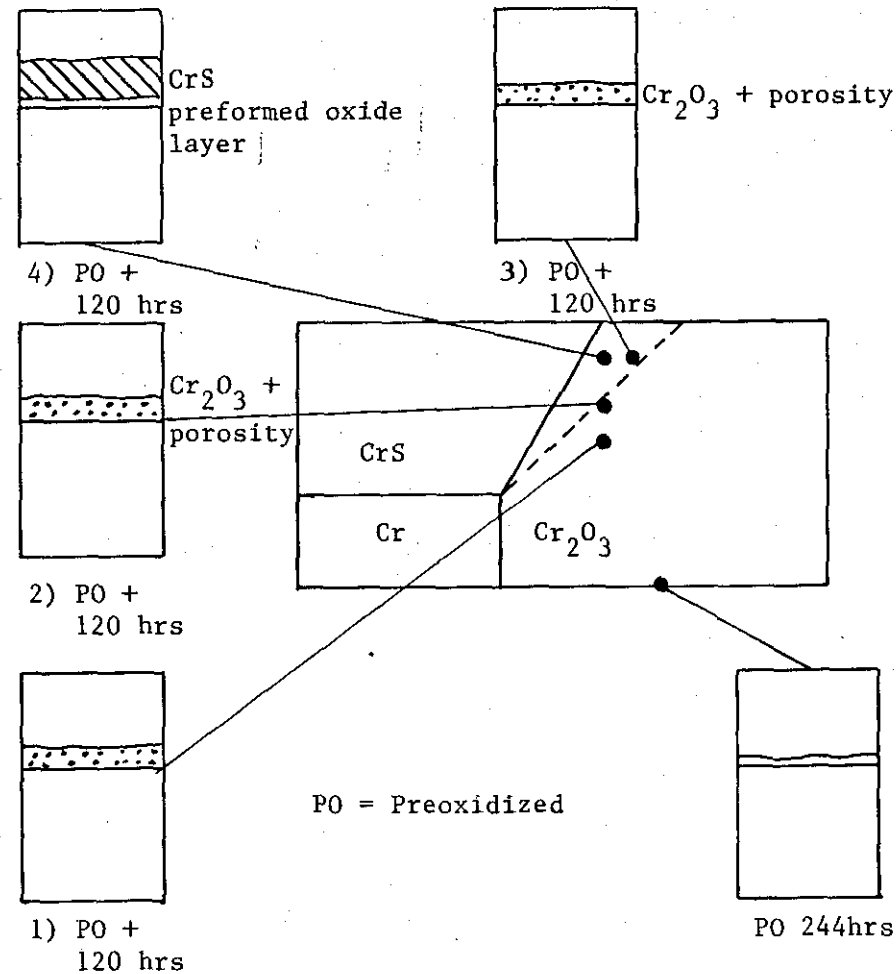


Figure 2.98

Schematic diagram showing the corrosion morphologies obtained when preoxidized Cr is exposed to gases either side of the kinetic boundary at 875°C.

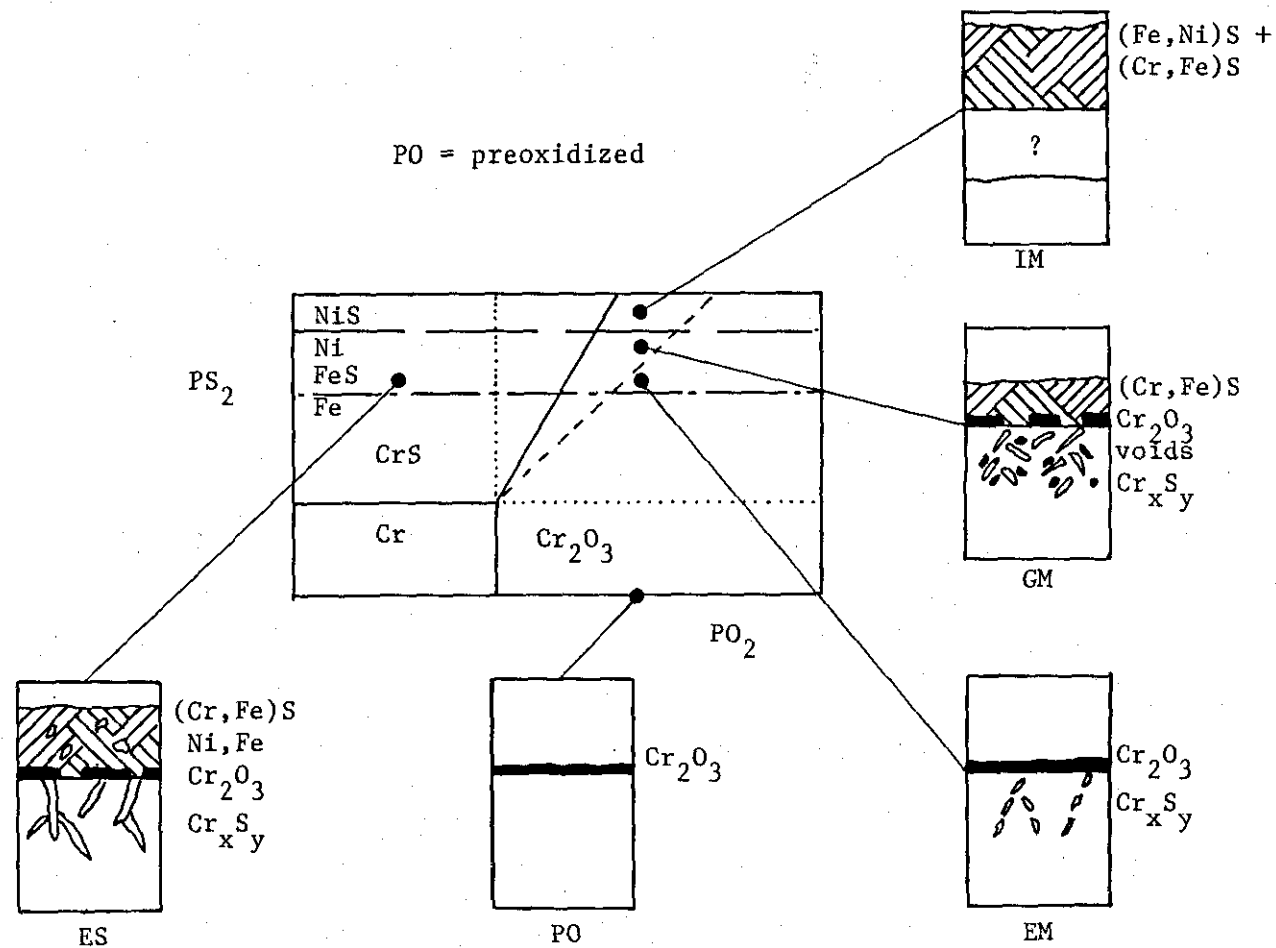


Figure 2.99

Schematic diagram showing the corrosion morphologies obtained when preoxidized Incoloy 800 was exposed to gases either side of the kinetic boundary at 875°C .

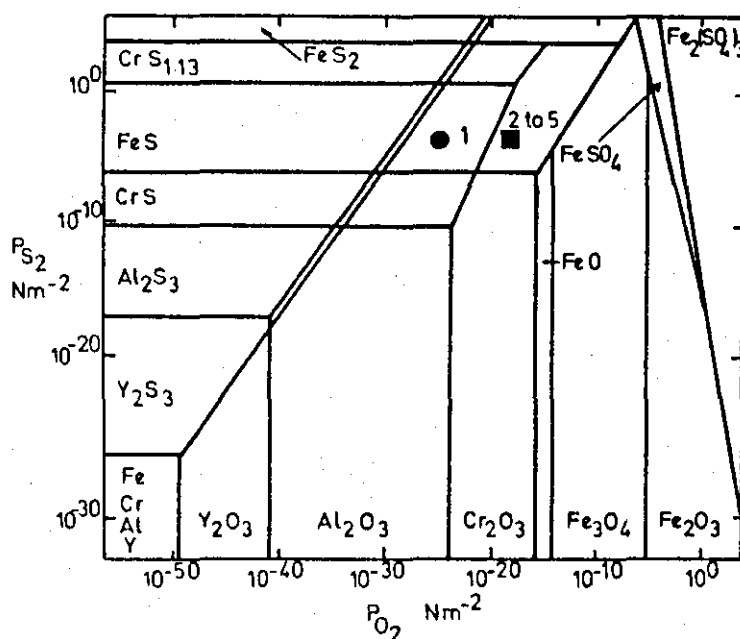


Figure 2.100

Thermodynamic phase stability diagram for the M-S-O system, where M = Cr, Al, Y, at 750°C. The positions 1 to 5 indicate the gas compositions used by Stott et al (183-185).

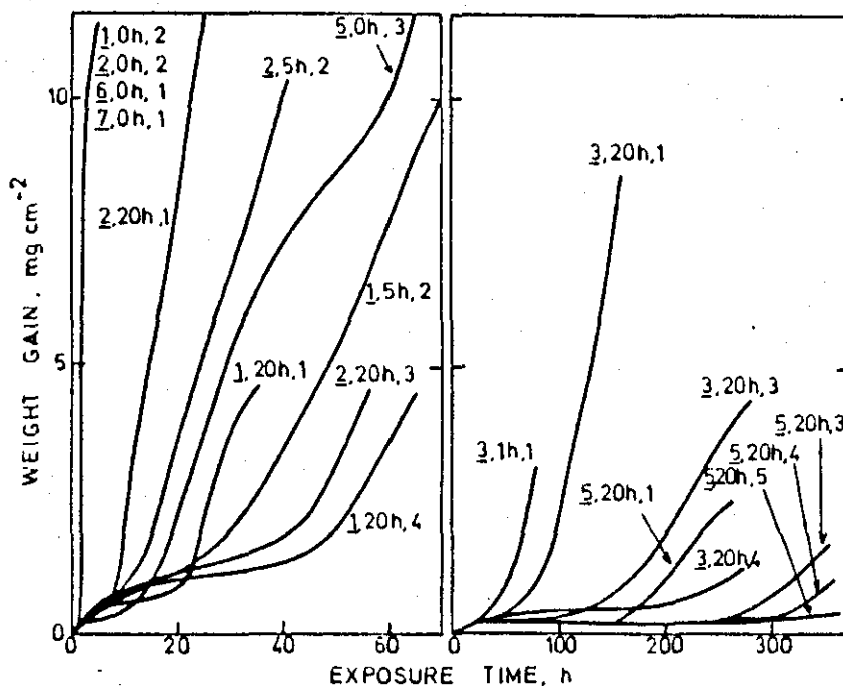


Figure 2.101

Corrosion kinetics for various alloys exposed to $H_2/H_2O/H_2S$ gases; used by Stott et al at 750°C. Each curve is labelled with the alloy, time of preoxidation, and gas composition shown in figure 2.100. 1 Fe-28Cr, 2 Fe-27Cr-0.8Y, 3 Fe-27Cr-1Al, 4 Fe-27Cr-4Al-0.023Y, 5 Fe-26Cr-4Al-0.8Y, 6 Incoloy 800, 7 SS310 (183-185).

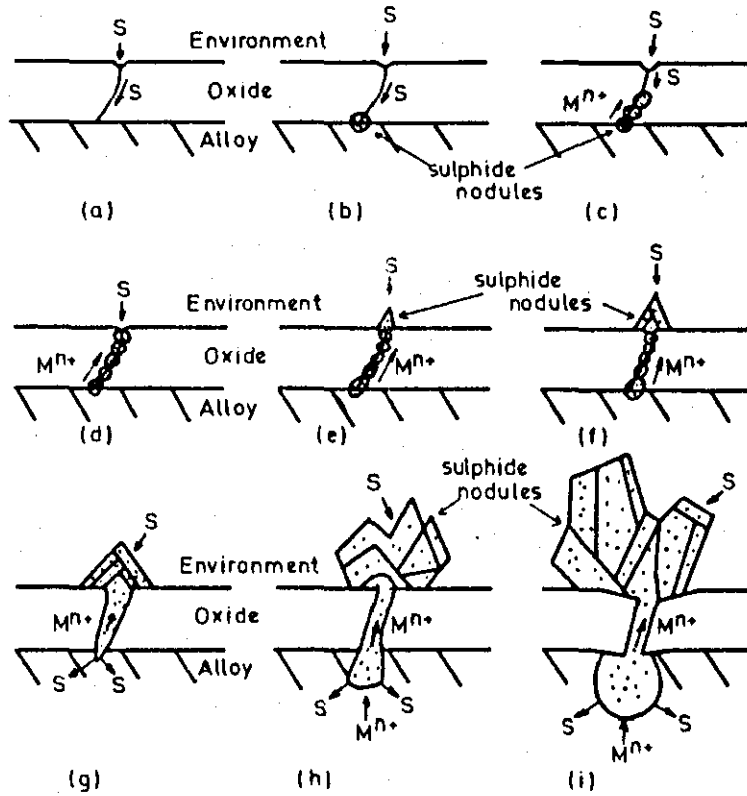


Figure 2.102

Schematic representation of the progressive development of sulphides through Al_2O_3 or Cr_2O_3 scales on preoxidized Fe-Cr-Ni alloys at high temperatures (183-185).

2.4. RESEARCH REQUIREMENTS EMERGING FROM THE LITERATURE REVIEW

The literature review has shown that metallic components, such as heat exchangers, in coal gasification and fluidized bed combustion processes will have to operate at high temperatures in atmospheres containing low partial pressures of oxygen, high partial pressures of sulphur and a significant carbon activity. Thus it is theoretically possible for oxidation, sulphidation and carburization to take place either independently or in association with each other.

The review has also shown that the mechanisms by which metals and alloys corrode in oxidizing, sulphidizing, carburizing, oxidizing/carburizing and carburizing/sulphidizing atmospheres are relatively well understood.

A vast amount of very poor quality research has also taken place in sulphidizing/oxidizing environments. Most of this has been concentrated in atmospheres containing relatively high levels of sulphur where sulphidation processes are dominant and the high corrosion rates make conventional high temperature alloys unusable. Only a limited amount of work has taken place in atmospheres containing lower levels of sulphur, where oxidation processes tend to dominate. The researchers who have worked in this latter area have only done one of the following :

- (i) Concentrated on the early stages of the corrosion process (up to 25 hours) and then stopped.
- (ii) Exposed a large number of alloys for a few hundred hours and tried to interpret their findings, sometimes incorrectly.
- (iii) Carried out long-term testing for up to 10000 hours and found that after several thousand hours the protective oxide scales broke-down, to form non-protective sulphides. Unfortunately they did not analyse their results to establish why this happened.

The review also showed that research in this area to date has :

- (i) Often ignored the role of carbon, which is usually present both in the gaseous environment and in the alloy.
- (ii) Given little attention to the possibility of protection from an SiO_2 layer which has proved to be very beneficial in oxidizing/carburizing environments.
- (iii) Seldom considered the effect surface finish can have on the corrosion process.

Thus in summary a definitive study is needed to establish systematically how and why the corrosion process develops from the first few minutes through to several thousand hours; to determine the mechanisms which can lead to breakaway corrosion and to assess the role of carbon, silicon and surface finish in this process.

3. EXPERIMENTAL

3.1. MATERIALS AND THEIR PREPARATION

Alloy Composition

The superior corrosion resistance of stainless steels exposed at high temperatures in aggressive environments results from this class of alloy having the potential to form protective oxide scales. There are three main oxide forming elements which can be present in commercial alloys namely chromium, aluminium and silicon. In practice, however, protection is primarily provided by the formation of a continuous Cr_2O_3 scale on the surface of the alloy, although in some cases the presence of internal Al_2O_3 and SiO_2 layers can be of additional benefit. Work by Croll and Wallwork⁽¹⁸⁶⁾ has shown that a chromium content $> 18\%$ is required to obtain a continuous Cr_2O_3 layer. Unfortunately, increasing the chromium content reduces the high temperature strength of the material and also leads to embrittlement at low temperature. Nickel is therefore added to increase the creep strength and the associated ductility. Alloys containing 25Cr-20Ni exhibit a tendency to form the brittle sigma phase in the temperature range $500^\circ\text{--}900^\circ\text{C}$ which is countered by the use of high nickel contents. A class of commercial 25Cr-35Ni alloys has therefore been developed which combine corrosion resistance with good mechanical properties and this study has also included this type of alloy.

The compositions of the specific alloys selected are given in table 3.1. As commercial alloys contain several minor alloying additions such as manganese, silicon, titanium, niobium, carbon etc. many possible reactions can take place in the corrosion process. To simplify the situation and assist in the interpretation of results a pure ternary 25Cr-35Ni-40Fe alloy was studied. By comparing the behaviour of this alloy with that of the commercial alloys it was possible to establish the effect of the minor alloying elements on the corrosion mechanisms. The commercial 25Cr-35Ni alloys, HP40Nb and HP40Al contain additions of silicon, manganese, niobium and carbon with the HP40Al alloy also containing 3.5% aluminium. By comparing the behaviour of these two alloys it was possible to determine the effect of aluminium on the

corrosion behaviour. Alloy 800H is a commercial 20Cr-33Ni alloy of importance because of its excellent high temperature mechanical properties. The alloy contains alloying additions of silicon, manganese, titanium and aluminium. Finally to assess the effect of silicon on corrosion resistance a commercial 25Cr-20Ni alloy AISI 314 was included. This alloy has a relatively high silicon addition (2 %) and also contains a significant amount of manganese.

Alloy Macrostructure

The metallurgical form and structure of an alloy can have a significant effect not only on the corrosion resistance of a material but perhaps much more importantly upon the mechanical properties. Steels containing < 0,15 % carbon are ductile over a large temperature range and can be hot worked and therefore supplied as wrought products such as bar, plate and tube. High carbon steels however have a much higher deformation resistance due to the potential of carbon to act as a strengthening element. These alloys are therefore usually supplied as castings. The metallurgical form and heat treatments given to alloys used in this study are given in table 3.2.

The high-purity ternary model alloy (25Cr-35Ni-40Fe) was produced by Brown-Firth Research Laboratories, U.K. The ingot had a typical cast structure with (0,5 mm) chill crystals at the surface, large columnar grains (10 mm x 1 mm) growing inwards and equiaxed grains (2 mm) at the centre, figure 3.1a.

Two commercial 25Cr-35Ni alloys HP40Nb and HP40Al were supplied as centrifugally cast tube by Fonderies et Acieries du Manoir, France. The HP40Nb alloy exhibited a mainly equiaxed structure (interdendritic spacing 30 μ m) with a region of columnar grains (interdendritic spacing 40 μ m) extending one-third of the way through the section, figure 3.1b. The HP40Al alloy consisted entirely of columnar grains (interdendritic spacing 30 μ m), figure 3.1c.

Alloy 800H was supplied by Henry Wiggin as wrought bar. The material was subsequently solution treated at 1150°C for 1 hour followed by water-quenching. The alloy had an equiaxed structure with the grain size

varying from 100-300 μm , figure 3.1d. Finally AISI 314 was also supplied as wrought bar from Pose-Marie and had a homogeneous equiaxed structure, the grain size was very small $\sim 10 \mu\text{m}$ and the macrostructure is therefore not shown in Fig. 3.1. This alloy received no subsequent heat treatment.

Alloy Microstructure

The microstructure of an alloy can exert a significant influence upon its reaction with a gas at high temperature. The grain size and precipitates in the material are important since grain boundaries can act as preferential diffusion paths and precipitates can act as nucleation sites for the internal precipitation of corrosion products e.g. sulphides, oxides and carbides. All alloys included in this study consisted essentially of single phase austenite with a face-centred cubic structure. The extent and nature of the precipitates present in each alloy was, of course, dependent of the respective chemical compositions and the heat treatments of the materials.

Figure 3.2 shows the microstructures of the alloys investigated. The model alloy consisted simply of single phase austenite whilst the centri-cast HP40Nb alloy contained an additional two types of carbide precipitate, i.e. M_7C_3 (where M was predominantly chromium) and niobium-rich MC. The HP40Al alloy was more complex and contained 3 types of carbides, i.e. M_7C_3 , MC, M_6C and an intermetallic compound NiAl. Alloy 800H had an equiaxed single phase austenitic structure with a grain size varying from 100 to 300 μm . Mechanical twins were present in some of the grains. Pink-coloured ("block"-like) titanium carbide precipitates, cuboid in shape, were evenly distributed throughout the material. AISI 314 also had an equiaxed single phase austenitic structure with a fine grain size $\sim 10 \mu\text{m}$. A few M_{23}C_6 precipitates were present at the grain boundaries.

Specimen Preparation

Standard rectangular specimens 10 x 8 x 6 mm were machined from the test materials in such a way that for the centrifugally cast alloys the columnar growth direction was parallel to the major surface of the

specimen as shown in figure 3.3. Special care was taken during the machining operation to avoid surface deformation.

Studies by Harrison et al.⁽¹⁰⁰⁾, Allan and Dean⁽¹⁸⁷⁾ and Strafford et al.⁽⁹⁰⁾ have shown that the initial surface finish can have a significant influence on the corrosion resistance of materials. Firstly, the degree of roughness of the surface affects the true area in contact with the environment and secondly, surface working can modify the grain structure of the alloy and hence the sub-surface diffusion rates. A further point is that segregated cast structures may, to some extent, be mechanically homogenised. In order to assess the importance of surface condition, therefore, two methods of surface preparation were used. In one case a worked layer approximately 2 μm deep was induced in the regions of all specimen surfaces, by grinding on '180 grade' SiC paper whilst in the other case work free surfaces were produced by electropolishing.

An automatic grinding technique was used to obtain a worked layer of reproducible depth. The technique is shown schematically in figure 3.4. The apparatus enabled variables such as grinding pressure, speed, time, condition of the SiC paper and the lubricant to be controlled. Three different faces of machined specimens could be prepared simultaneously. A total load of 2,38 kg was used. The bottom plate with the SiC paper rotated at 250 r.p.m. The preparation plate containing the specimens rotated contrary to the bottom plate and paper at 50 r.p.m. Each of the specimen faces was ground for 30 seconds with water flowing steadily over the contact areas. The '180 grade' SiC paper used was discarded after each complete preparation.

Any surface stresses resulting from the machining operation were removed by electropolishing under controlled conditions. The apparatus used is shown in figure 3.5. The machined specimens were initially ground on '600 grade' SiC paper until all visible signs of working had been removed. They were then immersed in an electrolytic bath of 15 % H_2SO_4 in methanol. A 10-15 V potential was applied between a platinum cathode and the specimen anode, with the electrolyte being magnetically stirred. The temperature of the solution was controlled between 15 and 20°C and the specimens were polished for a period of 60 minutes.

After surface preparation by either of the methods described, each specimen was given a unique identification, accurately measured ($\pm 0,01$ mm) and ultrasonically cleaned in ethanol. The specimens were then dried in a desiccator before being weighed on a Mettler HK60 balance. The specimens were stored in a desiccator prior to insertion in the corrosion autoclave.

3.2. GAS CHARACTERISATION

The thermodynamic considerations involved in the selection of these multi-component gas mixtures have already been described earlier and so it is sufficient to present the compositions of these atmospheres in table 3.3 along with their subsequent thermodynamic characterisation. The gas mixtures were primarily H_2 bal - 7 % CO with varying amounts of H_2S added so that the influence of sulphur activity could be studied in a systematic manner, e.g. at the test temperature of $800^\circ C$ the partial pressure of sulphur (p_{S_2}) was increased incrementally by one order of magnitude, whilst the partial pressure of oxygen (p_{O_2}) and the carbon activity (a_c) were kept constant. A sulphur-free gas was also used as a reference mixture to provide base-line data. The position of these gases are shown on a 2-dimension metal stability diagram, figure 3.6., and a 3-dimensional metal stability diagram, figure 3.7.

The gases were supplied in premixed, certificated, bottles by 1'Air Liquide, France and Matheson, Belgium. In each case, bottles were only accepted when the thermodynamic characterisation of the actual analysis came close to (within 0,1 of an order of magnitude of) the required partial pressure, e.g. for $p_{S_2} = 1 \times 10^{-9}$ bar, 0.9 to 1.1×10^{-9} bar was acceptable. The maximum permitted impurity levels (in v.p.m.) and values for the accuracy of certification for both manufacturers are given in table 3.4.

The oxygen activity was controlled by the addition of moisture to these pre-mixed gases by passing the gas through a humidification unit positioned immediately prior to the corrosion autoclave. The temperature of the wetting chamber was governed by the level of water required in the gas.

3.3. CORROSION AUTOCLAVES AND EXPERIMENTAL PROCEDURE

The equipment used for exposing the alloy specimens in the various corrosive gas mixtures at high temperatures consisted of a reaction vessel and a gas supply and control system.

Corrosion Autoclaves

A schematic diagram of the reaction system is shown in figure 3.8. In view of the potentially explosive and toxic nature of the test atmospheres used in these studies, a system was designed which consisted of a central reaction chamber and an outer, argon-purged safety vessel. The reaction chamber itself has two parts; the lower section consists of a closed end alumina furnace tube (1) located in the stainless steel vessel. The upper section holds a hollow alumina specimen support tube (2) a central closed end alumina thermocouple sheath (3) and 3 Pt/Pt-Rh thermocouples (4). The top chamber is water cooled and contains the inlet and outlet parts for the active and inert gases. The specimens are contained in individual alumina crucibles (5) which sit on alumina discs (6) which in turn slide over the central thermocouple sheath. Alumina discs are positioned at the bottom of the stack to create turbulence in the gas thereby ensuring a homogeneous mixture. The Pt/Pt-Rh thermocouples contained in the sheath are positioned so that they are adjacent to the top, middle and bottom of the specimen hot-zone.

The active gas flows through the reaction chamber as indicated in the diagram. In this way the gas is preheated as it passes between the furnace tube and the specimen support tube before passing upwards over the specimens.

The argon filled vessel which surrounds the reaction chamber contains the three-zone furnace (7). An alumina sheathed Pt/Pt-Rh control thermocouple (8) is positioned at the furnace tube in each of the zones. Also situated in each zone is a low melting-point (M.Pt = 1130°C) gold fuse (9) to protect the furnace windings from overheating.

Plunger Modification

The conventional autoclaves were modified for certain experiments which required much faster heating and/or cooling cycles. This was achieved by removing the central thermocouple sheath and replacing it with a ceramic/stainless steel rod. Discs and crucibles were attached to the rod as shown in figure 3.9. During the experiment the rod could be moved vertically up and down enabling the specimens to be inserted or extracted from the hot zone of the furnace. A set of crucibles was positioned at the bottom of the plunger to enable some specimens to be heated and cooled as in a conventional experiment for comparison purposes. This device was particularly useful for short-term experiments, i.e. those in which the exposure at temperature needed to be much shorter than the actual heating/cooling cycle possible with a conventional autoclave.

Gas Control System

The temperature, gas pressure and flow are regulated and monitored by the control system which is situated between the gas supply grid and the autoclave. Control of the furnace temperature is achieved by means of three eurotherm thyristors in conjunction with Pt/Pt-Rh thermocouples situated near the furnace tube wall. The gold heat fuses are also connected to the thyristors. A schematic diagram of the gas supply circuitry is shown in figure 3.10. The pressure is controlled by a "Brooks" E.L.F. pressure regulator, which has an operating range of 0 to 2 bar. A gauge manometer and a "Viatran" pressure transducer are used to monitor the pressure. The gauge manometer has safety contact limits which when transgressed result in the termination of an experiment in a "safety" mode. In this mode, heating is stopped and the system flushed with argon by the de-activation of the three-way magnetic valve. The gas flow through the gas chamber is regulated by a "Brooks" needle control valve on the outlet side. The flow is monitored by a "Brooks" flow meter fitted with inductive safety alarms. When the higher flow limit is exceeded the experiment is stopped in the "safety" mode whereas a flow below the limit activates the "experimental" mode. In this mode heating is stopped and the system isolated by magnetic valves at the inlet and outlet points.

Experimental Procedure

Conventional Autoclaves

The specimens (prepared as previously described) were placed in the reaction chamber. Prior to commencing the experiment the system was filled with argon, isolated and tested for leak-tightness over a period of 16 hours. The system was then evacuated and re-filled five times with active gas. The gas was then allowed to flow through the whole system for 3 hours to ensure saturation of the humidification unit with active gas. The system was then depressurised and the humidification unit isolated. The pressure in the reaction chamber was then set to 1.1 bar and heating commenced. When the temperature had reached 120°C (after ~1/2 hour) the system was evacuated and re-filled five times with active gas to remove any traces of water vapour. Heating then continued at a rate of approximately 10°/minute. At 400°C the system was depressurised. When the test temperature was reached the system was depressurised and the humidification unit inserted into the system and the pressure increased steadily to the required value. The gas was then allowed to flow at rates within the range 20-30 litres/hour, depending on the number of specimens, i.e. the reactive surface area, present in the autoclave. On completion of the experiment the system was isolated and allowed to cool in static active gas: In the conventional autoclave, i.e. without the plunger modification, the specimens cooled to room temperature over a period of approximately 24 hours. When the temperature was below 100°C the system was flushed with argon and the specimens removed.

Plunger Modification

The rig was heated up under the procedure described in the previous section. The gas was allowed to flow for 3 hours to ensure that equilibrium conditions were achieved. The specimens were then plunged into the hot zone reaching the test temperature in < 5 minutes as opposed to approximately 2 hours in a conventional experiment. In a similar manner specimens could be cooled rapidly by withdrawing the rod and moving the specimens out of the hot zone, cooling taking approximately 5 minutes as opposed to 24 hours in the conventional rig.

3.4.. ANALYTICAL TECHNIQUES

Hot Stage Microscope

A hot stage microscope was used to establish the temperatures at which some of these products transformed during cooling from the test temperature.

A schematic diagram of the hot-stage microscope is shown in figure 3.11. The environmental chamber consists of a small Al_2O_3 furnace heated by a Kanthal element. The furnace is surrounded by a water cooled stainless steel reaction chamber with a window at the top for viewing the specimen. The temperature is monitored with a Pt/Pt-Rh thermocouple connected to the specimen support stage. A 3-way valve enables the chamber to be evacuated or filled with active gas. The gas is supplied from a small 1 litre reservoir containing gas at the required operating pressure. A camera attached to the microscope enables changes occurring on the surface of the sample during the experiment to be recorded.

Polished sections of scales removed from specimens previously exposed in the corrosion autoclave were also re-heated to the test temperature in the sulphur-free gas. This enabled the transformation temperatures of these phases to be accurately determined.

Scanning Electron Microscopy

The morphology and distribution of the scales formed on the alloy surface were investigated using a J.S.M.-35 electron microscope. In this technique the surface of the sample is bombarded by a beam of electrons. The secondary and/or backscattered electrons are collected to form an image of the specimen surface. In practice the finely focussed beam of electrons is scanned across the specimen surface in a raster fashion. The image signal is amplified and displayed on a cathode ray tube. For normal use the specimens were tilted at 10° to the incident beam. Stereomicrographs were obtained by photographing the same area at 10° and 22° tilt.

This instrument was especially used for monitoring the nucleation and growth processes on the surface of the alloys. This was achieved by indexing the surface (with a scratch) before re-exposing the specimen in the autoclave and subsequently monitoring the same area again. This was in some cases repeated several times and was a particularly valuable technique for sequential monitoring of the nucleation and growth of sulphide phases on top of pre-existing oxides, in mixed environments where both phases are stable.

The scanning electron microscope was linked to a T.N. 1700 energy dispersive analyser to provide qualitative data on the chemical composition of the various phases.

X-Ray Diffraction

X-ray diffraction allows the crystal structure of a phase to be determined. The positions of the reflected beams in the diffraction pattern are determined by the size and shape of the unit cell and the intensities by the distribution and type of atom present. The diffraction pattern obtained can be compared with reference data to identify the phases formed. Deviations from the expected patterns provide further information on structure.

In this study a Philips 1700 automated powder diffractometer system was used. This system combined a proven goniometer design with modern principles of microprocessor and computer controlled data acquisition. The corrosion products were examined in-situ using a specially designed specimen holder. In some cases (particularly for thick scales), it was necessary to remove the corroded layer and grind it to a powder. Phases contained within the material e.g. carbides and σ phase were extracted electrolytically using a solution of 10 % HCl in methanol at a current density of 10-60 mA/cm². Cr-K radiation was used so as to minimise background fluorescence which occurs when other types of radiation are used on alloys or phases containing appreciable amounts of Cr and Fe.

The diffraction data was then processed using a Sandman-search, match and identify computer programme⁽¹⁸⁸⁾. Essentially this programme provided the possibility of searching the whole of the J.C.P.D.S. data

base⁽¹⁸⁹⁾ for possible matching patterns, although, in practice, a number of limits were imposed to reduce the search-time. Having obtained a listing of possible phases it was feasible to identify the specific phases present. The lattice parameters were then calculated from the relevant lines and the results plotted.

Electron Spectroscopy

Electron spectroscopy can be used to establish the chemical composition of very thin surface layers. The equipment used in this study was a Vacuum Generators ESCA-3 which enabled Auger spectroscopy (AES) and X-ray photo-electron spectroscopy (XPS) to be carried out in conjunction with each other. During Auger spectroscopy, the sample is bombarded with a beam of electrons and the energy of the Auger electrons emitted measured, whereas in photo-electron spectroscopy X-rays are used to excite the electron spectrum of the sample.

Composition depth profiles through scales could be obtained by simultaneous AES and argon-ion sputtering. By combining the sputtering with XPS a direct determination of composition including information on chemical states and bonding character in the surface layers could be made. Ta_2O_5 reference samples of known thickness were used to calibrate the machine for depth profiling.

Optical Microscopy

Two methods were used to prepare specimens for cross-sectional metallography. The nature and extent of the corrosion products determined which method was used. Severely corroded samples with thick, defective, friable scales were mounted in a cold setting araldite resin (Epofix). This was carried out under vacuum to ensure that all voids were filled with resin. Less severely attacked specimens were either vapour deposited with a thin layer of gold ($< 1 \mu\text{m}$) or given a flash coating of silver using the Brashear process⁽¹⁴⁰⁾, to ensure good electrical conductivity. The coated specimens were then electroplated with copper for 3 hours at 0,3 A resulting in a coating thickness of $\sim 30 \mu\text{m}$. Finally the specimens were mounted in bakelite.

After curing, both the araldite and bakelite mounts were ground on an Al_2O_3 wheel. The specimens were thoroughly cleaned in ethanol and dried before impregnating with araldite to fill any holes or cavities that may have occurred in the grinding operation. Finally the specimens were ground on '180 and 600 grade' SiC papers. This was followed by polishing on cloths impregnated with successively finer grades of diamond paste using an oil based lubricant.

The polished specimens were examined and photographed on a Leitz L.M.6. microscope.

An interference film microscopic 'Pepperhoff' technique was developed to identify the various corrosion products and phases contained within the alloys. The technique involves coating a polished specimen with an optically transparent film so that different phases appear as different colours. Complex mathematical explanations of the theory are given in the published literature⁽¹⁹¹⁻¹⁹⁸⁾. In simple terms the principle of the process is as follows :

If a polished metal surface is coated with a thin transparent film, light is reflected from both the outer surface of the film and from the metal/film interface. The two reflected beams of light are out of phase and thus partial extinction of some of the light occurs. The wavelength (λ_{\min}) and hence the colour of the light extinguished is dependent on the film thickness (d), the refractive index of the film (n_f) and the optical phase change at the metal film interface (δ_r) according to the equation :

$$\lambda_{\min} = \frac{2\pi (2 n_f d)}{\delta_r} \quad (3.1)$$

The colour observed is the complement of the spectrum not extinguished. This colour can be determined by drawing a straight line through the middle point E on figure 3.12. For example if the film is thin, blue light having a short wavelength (480 nm) will be extinguished and the metal will appear yellow. If the film thickness is increased λ_{\min} will increase and hence the colour of the metal will progressively change

from yellow to orange, red, purple, dark purple and finally blue as the red end of the spectrum is extinguished.

In practice, different phases in the metallic material and corrosion products have different refractive indices (n_p) and absorption coefficients (k_p) which determine the phase change at the metal film interface according to equation :

$$\tan \delta_r = \frac{2 n_f k_p}{n_f^2 - n_p^2 - k_p^2} \quad (3.2)$$

Thus, for a film of constant thickness and refractive index, the different refractive indices and absorption coefficients of the phases result in different optical phase changes which in turn result in extinction of different parts of the spectrum and hence appearance of different colours for different phases.

The contrast between phases can be maximised by using different coating materials. In this study it was necessary to distinguish between a large number of phases and thus, to allow consistent comparisons between phases, a ZnSe film material having a refractive index in the middle of the range was used. The contrast was optimised by setting the colour of the austenite to dark yellow to distinguish between sulphides, pink to distinguish between carbides and metallic phases and magenta to distinguish between oxides and sulphides. The colour of the various phases whose composition was confirmed by EPMA and X-ray diffraction are given in table 3.5.

Electron Probe Microanalysis

The electron probe microanalyser is a very important research tool for establishing local chemical compositions of the corrosion products formed on the alloy surface and also diffusion profiles in the bulk of the alloy. The instrument used in this study was a Jeol JXA-50A scanning electron microscope/microprobe combination which enabled high resolution microscopy to be combined with accurate chemical microanalysis. The instrument contains a lanthanum hexaboride gun which provides a higher

brightness electron source than the standard tungsten filament. The machine is also equipped with two crystal spectrometers and an energy dispersive Si-Li detector.

Detailed descriptions of the principles and mode of operation of the electron probe microanalyzer have been published elsewhere (199-200) and are therefore not included here. In this study the instrument was used in three modes; firstly to provide accurate point analyses, secondly for line scans to establish diffusion profiles and thirdly to give element distribution maps. In the first case the electron beam, of diameter $\sim 1 \mu\text{m}$, is focussed on the point to be analysed and the resultant X-ray spectrum determined and analysed. The intensity of an X-ray peak is a measure of the quantity of the element present but certain corrections must be made for atomic number, X-ray fluorescence and absorption effects. A specially designed computer programme is used to separate overlapping peaks. In the case of line scans, the specimen is moved by increments of $1 \mu\text{m}$ along an axis whilst point analyses are made. Elemental profiles can then be obtained by plotting the chemical compositions of each point against the distance travelled. Finally X-ray maps for the elements of interest are established by setting a crystal spectrometer to the corresponding angular setting for the element of interest. The resultant signal detected is amplified and used to modulate the brightness of the cathode-ray tube, the time base of which is synchronised with the time base of the electron probe. In this way, an image showing the optical distribution of any chosen element is built up.

MATERIAL	CHEMICAL COMPOSITION wt %														
	C	Cr	Ni	Fe	Si	Mn	Nb	Mo	Ti	Al	P	S	N	O	Cu
Model 25-35	0,017	24,90	34,94	Bal.	0,02	0,01	-	< 0,01	< 0,001	0,003	0,001	0,004	0,007	0,013	< 0,01
HP40Nb	0,43	24,35	32,20	Bal.	1,22	1,11	0,84	0,04	-	0,03	0,015	0,010	0,064	-	-
HP40Al	0,44	23,35	34,29	Bal.	1,59	1,23	0,80	0,078	-	3,49	0,004	0,011	-	-	-
Alloy 800H	0,06	20,05	31,35	Bal.	0,37	0,66	-	-	0,48	0,28	-	-	0,01	-	-
AISI 314	0,06	24,07	20,30	Bal.	2,04	1,12	-	-	-	-	0,023	0,006	0,040	-	-

Table 3.1 : Chemical Composition of the Alloys

MATERIAL	SUPPLIER	METALLURGICAL FORM	HEAT TREATMENT
Model 25-35	Brown-Firth U.K.	Laboratory cast ingot.	-
HP40Nb	Fonderies et Acieries du Manoir, France	Centrifugally cast tube	-
HP40Al	Fonderies et Acieries du Manoir, France	Centrifugally cast tube	-
Alloy 800H	Henry Wiggin, U.K.	Wrought bar	Solution treated at 1150°C for 1 hour. Followed by water quenching.
AISI 314	Pose-Marie, Germany	Wrought bar	-

Table 3.2. : Metallurgical Condition of the Alloys

Table 3.3.. Test Gas Mixtures used to Investigate Alloy
Corrosion Behaviour in Complex S-O-C Environments

Composition of Gas Mixture (R.T.)				Characterisation		
H ₂	CO	H ₂ O	H ₂ S	800°C		
				pO ₂	a _c	pS ₂
Bal.	7 %	1.5 %	-*	10 ⁻²¹ bar	0.3	-
Bal.	7 %	1.5 %	0.2 %	10 ⁻²¹ bar	0.3	10 ⁻⁹ bar
Bal.	7 %	1.5 %	0.6 %	10 ⁻²¹ bar	0.3	10 ⁻⁸ bar
Bal.	7 %	1.5 %	2.0 %	10 ⁻²¹ bar	0.3	10 ⁻⁷ bar

* Sulphur-free reference gas mixture.

NOMINAL GAS COMPOSITION		ACCURACY OF CERTIFICATION		MAXIMUM PERMITTED LEVEL OF IMPURITIES							
		CO	H ₂ S	O ₂	H ₂ O	N ₂	Ar	CH ₄	C _n H _m	CO ₂	
H ₂ - 7 % CO	A	7,0 +/- 0,15	-	1	2	2	12	5	-	-	
	M	7,0 +/- 0,14	-	8	5	25	-	9	-	1	
H ₂ - 7 % CO - 0,2 % H ₂ S	A	7,0 +/- 0,15	0,2 +/- 0,006	2	3	2	12	5	2	3	
	M	+/- 0,14	0,2 +/- 0,004	8	5	25	-	9	6	1	
H ₂ - 7 % CO - 0,6 % H ₂ S	A	7,0 +/- 0,15	0,6 +/- 0,013	2	5	4	12	5	6	10	
	M	+/- 0,14	0,6 +/- 0,012	8	5	25	-	9	16	1	
H ₂ - 7 % CO - 2,0 % H ₂ S	A	7,0 +/- 0,15	2,0 +/- 0,060	2	12	11	12	5	20	30	
	M	+/- 0,14	2,0 +/- 0,040	9	5	16	-	9	54	1	

A = L'Air Liquide
M = Matheson

Table 3.4. : Accuracy of certification and maximum permitted level of impurities of the gases used.

a)

Sulphides	Colour
Austenite	yellow
Ni_2Fe	yellow
Ni_3S_2	pink
Cr_xS_y	light brown
FeCr_2S_4	dark brown
$(\text{Fe},\text{Cr})_7\text{S}_8$	light brown
$(\text{Fe},\text{Cr})\text{S}$	light brown
$\text{Fe}_{4,5}\text{Ni}_{4,5}\text{S}_8$	dark purple
(oxides)	(blue)

b)

Carbides and metallic phases	Colour
M_{23}C_6	yellow
σ	yellow
M_7C_3	dark yellow
Austenite	pink
MC	light purple
M_6C	dark purple
TiC	very dark purple
NiAl	grey
(oxides)	(blue)

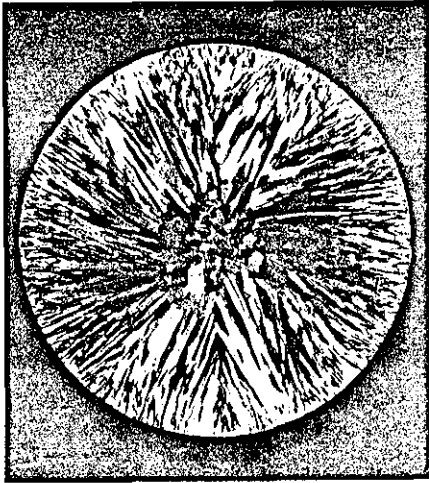
c)

Oxides and sulphides	Colour
Austenite	Magenta
$\text{Cr}_2\text{O}_3/\text{M}_3\text{O}_4$	dark blue/grey
SiO_2 containing layer	light blue
Cr rich sulphides	light brown
Cr/Fe rich sulphides	light purple
Cr/Mn rich sulphides	dark purple

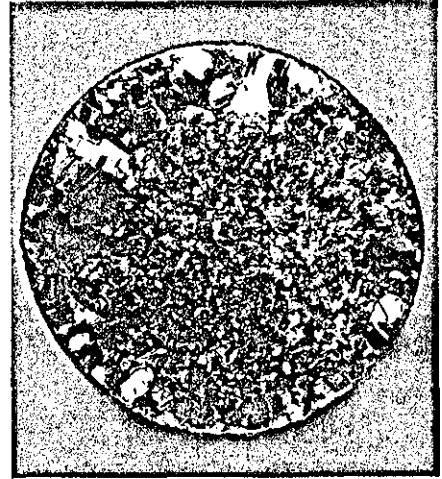
Table 3.5.

Different colours produced after vapour deposition of ZnSe coating on polished specimens.

- a. with austenite yellow
- b. with austenite pink
- c. with austenite magenta.

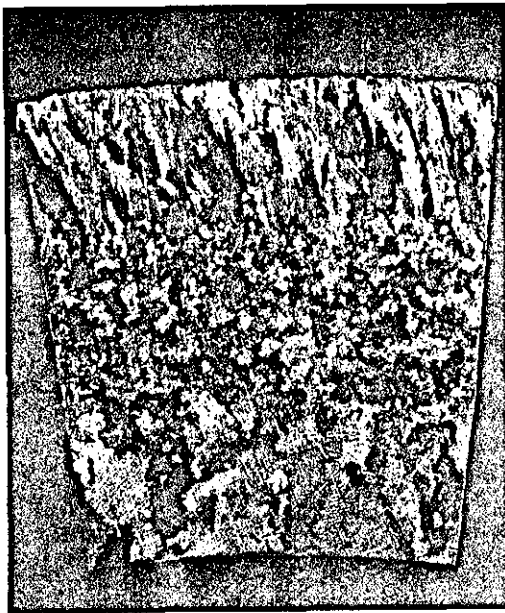


a) Model 25Cr-35Ni-Fe 10mm



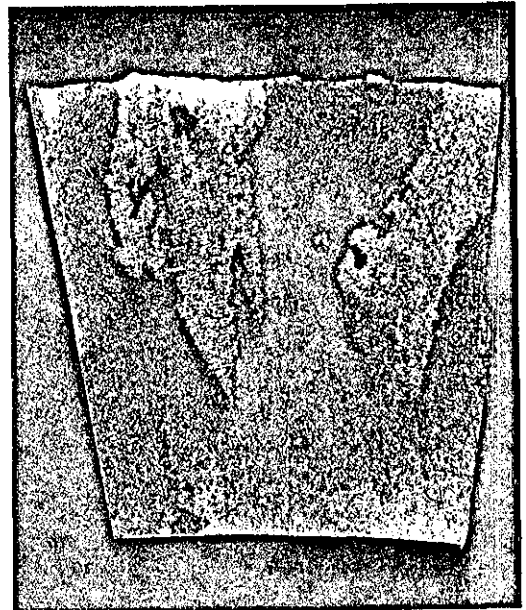
d) Alloy 800H

2mm



b) HP40Nb

2mm



c) HP40Al

2mm

Figure 3.1 Macrostructure of the alloys

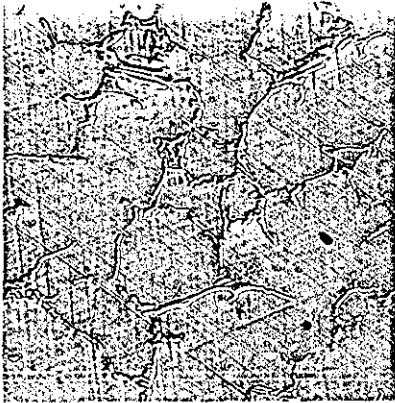
(AISI 314 not shown due to small grain size $\sim 10\mu\text{m}$)



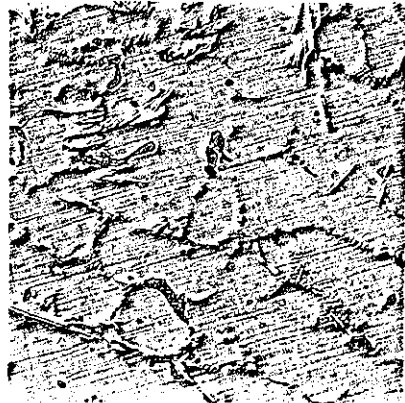
Figure 3.2

**Microstructure
of the alloys**

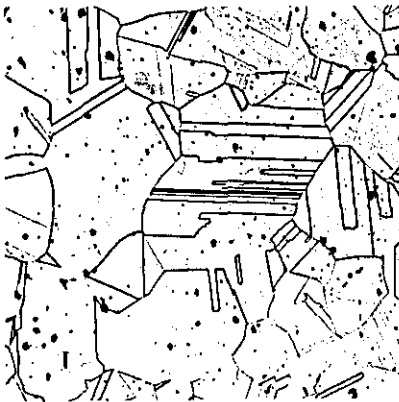
a) Model 25Cr-35Ni-Fe 100um



b) HP40Nb 50um



c) HP40Al 50um



d) Alloy 800H 100um



e) AISI 314 50um

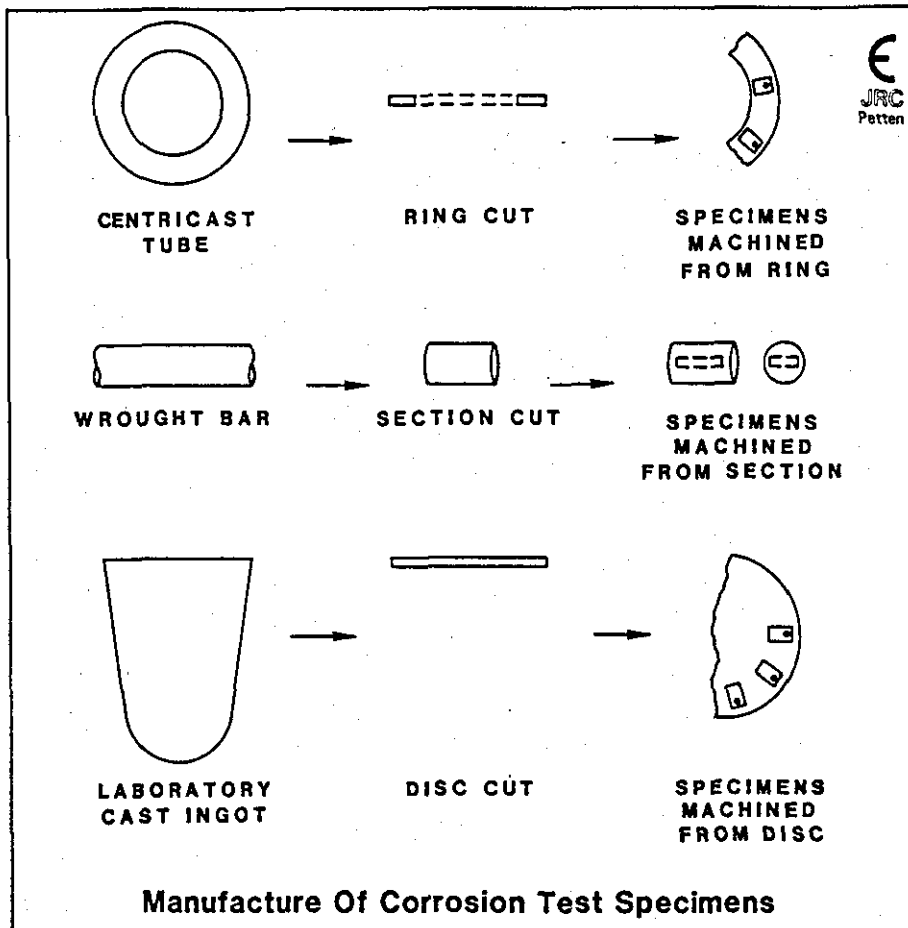


Figure 3.3
Manufacture of corrosion test specimens.

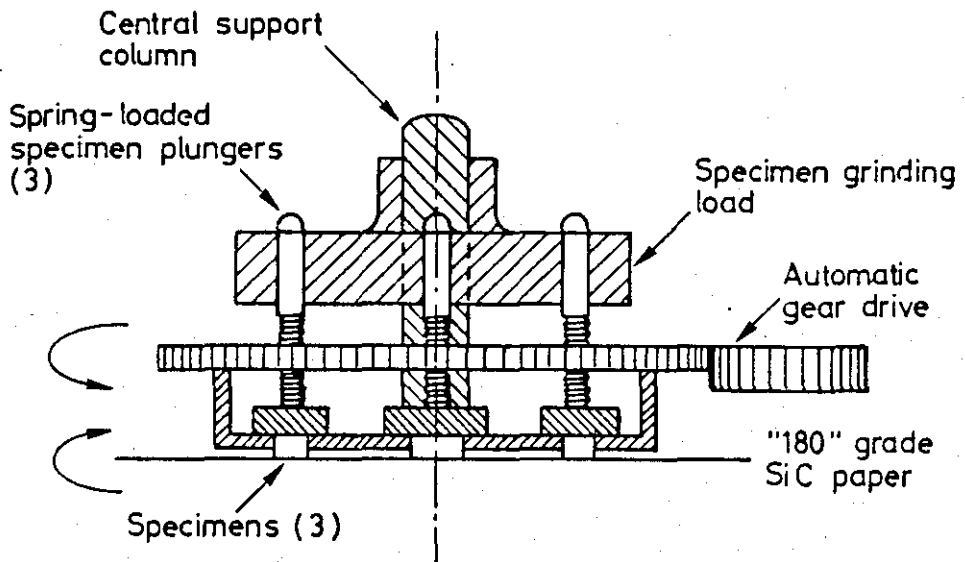


Figure 3.4
Schematic diagram of the apparatus for surface grinding of specimens.

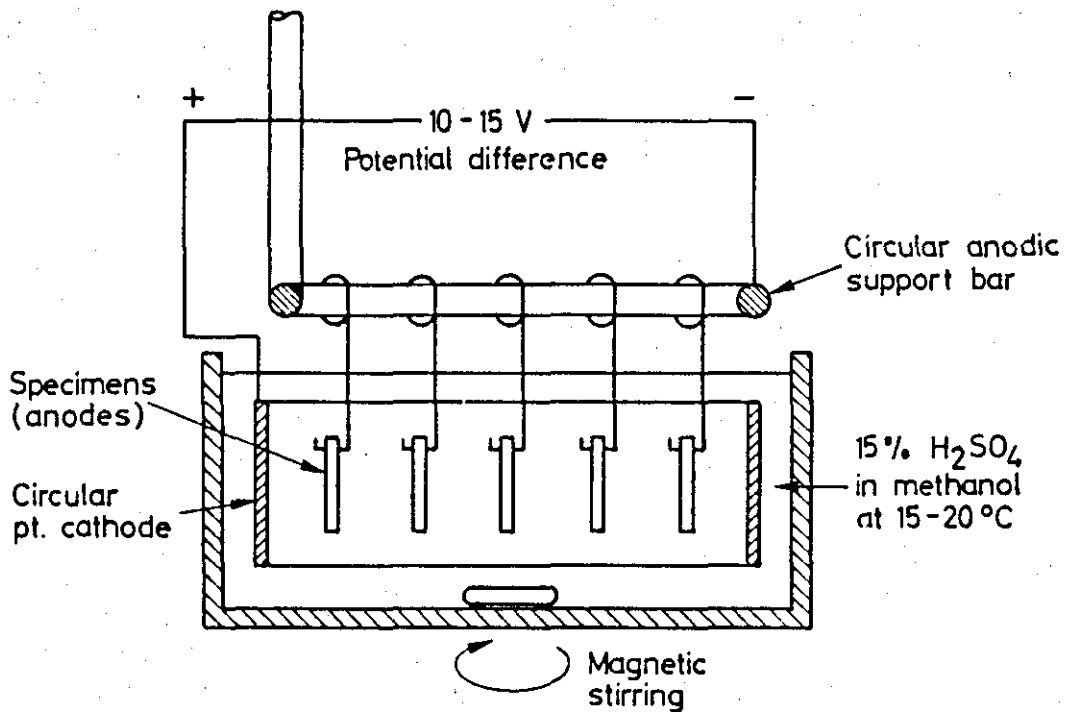


Figure 3.5
Schematic diagram of the apparatus for electropolishing specimens.

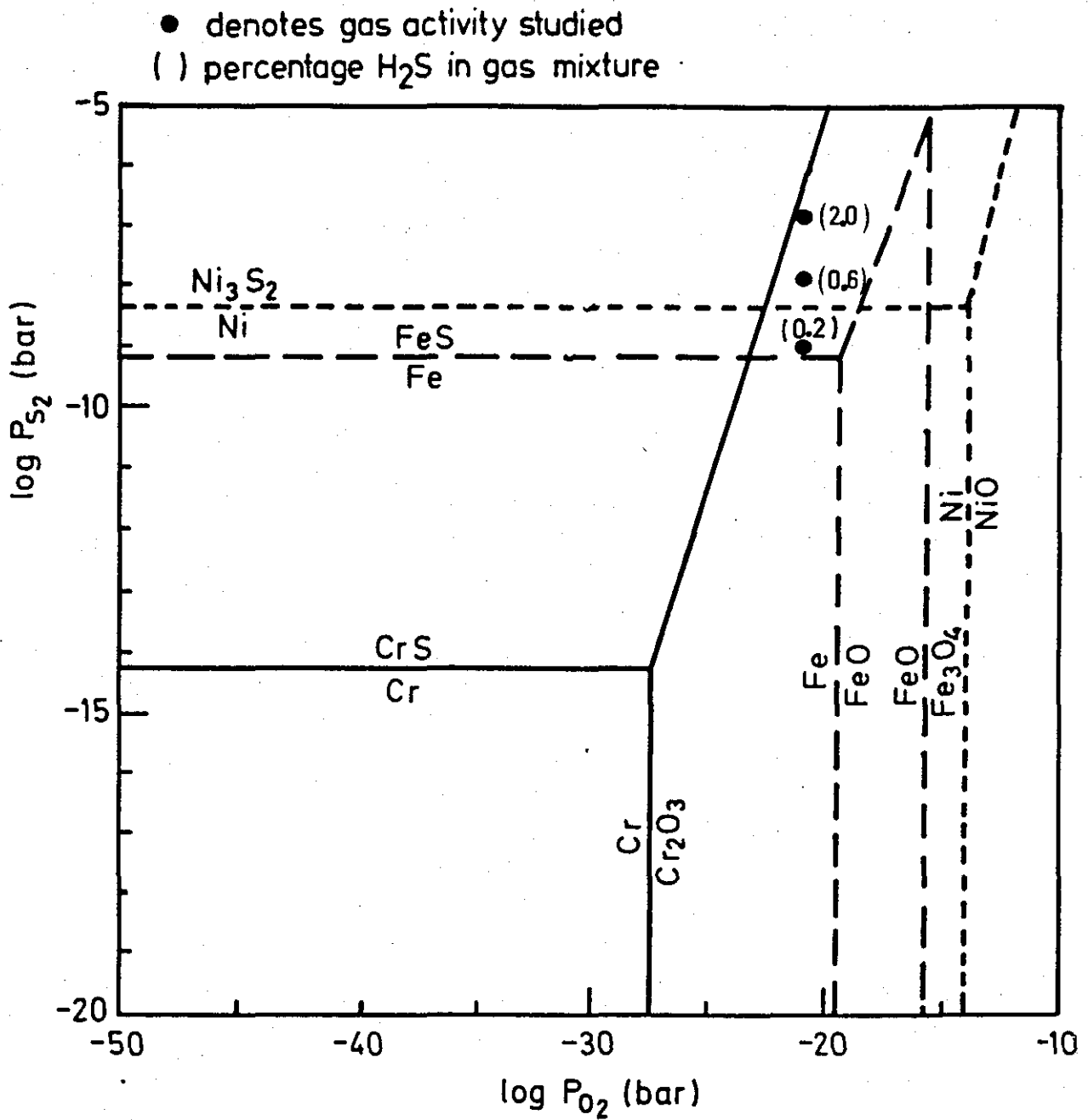


Figure 3.6

Superimposed stability diagram for the Cr-Fe-Ni-S-O system at 800°C.

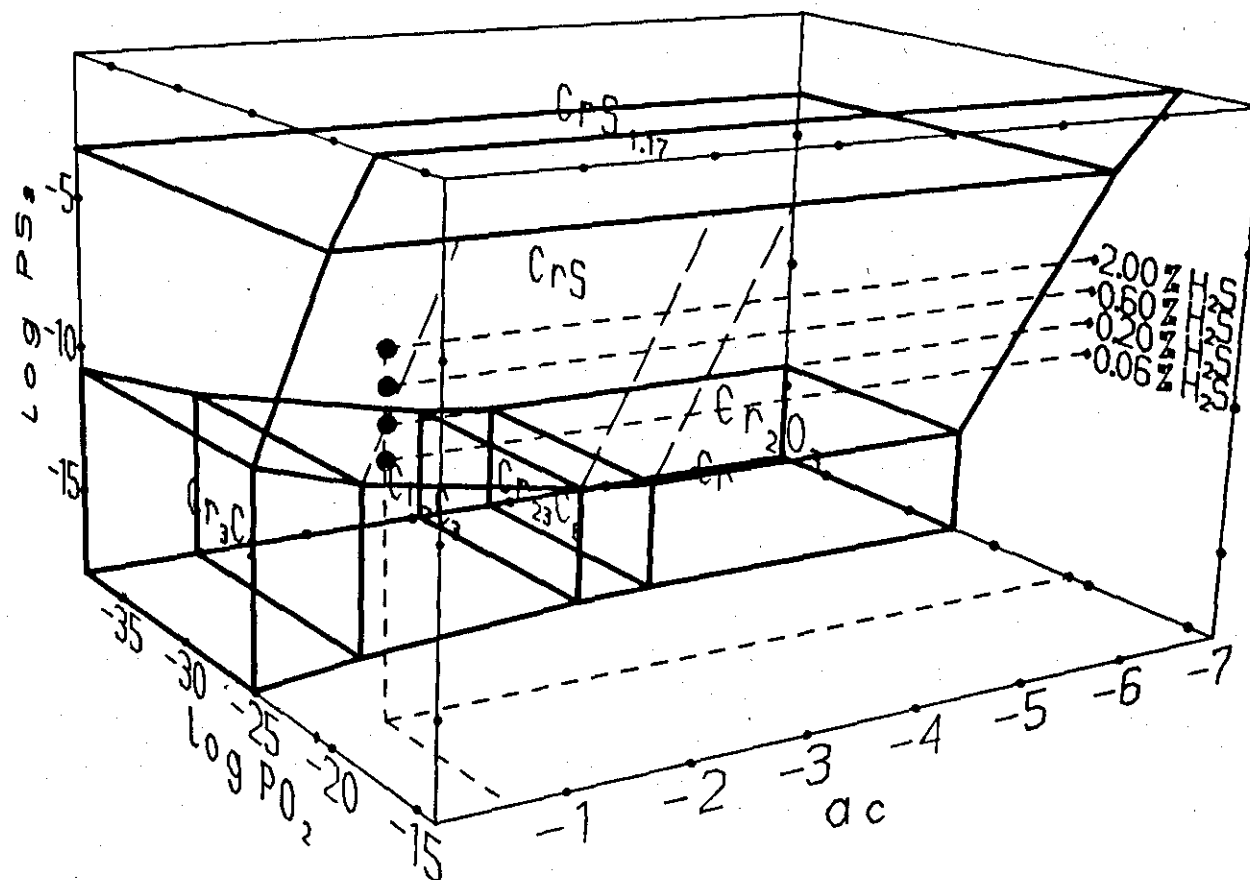
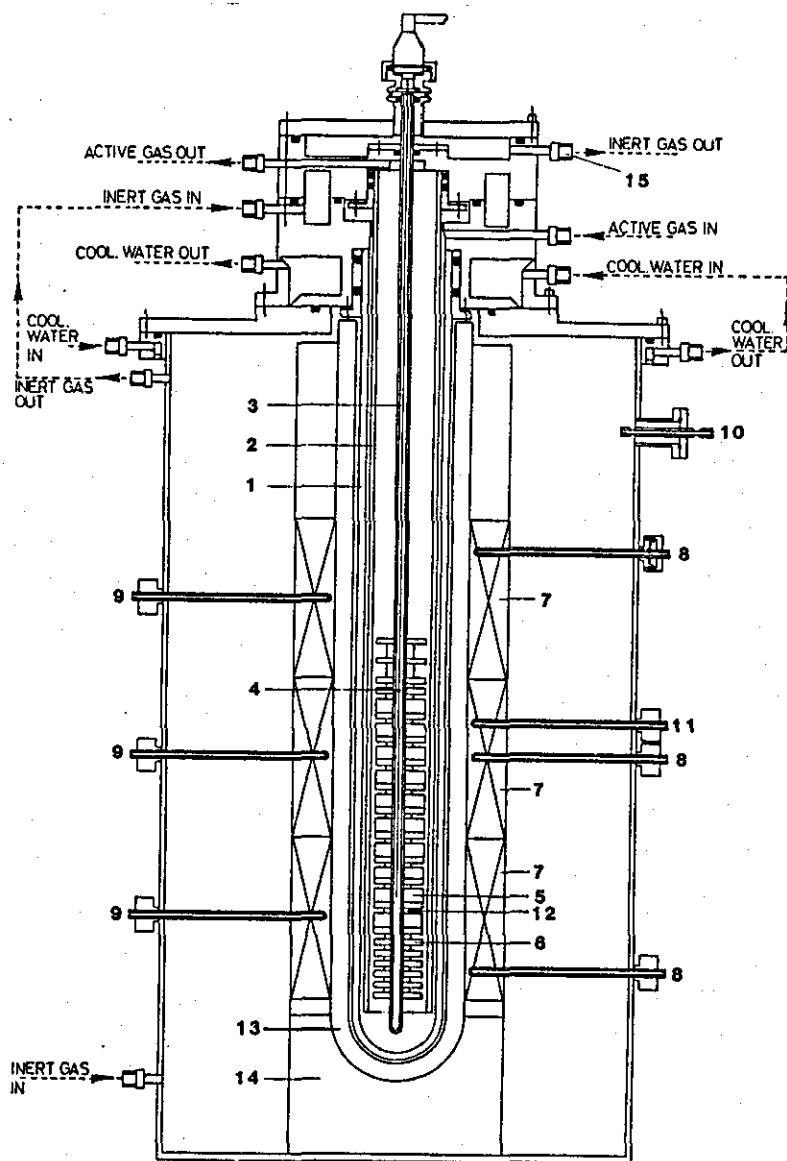


Figure 3.7
3-Dimensional stability diagram for the Cr-O-S-C system at 800°C.



N° DESCRIPTION

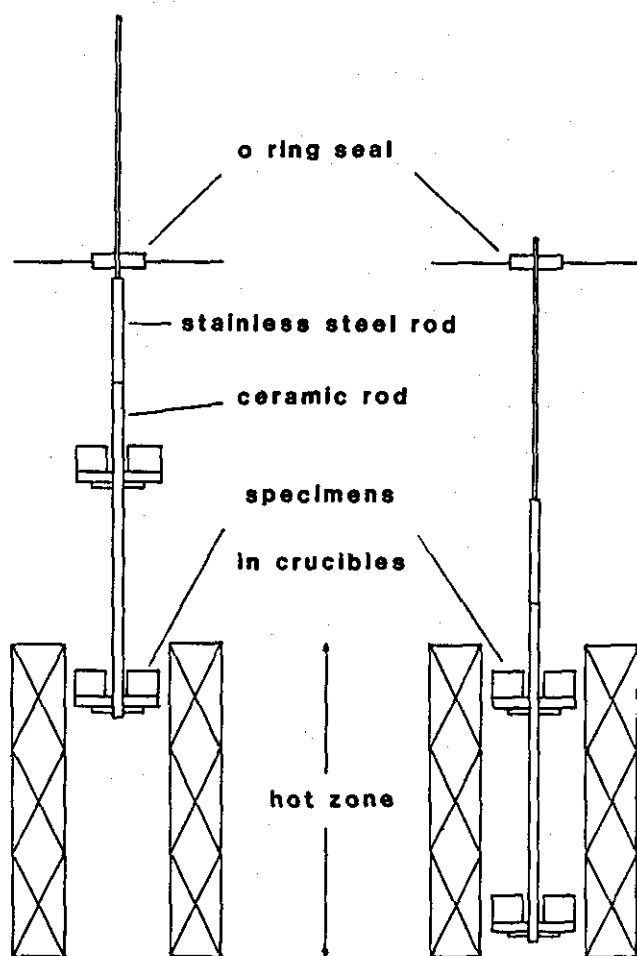
1. Furnace tube, Al_2O_3
2. Specimen support tube, Al_2O_3
3. Central thermocouple sheath Al_2O_3
4. Thermocouple (Experimental temperature), Pt/Pt-Rh 10 %
5. Alumina crucible containing specimen
6. Discs, Al_2O_3
7. Heating elements, Kanthal.

N° DESCRIPTION

8. Thermocouples for controllers
9. Overheating fuses
10. Power feed through
11. Thermocouples for recorder
12. Spacer
13. Ceramic tube
14. Supporting brick
15. Standard Swagelok fitting

Figure 3.8

Schematic diagram of the corrosion test autoclave for use with gaseous atmospheres.



a) Plunger withdrawn

b) Plunger inserted

Figure 3.9

Schematic diagram of the plunger attachment.

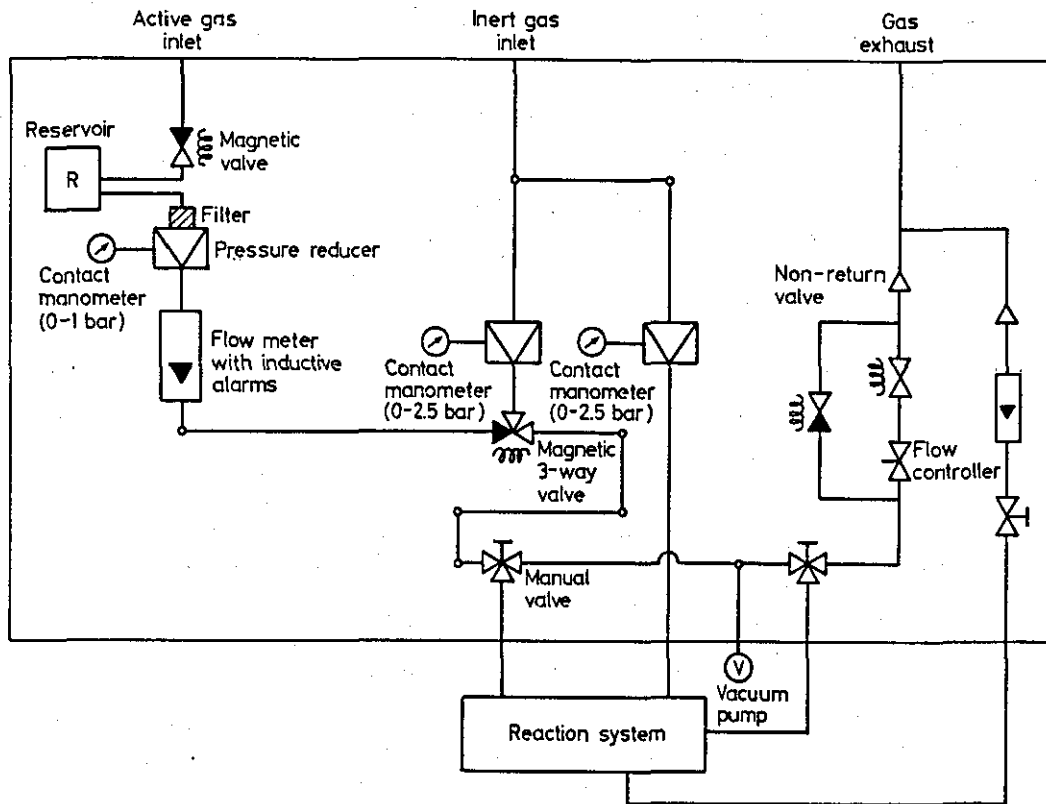


Figure 3.10
Schematic diagram of the gas supply circuitry.

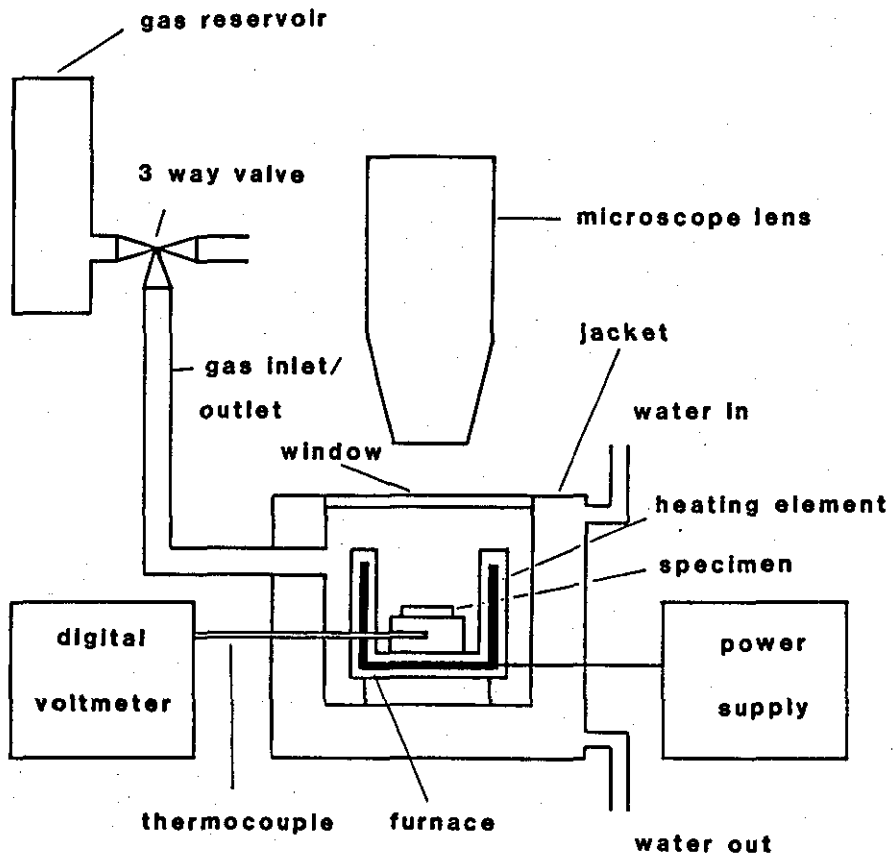


Figure 3.11
Schematic diagram of the hot stage microscope.

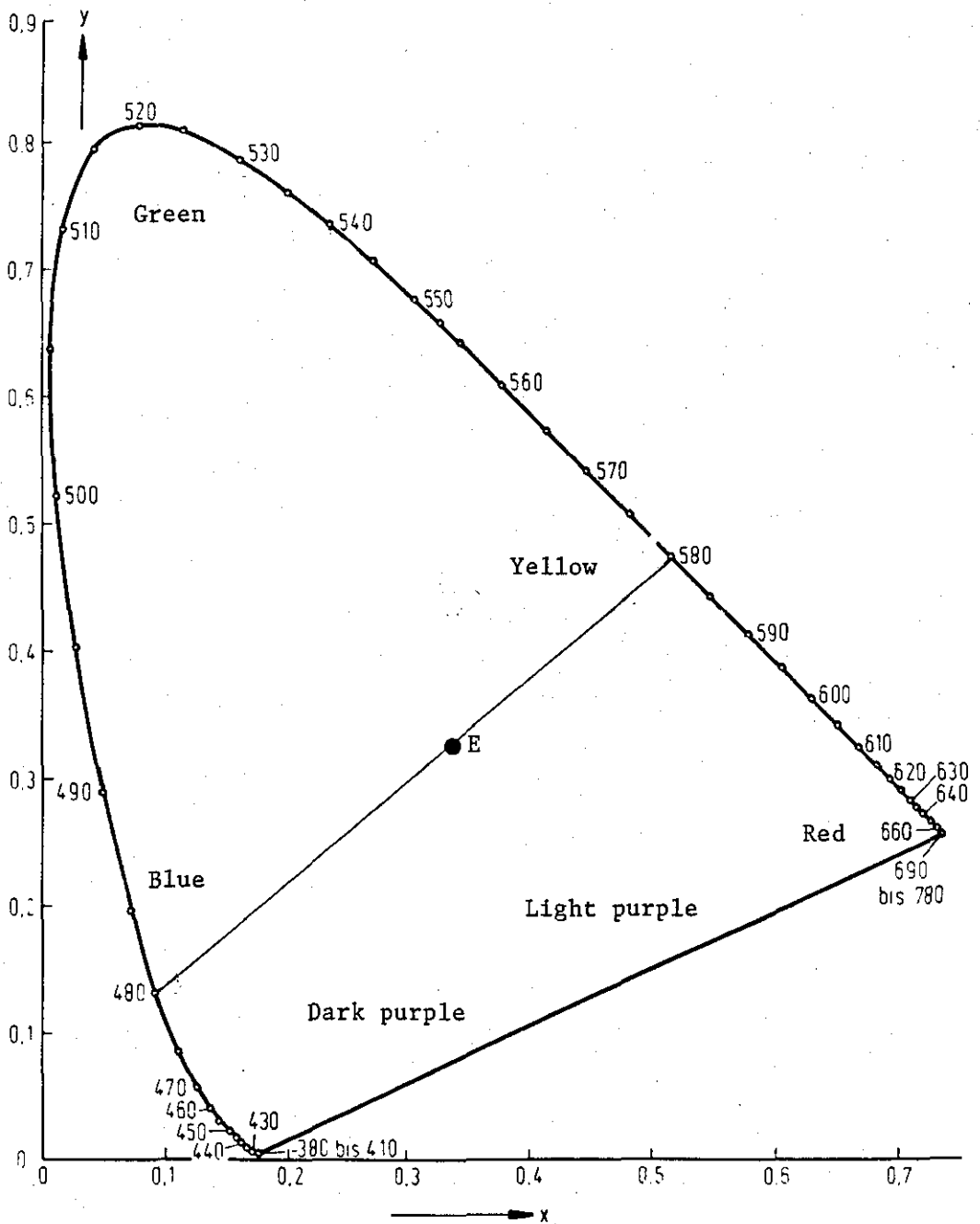


Figure 3.12

Diagram showing the colours visible when light of the given wavelength is extinguished (191).

4. RESULTS AND THEIR INTERPRETATION

Before considering the corrosion behaviour of the five alloys in the different gaseous environments, it is advantageous to have a general overview of the findings of this study. As described previously the gases were designed so that the oxygen partial pressure ($p_{O_2} = 10^{-21}$ bar) and carbon activity ($a_c = 0.3$) at 800°C were kept constant, whilst the sulphur partial pressure was varied systematically. The behaviour in each environment can be illustrated by plotting the weight uptake against time for the model alloy, figure 4.1. It is clear from this figure that the environments can be divided into two distinct regimes.

- (i) An oxidation governed regime, typified by the sulphur-free and the 0.2 % H_2S ($p_{S_2} = 10^{-9}$ bar) gases. In this case the weight gains were low ($< 10 \text{ mg/cm}^2$ in 5000 hours).
- (ii) A sulphidation governed regime typified by the 0.6 and 2 % H_2S ($p_{S_2} = 10^{-8}$ and 10^{-7} bar) gases. In this case the weight gains were high ($> 50 \text{ mg/cm}^2$ in only 100 hours).

The presentation of the results are therefore divided into these two regimes.

The oxidation regime is sub-divided into four sections. In the first section the corrosion behaviour of the 'simple' Model 25Cr-35Ni-Fe alloy is described in the sulphur-free and 0.2 % H_2S gases. In the second section the effect of Si and Mn on the corrosion mechanisms are established by examining the behaviour of the commercial equivalent 25Cr-35Ni alloy, HP40Nb, under the same exposure conditions. The Si level of this alloy is borderline for the formation of an additional SiO_2 layer and thus to clarify the situation results for a commercial alloy, AISI 314, having a higher Si level, are included in the third section. Finally the effect of a 3.5 % Al addition to the HP40Nb alloy is determined by examining the behaviour of the HP40Al alloy.

In the sulphidation regime the corrosion behaviour of the three 25Cr-35Ni alloys (i.e. the Model, HP40Nb and HP40Al) are described in the 0.6 % H_2S containing gas.

Finally the findings of an additional study on 800H are presented in both the oxidation and sulphidation regimes. This alloy was included in the study because of its relatively good mechanical properties.

4.1. OXIDATION GOVERNED REGIME AT 800°C

4.1.1. Model 25Cr-35Ni-Fe Alloy

This material is a ternary 25Cr-35Ni-Fe alloy which was supplied as a laboratory cast ingot. The alloy consisted of single phase austenite with a large grain size, typically 10 mm x 1 mm.

a) S-free gas

The corrosion kinetics in the sulphur free gas are given in figure 4.2. This shows that the weight uptake for the 180 grit surface finished material (1.1 mg/cm^2 in 4000 hours) was higher than the electropolished (EP) material (0.5 mg/cm^2 in 4000 hours). To obtain a clearer understanding of the corrosion process it was helpful to replot these data in terms of weight gain squared against time, figure 4.3 a and b. This showed that initially the kinetic rates were quite high but quickly slowed down before becoming parabolic after approximately 5 hours. The corrosion rates then remained constant for the rest of the exposure period. The corrosion rate for the 180 grit material was approximately one order of magnitude higher than on the electropolished material, table 4.1.

Electropolished condition

Structural analysis examinations were carried out after 5 minutes, 30 minutes, 1 hour, 2 hours, 5 hours, 100 hours and 2000 hours.

5 minutes

Surface SEM examination showed that a discontinuous surface layer formed which consisted of a mixture of carbide and oxide particles, figure 4.4.a. X-ray diffraction using surface reflection indicated that this layer consisted of predominantly M_{23}C_6 and M_3O_4 with small amounts of Cr_2O_3 , table 4.2. The lattice parameter of the oxide M_3O_4 spinel

indicated that its composition was MnCr_2O_4 , figure 4.5. ESCA-Auger depth profile analysis confirmed that the surface layer was predominantly Cr-rich with a small amount of Fe, even less Ni and no Mn present, figure 4.6. It was therefore concluded that the discontinuous surface layer consisted of a mixture of (Cr,Fe) rich- M_{23}C_6 , (Fe,Mn)-rich M_3O_4 and Cr_2O_3 particles.

30 minutes
.....

Surface SEM examination showed that the discontinuous surface layer still consisted of a mixture of carbide and oxide particles, figure 4.4.b. The carbides were larger and more globular but the oxide particles remained the same.

1 hour
.....

X-ray diffraction analysis using surface reflection indicated that the discontinuous surface layer still consisted of predominantly M_{23}C_6 and M_3O_4 , with small amounts of Cr_2O_3 also present, table 4.2. The lattice parameter of the M_3O_4 spinel had decreased indicating that the composition was FeCr_2O_4 , figure 4.5. The lattice parameter of the Cr_2O_3 phase corresponded to that of pure Cr_2O_3 , figure 4.7.

2 hours
.....

Surface SEM examination again showed that the discontinuous surface layer consisted of large (1-2 μm diameter) carbide particles and smaller (< 1 μm diameter) oxide particles, figure 4.4.c.

5 hours
.....

X-ray diffraction analysis using surface reflection indicated that the surface layer now consisted of 4 phases : M_{23}C_6 , M_3O_4 , Cr_2O_3 and a new M_7C_3 phase, table 4.2. Extraction of the corrosion products followed by X-ray powder diffraction indicated that some of the M_{23}C_6 phase was situated beneath the surface layer in the alloy substrate. The lattice parameter of the M_{23}C_6 had increased indicating that more Fe and Ni were becoming incorporated into this phase. Thus it was concluded that as the

carbon activity on the surface increased the $M_{23}C_6$ carbides were converted to M_7C_3 . Some carbon diffused into the alloy and led to formation of $M_{23}C_6$ precipitates in the alloy substrate.

100 hours
.....

Surface SEM examination showed that the surface layer was now continuous and consisted of only oxide particles, figure 4.4.d. The carbides were no longer visible. X-ray diffraction using surface reflection confirmed that the surface layer now contained predominantly Cr_2O_3 with some M_3O_4 , table 4.2. Thus it was concluded that once the surface layer became continuous, thermodynamics determined that only the oxide could come to stable equilibrium with the gas and thus the M_7C_3 was converted to Cr_2O_3 and $M_{23}C_6$ to M_3O_4 , with the carbon released in the process diffusing into the alloy substrate.

2000 hours
.....

Cross-sectional examination showed that the corrosion morphology consisted of a thin uniform (3 μm thick) oxide layer and some internal carbide precipitates at grain boundaries in the alloy substrate, figure 4.8.a. X-ray diffraction using surface reflection confirmed that the oxide layer was now almost totally Cr_2O_3 with a few traces of M_3O_4 also present, table 4.2. The lattice parameter of the Cr_2O_3 phase had increased indicating that the oxide had become doped with some other element such as Fe, figure 4.7. An EPMA line scan, however, showed that the outer regions of the oxide layer contained only 0.5 % Fe, 0.3 % Mn and 0.2 % Ni, figure 4.9. The Fe content (1.25 %) was slightly higher in the inner regions of the oxide layer. X-ray mapping also indicated that there was little Fe, Mn or Ni in the oxide layer. It should be pointed out that as this layer was only 3 μm thick it was virtually impossible to determine whether the Fe at the scale/alloy interface was in the scale or in the alloy. Thus it was tentatively concluded that the oxide layer was predominantly Cr_2O_3 doped with a small amount of Fe with a few traces of $FeCr_2O_4$ situated at the scale/alloy interface.

Cross-sectional examination showed that even after 2000 hours virtually no carburization had taken place. The grain boundaries in the alloy

were decorated with carbide precipitates. However annealing in argon at 800°C showed that this was an aging effect of the material. Only a few extremely small carbide precipitates in the vicinity of the grain boundaries could be attributed to carbon ingress from the gas.

Thus in summary, a discontinuous layer of carbides and oxides formed on the alloy surface in the early stages. After a few hours the surface layer became continuous and the carbides were converted to oxides to leave a thin uniform predominantly Cr_2O_3 oxide layer. The carbon released from the former surface carbides diffused into the alloy substrate. Once the oxide layer had formed, it provided a very effective barrier to any further carbon injection from the gas.

S-free gas

'180' grit condition

Structural analysis examinations were carried out after 5 minutes, 1 hour, 5 hours, 100 hours, 2000 hours and 5000 hours.

5 minutes

Surface SEM examination showed that a thin continuous fine grained oxide layer formed on the alloy surface, figure 4.10a. X-ray diffraction using surface reflection indicated that this oxide layer was Cr_2O_3 , table 4.3. The Cr_2O_3 lattice parameter was similar to that of pure Cr_2O_3 , figure 4.7. ESCA-Auger analysis also confirmed that the oxide was Cr_2O_3 , figure 4.11.

1 hour

Surface SEM examination showed that the oxide layer was unchanged, figure 4.10b. X-ray diffraction using surface reflection again detected only Cr_2O_3 , table 4.3.

5 hours

Surface SEM examination showed that the oxide layer was now rather uneven, figure 4.10c. X-ray diffraction using surface reflection again

confirmed that the oxide was Cr_2O_3 , table 4.3. The Cr_2O_3 lattice parameter corresponded to that of pure Cr_2O_3 , figure 4.7.

100 hours
.....

Cross-sectional examination showed that the corrosion morphology consisted of the oxide layer on the alloy surface and some localized internal carburization around the grain boundaries, figure 4.8.b.

The oxide layer was uneven (1-3 μm thick). This was also clear from the surface SEM examination, figure 4.10d. X-ray diffraction again confirmed that the oxide was Cr_2O_3 , with the lattice parameter still corresponding to that of pure Cr_2O_3 , table 4.3., and figure 4.7.

A few carbides were present in the alloy substrate near the grain boundaries. The grain boundaries throughout the alloy had carburized but this was attributed to the aging of the material. No carbides were visible in the Cr-depleted alloy substrate immediately below the oxide layer.

2000 hours
.....

Cross-sectional examination showed that the corrosion morphology consisted of the oxide layer and some internal carburization of the alloy substrate, figure 4.8.c.

The oxide layer was very uneven (5-10 μm thick) and contained a number of cracks and pores. X-ray diffraction using surface reflection again indicated that the oxide was Cr_2O_3 , table 4.3. The lattice parameter of the Cr_2O_3 had increased indicated that this phase had become doped with another cation such as Fe or Mn, figure 4.7. ESCA-Auger analysis detected small amounts of Si and Mn on the external surface of the oxide but found no trace of Fe, figure 4.12.

Cross-sectional examination showed that the amount of carburization had increased with carbides visible throughout the alloy substrate, figure 4.13. The overall volume of carbides precipitates was however

quite small. Again no carbides were visible in the Cr-depleted alloy substrate immediately beneath the oxide layer.

5000 hours
.....

Cross-sectional examination again showed that the corrosion morphology consisted of the oxide layer and some internal carburization, figure 4.8d.

The uneven oxide layer (now 6-11 μm thick) still contained a number of cracks and pores. X-ray diffraction confirmed that the oxide was still Cr_2O_3 , with the lattice parameter indicating doping with another cation, figure 4.7.

The amount of internal carburization had increased considerably. Again no carbides were visible in the Cr-depleted substrate immediately below the surface oxide layer.

Thus in summary a Cr_2O_3 surface layer formed on the '180' grit material. Although the oxide layer grew at a faster rate than on the electropolished material it contained large number of cracks and pores which allowed the penetration of carbon containing gaseous species. This led to a considerable amount of internal carburization of the alloy substrate.

b) 0.2 % H_2S gas

The corrosion kinetics for the model 25Cr-35Ni-Fe alloy in the 0.2 % H_2S gas are given in figure 4.14. Two features emerge from this figure. Firstly the weight uptake was higher than in the S-free gas and secondly a higher weight gain was obtained for the 180 grit material than the electropolished material.

When the kinetic data were replotted as weight gain squared against time some interesting features emerged, figure 4.15. In the case of the electropolished material the initial corrosion rate was quite high. This then progressively slowed down until becoming parabolic after 1000

hours. This rate was slightly higher than in the S-free gas, table 4.1. A slight increase in the rate occurred again after 4500 hours.

A similar trend occurred for the 180 grit material. In this case the initial corrosion rate was much higher and although the kinetics progressively slowed down they did not become parabolic until after 2000 hours exposure. From 2000 hours onwards the rate was parabolic and approximately the same as in the S-free gas, table 4.1.

Electropolished (EP) Material

Structural analysis examinations were carried out after 5 minutes, 1 hour, 5 hours, 100 hours, 1000 hours, 2000 hours and 5000 hours.

5 minutes
.....

Cross-sectional examination showed that the corrosion morphology consisted of a thin (1 μm) discontinuous layer on the alloy surface, figure 4.16a. X-ray diffraction using surface reflection indicated that this layer contained Cr_2O_3 and M_3O_4 , table 4.4. The lattice parameter of the Cr_2O_3 phase corresponded to that of pure Cr_2O_3 , figure 4.7. ESCA-Auger analysis indicated that the discontinuous layer contained $\sim 7\%$ sulphur. It was concluded that the discontinuous layer consisted of a mixture of Cr_2O_3 , FeCr_2O_4 and Cr_xS_y .

1 hour
.....

Surface SEM examination indicated that a few filamentary growths were starting to form on top of the initial surface layer, figure 4.17a. X-ray diffraction using surface reflection indicated that these were probably M_7S_8 , table 4.4. M_3O_4 was also detected. Thus it appeared that some M_7S_8 filamentary growths were starting to form on top of the mixed Cr_2O_3 , FeCr_2O_4 , Cr_xS_y surface layer.

5 hours
.....

Surface SEM examination revealed that the filamentary growths on top of the initial surface layer had become much larger, figure 4.17b. X-ray diffraction using surface reflection detected Cr_2O_3 and M_3O_4 , table 4.4.

100 hours
.....

Cross-sectional examination showed that the corrosion morphology consisted of 4 regions : filamentary growths on the outer surface, the original surface layer, internal sulphide precipitates at grain boundaries in the alloy substrate and grain boundary carbides deeper in the alloy, figure 4.16b.

Surface SEM clearly showed the presence of the filamentary growths on the outer surface, figure 4.17c. An EPMA line scan taken through one of these filamentary growths showed that it consisted of predominantly chromium oxide containing 1 % Fe and 0.3 % Mn on the outside and chromium sulphide containing a few traces of Fe on the inside, figure 4.18.

X-ray mapping showed that the original surface layer consisted of an outer chromium oxide layer and an inner almost continuous chromium sulphide layer, figure 4.18. X-ray diffraction analysis using surface reflection confirmed the presence of Cr_2O_3 and Cr_7S_8 , table 4.4.

The EPMA line scan also showed that the alloy substrate immediately beneath the surface layer contained approximately 15 % Cr. Cross-sectional examination revealed that virtually no internal sulphidation had taken place. The exception to this was at the grain boundaries where small spherical chromium sulphide precipitates had formed to depths of 20 μm . The grain boundaries beneath the sulphide precipitates had carburized. This carburization was attributed to aging processes in the alloy.

Thus it appeared that once the surface layer had become complete the oxides overgrew the sulphides to produce a scale consisting of an outer Cr_2O_3 layer and an inner chromium sulphide layer. The chromium sulphide filaments also became encapsulated in Cr_2O_3 . A few internal chromium sulphide precipitates formed at grain boundaries and grain boundary carbides formed deeper in the alloy due to aging processes.

1000 hours
.....

The corrosion kinetics became parabolic at this point. Surface SEM examination showed that the filamentary growths still existed on top of the original surface layer, figure 4.17d.

2000 hours
.....

Cross-sectional examination showed that the corrosion morphology still consisted of 4 regions : a few filamentary growths on the external surface, the thin fairly uniform surface layer, some localized internal sulphide precipitates at grain boundaries and grain boundary carbides deeper in the alloy, figure 4.16c.

Fewer filamentary growths were now present. Otherwise they appeared to be similar to those present after 100 hours.

An EPMA line-scan showed that the surface layer consisted of predominantly Cr_2O_3 with small amounts of chromium sulphide at the scale/alloy interface, figure 4.19. X-ray diffraction analysis using surface reflection confirmed the presence of Cr_2O_3 and also detected a small amount of M_3O_4 , table 4.4. The Cr_2O_3 lattice parameter had increased, indicating that this phase now contained another cation. The line scan however showed that the oxide contained < 1 % Fe and 0.3 % Mn.

The alloy substrate immediately beneath the oxide layer now contained approximately 14 % Cr. The localized sulphide precipitates had become larger and were now present to a depth of 30 μm , figure 4.16c. The amount of carburization had not changed.

Thus it appeared that the sulphides formerly present in the inner sulphide layer had started to either diffuse down grain boundaries to form internal chromium sulphide precipitates or in areas away from grain boundaries diffused into sulphide filaments in the scale.

5000 hours
.....

Cross-sectional examination showed that the corrosion morphology consisted of 4 regions : a few external blisters, a thin uniform Cr_2O_3

surface layer, some localized internal sulphide precipitates at grain boundaries and grain boundary carbides deeper in the alloy, figure 4.16d and e.

The major part of the scale consisted of the thin oxide layer (5 μm thick). An EPMA line-scan taken through this layer confirmed that it was Cr_2O_3 which contained small amounts of Fe (0.7 %) and Mn (0.3 %), figure 4.20. X-ray mapping indicated that the chromium sulphides which had been present along the whole of the scale/alloy interface after 100 hours, were now restricted to a few isolated places. The chromium level in the depleted alloy substrate immediately beneath the oxide layer had now increased to 19 % indicating that Cr had back-diffused from the matrix. X-ray diffraction using surface reflection confirmed the presence of Cr_2O_3 , table 4.4.

No internal sulphide precipitates had formed except at grain boundaries, where the former chromium sulphide precipitates had increased in size and penetrated deeper into the alloy (50-75 μm), figure 4.16d. The grain boundary carbides were still present beneath these sulphide precipitates. No carburization due to carbon injection from the gas appeared to have taken place.

In a few isolated areas the external filamentary growths now appeared to have developed into quite large blisters, figure 4.16e. An EPMA line scan taken through a blister revealed that it consisted of Cr_2O_3 on the outside, chromium sulphide in the middle and Cr_2O_3 at the scale/alloy interface, figure 4.21. The oxide contained only 0.2 % Fe and 0.3 % Mn and the sulphide 0.4 % Fe and 0.3 % Mn. These sulphides were obviously providing an easier medium for the outward diffusion of chromium and hence causing localized thickening of the scale. This led to the alloy substrate becoming depleted in Cr to only 10 %. A few small internal chromium sulphide precipitates were starting to form in this region.

Thus in summary, an initial surface layer formed which consisted of Cr_2O_3 , FeCr_2O_4 , Cr_xS_y . These oxides and sulphides grew side by side until the surface layer became complete. In some places chromium sulphide filaments grew on top of this layer. Once the surface layer became complete the oxides overgrew the sulphides to produce a scale

consisting of an outer Cr_2O_3 layer and an inner chromium sulphide layer. The chromium sulphide filaments also became encapsulated in Cr_2O_3 . A few internal chromium sulphide precipitates started to form at grain boundaries in the alloy substrate, and grain boundary carbides formed deeper in the alloy due to aging processes. After approximately 1000 hours the kinetics became parabolic and the corrosion process proceeded at a slightly higher rate than in the sulphur-free gas. Most of the scale now consisted of the Cr_2O_3 layer. The sulphur formerly present in the inner chromium sulphide layer either diffused down grain boundaries to form large internal chromium sulphide precipitates or diffused into the former sulphide filaments to form large blisters.

0.2 % H_2S

180 grit condition
.....

Structural analysis examinations were carried out after 5 minutes, 1 hour, 5 hours, 100 hours, 500 hours and 5000 hours.

5 minutes
.....

Cross-sectional examination using the Pepperhoff technique showed that the corrosion morphology consisted of a discontinuous predominantly oxide surface layer and a zone of internal sulphide precipitates, figure 4.22a.

The structure of the discontinuous surface layer was complex. The major proportion of the layer (4 μm thick) consisted of oxide particles, however some sulphide particles had nucleated on both the alloy surface and on the oxide particles. In some places oxides had nucleated on sulphide particles. X-ray diffraction using surface reflection confirmed that most of the scale was Cr_2O_3 with traces of M_3O_4 also present, table 4.5. The Cr_2O_3 lattice parameter corresponded to that of pure Cr_2O_3 , figure 4.7. The M_3O_4 lattice parameter indicated that the oxide spinel was FeCr_2O_4 , figure 4.5. The volume of sulphide particles at this stage was too small to be detected by this technique. ESCA-Auger depth profile analysis also confirmed that the major part of this layer was Cr_2O_3 . The overall level of S in the layer at this stage was 7 %, figure 4.23a.

Cross-sectional examination showed that a few extremely small sulphide precipitates had formed in the alloy substrate (depth 4 μm), figure 4.23a.

Thus in summary a discontinuous layer containing Cr_2O_3 , FeCr_2O_4 and Cr_xS_y formed on the alloy surface and simultaneously a few extremely small internal sulphide precipitates formed in the alloy substrate.

1 hour
.....

Cross-sectional examination showed that the corrosion morphology now consisted of a discontinuous filamentary outer layer on top of the original oxide surface layer with a zone of internal sulphide precipitates in the alloy substrate, figure 4.24b.

Cross-sectional examination using the Pepperhoff technique revealed that the discontinuous filamentary outer layer consisted of predominantly sulphides with some oxides forming on the sulphides. X-ray diffraction using surface reflection indicated that the sulphides were Cr_7S_8 , table 4.5. ESCA-Auger analysis confirmed that the overall amount of S on the surface had increased from 7 % to 12 %, figure 4.23b. Surface SEM examination also showed the very filamentary nature of this layer, figure 4.25a.

The thin (4 μm) predominantly oxide layer at the original alloy surface now appeared to be continuous and contained a number of sulphide particles. X-ray diffraction using surface reflection indicated that the oxide was Cr_2O_3 with some FeCr_2O_4 also present, table 4.5.

A large amount of very small chromium sulphide precipitates were now present in the alloy substrate (depth 6 μm). There was no sign of any carburization at this stage.

Thus in summary the surface layer containing Cr_2O_3 , FeCr_2O_4 and Cr_xS_y became continuous. A new discontinuous outer layer containing a number of chromium sulphide filamentary growths started to form on top of this surface layer. The internal chromium sulphide precipitates increased in size and number.

5 hours
.....

Cross-sectional examination using the Pepperhoff technique showed that the corrosion morphology still consisted of the discontinuous filamentary outer layer, the original predominantly oxide layer and the zone of internal sulphide precipitates, figure 4.22b.

The discontinuous filamentary layer was now much thicker (14-15 μm). The layer still consisted of a large number of sulphide filaments with some oxide particles forming on the surface of these of the sulphides, figure 4.26a. X-ray diffraction again indicated that the sulphides were Cr_7S_8 , table 4.5. ESCA-Auger analysis confirmed that the overall amount of S on the surface had now increased to 22 %, figure 4.23c. Surface SEM examination also showed the filamentary nature of the outer layer, figure 4.25b.

The thin predominantly oxide layer at the original alloy surface was unchanged and still contained a number of sulphide particles. X-ray diffraction using surface reflection indicated that the oxide was Cr_2O_3 .

The zone of internal precipitation was now 6-7 μm deep. The chromium sulphides in this zone were larger but fewer in number. A few traces of carbide precipitates were now visible at the grain boundaries but this was attributed to aging processes in the alloy.

Thus in summary a number of oxide particles started to form on the filamentary sulphide growths in the discontinuous outer layer. The original surface layer now consisted of predominantly Cr_2O_3 with small amounts of chromium sulphide and FeCr_2O_4 also present. The internal chromium sulphide precipitates advanced deeper into the alloy with the larger precipitates starting to grow at the expense of the smaller ones.

100 hours
.....

Cross-sectional examination showed that the corrosion morphology consisted of a continuous very porous outer layer, the original surface layer, a zone of internal sulphide precipitates and a zone of internal carburization, figure 4.24d.

The uneven porous outer layer (14 μm thick) now consisted of mainly oxide with the former sulphide filaments contained within it. X-ray diffraction using surface reflection now only detected Cr_2O_3 and small amounts of FeCr_2O_4 , table 4.5. Thus it appeared that the oxide particles which had been forming on the sulphide filaments were coalescing together to encapsulate the sulphide filaments to produce the uneven porous layer. The porous nature of this layer was also clear from surface SEM examination, figure 4.25c.

The thin original surface layer appeared to be unchanged.

The zone of internal sulphide precipitates was now 25 μm deep. Again the large chromium sulphides had grown at the expense of the smaller precipitates.

A zone (25 μm deep) containing a few M_{23}C_6 precipitates was now visible beneath the zone of internal sulphides. Carbides were now also present at the grain boundaries throughout alloy. This grain boundary carburisation was attributed to aging processes within the alloy.

Thus in summary the Cr_2O_3 particles coalesced together to encapsulate the filamentary sulphide growths to form a continuous porous outer layer which contained Cr_2O_3 , Cr_xS_y and small amounts of FeCr_2O_4 . The original surface layer was relatively unchanged and still consisted of Cr_2O_3 , with small amounts of chromium sulphide and FeCr_2O_3 also present. The internal chromium sulphide precipitates continued to grow and advance deeper into the alloy. A new zone of internal carburization started to form beneath the internal sulphide precipitate zone.

500 hours
.....

Cross-sectional examination using the Pepperhoff technique showed that the corrosion morphology still consisted of the outer porous layer, the thin predominantly oxide layer at the original alloy surface, a zone of internal sulphide precipitates and a zone of carburization, figure 4.22c. The extent of the corrosion attack was very uneven. For clarity of presentation the description of this attack can be subdivided into two types of area.

- (i) Areas consisting of a thick outer porous layer and only a small amount of internal sulphide precipitates
- (ii) Areas consisting of a thin outer porous layer and a large amount of internal sulphide precipitates.
- (i) Areas consisting of a thick outer porous layer and only a small amount of internal sulphide precipitates

Cross-sectional examination using the Pepperhoff technique showed that thicker areas of the porous outer oxide layer contained a considerable number of the sulphide filaments, figure 4.26b. It appeared that these sulphides were acting as short circuit diffusion paths for the outward diffusion of Cr and thus leading to a enhanced thickening of this layer.

The thin predominantly oxide layer was still present at the original alloy surface.

The amount of internal sulphide precipitates beneath the thicker areas of the porous outer oxide layer had not increased significantly. A few carbides were present deeper in the alloy.

- ii) Areas corresponding to a thin outer porous layer and a large amount of internal sulphide precipitates

Cross-sectional examination using the Pepperhoff technique showed that the thinner areas of the porous outer oxide layer contained only a few small sulphide particles. Instead a few isolated metallic particles were visible in the oxide, figure 4.22c.

The thin predominantly oxide layer was still present at the original alloy surface.

The volume of internal sulphide precipitates had significantly increased. A zone of carburization was also visible moving ahead of the sulphide precipitates. This appeared to be aiding the inward

diffusion of sulphur by allowing the carbides to be transformed to sulphides.

Thus in summary it appeared that in these areas the former sulphide filaments in the porous outer layer had converted to oxide and metallic particles with the sulphur released in the process diffusing through the original predominantly oxide surface layer into the alloy substrate to increase the amount of internal sulphidation.

5000 hours
.....

Cross-sectional examination using the Pepperhoff technique showed that the corrosion morphology consisted of a new compact oxide layer, a few traces of localized internal oxidation, a zone of internal sulphide precipitates and a zone of internal carbide precipitates, figure 4.22b.

Cross-sectional examination using the Pepperhoff technique revealed that the former porous outer layer and original surface layer now corresponded to one compact oxide layer which contained a number of metallic particles but hardly any sulphides or pores.

A few cracks were present which were leading to some spallation of the scale. An EPMA line scan confirmed that the oxide was Cr_2O_3 which now contained very little sulphur, figure 4.27. The sulphur that did remain tended to be concentrated at the scale/alloy interface. X-ray diffraction using surface reflection confirmed that the major proportion of the oxide layer was Cr_2O_3 with small amounts of FeCr_2O_4 spinel also present. The Cr_2O_3 lattice parameter had increased indicating that another cation was becoming incorporated into the lattice, figure 4.27. X-ray mapping indicated that isolated areas rich in Si were also present in the scale and that the metallic particles were rich in Fe and Ni. Thus it was concluded that this layer consisted predominantly of Cr_2O_3 which contained some (Fe,Ni) rich metallic particles, a few traces of (Fe,Mn) rich M_3O_4 spinel and some areas rich in Si which was probably contamination from the grinding process. The EPMA line scan confirmed that the matrix just beneath the oxide layer contained 13 at % Cr.

A few traces of internal oxidation were starting to occur with some of the former sulphide precipitates starting to transform to oxides.

The sulphides which had been formerly present in the oxide layer now appeared to have become redistributed into the alloy substrate. The larger internal sulphide precipitates had grown at the expense of the smaller ones. Thus although the volume of internal sulphide precipitates had increased the overall volume of sulphides in the oxide and the substrate had only increased very slightly between 500 and 5000 hours. The EPMA line scan confirmed that the internal sulphide precipitates were chromium sulphides which contained small amounts of Mn (0.5 %) and Fe (0.5 %), figure 4.27.

The number internal carbide precipitates beneath the internal precipitation zone had increased significantly. The overall amount of carburization was approximately equal to that for the equivalent specimen exposed to the S-free gas for 5000 hours.

Thus the corrosion process for the 180 grit material can be summarized as follows. Initially a surface layer containing Cr_2O_3 , FeCr_2O_4 and Cr_xS_y formed on the alloy surface. Filamentary chromium sulphide growths then started to form on top of this layer. Simultaneously internal chromium sulphide precipitates formed in the alloy substrate. Oxide particles then started to form on the sulphide filamentary growths and eventually encapsulated them. Internal sulphidation continued and some internal carburization started to take place. In some areas the sulphide filaments in the oxide layer led to localized thickening of the scale. In other areas the sulphur diffused into the alloy substrate increasing the size of the internal sulphide precipitates. Eventually nearly all of the sulphur redistributed itself from sulphides in the oxide scale into sulphides in the alloy substrate. No further ingress of sulphur took place and the kinetic rate became parabolic and equivalent to that in the sulphur free gas. Even though the ingress of sulphur from the gas ceased carburization continued to take place.

Summary for the Model 25Cr-35Ni-Fe alloy in the oxidation governed regime

Sulphur-free gas

Electropolished condition
.....

The corrosion process for the electropolished material in the sulphur-free gas is summarised schematically in figure 4.28. Initially a discontinuous layer containing $M_{23}C_6$, $Fe(Mn)Cr_2O_4$ and Cr_2O_3 formed on the alloy surface, figure 4.28a. In the early stages the $M_{23}C_6$ surface carbides increased in size and a small amount of carbon diffused into the alloy substrate, figure 4.28b. Once the carbon activity on the alloy surface reached a certain level the $M_{23}C_6$ surface carbides started to transform to M_7C_3 , figure 4.28c, resulting in discontinuous surface layer containing $M_{23}C_6$, M_7C_3 , M_3O_4 and Cr_2O_3 . These phases continued to grow until the surface layer became continuous. Thermodynamics then determined that only the oxide could come to stable equilibrium with the gas and thus the M_7C_3 was converted to Cr_2O_3 and the $M_{23}C_6$ to $FeCr_2O_4$, with the carbon released in this process diffusing into the alloy substrate, figure 4.28d. From this point onwards the kinetics became parabolic and the rate of reaction was controlled by the outward diffusion of Cr through the predominantly Cr_2O_3 layer. The $FeCr_2O_4$ remained at the scale/alloy interface, figure 4.28e. This thin uniform dense Cr_2O_3 layer acted as an extremely effective barrier to any further ingress of carbon from the gas. The carbide precipitates which did form at the grain boundaries were predominantly due to aging processes within the alloy. The corrosion morphology after a long-term exposure is shown in figure 4.29a.

After long-term exposures such as 2000 hours the Cr_2O_3 lattice parameter increased indicating that another cation such as Fe or Mn was incorporated into the lattice. EPMA analysis however showed that the oxide layer only contained very small quantities of these elements.

180 grit condition
.....

In the case of the 180 grit material the corrosion process was much simpler. Initially only Cr_2O_3 formed on the surface. These nuclei soon

formed a continuous scale which grew at a much faster parabolic rate than on the electropolished (EP) material, figure 4.29b. The scale however was rather uneven and contained a number of physical defects such as cracks and pores. These allowed carbon containing molecules to penetrate the scale which in turn led to the formation of $M_{23}C_6$ carbide precipitates within the alloy, figure 4.29(b-d). No precipitates formed in the chromium-depleted zone immediately beneath the alloy surface. As in the case of the work-free material the Cr_2O_3 lattice parameter increased after long exposure times. This appeared to be associated with Mn and Si becoming incorporated into the outer regions of the scale.

0.2 % H_2S gas

Electropolished condition

The corrosion process for the model 25Cr-35Ni-Fe alloy electropolished condition in the 0.2 % H_2S gas can be summarized in a number of stages.

- Stage 1 (5mins)

Initially a discontinuous surface layer formed which consisted of Cr_2O_3 , $FeCr_2O_4$ and Cr_xS_y , figure 4.29e.

- Stage 2 (1 hour and 5 hours)

The oxides and sulphides grew side by side until the surface layer became complete. In some places chromium sulphide filaments grew on top of the surface layer, figure 4.29f.

- Stage 3 (100 hours)

Once the surface layer became complete the oxides overgrew the sulphides to produce scale consisting of an outer Cr_2O_3 layer and an inner Cr_xS_y layer, figure 4.29g. The chromium sulphide filaments also became encapsulated in Cr_2O_3 . A few internal chromium sulphides precipitates formed at grain boundaries. Grain boundary carbides formed deeper in the alloy due to aging processes.

- Stage 4 (2000 hours)

After approximately 1000 hours the kinetics became parabolic and corrosion proceeded at a slightly higher rate than in the sulphur-free gas. The sulphur which had been present in the inner Cr_xS_y layer

started to either diffuse down grain boundaries to form internal chromium sulphide precipitates or in areas away from grain boundaries diffused into the sulphide filaments in the scale, figure 4.29h.

- Stage 5 (5000 hours)

The process continued in a similar manner. The majority of the scale consisted of the Cr_2O_3 layer. The sulphur had now either diffused down the grain boundaries to form internal sulphide precipitates or diffused into sulphides in the scale to form large blisters consisting of Cr_2O_3 on the outside, Cr_xS_y in the middle and Cr_2O_3 at the scale/alloy interface, figure 4.29i. No internal carburization took place except for the formation of carbide precipitates at grain boundaries, most of this could be attributed to aging processes in the alloy.

180 grit condition
.....

The features which occurred in the corrosion process were more pronounced in the case of the 180 grit material. The corrosion process can be summarized as a number of stages.

- Stage 1 (5 mins)

Initially a discontinuous layer containing Cr_2O_3 , FeCr_2O_4 and Cr_xS_y formed on the alloy surface. Simultaneously a few extremely small internal sulphide precipitates formed in the alloy substrate, figure 4.29j.

- Stage 2 (1 hour)

The surface layer containing Cr_2O_3 , FeCr_2O_4 and Cr_xS_y became continuous. A new discontinuous outer layer containing a number of chromium sulphide filamentary growths started to form on top of the surface layer. The internal chromium sulphide precipitates increased in size and number.

- Stage 3 (5 hours)

A number of oxide particles started to form on the filamentary sulphide growths in the discontinuous outer layer, figure 4.29k. The original surface layer now consisted of predominantly Cr_2O_3 with

small amounts of chromium sulphide and FeCr_2O_4 also present. The internal chromium sulphide precipitates advanced deeper into the alloy with the larger precipitates growing at the expense of the smaller ones.

- Stage 4 (100 hours)

The Cr_2O_3 particles coalesced together to encapsulate the filamentary sulphide growths to form a continuous porous outer layer which contained Cr_2O_3 , Cr_xS_y and small amounts of FeCr_2O_4 , figure 4.29l. The original surface layer was relatively unchanged and still consisted of Cr_2O_3 , with small amounts of chromium sulphides and FeCr_2O_4 also present.

The internal chromium sulphide precipitates continued to grow and advance deeper into the alloy. A new zone of internal carburization started to form beneath the internal sulphide precipitate zone.

- Stage 5 (500 hours)

In some areas the sulphide filaments in the outer porous layer acted as short circuit diffusion paths for the outward diffusion of chromium and led to localized thickening of this layer, figure 4.29m. The original surface layer, the zone of internal sulphide precipitates and zone of carburization did not change significantly beneath these areas. In other areas the sulphide filaments in the outer porous layer started to transform to Cr_2O_3 and metallic particles. The sulphur released in the process penetrated the original surface layer and increased the amount of internal sulphide precipitates. These sulphides appeared to advance deeper into the alloy substrate by converting the internal carbides to sulphides with the carbon released in the process diffusing deeper into the alloy.

- Stage 6 (5000 hours)

The former porous outer layer and the original surface layer now corresponded to one compact predominantly Cr_2O_3 oxide layer which contained a number of (Fe, Ni) metallic particles, a few traces of FeCr_2O_4 , but hardly any sulphides or pores, figure 4.29n. The internal chromium sulphides had grown larger and had advanced deeper into the alloy. The amount of internal carburization had increased

significantly. Some of the internal sulphide precipitates near the substrate were starting to convert to oxides. It therefore appeared that the sulphide filaments had converted to oxides and metallic particles with the sulphur driven into the alloy to increase the size of the internal chromium sulphide precipitates. The total amount of sulphur formerly present in the porous outer oxide layer and the zone of internal sulphide precipitates and now only present in the zone of internal precipitates had not increased significantly. This observation together with the kinetic rate slowing down to that of the sulphur free gas led to the conclusion that no further S ingress from was taking place. A considerable amount of carbon ingress from the gas did however continue to take place.

Environment	Surface Finish	Reaction Rate Constant ($\text{mg}^2 \cdot \text{cm}^{-4} \cdot \text{h}^{-1}$)
Sulphur free	EP	5.6×10^{-5}
	180	2.8×10^{-4}
$p\text{S}_2 = 10^{-9}$ bar	EP	1.3×10^{-4}
	180	2.1×10^{-4}

Table 4.1

Reaction rate constants for the model 25Cr-35Ni-Fe alloy at 800°C
 $(p\text{O}_2 = 10^{-21}$ bar, $a_c = 0.3)$.

Exposure time	Phases Identified (Intensity/Parameter A)				
	Austenite	Cr ₂ O ₃	M ₃ O ₄	Cr ₇ C ₃	M ₂₃ C ₆
5 mins	75/3.592	1/traces	5/8.422	-	10/10.613
1 hour	711/3.590	1/4.954-13.584	7/8.409	-	15/10.614
5 hours	208/3.590	3/4.961-13.611	5/8.386	6/4.506-13.965	1st ext. 40/10.616 2nd ext. 45/10.628
100 hours	805/3.584	9/4.950-13.651	3/8.395	-	-
2000 hours	324/3.582	31/4.983-13.644	traces	-	-

Table 4.2

X-ray diffraction data for the model 25Cr-35Ni-Fe alloy exposed to the sulphur-free environment at 800°C ($pO_2 = 10^{-21}$ bar, $a_c = 0.3$). Electropolished condition.

Exposure Time	Phase Identified (Intensity/Parameter A)			
	Austenite	Cr ₂ O ₃	M ₃ O ₄	M ₂₃ C ₆
5 mins	301/3.585	4/4.955-13.603	-	-
1 hour	262/3.585	10/4.958-13.657	-	-
5 hours	294/3.584	8/4.956-13.608	-	-
2000 hours	58/3.583	50/4.980-13.615	-	-
5000 hours	50/3.583	100/4.982-13.624	-	-

Table 4.3

X-ray diffraction data for the model 25Cr-35Ni-Fe alloy exposed to the sulphur-free environment at 800°C ($pO_2 = 10^{-21}$ bar, $a_c = 0.3$). Surface worked '180 grit' condition.

Exposure time	Phases Identified (Intensity/Parameter A)				
	Austenite	Cr ₂ O ₃	M ₃ O ₄	Cr ₇ S ₈	M ₂₃ C ₆
5 mins	162/3.581	2/4.954-13.584	1/8.442	-	-
1 hour	949/3.586	-	2/8.374	traces	-
5 hours	999/3.585	6/4.949-13.585	6/8.439	-	-
100 hours	54/3.580	17/4.955-13.577	-	11/3.46-5.75	-
2000 hours	919/3.584	34/4.986-13.645	5/8.432	-	-
5000 hours	150/3.584	31/4.974-13.648	-	-	-

Table 4.4

X-ray diffraction data for the model 25Cr-35Ni-Fe alloy exposed to the 0.2 % H₂S environment at 800°C ($pO_2 = 10^{-21}$ bar, $pS_2 = 10^{-9}$ bar, $a_c = 0.3$). Electropolished work-free condition.

Exposure time	Phases Identified (Intensity/Parameter A)				
	Austenite	Cr ₂ O ₃	M ₃ O ₄	Cr ₇ S ₈	M ₂₃ C ₆
5 mins	234/3.587	7/4.940-13.950	traces	-	-
1 hour	112/3.584	13/4.949-13.603	7/8.391	I = 3	-
5 hours	101/3.584	13/4.950-13.577	-	I = 3	-
100 hours	36/3.585	38/4.954-13.587	2/8.369	-	-
2000 hours	18/3.582	38/4.975-13.585	2/8.421	-	-
5000 hours	8/3.588	35/4.966-13.600	5/8.408	-	-

Table 4.5

X-ray diffraction data for the model 25Cr-35Ni-Fe alloy exposed to the 0.2 % H₂S environment at 800°C ($p_{O_2} = 10^{-21}$ bar, $p_{S_2} = 10^{-9}$ bar, $a_c = 0.3$). Surface worked condition.

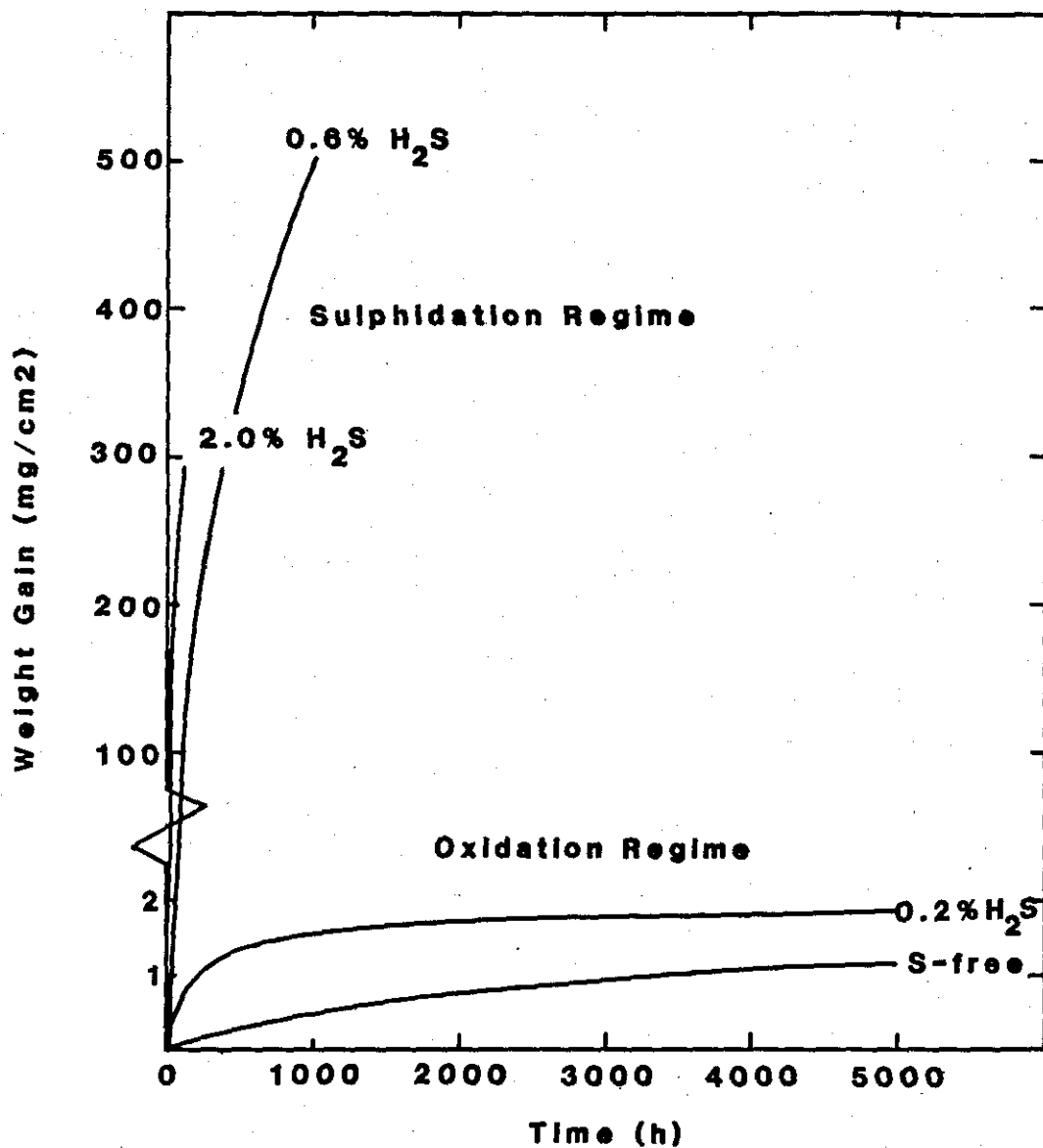


Figure 4.1
Kinetic data for the model 25Cr-35Ni-Fe alloy exposed at 800°C,
 $p_{O_2} = 10^{-21}$ bar, $a_c = 0.3$

Model 25Cr-35Ni-Fe, $P_{O_2}=10^{-21}$ bar, $a_C=0.3$, 800degC

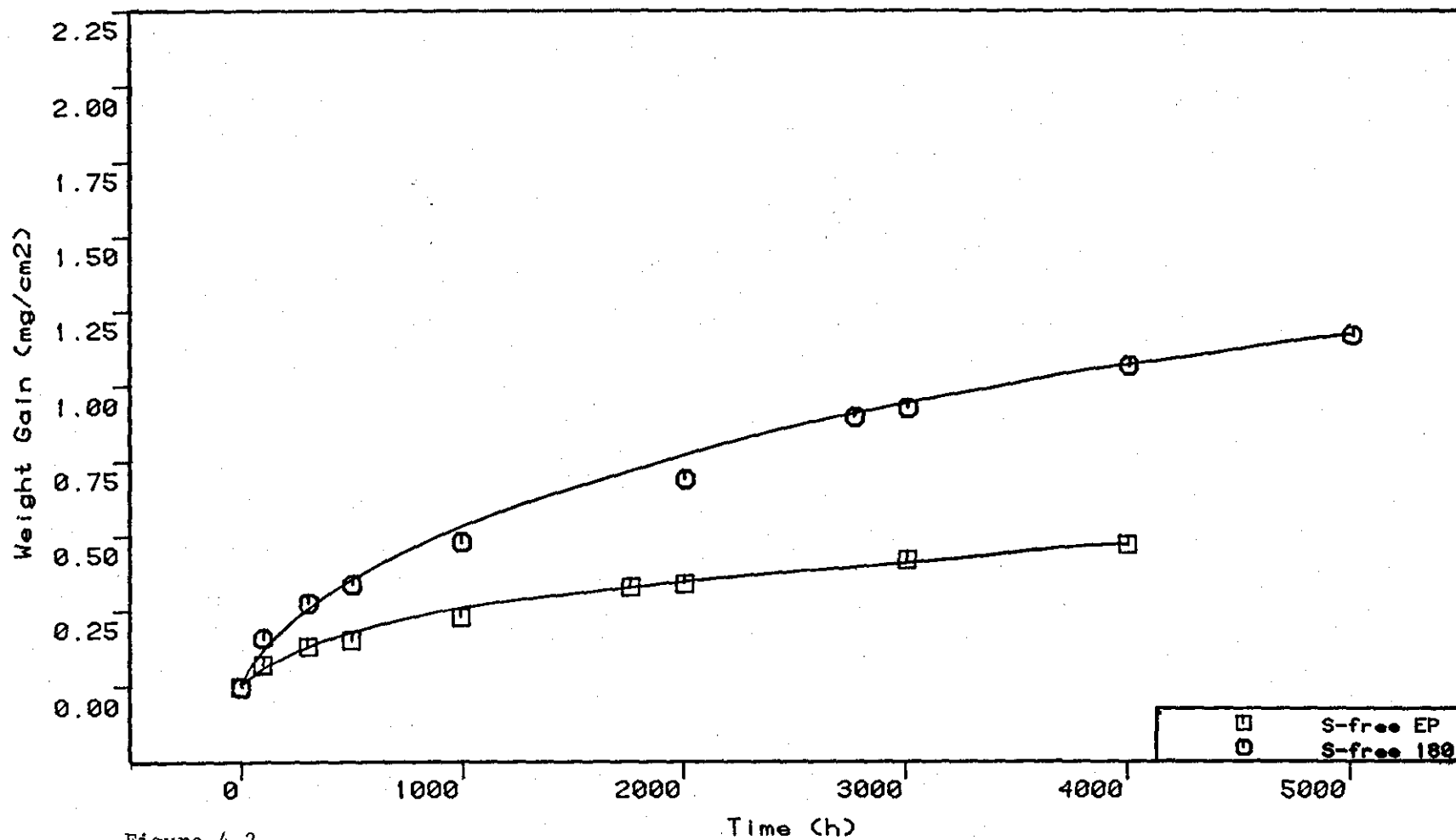
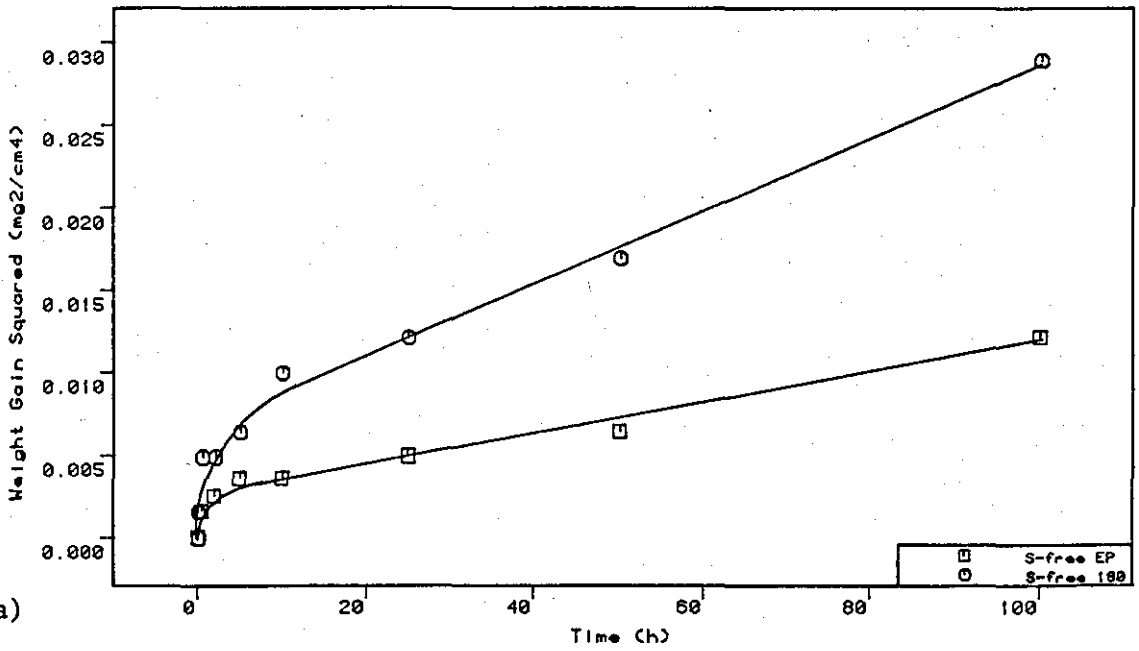


Figure 4.2

Kinetic data for the Model 25Cr-35Ni-Fe alloy exposed to sulphur-free gas at 800°C.

Model 25Cr-35Ni-Fe, P_{O2}=10⁻²¹ bar, a_C=0.3, 800degC



Model 25Cr-35Ni-Fe, P_{O2}=10⁻²¹ bar, a_C=0.3, 800degC

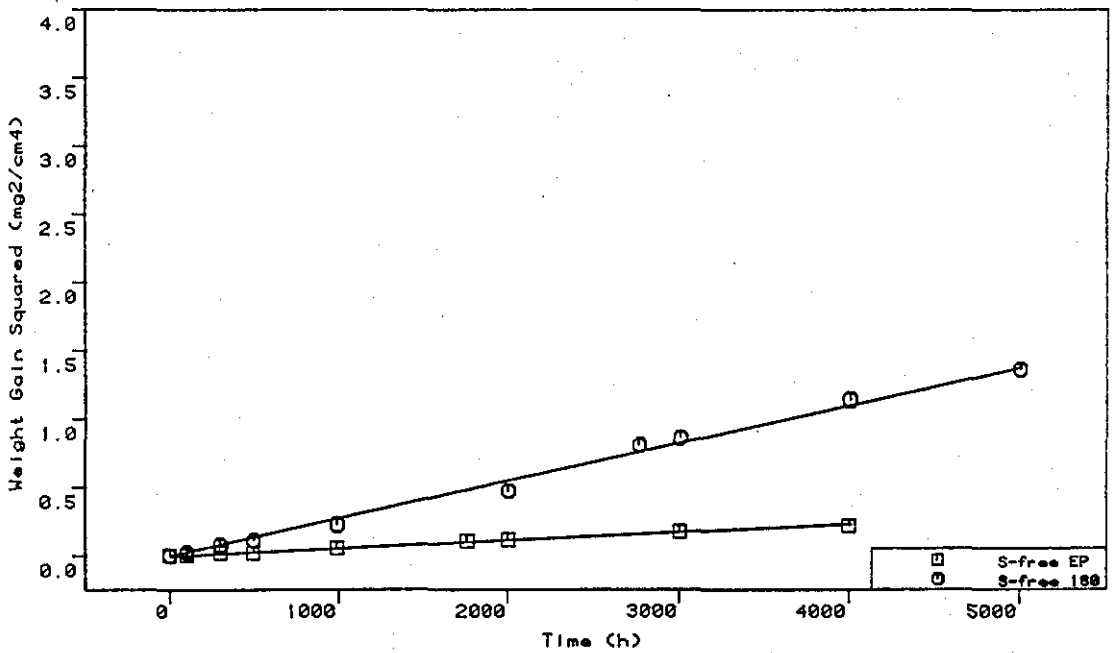
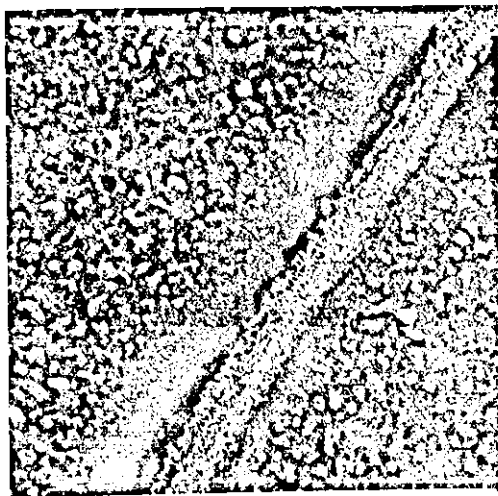


Figure 4.3

Plots of weight gain squared against time for the model 25Cr-35Ni-Fe alloy exposed to the sulphur-free gas at 800°C.

(a) Short term exposures in the sulphur-free gas at 800°C.

(b) Long term exposures in the sulphur-free gas at 800°C.



a) 5mins 3µm

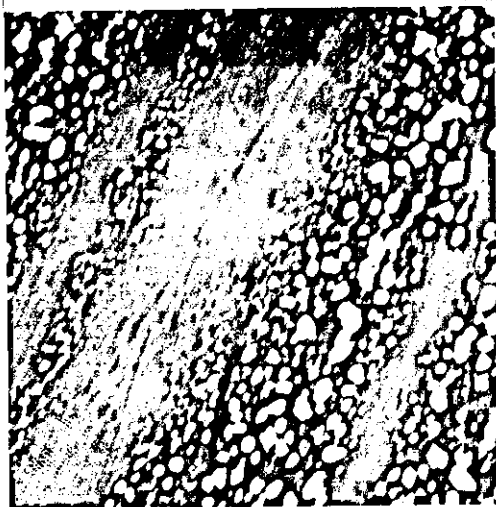
Surface SEM

Model 25Cr-35Ni-Fe

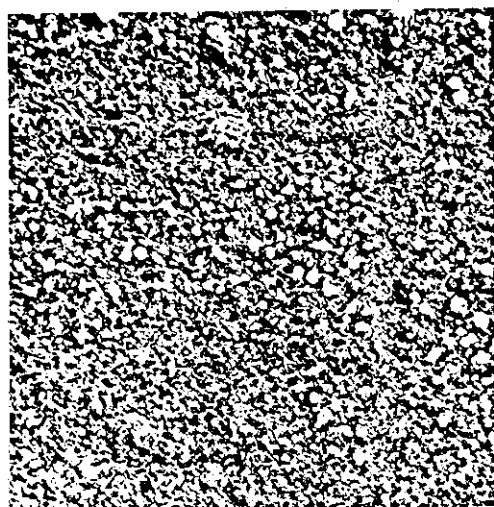
S-free environment

800 deg.C

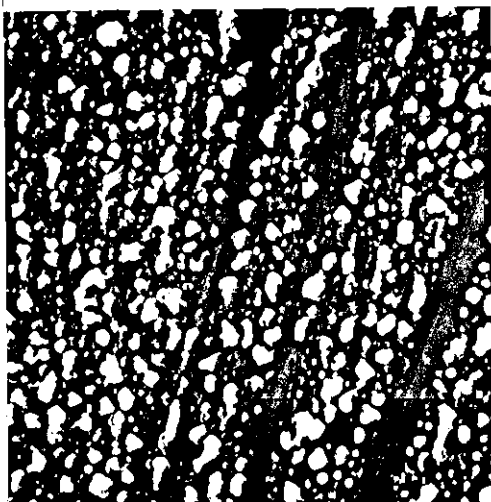
Electropolished



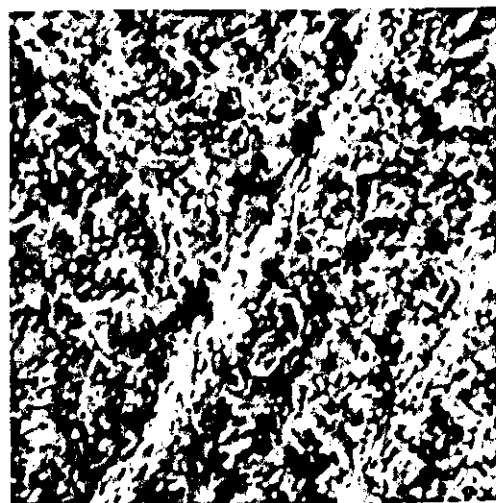
b) 0.5hours 3µm



d) 100 hours 3µm



c) 2hours 3µm



e) 2000hours 3µm

Figure 4.4

Surface SEM examination of the model 25Cr-35Ni-Fe alloy exposed to the sulphur-free gas at 800°C (electropolished condition).

Model 25Cr-35Ni-Fe, Oxide Spinel Lattice Parameters.

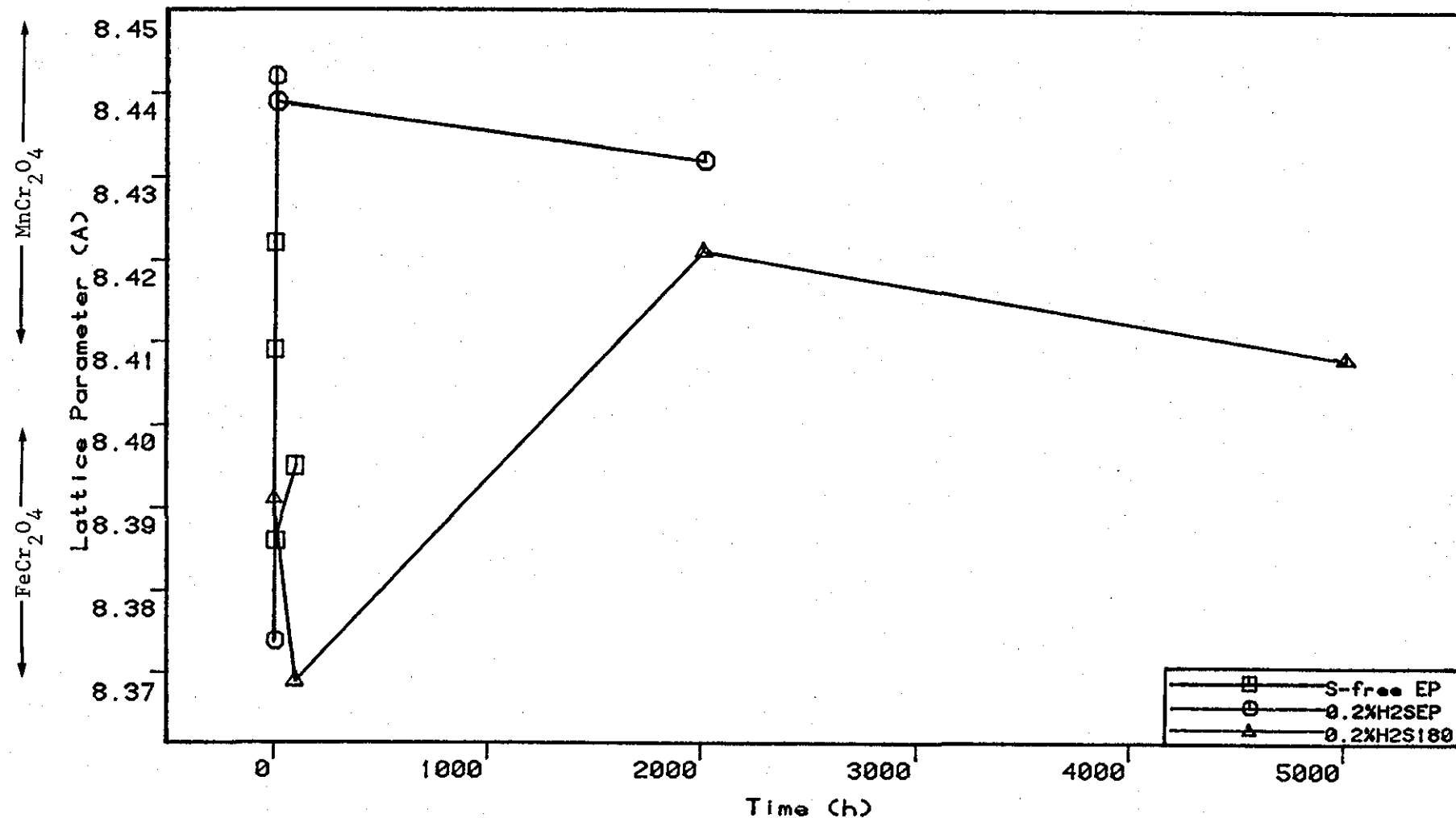


Figure 4.5

Plots of oxide spinel lattice parameter against time for the scale formed on the model 25Cr-35Ni-Fe alloy exposed to the sulphur-free and 0.2% H₂S gases at 800°C.

Model 25Cr-35Ni EP , S-free , 800 deg.C , 5 mins

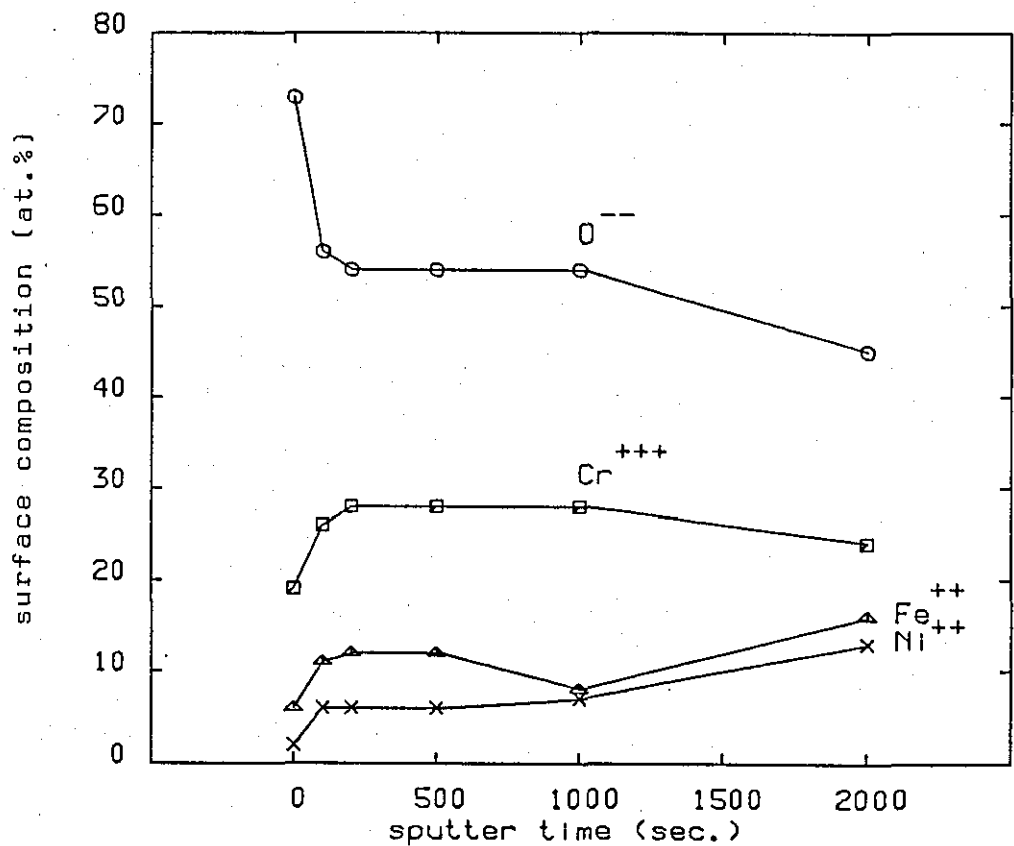


Figure 4.6

ESCA-AUGER analysis of the scale formed on the model 25Cr-35Ni-Fe alloy exposed to the sulphur-free gas for 5 minutes at 800°C (electropolished condition).

Model 25Cr-35Ni-Fe, Chromia Lattice Parameters

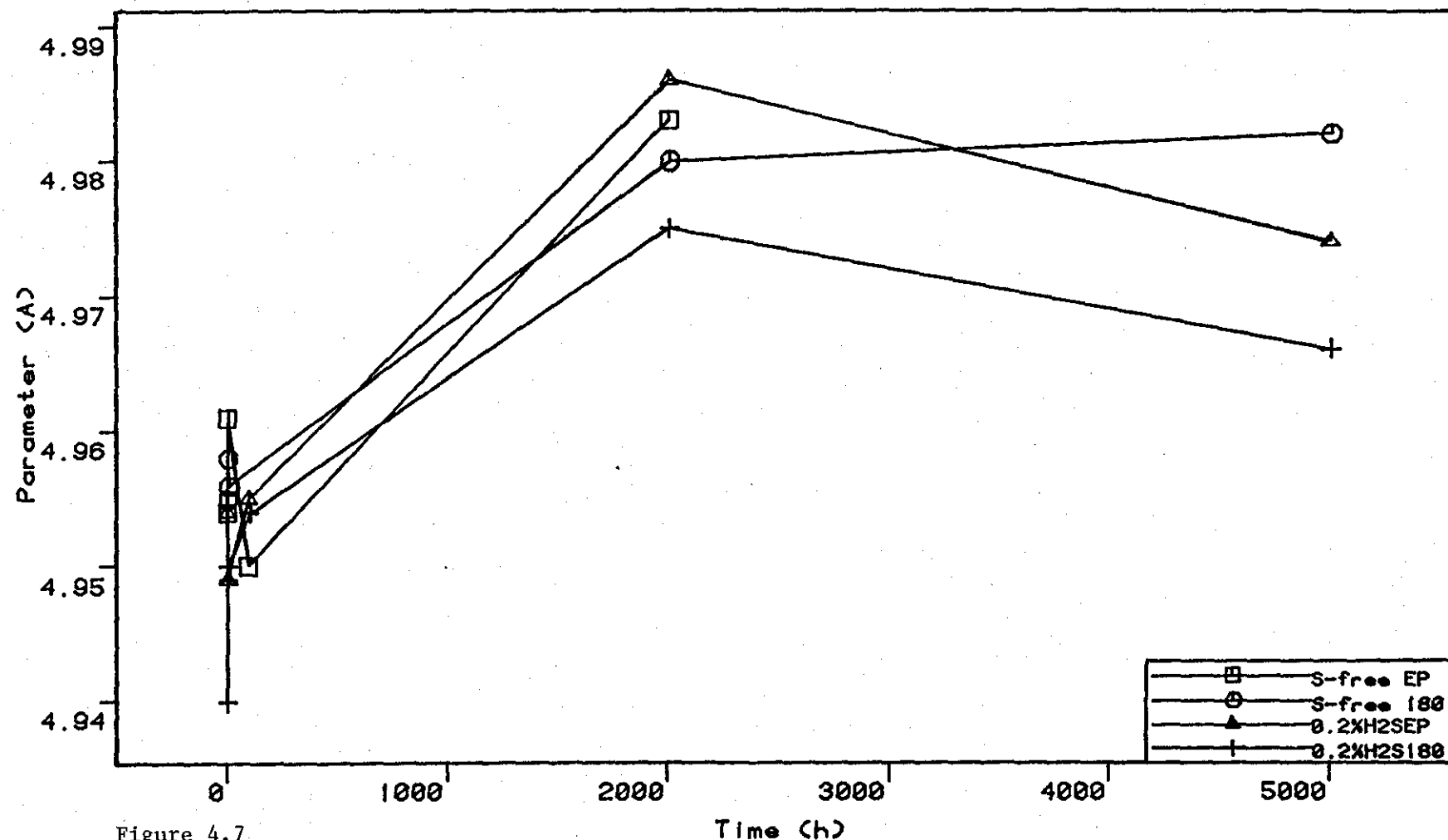


Figure 4.7

Plots of Cr_2O_3 lattice parameter against time for the scale formed on the model alloy exposed to the sulphur-free and 0.2% H_2S gases at 800°C .

Model 25Cr-35Ni-Fe sulphur-free environment 800°C

electropolished

180 grit

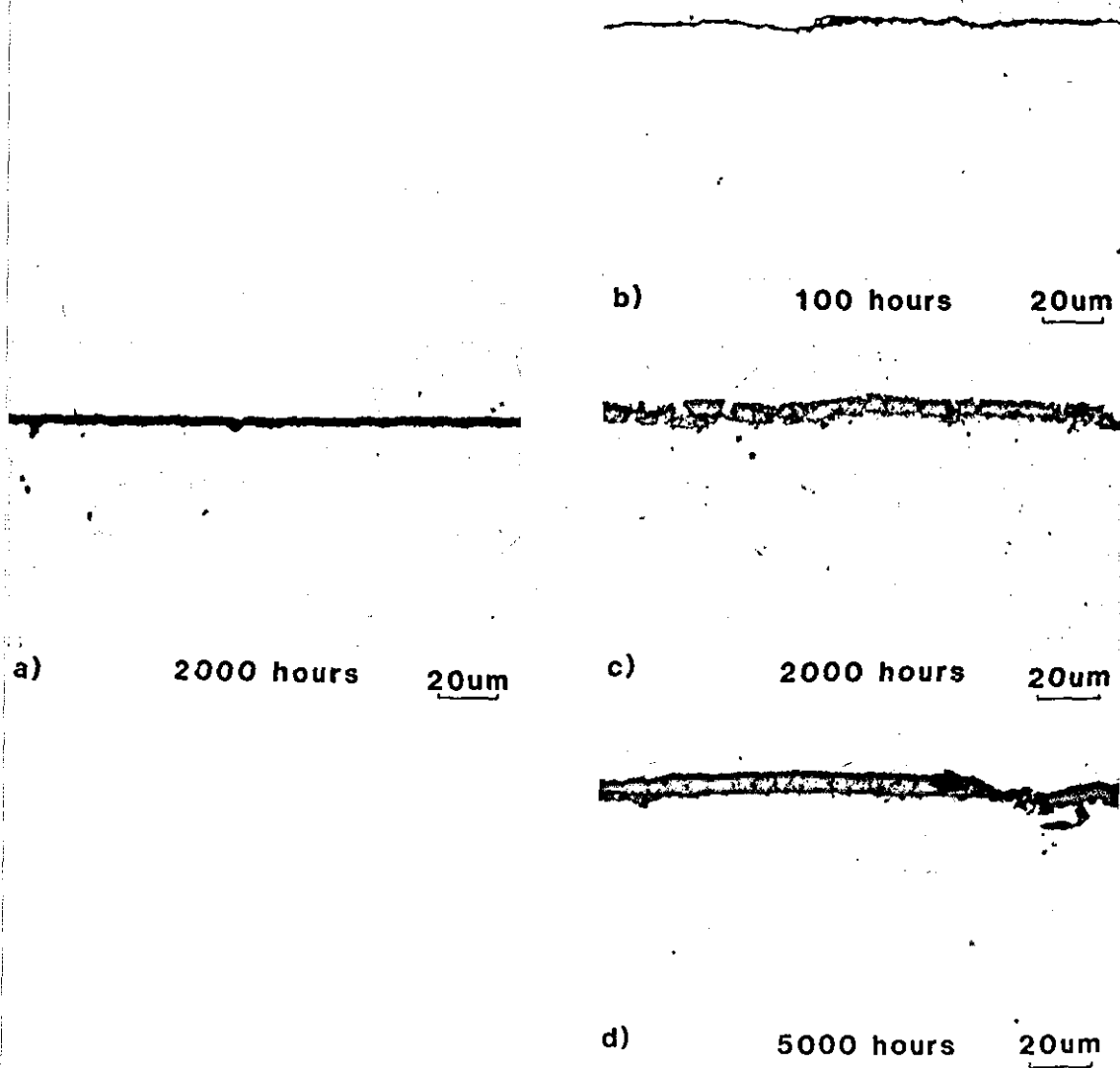


Figure 4.8

Cross-sectional metallographic examination of the model 25Cr-35Ni-Fe alloy exposed to the sulphur-free gas at 800°C.

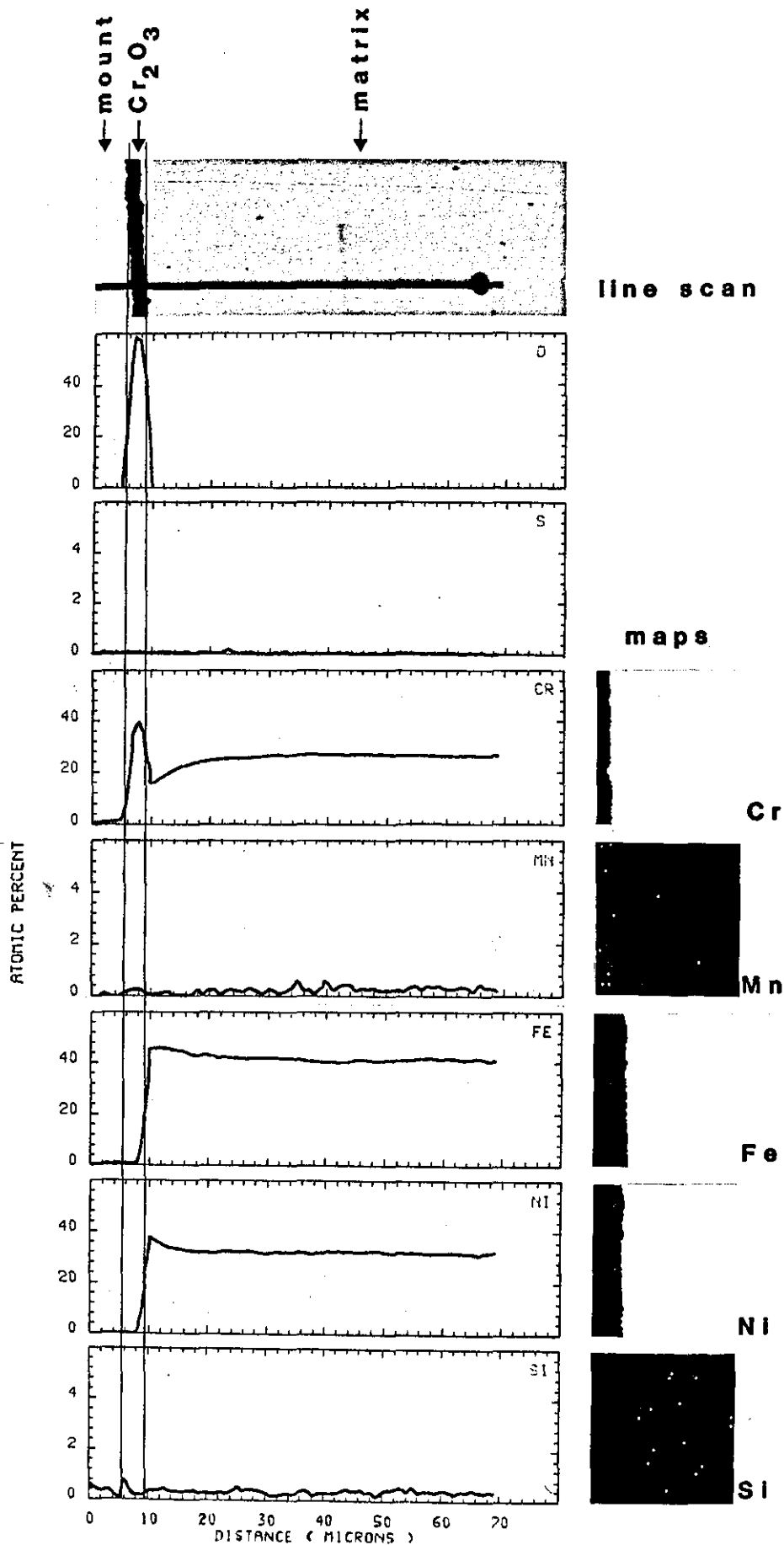
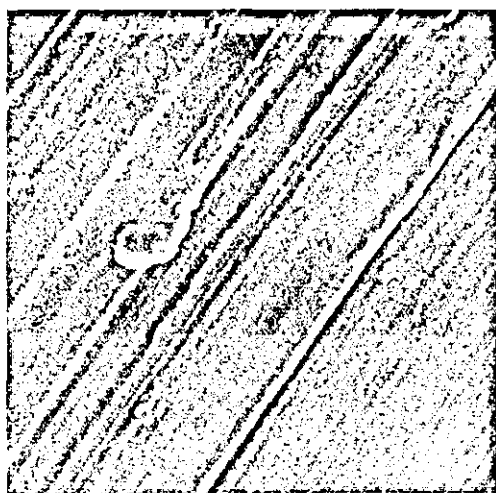


Figure 4.9

EPMA line scan and elemental concentration maps on the model 25Cr-35Ni-Fe alloy exposed for 2000 hours in the sulphur-free gas at 800°C (electropolished condition).



a) 5mins 10um

Surface SEM

Model 25Cr-35Ni-Fe

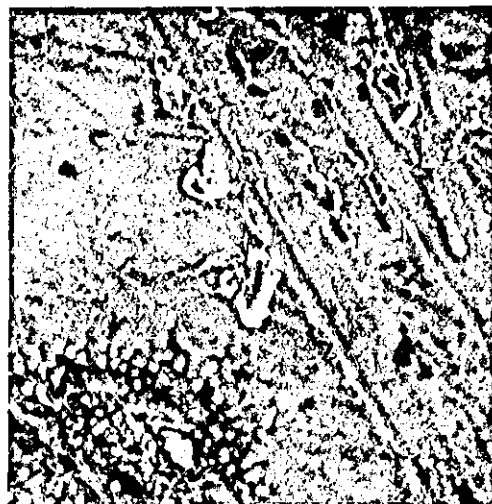
S-free environment

800 deg.C

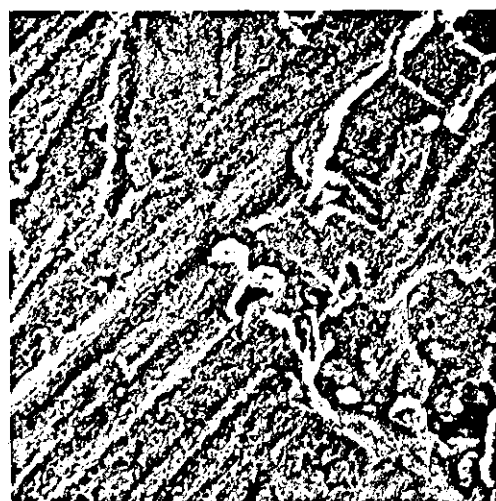
180 grit



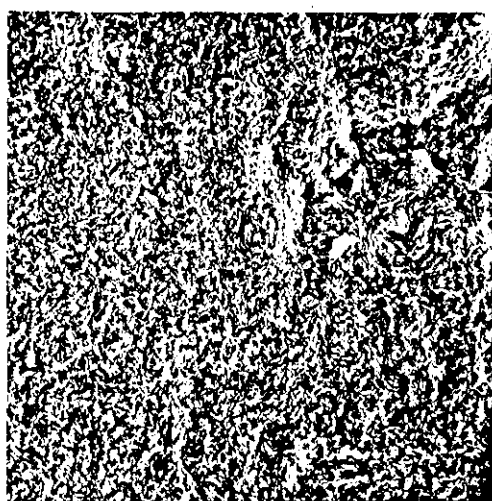
b) 1hour 10um



d) 100hours 10um



c) 5hours 10um



e) 5000hours 10um

Figure 4.10

Surface SEM examination of the model 25Cr-35Ni-Fe alloy exposed to the sulphur-free gas at 800°C (surface worked '180 grit' condition).

Model 25Cr-35Ni 180 , S-free , 800 deg.C , 5 mins

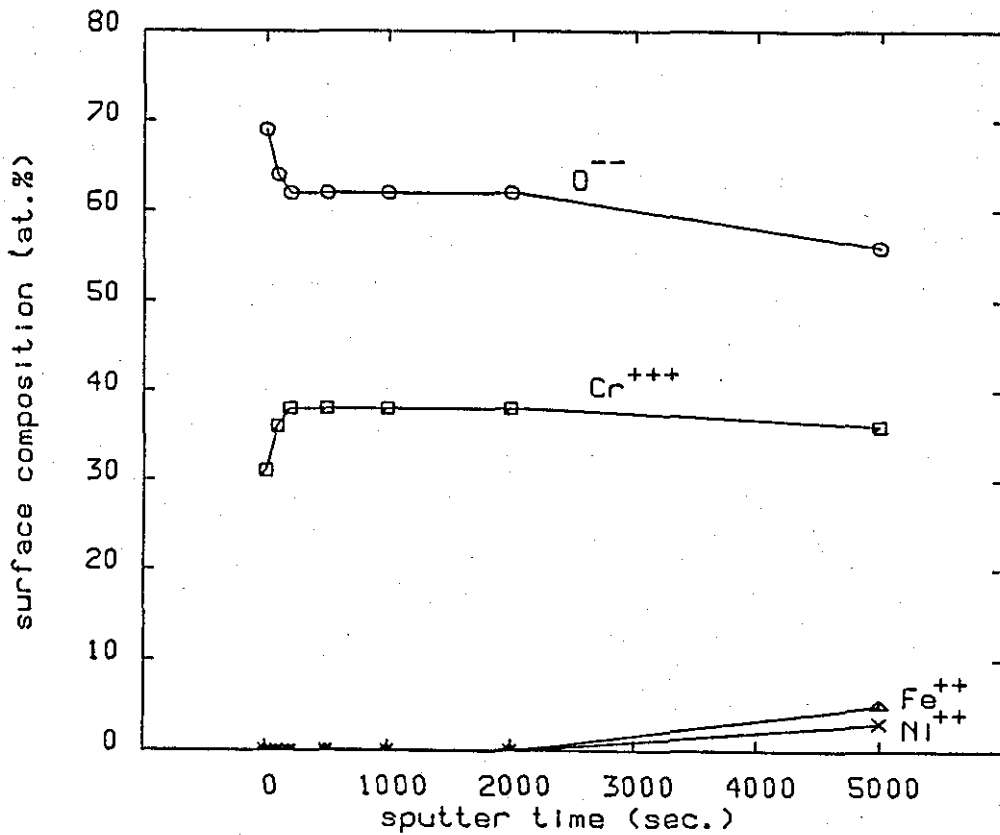


Figure 4.11

ESCA-AUGER analysis of the scale formed on the model 25Cr-35Ni-Fe alloy exposed to the sulphur-free gas for 5 minutes at 800°C (surface worked '180 grit' condition).

Model 25Cr-35Ni 180 , S-free , 800 deg.C , 2000 hrs

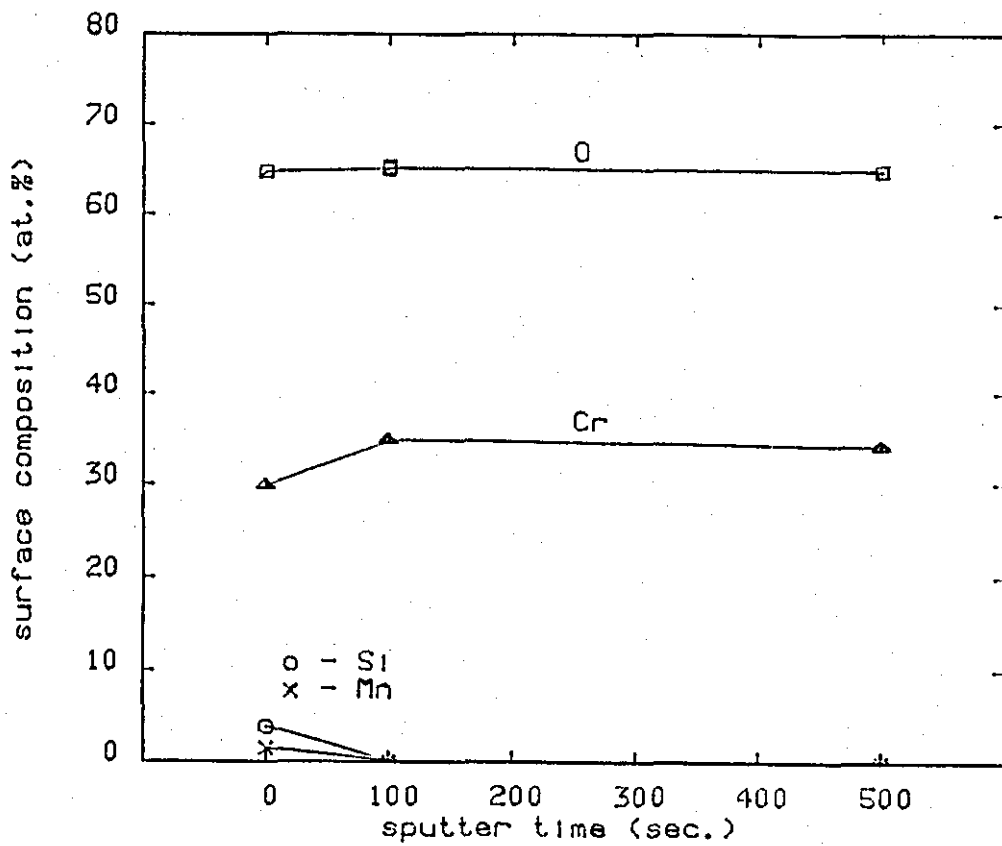


Figure 4.12

ESCA-AUGER analysis of the external surface of the scale formed on the model 25Cr-35Ni-Fe alloy exposed to the sulphur-free gas for 2000 hours at 800°C (surface worked '180 grit' condition).

Model 25Cr-35Ni-Fe 180, S-free environment, 800 deg. C

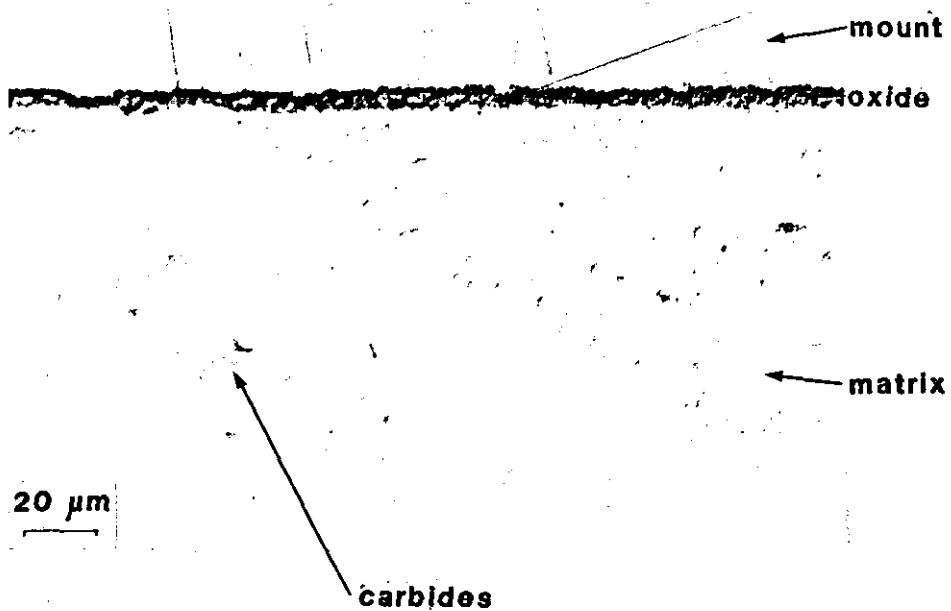


Figure 4.13

Cross-sectional metallographic examination using interference contrast to illustrate the amount of internal carburization in the model 25Cr-35Ni-Fe alloy after 2000 hours exposure to the sulphur-free gas (surface worked '180 grit' condition).

Model 25Cr-35Ni-Fe, $P_{O_2}=10^{-21}$ bar, $a_C=0.3$, 800degC

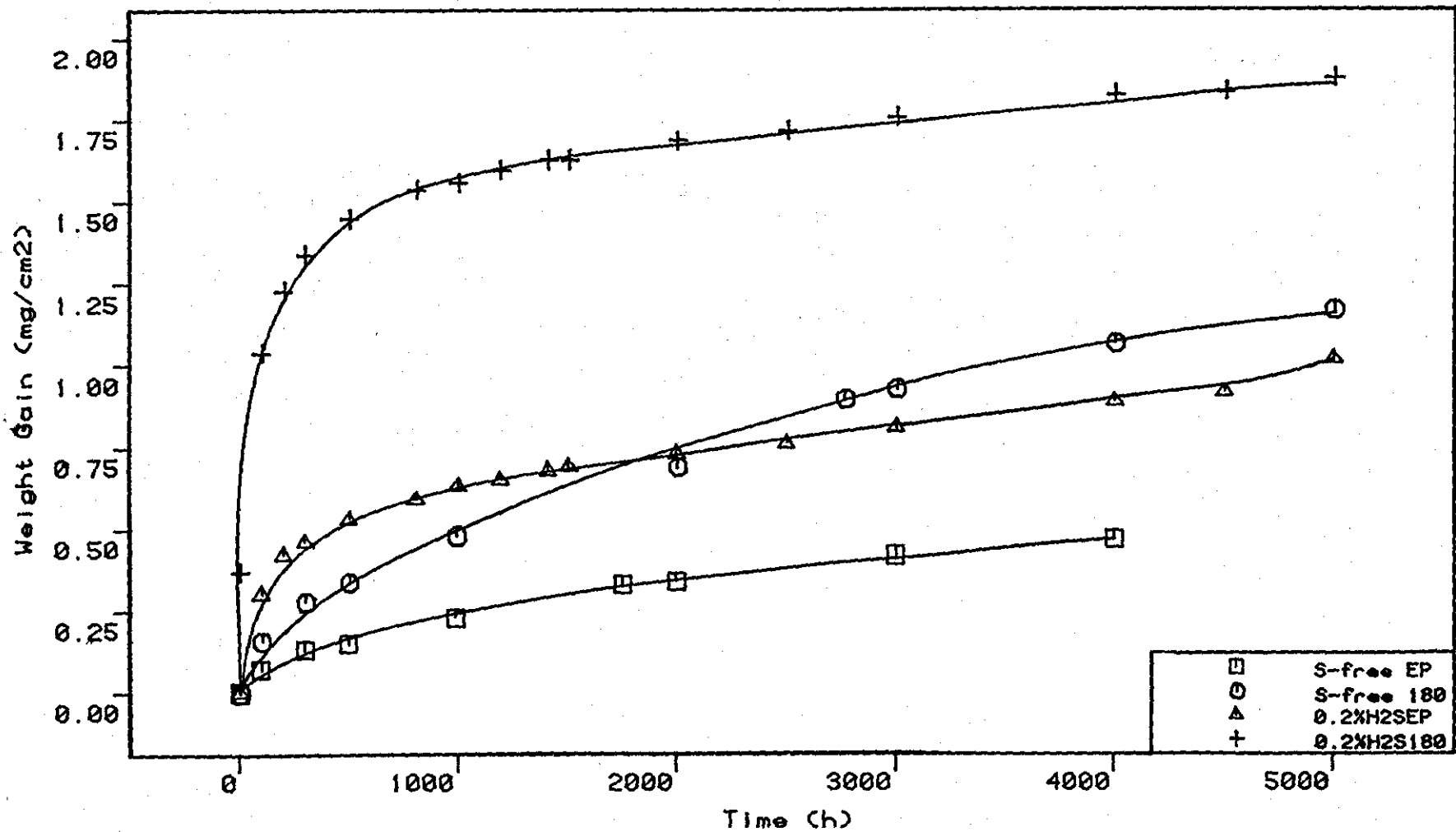


Figure 4.14

Kinetic data for the model 25Cr-35Ni-Fe alloy exposed to the sulphur-free and 0.2% H_2S gases at 800 C

Model 25Cr-35Ni-Fe, $P_{O_2}=10^{-21}$ bar, $a_C=0.3$, 800degC

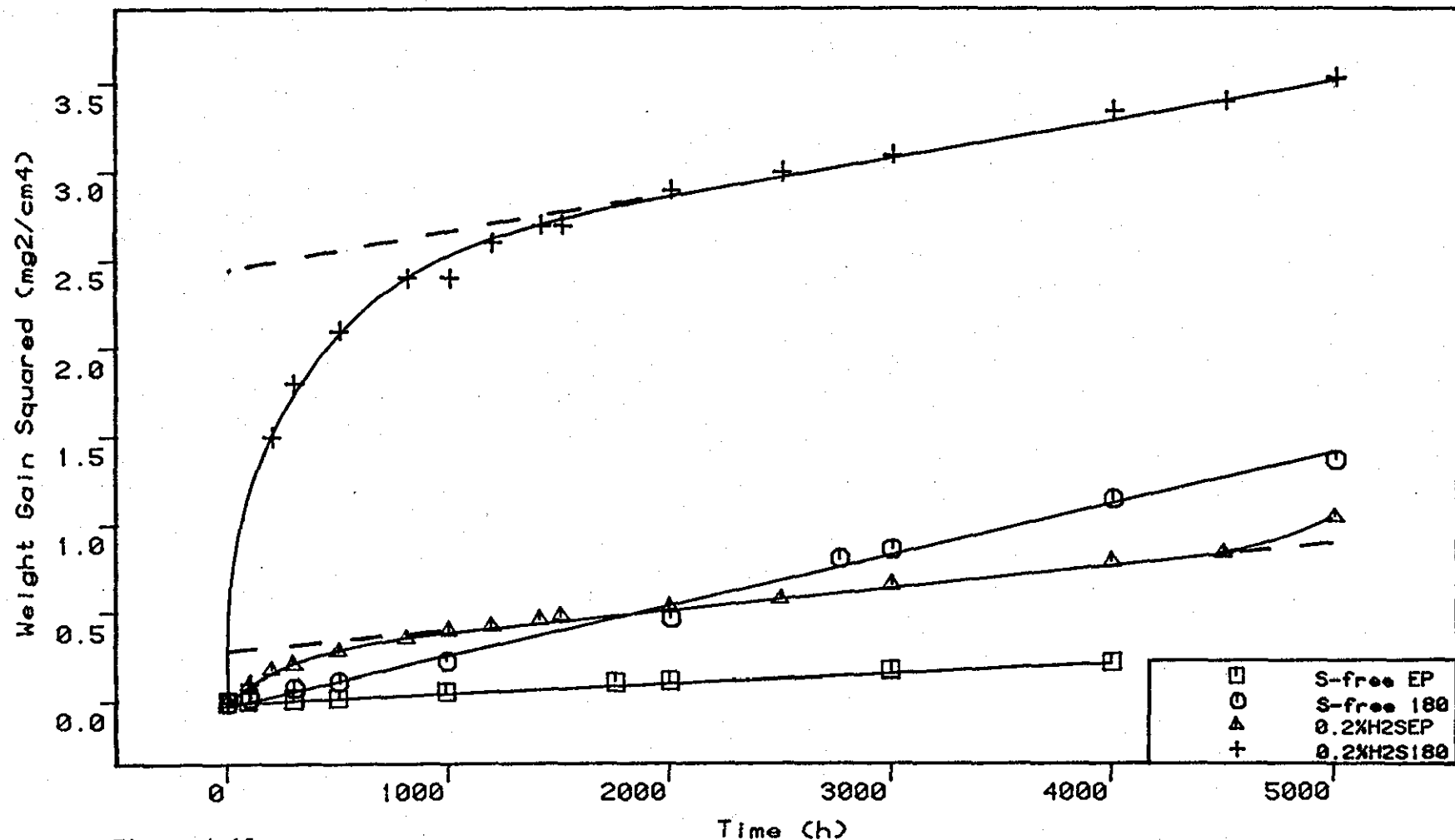


Figure 4.15

Plots of weight gain squared against time for the model 25Cr-35Ni-Fe alloy exposed to the sulphur-free and 0.2% H₂S gases at 800°C.

Model 25Cr-35Ni-Fe EP, 0.2% H₂S, 800 deg. C

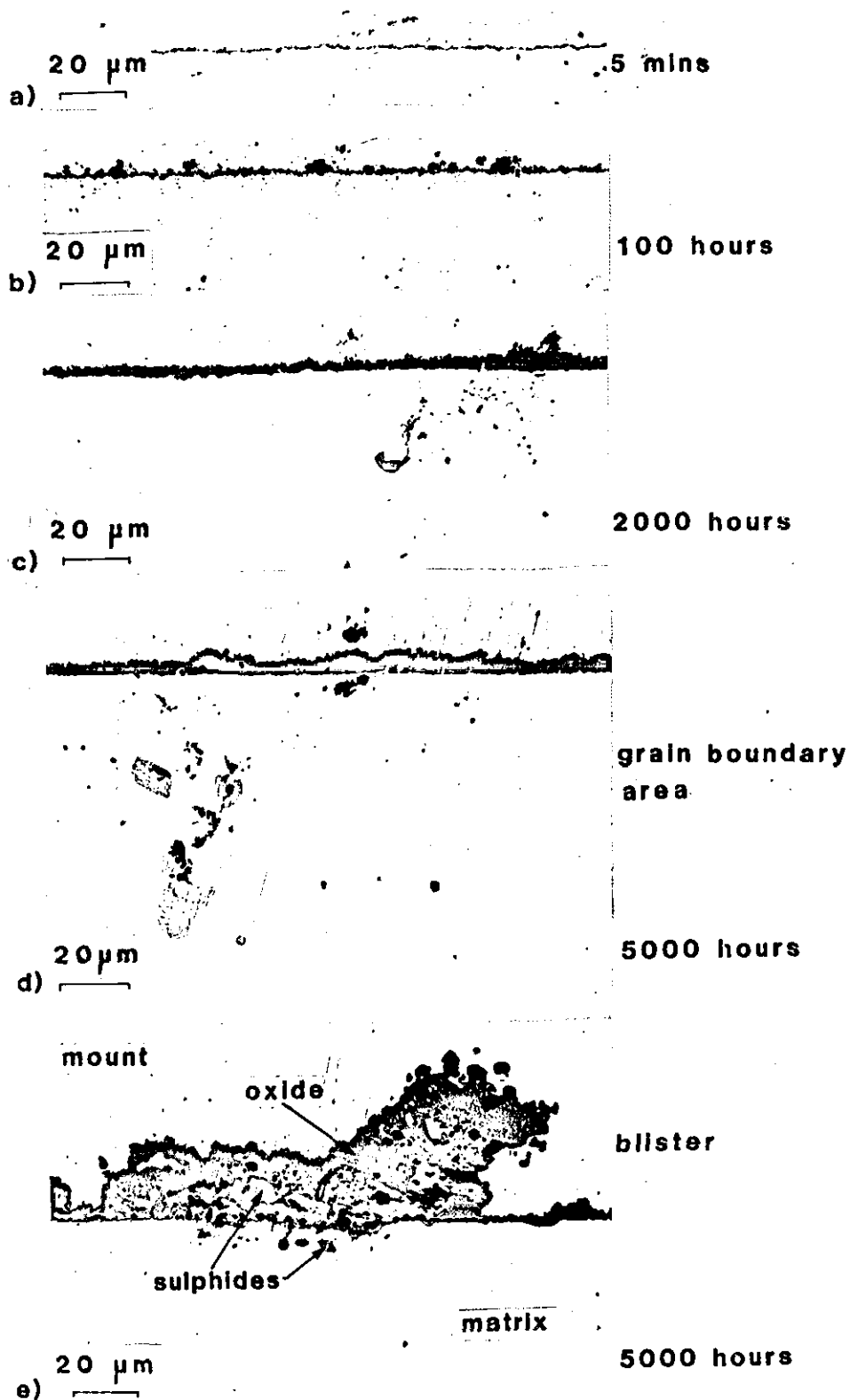
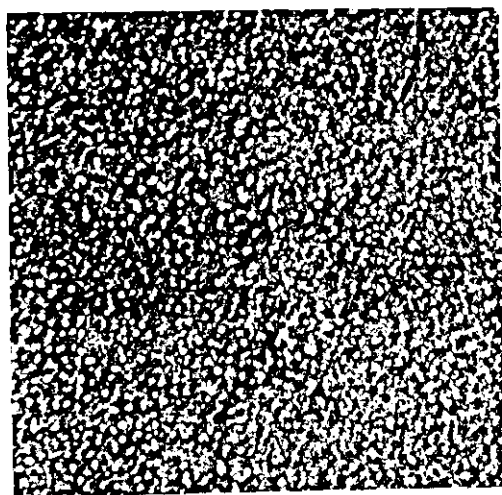
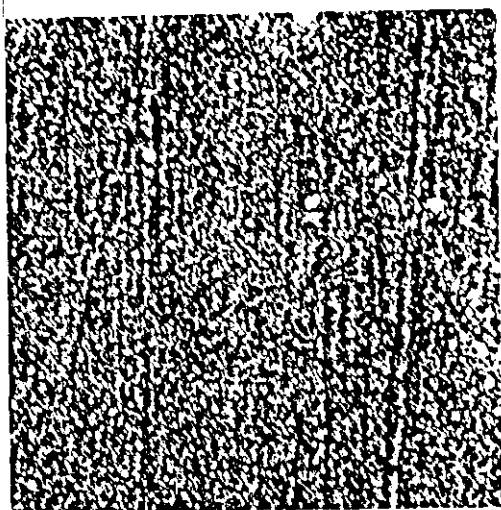


Figure 4.16

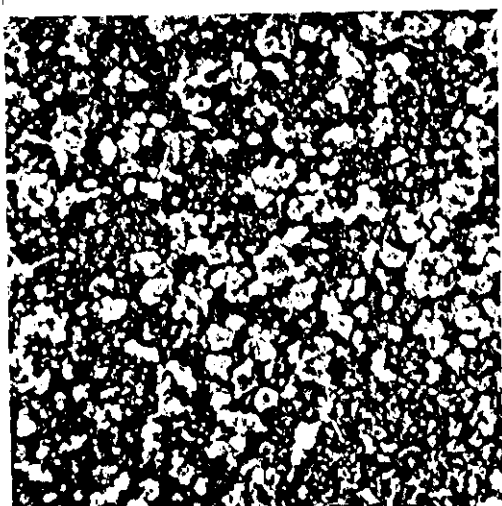
Cross-sectional metallographic examination of the model 25Cr-35Ni-Fe alloy exposed to the 0.2 % H₂S environment at 800°C (electropolished condition).



a) 1 hour 10µm



b) 5 hours 10µm



c) 100 hours 10µm

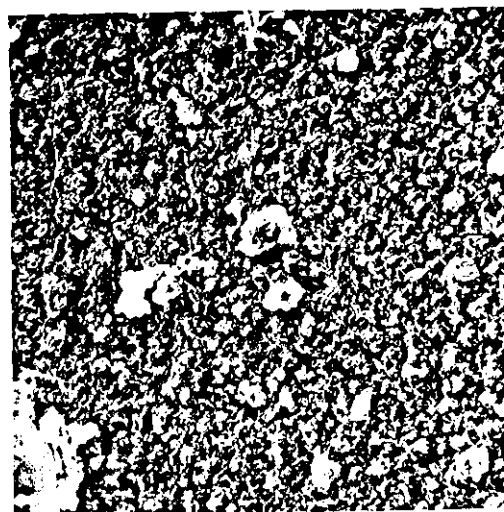
Surface SEM

Model 25Cr-35Ni-Fe

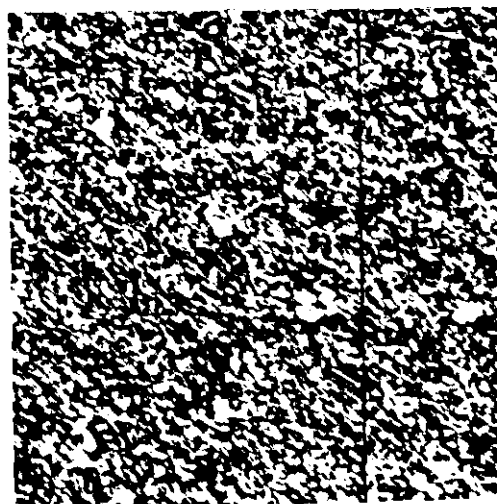
0.2% H_2S environment

800 deg.C

Electropolished



d) 1000 hours 10µm



e) 5000 hours 10µm

Figure 4.17

Surface SEM examinations of the model 25Cr-35Ni-Fe alloy exposed to the 0.2 % H_2S environment at 800°C (electropolished condition).

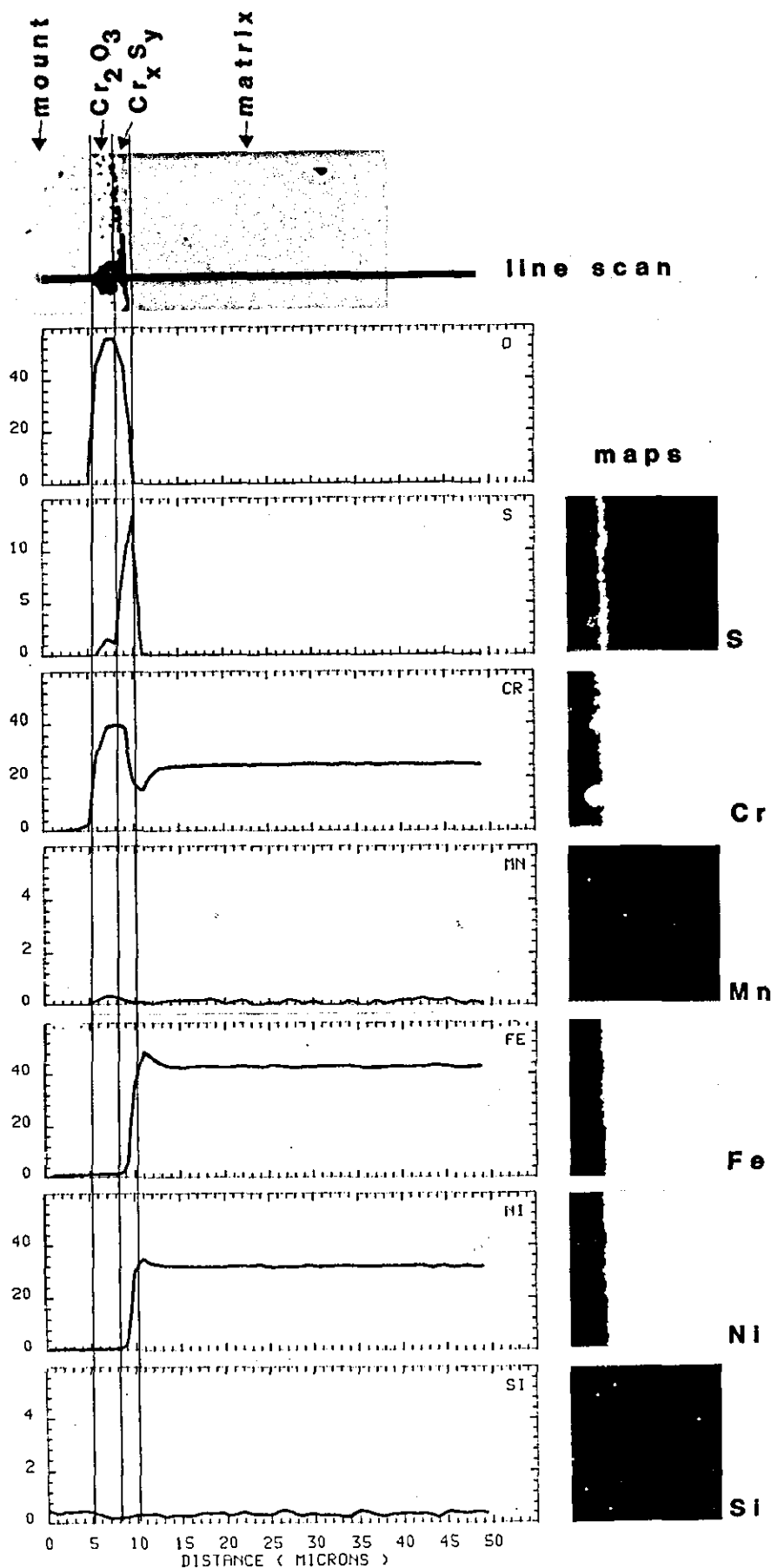


Figure 4.18

EPMA line scan through a filamentary growth and elemental concentration maps on the model 25Cr-35Ni-Fe alloy exposed for 100 hours in the 0.2 % H₂S environment at 800°C (electropolished condition).

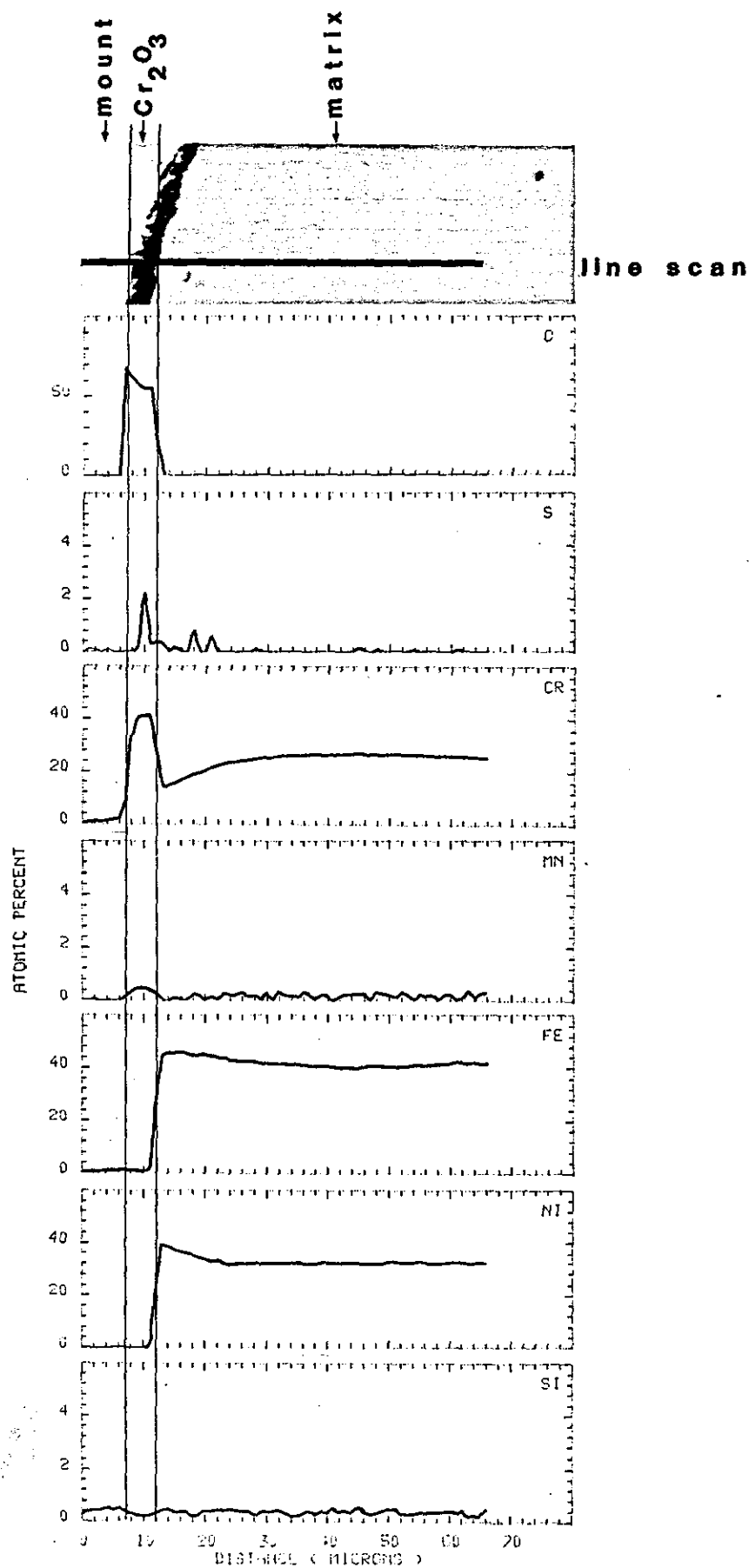


Figure 4.19

EPMA line scan on the model 25Cr-35Ni-Fe alloy exposed for 2000 hours in the 0.2 % H₂S environment at 800°C (electropolished condition).

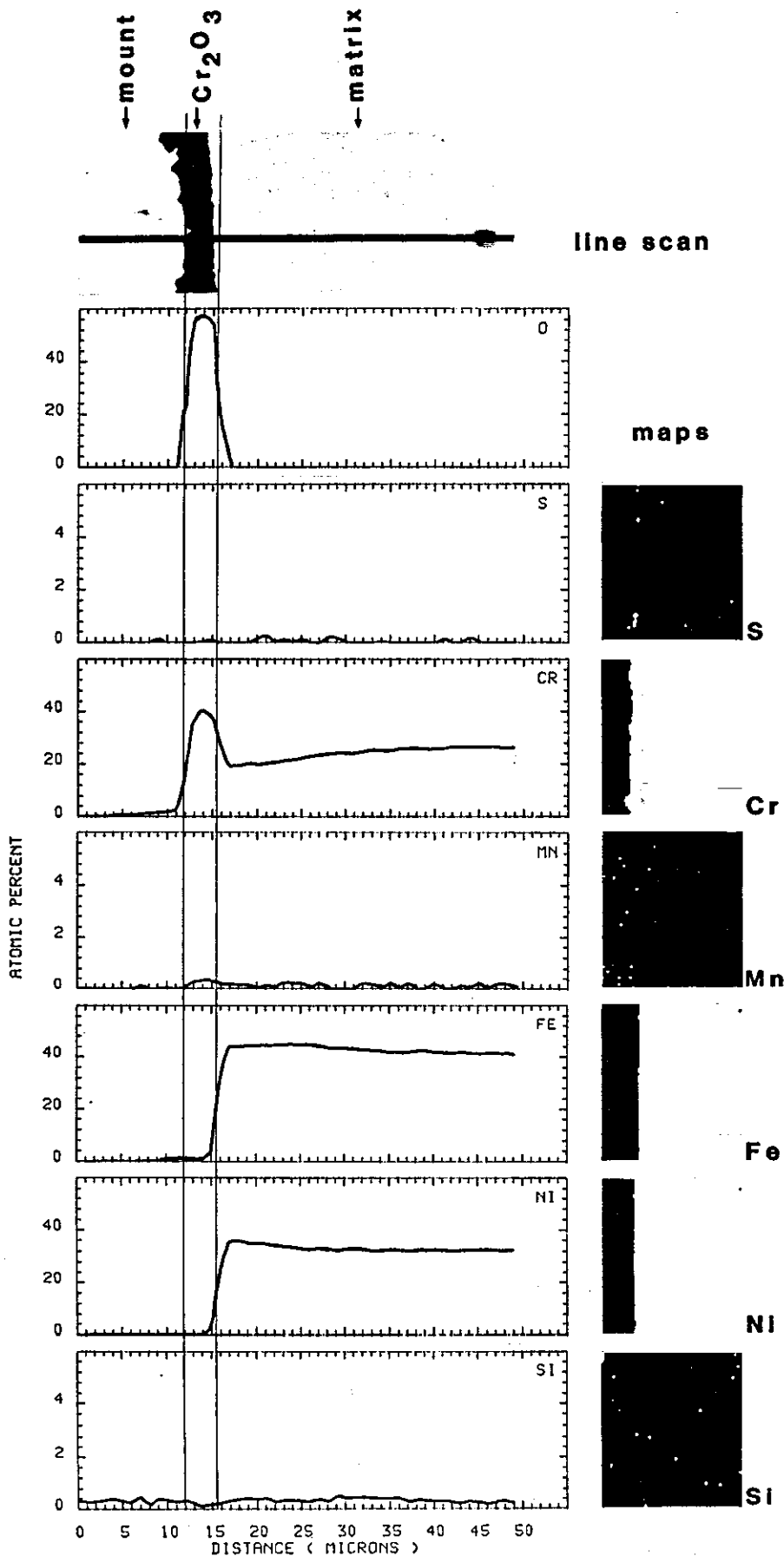


Figure 4.20

EPMA line scan and elemental concentration maps through a normal area of the scale formed on the model 25Cr-35Ni-Fe alloy exposed for 5000 hours in the 0.2 % H₂S environment at 800°C (electropolished condition).

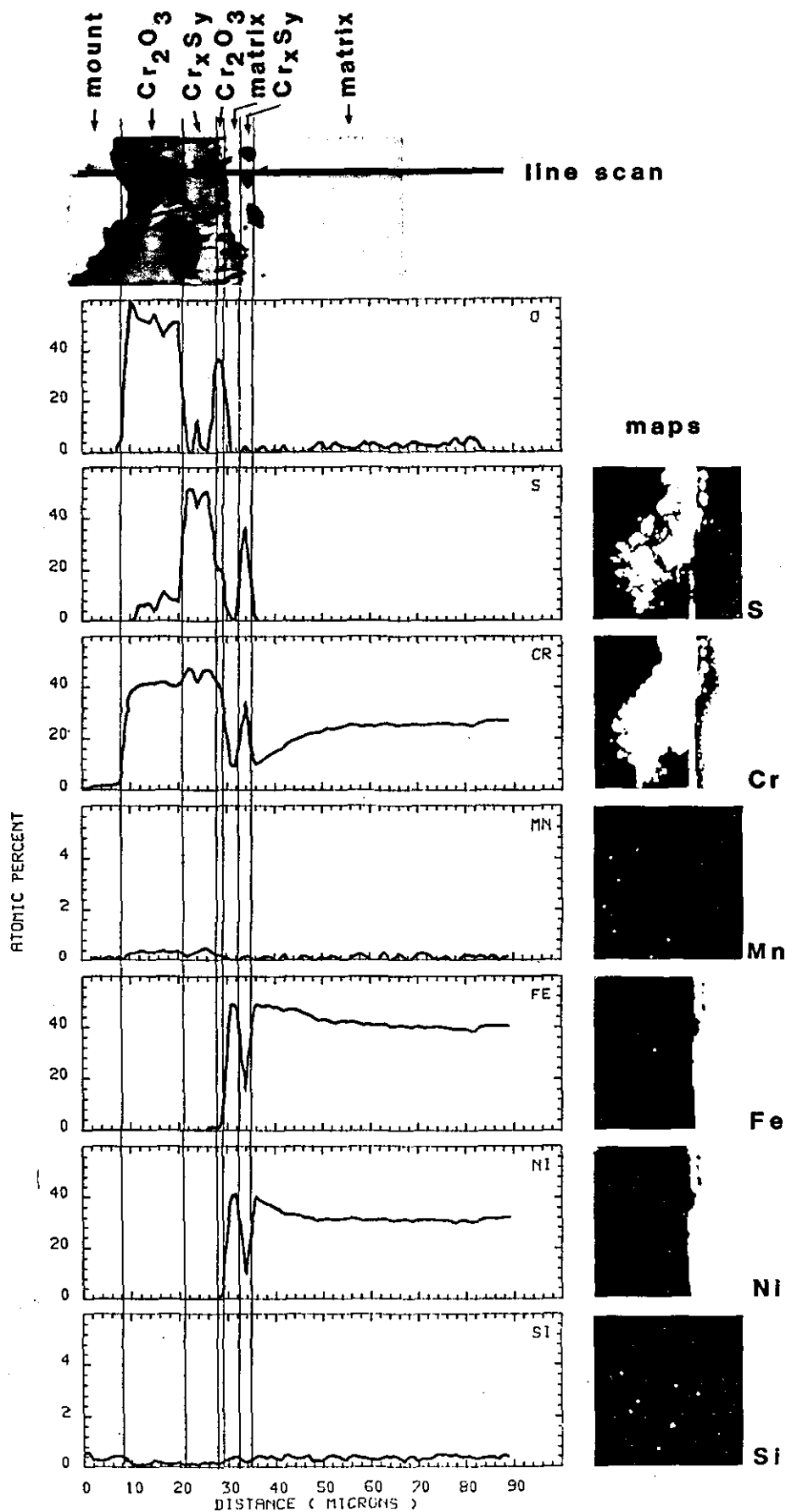


Figure 4.21

EPMA line scan and elemental concentration maps through a blistered area of the scale formed on the model 25Cr-35Ni-Fe alloy exposed for 5000 hours in the 0.2 % H₂S environment at 800°C (electropolished condition).

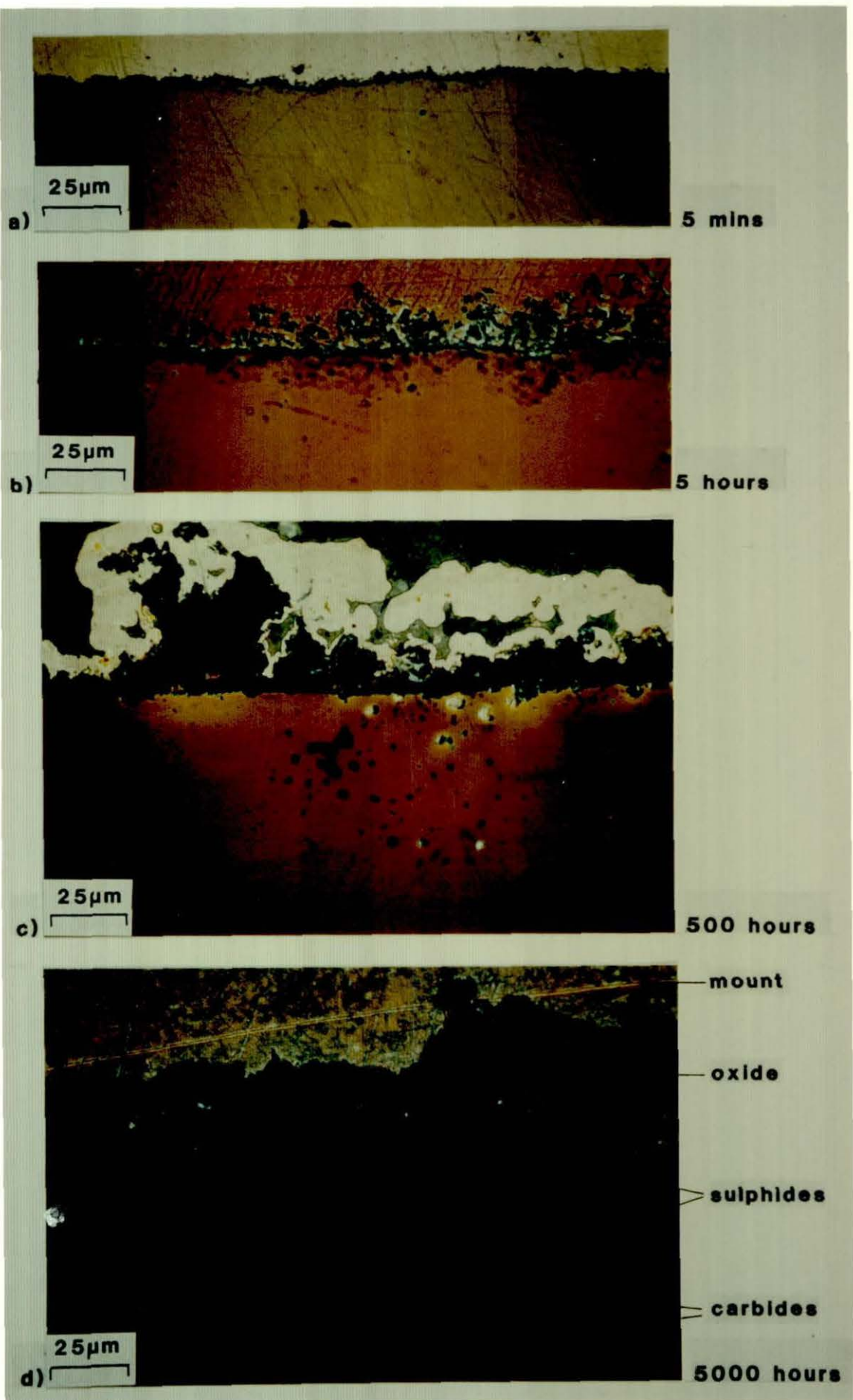


Figure 4.22
Cross-sectional metallographic examination using the Pepperhoff technique for the model 25Cr-35Ni-Fe alloy exposed to the 0.2 % H_2S environment at 800°C (surface-worked '180 grit' condition).

Model 25Cr-35Ni 180 , 0.2% H₂S , 800 deg.C

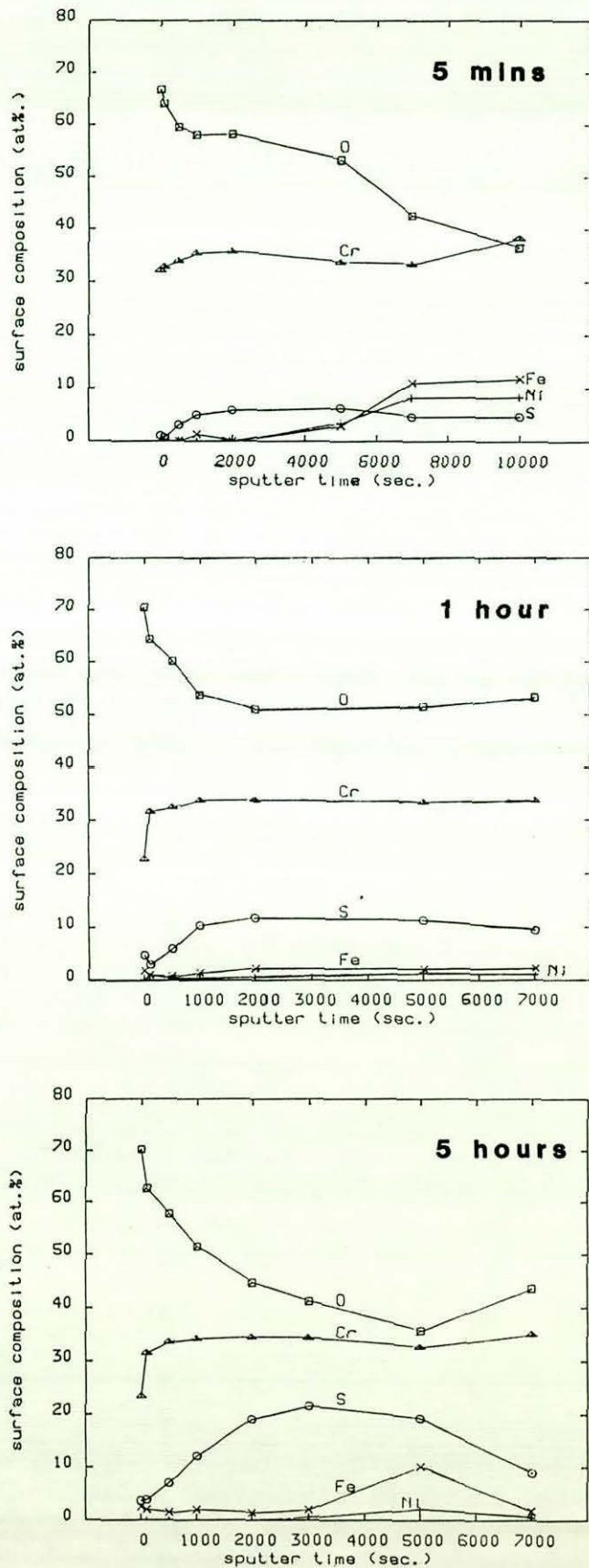


Figure 4.23

ESCA-AUGER analysis of the scale formed on the model 25Cr-35Ni-Fe alloy exposed to the 0.2 % H₂S gas at 800°C (surface-worked '180 grit' condition).

Model 25Cr-35Ni-Fe 180, 0.2% H₂S, 800 deg. C

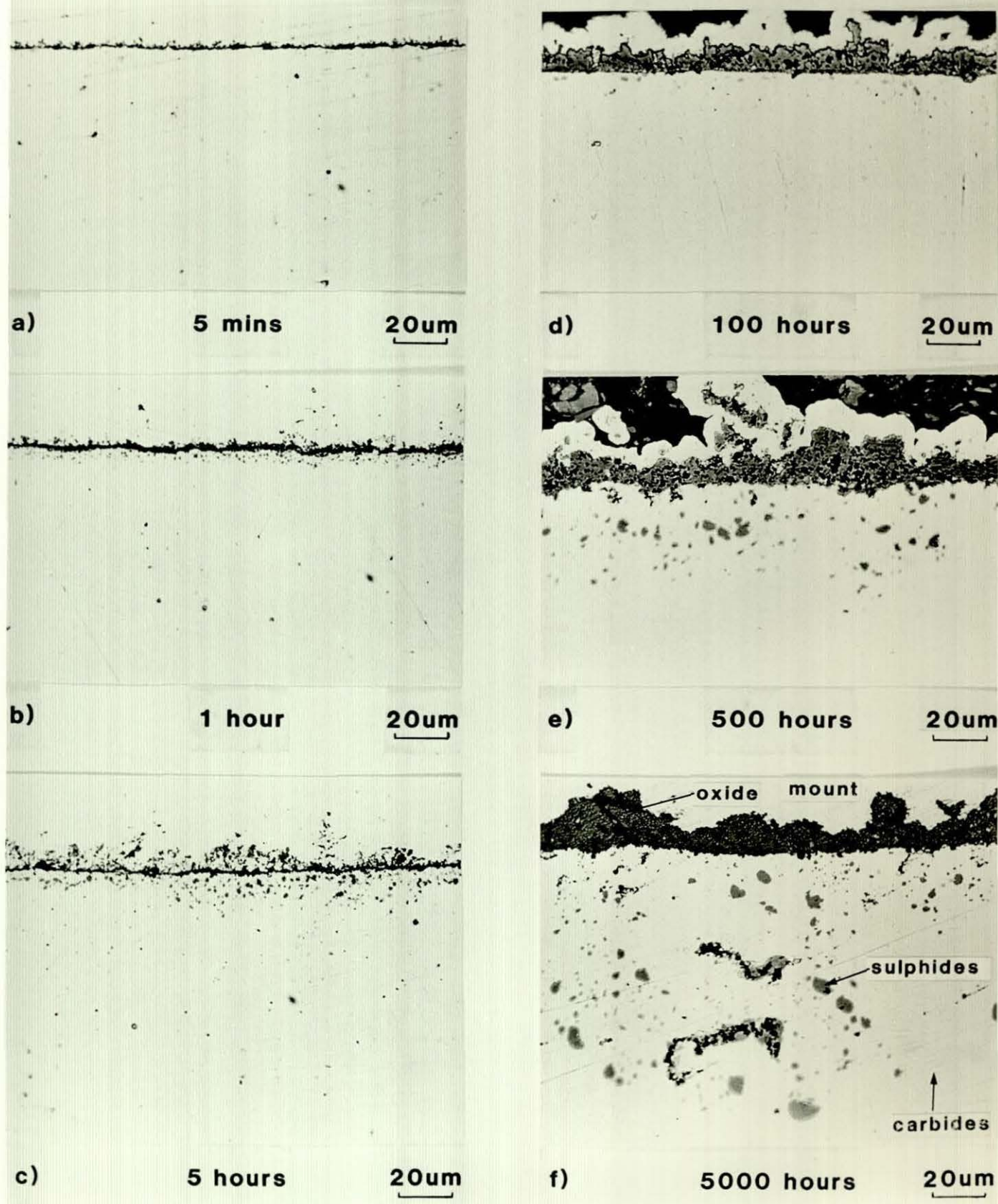
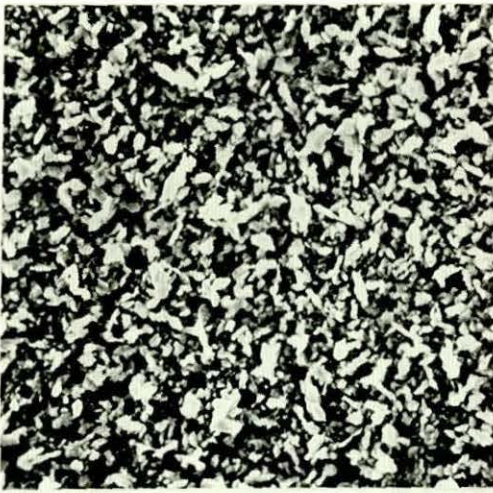


Figure 4.24

Cross-sectional metallographic examination of the model 25Cr-35Ni-Fe alloy exposed to the 0.2 % H₂S environment at 800°C (surface-worked '180 grit' condition).



a) 1 hour 10μm

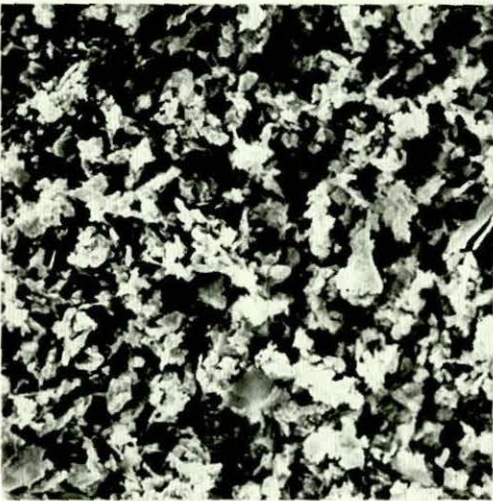
Surface SEM

Model 25Cr-35Ni-Fe

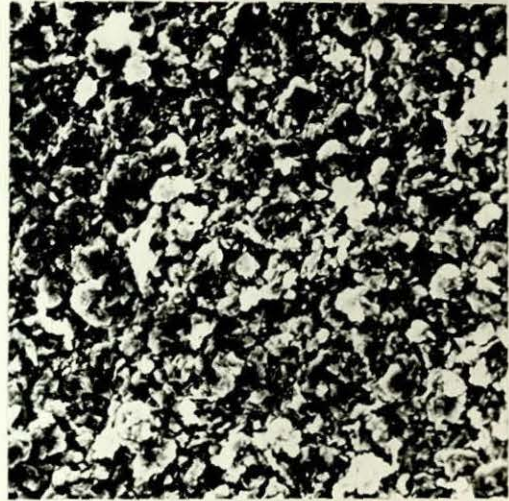
0.2% H₂S environment

800 deg.C

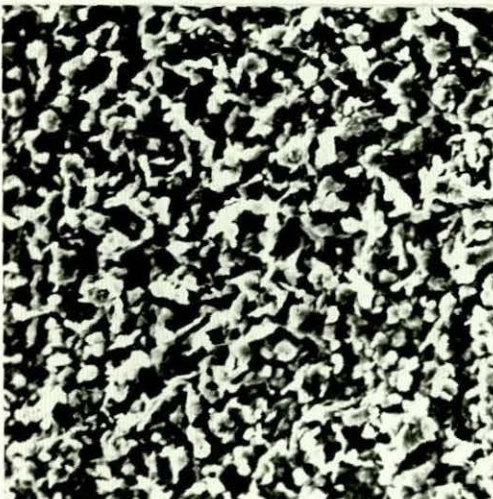
180 grit



b) 5 hours 10μm



d) 1000 hours 10μm



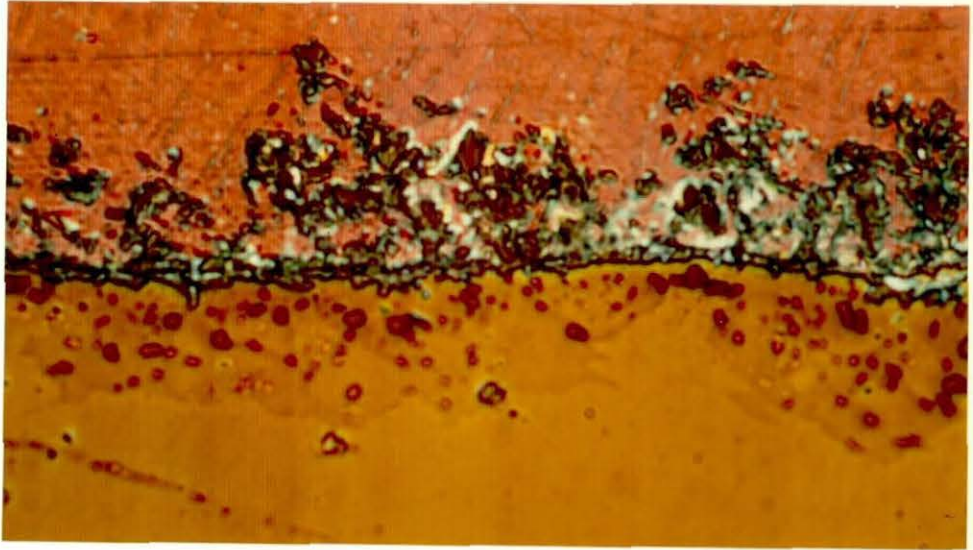
c) 100 hours 10μm



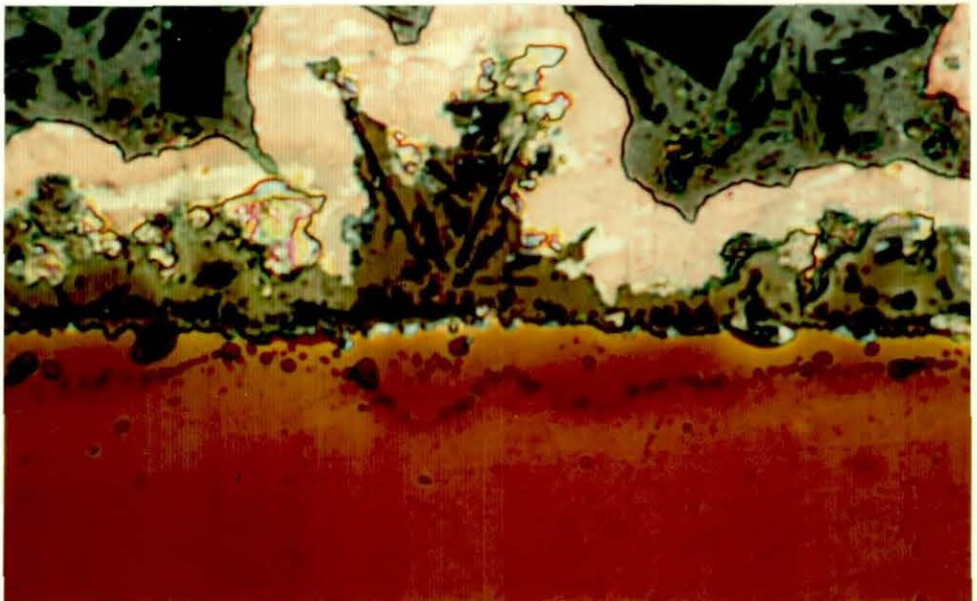
e) 5000 hours 10μm

Figure 4.25

Surface SEM examination of the model 25Cr-35Ni-Fe alloy exposed to the 0.2 % H₂S environment at 800°C (surface-worked '180 grit' condition).



5 hours



500 hours

Figure 4.26
Cross-sectional metallographic examination using the Pepperhoff technique for the model 25Cr-35Ni-Fe alloy exposed to the 0.2 % H_2S environment at 800°C (surface-worked '180 grit' condition).

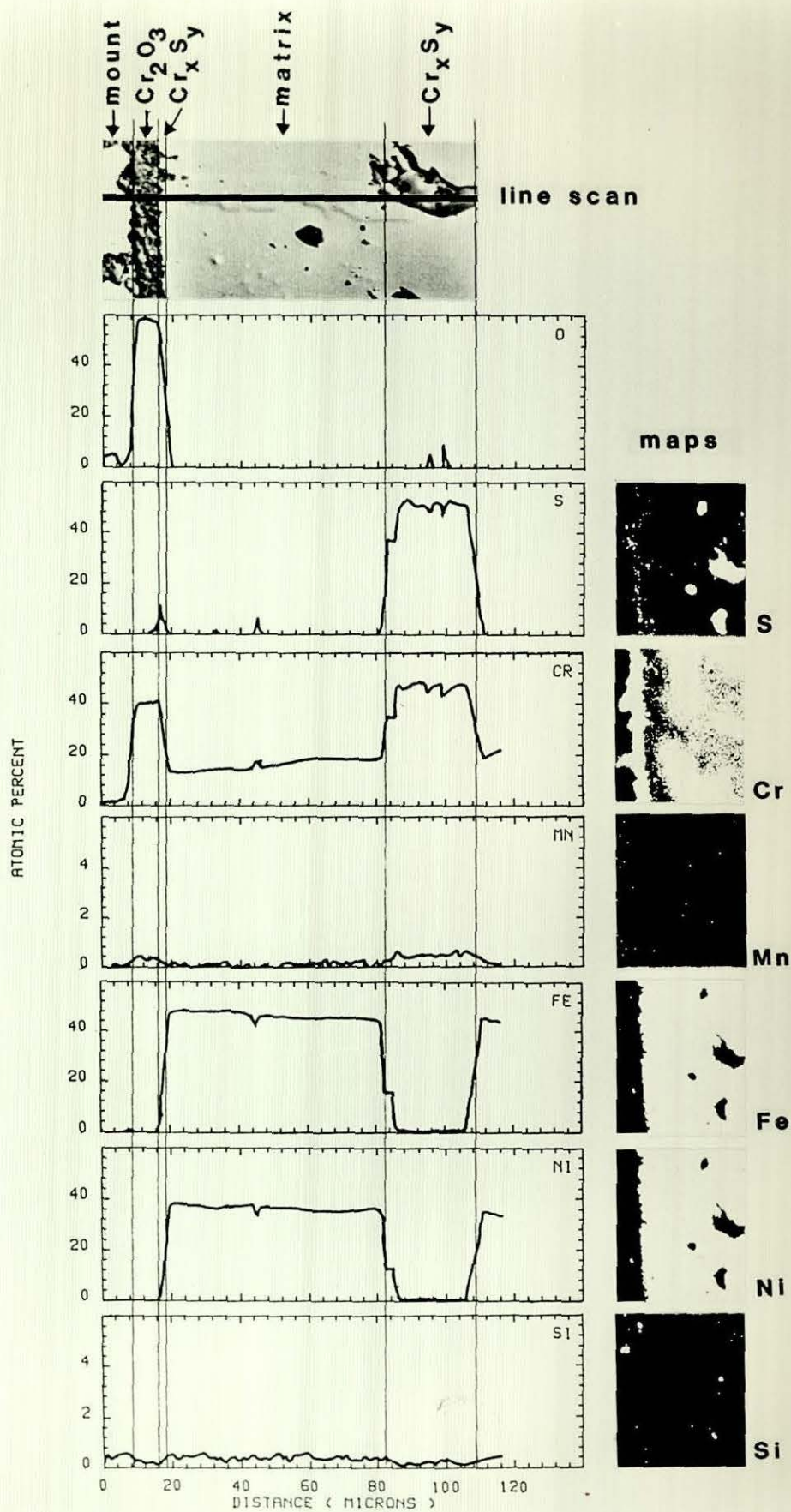


Figure 4.27

EPMA line scan and elemental concentration maps on the model 25Cr-35Ni-Fe alloy exposed for 5000 hours in the 0.2 % H₂S environment.

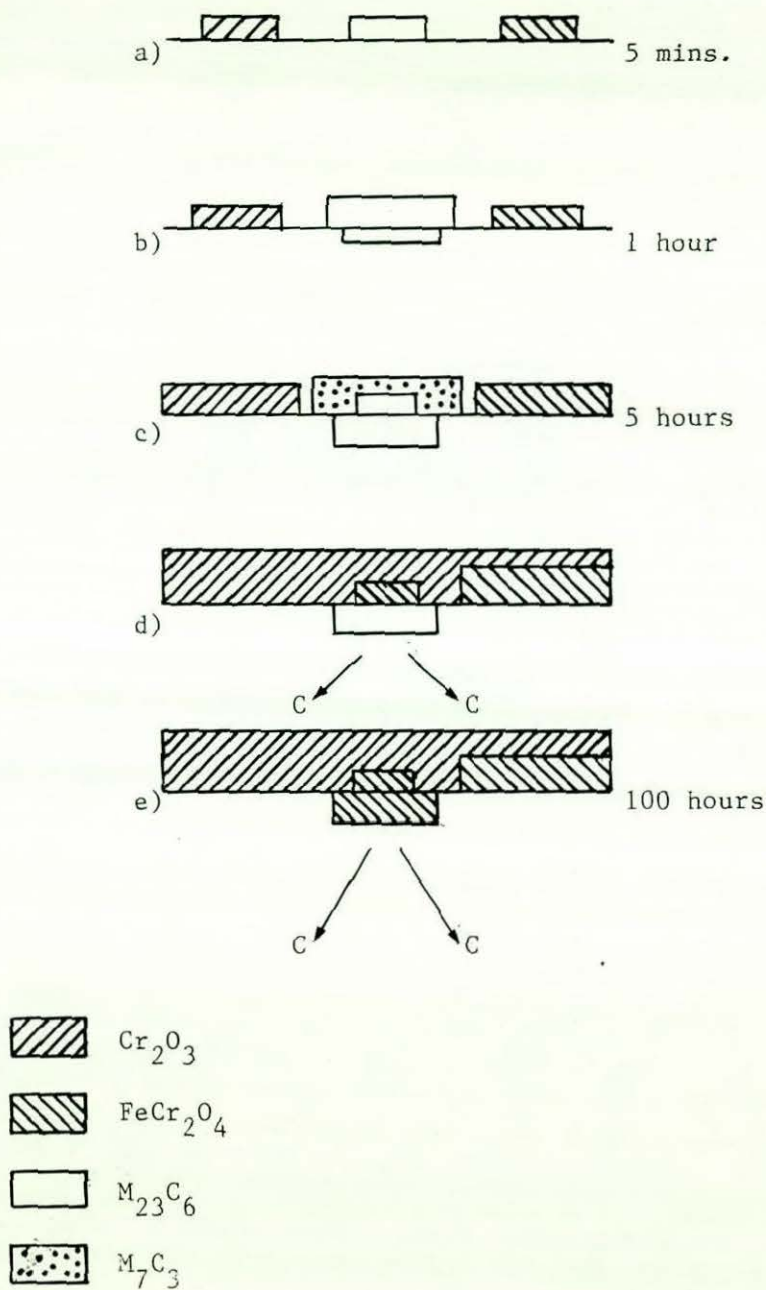


Figure 4.28

Schematic diagram summarizing the early stages of the corrosion behaviour of the model 25Cr-35Ni-Fe alloy in the sulphur-free gas (electropolished condition).

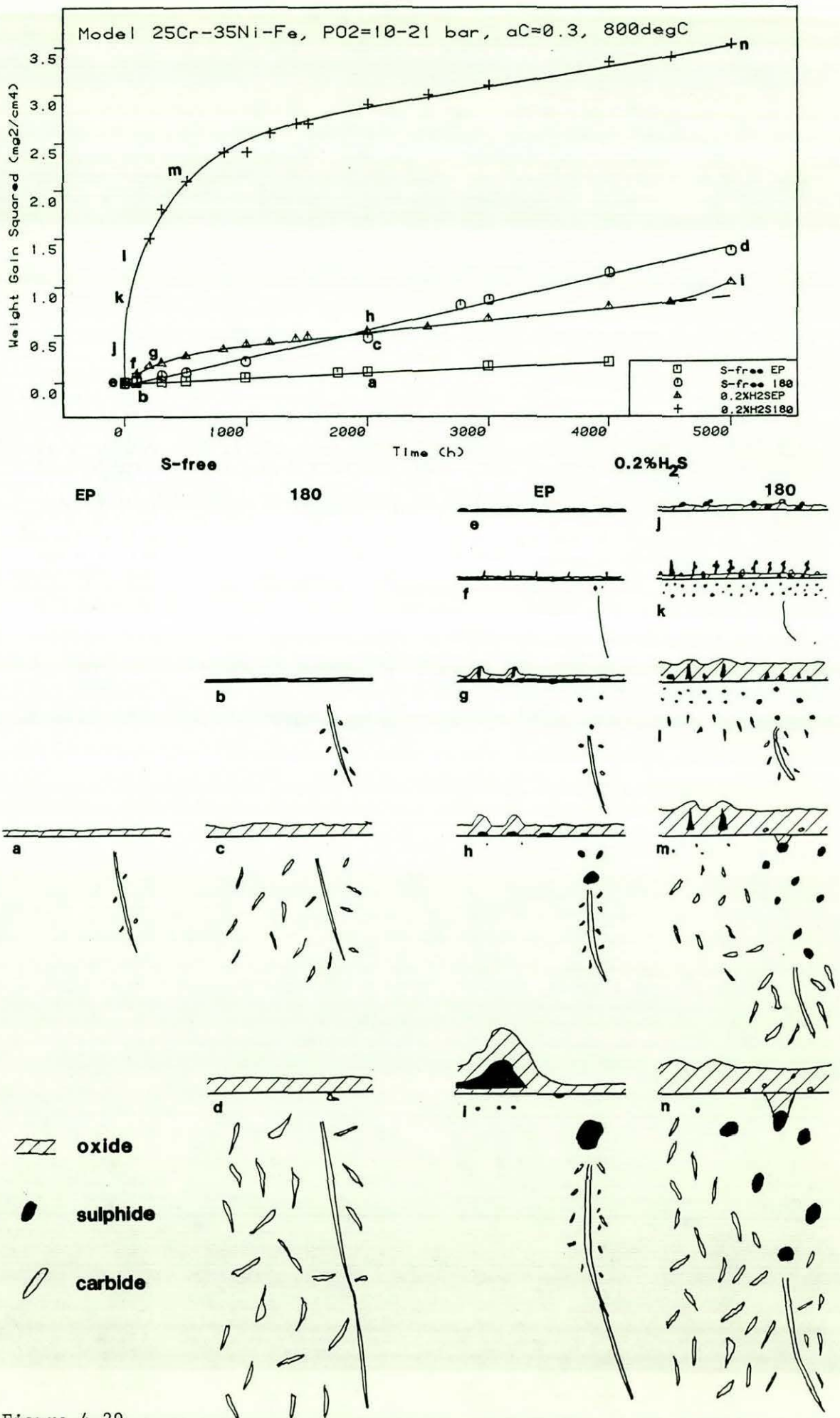


Figure 4.29

Schematic diagram summarizing the corrosion behaviour of the model 25Cr-35Ni-Fe alloy in the oxidation governed regime at 800°C.

4.1.2. HP40Nb

The HP40Nb alloy contained approximately the same amounts of Cr and Ni as the model 25Cr-35Ni-Fe alloy, but with significant additions of 1.22 % Si, 1.11 % Mn, 0.84 % Nb and 0.43 % C. The alloy was centrifugally cast and contained a considerable number of M_7C_3 and MC carbide precipitates.

To establish any microstructural changes due to aging processes, examinations were carried out on the cast material and on specimens annealed in argon at 800°C for 1 hour, 7.25 hours, 100 hours and 2000 hours.

As cast

Cross-sectional examination using the Pepperhoff technique showed that the alloy contained two primary carbides; M_7C_3 and MC, figure 4.30a. The carbides were electrolytically extracted for one hour and subsequently analysed by X-ray diffraction, which confirmed that they were M_7C_3 and MC, table 4.6.

1 hour

Cross-sectional examination using the Pepperhoff technique showed that a large number of very small secondary carbide precipitates had formed in the alloy substrate, figure 4.30b. These tended to be concentrated around the primary carbides. At this stage these carbides were too small to be identified by metallographic techniques. Electrolytic extraction for 1 hour, followed by X-ray powder diffraction analysis detected a new $M_{23}C_6$ carbide phase (table 4.6) and indicated that the relative intensities of the M_7C_3 and MC carbides had decreased, figure 4.31.

7.25 hours

Carbide extraction and subsequent X-ray diffraction analysis indicated that the intensity of the $M_{23}C_6$ carbides had increased, and the intensity of the M_7C_3 reduced. The intensity of MC remained approximately the same, figure 4.31.

100 hours
.....

Cross-sectional examination using the Pepperhoff technique showed that the primary M_7C_3 carbides appeared to have almost totally transformed to $M_{23}C_6$ with just a few traces of M_7C_3 remaining at the centre of the precipitates, figure 4.30c. The secondary $M_{23}C_6$ precipitates had grown and were starting to spread out into the matrix away from the primary carbides. The MC carbides were unchanged. Electrolytic extraction of the carbides followed by X-ray diffraction analysis, confirmed that the primary M_7C_3 carbides had transformed to $M_{23}C_6$ with the carbon released in the process forming $M_{23}C_6$ and a few M_6C secondary carbide precipitates, table 4.6 and figure 4.31.

2000 hours
.....

Cross-sectional examination using the Pepperhoff technique showed that the primary M_7C_3 carbides had totally transformed to $M_{23}C_6$. The MC primary carbides were unchanged and the secondary $M_{23}C_6$ carbides had grown, but were fewer in number, figure 4.30d.

5000 hours
.....

A similar microstructure was present after 5000 hours. The secondary $M_{23}C_6$ carbides had continued to coarsen, figure 4.30e.

Thus in summary the alloy in the as cast condition contained M_7C_3 and MC primary carbide precipitates. As time progressed at 800°C the primary M_7C_3 precipitates transformed to $M_{23}C_6$. The carbon released in the process led to the formation of a large number of secondary $M_{23}C_6$ precipitates and a few M_6C carbides in the alloy substrate. These secondary carbides subsequently grew and became fewer in number.

a. Sulphur-free gas

Kinetic data for the electropolished (EP) and 180 grit (180) surface finishes are presented in figure 4.32. The weight uptake for both surface finishes was small with the electropolished material (0.5 mg/cm²

in 4000 hours) slightly higher than the 180 grit material (0.3 mg/cm^2 in 4000 hours).

Replotting these data as weight-gain squared against time, showed that in the case of the electropolished material the initial corrosion rate was high, but soon slowed down before becoming parabolic after approximately 15 hours, figure 4.33a. The corrosion rate then remained constant at approximately the same rate as the model 25Cr-35Ni-Fe alloy, figure 4.33b. The kinetic rate is given in table 4.7.

In the case of the 180 grit material the corrosion rate was much lower, table 4.7, and parabolic from the start, figure 4.33 a and b.

180 grit condition

Structural analysis examinations were carried out after 5 minutes, 1 hour, 5 hours, 100 hours and 5000 hours.

5 minutes

Surface SEM examination showed that an oxide scale formed on the alloy surface, figure 4.34a. X-ray diffraction using surface reflection indicated that this was a mixture of M_3O_4 and Cr_2O_3 , table 4.8. M_{23}C_6 was also detected, but as no carbide particles were visible on the surface and as the oxide layer very thin, it was concluded that this signal came from carbide precipitates in the alloy. ESCA-AUGER analysis indicated that the oxide layer contained approximately 35-40 % Cr and 5 % Mn, figure 4.35a.

1 hour

Surface SEM examination showed that the oxide layer was similar to before but slightly uneven, figure 4.34b. X-ray diffraction using surface reflection again detected M_3O_4 and Cr_2O_3 , table 4.8. The M_3O_4 lattice parameter indicated that the spinel had the composition MnCr_2O_4 , figure 4.36. The Cr_2O_3 lattice parameter corresponded to pure Cr_2O_3 , figure 4.37.

5 hours
.....

Surface SEM examination again showed that the oxide had a similar appearance to before, figure 4.34c. X-ray diffraction using surface reflection now only detected MnCr_2O_4 , table 4.8. ESCA-AUGER analysis now showed that the amount of Mn in the scale had increased to 15-20 %, whilst the level of Cr had decreased to approximately 25-30 %, figure 4.35b. More importantly a significant amount of Si was now detected at the base of the oxide layer. The peak position indicated that this was present as Si^{4+} . Thus indicating the presence of SiO_2 .

100 hours
.....

Cross-sectional examination showed that a very thin ($< 1 \mu\text{m}$ thick) oxide layer had formed on the alloy surface, figure 4.38b. X-ray diffraction using surface reflection detected only MnCr_2O_4 , table 4.8. The lattice parameter of the oxide spinel indicated that it had a very high Mn content, figure 4.36.

2000 hours
.....

Cross-sectional examination showed that the oxide layer had thickened slightly to $1-2 \mu\text{m}$, figure 4.38c. X-ray diffraction again detected only MnCr_2O_4 . ESCA-AUGER analysis now showed that the oxide layer contained 20-25 % Mn and only 15-20 % Cr, figure 4.35a.

5000 hours
.....

Cross-sectional examination showed that the oxide layer was still only approximately $2 \mu\text{m}$ thick, figure 4.38d. An EPMA line scan taken through the oxide layer indicated that it consisted of 2 layers : an outer layer very rich in Mn and Cr and more significantly an inner layer rich in Si, figure 4.39. X-ray diffraction using surface reflection again detected MnCr_2O_4 , table 4.9, with the high lattice parameter value indicating a high Mn content, figure 4.36.

Thus in summary a continuous layer of MnCr_2O_4 and Cr_2O_3 particles formed on the alloy surface in the initial stages. After approximately 5 hours exposure an inner SiO_2 layer started to form. This started to block off the outward diffusion of Cr into the surface layer, with the result that the Cr_2O_3 was converted to MnCr_2O_4 and the oxide scale consisted of an outer MnCr_2O_4 layer and an inner SiO_2 layer. Mn continued to diffuse into the outer layer, increasing the Mn to Cr ratio, until the inner SiO_2 layer became complete. After approximately 100 hours no further outward diffusion of Mn occurred and the very thin scale consisted of an $\text{Mn}_{1+x}\text{Cr}_{2-x}\text{O}_4$ outer layer and an inner SiO_2 layer. Due to the complex carbide changes within the alloy it was impossible to determine if any carburization due to carbon injection from the gas had occurred.

Electropolished condition

Structural analysis examinations were carried out after 5 minutes, 30 minutes, 1 hour, 5 hours, 100 hours, 2000 hours and 4000 hours.

5 minutes

Surface SEM examination showed that carbides and oxides started to form on the alloy surface and the indigenous primary carbide precipitates, which intersected the surface, started to grow outwards, figure 4.40a. X-ray diffraction using surface reflection detected M_{23}C_6 , M_3O_4 and Cr_2O_3 , table 4.9.

30 minutes

Surface SEM examination showed that the carbide particles on the surface grew rapidly. The indigenous carbides intersecting the surface also continued to grow, figure 4.40b.

1 hour

X-ray diffraction using surface reflection indicated that the surface layer consisted of predominantly M_{23}C_6 , M_3O_4 and small amounts of Cr_2O_3 , table 4.9. The spinel lattice parameter indicated that the oxide spinel was MnCr_2O_4 , figure 4.36. The Cr_2O_3 lattice parameter corresponded to pure Cr_2O_3 , figure 4.37.

5 hours
.....

Surface SEM examination showed that the surface layer had become complete and that the smaller carbides were starting to convert to oxides, figure 4.40c. The primary carbides on the surface still remained. X-ray diffraction analysis indicated that the surface layer contained M_3O_4 , Cr_2O_3 and $M_{23}C_6$, table 4.9.

100 hours
.....

Surface SEM examination showed that all the carbides had been converted to oxides to form an oxide scale, figure 4.40d. The scale was thicker where the primary carbides had been. X-ray diffraction using surface reflection confirmed that the scale now consisted of Cr_2O_3 and M_3O_4 , table 4.9. Again the lattice parameter indicated that the oxide spinel was $MnCr_2O_4$ and the Cr_2O_3 was relatively pure.

2000 hours
.....

Cross-sectional examination showed that the corrosion morphology consisted of an oxide scale, with localized thickening and internal oxidation occurring where the primary $M_{23}C_6$ and MC carbides had been present in the vicinity of the surface, figure 4.38a.

An EPMA line scan taken through one of the normal areas of the scale showed that it consisted of 3 layers : an outer $MnCr_2O_4$ layer, an intermediate Cr_2O_3 layer and an inner layer rich in Si and Cr, figure 4.41. X-ray diffraction using surface reflection confirmed the presence of $MnCr_2O_4$ and Cr_2O_3 , table 4.9. A second line scan taken through a locally thickened area of the scale showed that the same three layered scale was present, figure 4.42. Some Fe and Ni were also detected in the local internal oxide, which was not surprising in view of the fact that this was a former carbide. In both cases traces of Nb were detected in the outer layer of the oxide scale.

4000 hours
.....

X-ray diffraction using surface reflection again detected M_3O_4 and Cr_2O_3 , table 4.9. The lattice parameter of the M_3O_4 had decreased

indicating that it perhaps now contained some Fe in addition to Mn, figure 4.37. The lattice parameter of the Cr_2O_3 phase still corresponded to that of pure Cr_2O_3 , figure 4.36.

Thus in summary in the initial stages Cr_2O_3 , MnCr_2O_4 and M_{23}C_6 formed on the alloy surface and the primary carbides, which intersected the surface, enlarged slightly. The small carbides grew rapidly until the scale became complete. Thermodynamics then determined that only one phase could come to stable equilibrium with the gas and thus the small M_{23}C_6 carbides started to transform to oxides. The carbon released in the process was driven deeper into the alloy substrate. Subsequently the enlarged primary M_{23}C_6 carbides on the surface were also converted to oxides, so that after approximately 100 hours exposure the external scale consisted of a mixture of Cr_2O_3 , MnCr_2O_4 and FeCr_2O_4 . Small amounts of SiO_2 were also starting to form beneath this external scale, however the Si content of the alloy without the assistance of surface working was insufficient to form a complete SiO_2 layer. Thus on subsequent exposure it appeared that the internal oxide became a mixture of SiO_2 and Cr_2O_3 . This allowed both Mn and Cr to diffuse outwards into the external scale. As Mn was the faster diffusing species it tended to concentrate at the scale/gas interface. This led to the oxide scale consisting of an outer MnCr_2O_4 layer, an intermediate Cr_2O_3 layer and an inner layer consisting of a mixture of SiO_2 and Cr_2O_3 . The primary indigenous M_{23}C_6 carbides continued to be converted to oxides resulting in a small amount of localized internal oxidation. The MC carbides remained relatively unattacked.

b. 0.2 % H₂S gas

Kinetic data for the electropolished (EP) and 180 grit (180) surface finishes are presented in figure 4.43. The weight uptake of the 180 grit material (4 mg/cm^2 in 2000 hours) was much larger than the electropolished material (1 mg/cm^2 in 2000 hours). Both these in turn were much higher than those in the sulphur-free gas ($0.1\text{-}0.2 \text{ mg/cm}^2$ in 2000 hours).

Replotting this data as weight gain squared against time showed that in the case of the 180 grit material the corrosion rate was high, but parabolic upto 3000 hours. After this time the corrosion rate slowly started to increase. The curve for the the Model 25Cr-35Ni-Fe alloy is also included in figure 4.44 to emphasize the high corrosion rate of the HP40Nb alloy in this surface condition.

In the case of the electropolished material the corrosion rate was never parabolic, but was much lower and similar to the Model 25Cr-35Ni-Fe alloy. The corrosion rates for both surface finishes are given in table 4.7.

180 grit condition

Structural analysis examinations were carried out after 5 minutes, 1 hour, 5 hours, 100 hours, 500 hours and 5000 hours.

5 minutes
.....

Cross-sectional examination using the Pepperhoff technique showed that the corrosion morphology consisted of a discontinuous layer of oxide and sulphide particles, with a small number of internal sulphide precipitates in the alloy substrate, figure 4.45a.

Surface SEM examination showed that the oxide and sulphide particles tended to be concentrated in clusters on the alloy surface, figure 4.46a. X-ray diffraction analysis using surface reflection indicated that the oxides were a mixture of Cr_2O_3 and M_3O_4 , table 4.40. The spinel lattice parameter was quite large indicating that its

composition was MnCr_2O_4 , figure 4.36. This was confirmed by ESCA-AUGER analysis, which showed that the surface layer contained 34 % Cr and

7 % Mn, figure 4.47. There was no sign of Fe in the surface layer at this stage. Although most of the surface layer was oxide about 2 % S was also detected, which cross-sectional examination using the Pepperhoff technique showed was present in the form of a few discrete sulphide particles, figure 4.45a. X-ray diffraction analysis using surface reflection also detected M_{23}C_6 , but this was attributed to carbides in the alloy substrate.

The alloy substrate contained very small sulphide precipitates upto a depth of 2 μm . There was no localized attack of the carbides at this stage.

Thus in summary a discontinuous surface layer formed, consisting of MnCr_2O_4 , Cr_2O_3 and a few sulphide particles. Some internal sulphide precipitates, formed in the alloy substrate.

1 hour
.....

Surface SEM examinations now showed that the whole surface was covered with a filamentary layer, figure 4.46b. X-ray diffraction analysis using a Guinier camera (which is more sensitive than the normal X-ray diffraction technique used in this study) identified the sulphide particles as M_3S_4 and confirmed the presence of Cr_2O_3 and M_3O_4 .

5 hours
.....

Cross-sectional analysis using the Pepperhoff technique showed that the corrosion morphology consisted of : an oxide scale which contained a considerable number of sulphide particles, a zone of internal sulphide precipitates, and some localized internal attack of the carbides, figure 4.45b.

The surface layer had now developed into a 6 μm oxide thick scale. This scale also contained a large number of sulphide particles. These observations were confirmed by ESCA-AUGER analysis, which showed that the scale now contained upto 22 % S, 10-15 % Fe in addition to 30-40 % O,

25 % Cr and 5 % Mn, figure 4.47b. The sulphides appeared to be concentrated below the oxide. X-ray diffraction using surface reflection also confirmed that the layer contained a mixture of Cr_2O_3 , M_3O_4 and M_3S_4 .

The amount of internal sulphide precipitates had also increased and penetrated deeper (5-6 μm) into the alloy substrate.

Localized attack of the indigenous carbides was now starting to take place. The two types of carbides behaved differently. The $\text{M}_7\text{C}_3/\text{M}_{23}\text{C}_6$ carbides transformed to predominantly oxides which contained some sulphides particles. The MC carbides did not oxidize, but instead acted as nucleation sites for the sulphide precipitates.

Thus it was concluded that the corrosion morphology consisted of a scale containing a mixture of $(\text{Fe,Mn})\text{Cr}_2\text{O}_4$, Cr_2O_3 and $(\text{Fe,Cr})_2\text{S}_4$, a zone of internal (Cr,Mn) rich sulphide precipitates and some localized internal oxidation/sulphidation of the M_{23}C_6 carbide precipitates.

32 hours
.....

Surface SEM examination showed that the outer regions of the scale were becoming coarser, figure 4.46c. ESCA/AUGER analysis indicated that the ratio of Mn to Fe in this region had increased and the amount of S decreased significantly, figure 4.47c. X-ray diffraction using surface reflection again detected M_3O_4 and Cr_2O_3 , table 4.10.

100 hours
.....

Cross-sectional examination showed that the corrosion morphology consisted of : an outer oxide layer, an inner oxide layer, a zone of internal sulphide precipitates and some localized attack of the carbide precipitates.

An EPMA line scan showed that the outer oxide layer consisted of a mixture of $(\text{Mn,Fe})\text{Cr}_2\text{O}_4$, Cr_2O_3 , sulphide particles and some metallic particles rich in Fe and Ni at the original alloy surface, figure 4.48.

X-ray mapping indicated that an inner oxide layer, rich in Si and Cr, had started to form, figure 4.48.

The line scan through an area of localized internal attack showed that this was rich in Si, Cr, Fe and Ni, figure 4.48. The presence of Fe and Ni was not surprising in view of the fact that this was a former $M_{23}C_6/M_7C_3$ carbide. The maximum concentration of sulphur was at the base of this layer and appeared to coincide with an increase in the chromium level, thus indicating the presence of chromium sulphides. These sulphides prevented the Si rich layer from forming a barrier to the outward diffusion of Cr, Fe and Mn.

X-ray mapping indicated that the internal sulphide precipitates were rich in Cr and Mn, figure 4.48. The Cr-content of the alloy substrate in this region was only 10 %.

500 hours
.....

Cross-sectional examination using the Pepperhoff technique showed that the corrosion morphology consisted of : the outer predominantly oxide layer, the inner oxide layer, localized attack of the primary carbides and a zone of internal sulphide precipitates, figure 4.45c.

The outer oxide layer was now 15-20 μm thick and contained considerably fewer sulphides than before.

The inner oxide layer had thickened slightly to 2-3 μm . The localized internal attack of the $M_{23}C_6$ primary carbides consisted of predominantly oxides, however some metallic particles and sulphides were also present in these areas, with the sulphides often occurring at the base of the transformed carbides. These sulphides prevented the Si rich layer from forming a barrier to the outward diffusion of Cr, Fe and Mn.

The internal sulphide precipitates were larger but fewer in number. No small secondary carbide precipitates were present in these Cr-depleted areas of the substrate.

2000 hours
.....

Some spallation of the outer oxide layer has started to take place. X-ray diffraction using surface reflection detected M_3O_4 and Cr_2O_3 , table 4.10.

3000 hours
.....

X-ray diffraction using surface reflection again confirmed the presence of M_3O_4 and Cr_2O_3 , table 4.10. The relative ratio of M_3O_4 to Cr_2O_3 had increased. The lattice parameter of the spinel indicated it had the composition $FeCr_2O_4$, figure 4.36. The Cr_2O_3 lattice parameter still corresponded to that of pure Cr_2O_3 , figure 4.37. X-ray diffraction using a guinea camera confirmed the presence of M_3O_4 and Cr_2O_3 and detected a few traces of M_3S_4 .

5000 hours
.....

Cross-sectional examination using the Pepperhoff technique showed that the corrosion morphology still consisted of : the external oxide layer, the internal oxide layer, a considerable amount of localized internal attack and a few internal sulphide precipitates, figure 4.45d.

An EPMA line scan indicated that the external oxide scale now consisted of two distinct layers; an outer M_3O_4 layer and an inner Cr_2O_3 , figure 4.49. The outer M_3O_4 layer (10 μm thick) contained approximately 11 % Mn and 3 % Fe. The inner Cr_2O_3 layer was much thicker (35 μm). Both layers contained small amounts of sulphur (2-10 %). X-ray diffraction using surface reflection confirmed the presence of M_3O_4 and Cr_2O_3 , table 4.10.

The internal oxide layer was again rich in Si and Cr and contained small amounts of Fe, Ni. The Fe and Ni appeared to be present in the form of metallic particles. The most significantly observation however was the presence of sulphides at the base of this layer which were preventing the SiO_2 from forming a barrier to the outward diffusion of Cr, Fe and Mn.

The localized internal attack of the primary $M_{23}C_6$ carbides had increased dramatically. Cross-sectional examination using the Pepperhoff

technique indicated that the transformed carbides appeared to consist of predominantly oxides, with some sulphides particles often situated at the deepest point of the attack, figure 4.45. An EPMA line scan taken through a transformed carbide indicated that the oxide was rich in Si and Cr around the edges and Cr and Fe in the middle, figure 4.50. This feature can also be seen from the elemental maps, figure 4.49.

The EPMA line scans showed that the Cr-level in the depleted substrate around the areas of localized attack contained only 8 % Cr, figure 4.49. A few sulphides were present in this area, particularly around the MC carbides. The MC carbides were unattacked. No secondary $M_{23}C_6$ carbide precipitates were present in these depleted areas of the substrate. These carbides became visible again when the Cr level of the substrate reached approximately 14 %. This zone contained an increased volume of carbides as a result of the carbon from the transformed carbides been driven deeper into the alloy.

Thus it was concluded that the large amount of localized internal attack was caused by the alloy substrate becoming severely depleted in Cr. The internal carbide precipitates became unstable and transformed rapidly to oxides and sulphides. The excess metal diffused outwards into the external scale. These transformed carbides then started to form continuous stringers which separated islands of depleted alloy substrate from the rest of the alloy. This made it difficult for Cr to diffuse from the bulk of the alloy to replenish the Cr level in the depleted region. Thus more Mn and Fe were incorporated into the external scale. The high diffusion rates of Mn and Fe led to the separation of the external scale into an outer $(Mn,Fe)Cr_2O_4$ layer and an inner Cr_2O_3 layer. Both these layers contained a significant amount of sulphur. A number of sulphides were also present in the internal oxide layer. These prevented a complete SiO_2 layer forming in this region and thus allowed Cr, Fe and Mn to diffuse outwards into the external scale.

Electropolished condition

Structural analysis examinations were carried out after 5 minutes, 1hour, 5 hours, 100 hours and 2000 hours.

5 minutes
.....

Surface SEM examination showed that a number of small oxide and carbide particles formed on the alloy surface, figure 4.51a. The primary carbides increased in size. X-ray diffraction using surface reflection identified the oxides as Cr_2O_3 , M_3O_4 and the carbides as M_{23}C_6 , table 4.11.

1 hour
.....

Surface SEM examination showed that the number of oxide and carbide particles had increased particularly on top of the primary carbides, figure 4.51b. X-ray diffraction using surface reflection again confirmed the presence of Cr_2O_3 , M_3O_4 and M_{23}C_6 , table 4.11. The Cr_2O_3 lattice parameter corresponded to pure Cr_2O_3 , figure 4.37. The spinel lattice parameter indicated that it had the composition MnCr_2O_4 , figure 4.36. No sulphides were detected.

5 hours
.....

Surface SEM examination showed that the oxide and carbide particles had become much coarser, figure 4.51c. X-ray diffraction using surface reflection now detected only Cr_2O_3 and M_3O_4 , indicating that the oxides were starting to overgrow the carbides, table 4.11.

100 hours
.....

X-ray diffraction using surface reflection detected Cr_2O_3 and M_3O_4 , table 4.11. The lattice parameter of the Cr_2O_3 phase corresponded to pure Cr_2O_3 , figure 4.37. The spinel lattice parameter indicated that it had the composition MnCr_2O_4 , figure 4.36.

2000 hours
.....

Cross-sectional examination using the Pepperhoff technique showed that the corrosion morphology consisted of an outer uneven oxide scale, an inner oxide layer, localized internal attack of the M_{23}C_6 carbides and

some internal sulphide precipitates, figure 4.52. For clarity of presentation the description is divided into two areas :

- (i) Areas corresponding to a thick oxide scale and a large amount of localized internal attack.
- (ii) Areas corresponding to a thin outer oxide scale and a large amount of localized internal attack.

- (i) Areas corresponding to a thick oxide scale and a large amount of localized internal attack.

A line scan AB showed that the outer oxide scale consisted of two distinct layers : an outer MnCr_2O_4 layer which contained small amounts of Fe and Nb on the outer surface and an inner Cr_2O_3 layer, figure 4.53. At the time this analysis was carried out difficulties were experienced in separating Nb and S during mapping. Thus the apparent enrichment of S at the scale/gas interface, shown on the elemental map in figure 4.53, is not a genuine feature. The signal came from the Nb, hence tying up with the findings of the line scans.

Localized internal attack occurred where M_{23}C_6 carbides had been in the vicinity of the surface. In these areas the carbides had been converted to a Si, Cr rich oxide which contained Fe, Ni rich metallic particles. Line scan EF, figure 4.54, confirmed that the centre of the transformed M_{23}C_6 carbides were rich in Cr and Fe, whilst the edges were rich in Si. The MC carbides had not been attacked but instead acted as nucleation points for internal sulphide precipitates. The line scan EF indicated that these sulphides were rich in Mn and Cr.

- (ii) Areas corresponding to a thin outer oxide scale and no localized internal attack

Line scan CD, figure 4.55, showed that the oxide scale consisted of 3 layers : an outer MnCr_2O_4 layer, an intermediate Cr_2O_3 layer and an inner layer rich in Si and Cr. All three layers contained little sulphur. The depleted alloy substrate beneath the scale contained approximately 15 % Cr.

Thus in summary the corrosion process was similar but less severe than the '180 grit' material. This was due to lower levels of sulphur becoming incorporated into the oxide layers and alloy substrate.

Summary for HP40Nb

Aging processes

The alloy in the as cast condition contained M_7C_3 and MC primary carbide precipitates. As time progressed at 800°C the primary M_7C_3 precipitates transformed to $M_{23}C_6$. The carbon released in the process led to the formation of a large number of secondary $M_{23}C_6$ precipitates and a few M_6C carbides in the alloy substrate. These secondary carbides subsequently grew and became fewer in number.

Sulphur-free gas '180 grit' condition

The weight uptake was very small with the corrosion rate being parabolic throughout the exposure period, figure 4.56. Surface-working eliminated the influence of the primary M_7C_3 and MC carbides, figure 4.56a. A continuous layer of $MnCr_2O_4$ and Cr_2O_3 particles formed on the alloy surface in the initial stages, figure 4.56b. After approximately 5 hours exposure an inner SiO_2 layer started to form, figure 4.56c. This cut off the outward diffusion of Cr into the surface layer, with the result that the Cr_2O_3 was converted to $MnCr_2O_4$ and hence the oxide scale consisted of an outer $MnCr_2O_4$ layer and an inner SiO_2 layer. Mn continued to diffuse into the outer layer, increasing the Mn to Cr ratio, until the inner SiO_2 layer became complete, figure 4.56d. After approximately 100 hours no further outward diffusion of Mn occurred and the very thin scale consisted of an $Mn_{1+x}Cr_{2-x}O_4$ outer layer and an SiO_2 inner layer, figure 4.56d. The inner SiO_2 layer continued to thicken as time progressed, figure 4.56d. Due to the complex changes in the carbide structure in the alloy it was impossible to determine if any carburization due to carbon injection from the gas had occurred.

Sulphur-free gas electropolished condition

The weight uptake was higher for the work-free electropolished material (figure 4.56) and the corrosion mechanism more complex. In the initial stages Cr_2O_3 , MnCr_2O_4 and M_{23}C_6 formed on the alloy surface, figure 4.56f. The primary carbides also enlarged slightly at the surface, figure 4.56f. After 1/2 hour, the amount of M_{23}C_6 particles on the surface increased significantly, figure 4.56g. The scale became complete after 5 hours, figure 4.56h. Thermodynamics then determined that only one phase could come to stable equilibrium with the gas and thus the small M_{23}C_6 carbides started to transform to oxides, figure 4.56h. The carbon released in this process was driven deeper into the alloy substrate. Subsequently the enlarged primary M_{23}C_6 carbides on the surface were also converted to oxides, so that after 100 hours exposure the external scale consisted of a mixture of Cr_2O_3 , MnCr_2O_4 and FeCr_2O_4 , figure 4.56i. Small amounts of SiO_2 were also starting to form beneath this external scale, however the Si content of this alloy without the assistance of surface working was insufficient to form a complete SiO_2 layer. Thus on subsequent exposure it appeared that the internal oxide became a mixture of SiO_2 and Cr_2O_3 , figure 4.56j. This allowed both Mn and Cr to diffuse outwards into the external scale. As Mn was the faster diffusing species it tended to concentrate at the scale/gas interface and in turn led to the formation of an outer MnCr_2O_4 layer and an inner Cr_2O_3 layer, figure 4.56j. The primary indigenous M_{23}C_6 carbides continued to be converted to oxides resulting in a small amount of localized internal oxidation. The MC carbides remained relatively unattacked.

0.2 % H_2S '180 grit' condition

The corrosion behaviour of the HP40Nb alloy in the 0.2 % H_2S gas can be summarised in a number of stages, figure 4.57.

- Stage 1 (5 minutes)

A surface layer containing Cr_2O_3 , MnCr_2O_4 and a few chromium rich sulphides formed on the alloy surface, figure 4.57b. Some internal sulphide precipitates, rich in Cr and Mn also formed in the alloy substrate.

- Stage 2 (1 hour)

The amount of sulphides in the surface layer and in the alloy substrate increased. The surface layer containing Cr_2O_3 , MnCr_2O_4 and chromium rich sulphides became complete, figure 4.47c.

- Stage 3 (5 hours)

The oxides in the surface layer overgrew the sulphides, figure 4.57d. The internal $\text{M}_7\text{C}_3/\text{M}_{23}\text{C}_6$ primary carbides in the vicinity of the surface started to transform to Cr-rich oxides and sulphides. These sulphides tended to be present at the base of the transformed carbides.

- Stage 4 (100-500 hours)

An inner layer started to form which consisted of a mixture of SiO_2 , Cr_2O_3 , FeCr_2O_4 and chromium sulphides, figure 4.57e. The presence of these sulphides prevented the SiO_2 from forming a barrier to the outward diffusion of Cr, Mn and Fe. The internal M_{23}C_6 carbides continued to transform to oxides and sulphides. The structure of these transformed carbides was similar to the inner layer. The sulphides which had been present in the external surface layer started to transform to oxides and metallic particles, with the sulphur released diffusing into the inner layer and the transformed carbides. A certain amount of spallation of the external layer started to take place.

- Stage 5 (3000-5000 hours)

After approximately 3000 hours a significant increase in weight uptake started to take place. This was attributed to the alloy substrate becoming severely depleted in Cr. The internal carbide precipitates became thermodynamically unstable and transformed rapidly to oxides and sulphides, figure 4.57f, with the excess metal diffusing outwards into the external layer. These transformed carbides then started to form continuous stringers which separated islands of depleted alloy substrate from the rest of the alloy. This made it difficult for Cr to diffuse from the bulk of the alloy to replenish the Cr level in the depleted region. Thus more Mn and Fe were incorporated into the external layer. The high diffusion rates of Mn and Fe led to the separation of the external scale into an outer $(\text{MnFe})\text{Cr}_2\text{O}_4$ layer and an inner Cr_2O_3 layer. Both these layers

contained a significant amount of sulphur. Sulphides were also present in the internal Si/Cr rich layer. These prevented the SiO_2 from forming a barrier to the outward diffusion of Cr, Fe and Mn in the external scale.

0.2 % H_2S electropolished condition

The corrosion process was similar but less severe than the '180 grit' material, figure 4.57h-i. This was due to lower levels of sulphur becoming incorporated into the oxide layers and alloy substrate.

Exposure Time	Phase Identified (Intensity/Parameter A)			
	M_7C_3	MC	$M_{23}C_6$	M_6C
As cast	95/14.000-4.515	60/4.442	-	-
1 hour	60/14.010-4.520	20/4.443	10/10.623	-
7.5 hours	47/14.006-4.514	35/4.441	51/10.608	-
100 hours	-	31/4.436	98/10.629	10/11.253

Table 4.6

X-ray diffraction data for carbides extracted from HP40Nb after annealing in argon at 800°C.

Environment	Surface Finish	Reaction Rate Constant ($\text{mg}^2\text{cm}^{-4}\text{h}^{-1}$)
Sulphur free	EP	5.0×10^{-5}
	180	1.7×10^{-5}
$p\text{S}_2 = 10^{-9}$ bar	EP	5.4×10^{-4} (not parabolic)
	180	7.0×10^{-3}

Table 4.7

Reaction rate constants for HP40Nb at 800°C ($p\text{O}_2 = 10^{-21}$ bar, $a_c = 0.3$).

Exposure time	Phases Identified (Intensity/Parameter A)					
	Austenite	Cr ₂ O ₃	M ₃ O ₄	M ₃ S ₄	M ₂₃ C ₆	MC
5 mins	186/3.587	2/-	2/-	-	10/10.592	-
1 hour	206/3.585	2/-	4/8.444	-	10/10.595	-
5 hours	181/3.584	-	4/-	-	10/10.615	-
100 hours	205/3.584	-	7/8.468	-	15/10.619	-
2000 hours	186/3.583	-	14/8.463	-	12/10.632	11/4.409
5000 hours	192/3.583	-	17/8.474	-	12/10.637	12/4.447

Table 4.8

X-ray diffraction data for HP40Nb exposed to the sulphur-free environment at 800°C ($pO_2 = 10^{-21}$ bar, $a_c = 0.3$). Surface worked '180 grit' condition.

Exposure time	Phases Identified (Intensity/Parameter A)					
	Austenite	Cr ₂ O ₃	M ₃ O ₄	M ₃ S ₄	M ₂₃ C ₆	MC
5 mins	71/3.587	1/-	1/-	-	7/10.590	-
1 hour	320/3.591	1/4.954-13.584	14/8.422	-	10/10.604	-
5 hours	77/3.587	7/4.946-13.609	8/8.410	-	12/10.589	-
100 hours	101/3.585	8/4.960-13.624	9/8.444	-	-	-
2000 hours	70/3.583	9/4.948-13.626	18/8.438	-	-	-
4000 hours	115/3.583	9/4.954-13.606	20/8.429	-	-	-

Table 4.9

X-ray diffraction data for HP40Nb exposed to the sulphur-free environment at 800°C ($p_{O_2} = 10^{-21}$ bar, $a_c = 0.3$). Electropolished condition.

Exposure time	Phases Identified (Intensity/Parameter A)					
	Austenite	Cr ₂ O ₃	M ₃ O ₄	M ₃ S ₄	M ₂₃ C ₆	MC
5 mins	175/3.588	3/4.949-13.572	3/8.428	-	7/10.501	-
5 hours	81/3.585	8/4.955-13.601	12/8.394	3/9.975	-	-
32 hours	85/3.586	24/4.966-13.602	17/8.406	-	-	-
2000 hours	15/3.587	11/4.953-13.584	27/8.420	-	-	-
3000 hours	25/3.588	6/4.962-13.595	35/8.407	-	-	-
5000 hours	-	8/4.958-13.593	34/8.414	-	-	-

Table 4.10

X-ray diffraction data for HP40Nb exposed to the 0.2 % H₂S environment at 800°C (pO₂ = 10⁻²¹ bar, pS₂ = 10⁻⁹ bar, a_c = 0.3). Surface worked '180 grit' condition.

Exposure time	Phases Identified (Intensity/Parameter A)					
	Austenite	Cr ₂ O ₃	M ₃ O ₄	M ₃ S ₄	M ₂₃ C ₆	MC
5 mins	196/3.580	1/4.954-13.584	1/8.291	-	6/10.595	-
1 hour	195/3.588	3/4.949-13.619	5/8.467	-	6/10.620	-
5 hours	177/3.584	8/4.955-13.586	6/8.410	-	-	-
100 hours	60/3.583	22/4.959-13.586	18/8.401	-	-	-
2000 hours	87/3.583	14/4.956-13.597	25/8.422	-	-	-

Table 4.11

X-ray diffraction data for HP40Nb exposed to the 0.2 % H₂S environment at 800°C (pO₂ = 10⁻²¹ bar, pS₂ = 10⁻⁹ bar, a_c = 0.3). Electropolished condition.

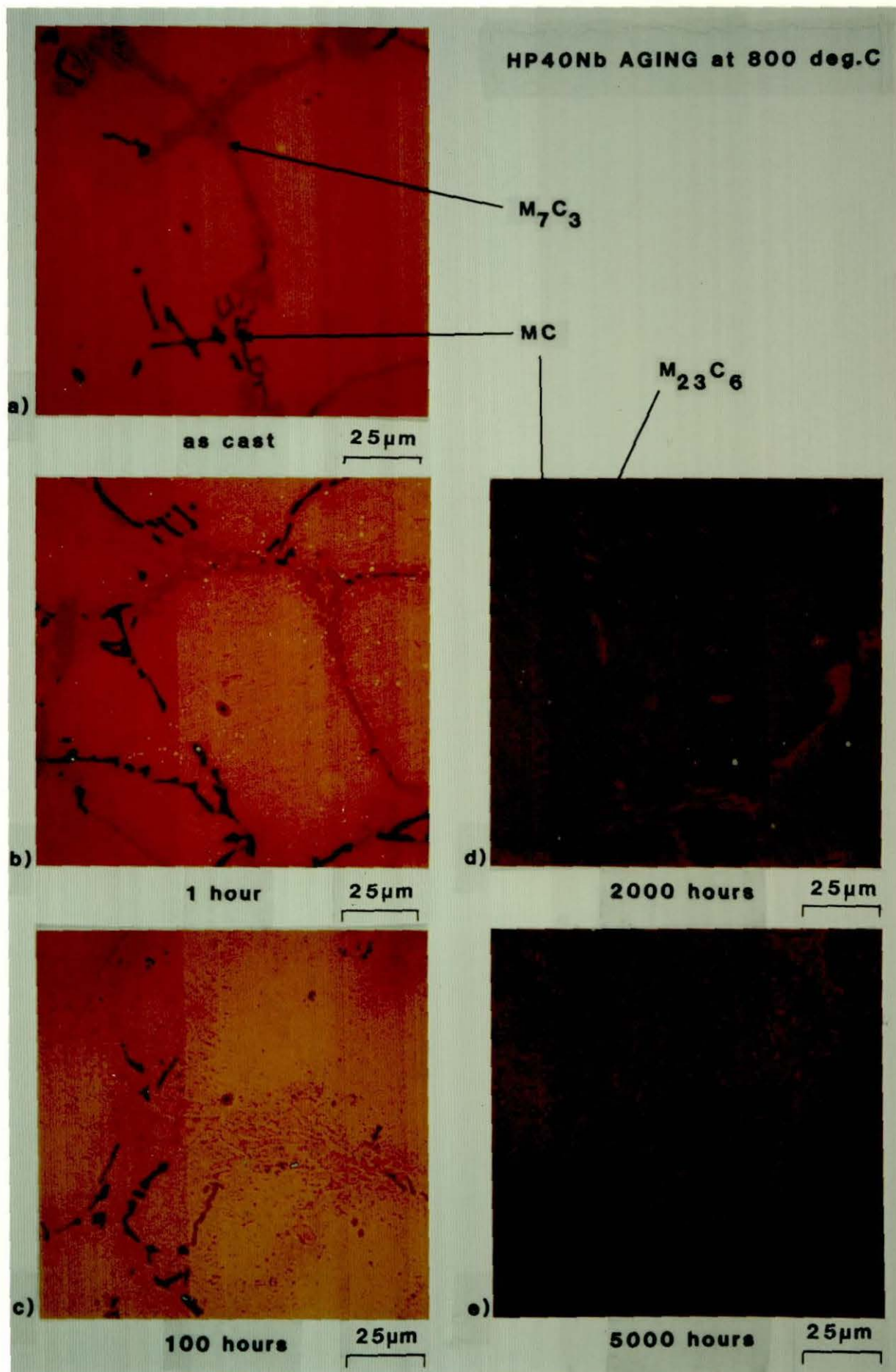


Figure 4.30

Cross-sectional metallographic examinations using the Pepperhoff technique to show changes in the carbide structures in HP40Nb alloy which result from aging processes at 800°C.

HP40Nb Carbide Transformations

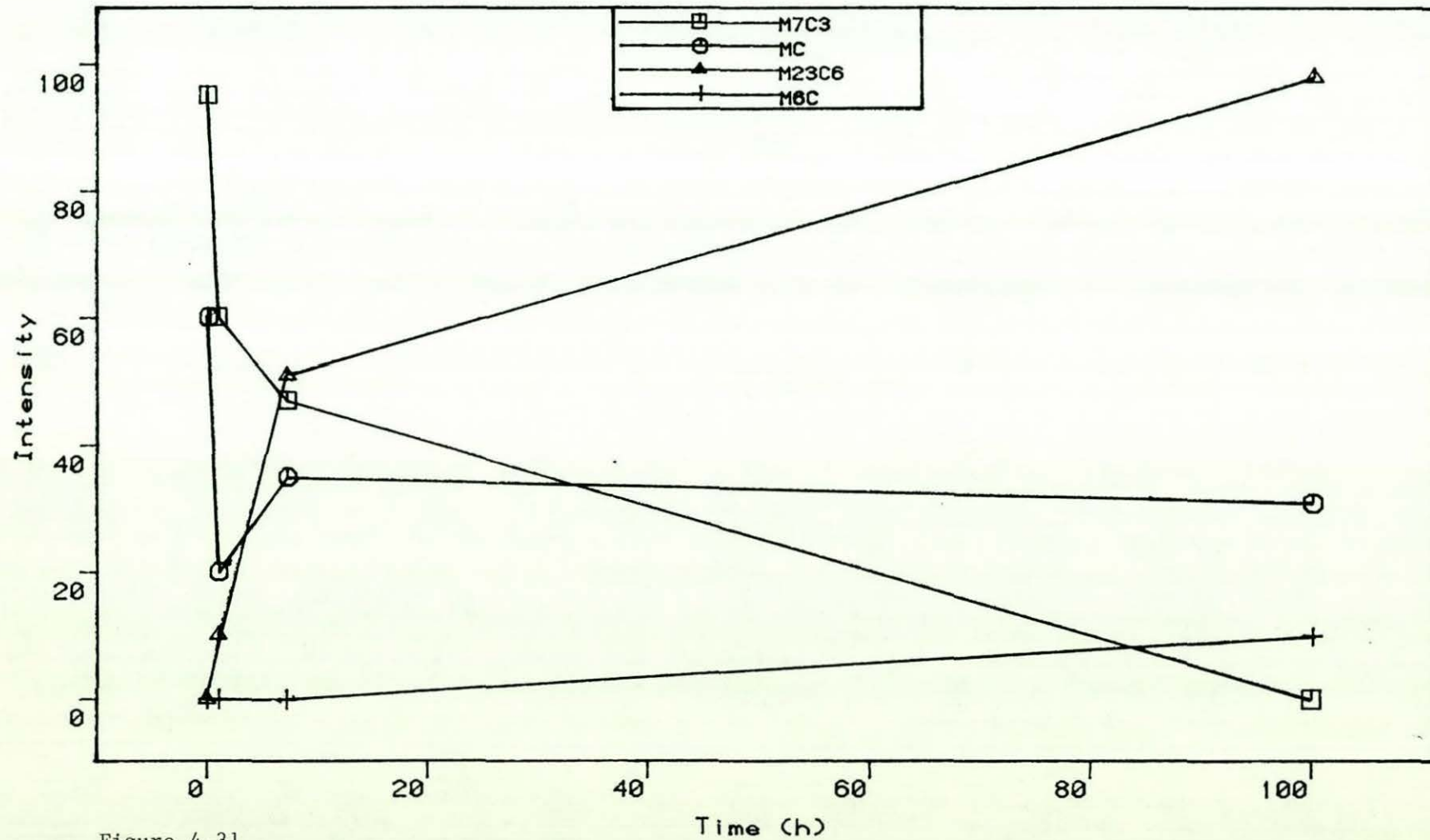


Figure 4.31

Plots of the intensity of the various carbides detected by X-ray diffraction after extraction from the HP40Nb alloy annealed in argon at 800°C.

HP40Nb, PO₂=10⁻²¹ bar, aC=0.3, 800degC

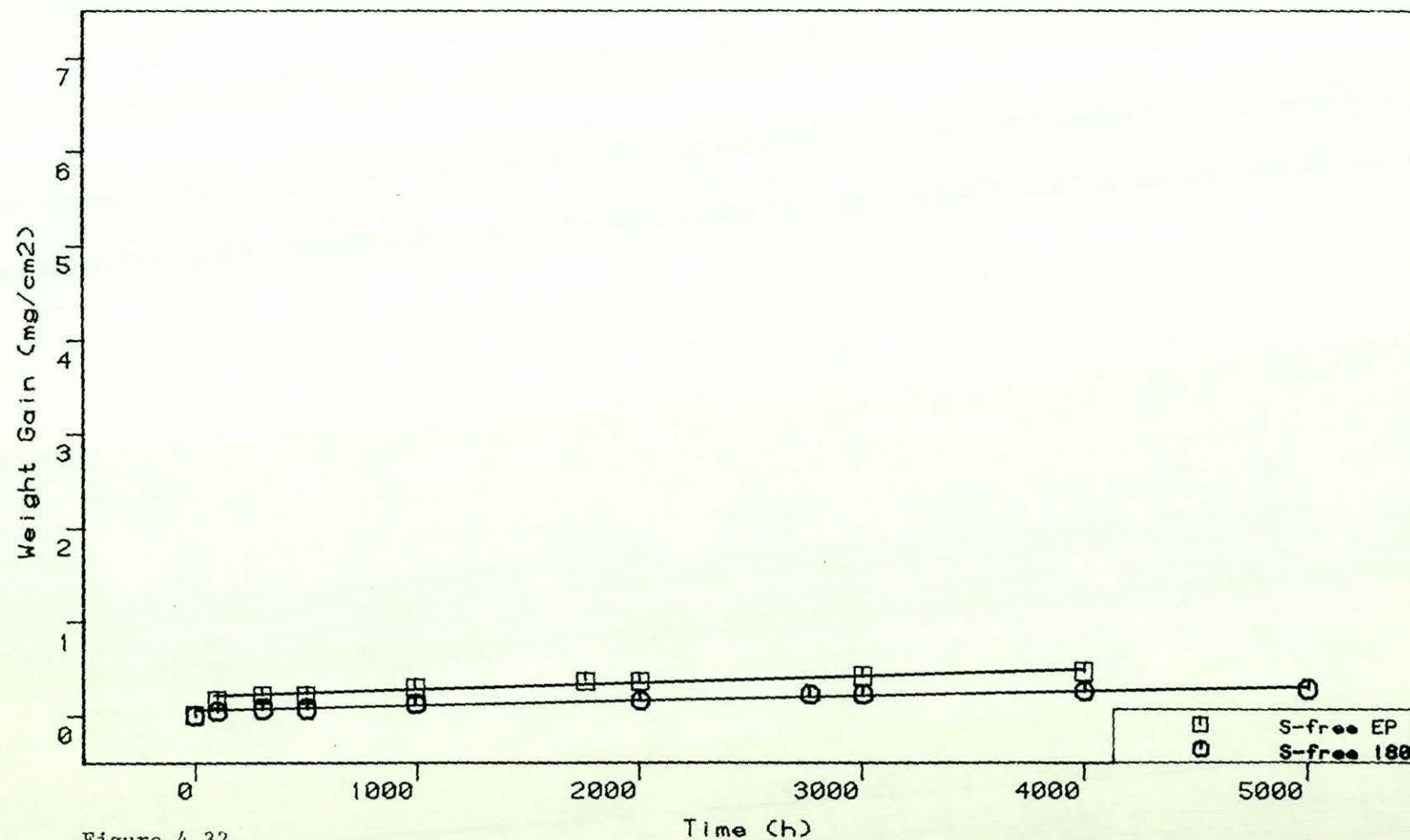


Figure 4.32

Kinetic data for the HP40Nb alloy exposed to the sulphur-free gas at 800°C.

HP40Nb, PO₂=10-21 bar, aC=0.3, 800degC.

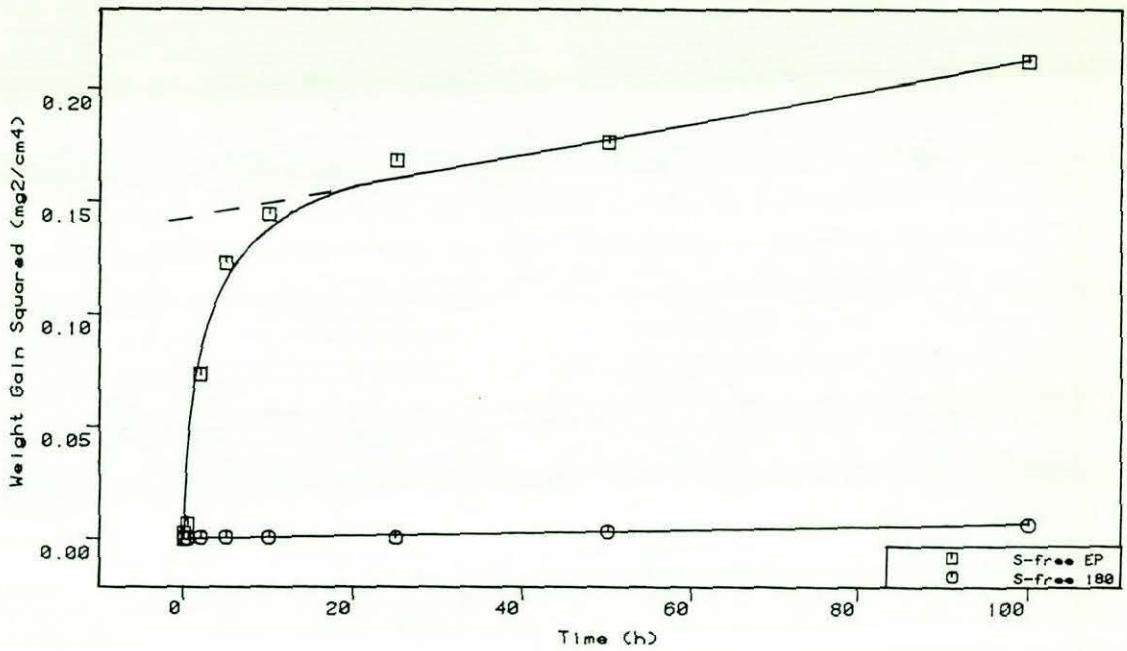


Figure 4.33a

Plots of weight gain squared against time for HP40Nb short-term exposures in the sulphur-free gas at 800°C.

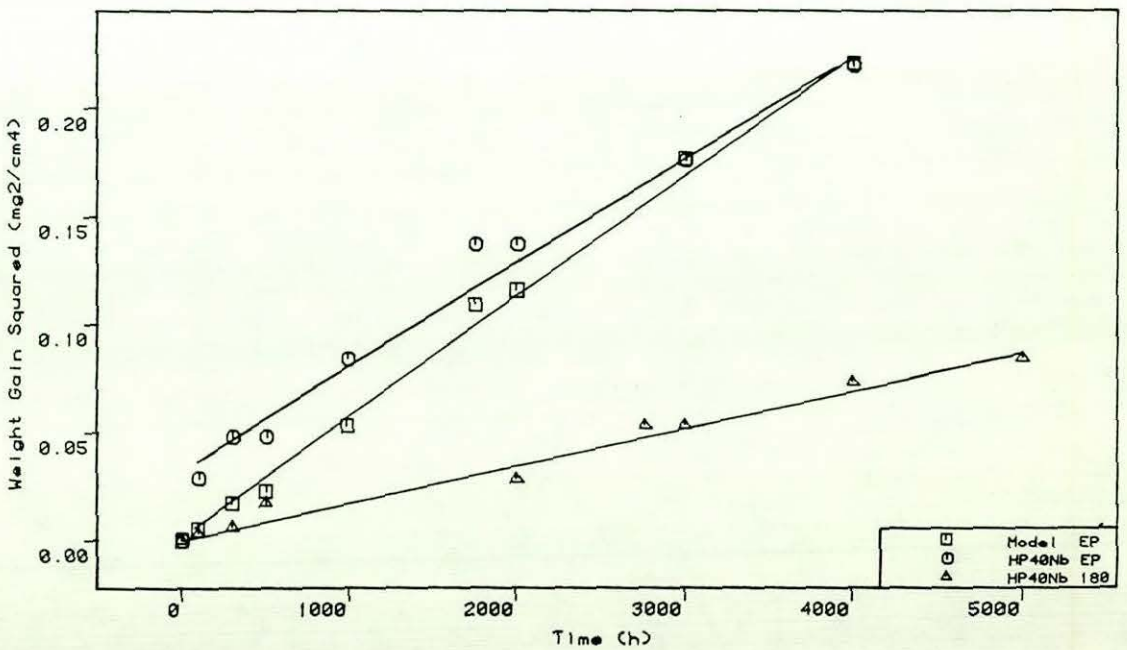
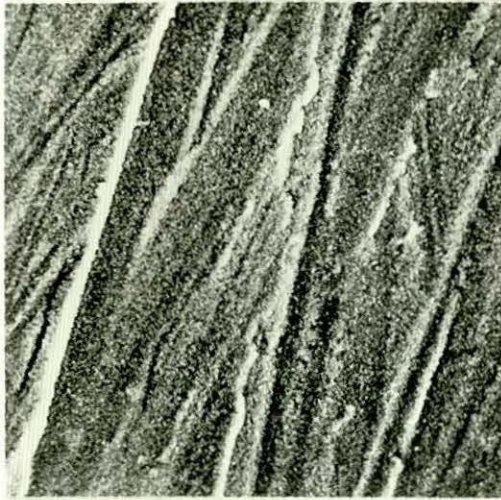


Figure 4.33b

Plots of weight gain squared against time which compare the corrosion behaviour of the model 25Cr-35Ni-Fe alloy and HP40Nb in the sulphur-free gas at 800°C.



a) 5 mins 10µm

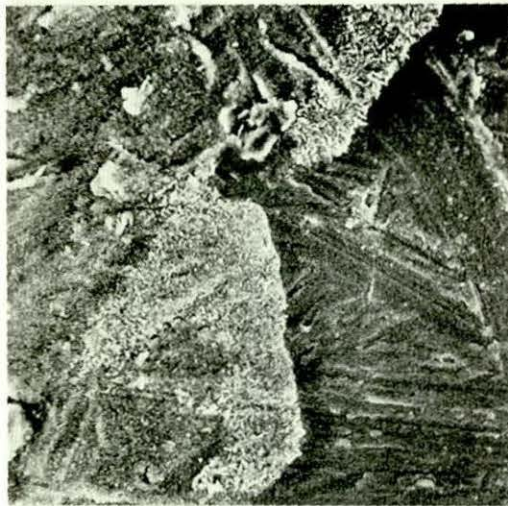
Surface SEM

HP40Nb

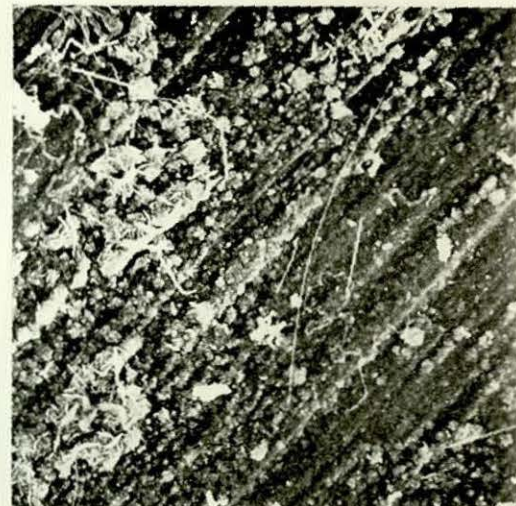
S-free environment

800 deg.C

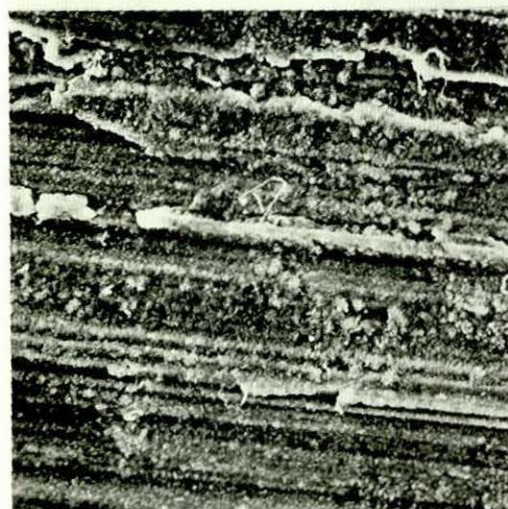
180 grit



b) 1 hour 10µm



d) 2000 hours 10µm



c) 100 hours 10µm



e) 5000 hours 10µm

Figure 4.34

Surface SEM examination of the HP40Nb alloy exposed to the sulphur-free gas at 800°C (surface worked '180 grit' condition).

HP40Nb 180 , S-free , 800 deg.C

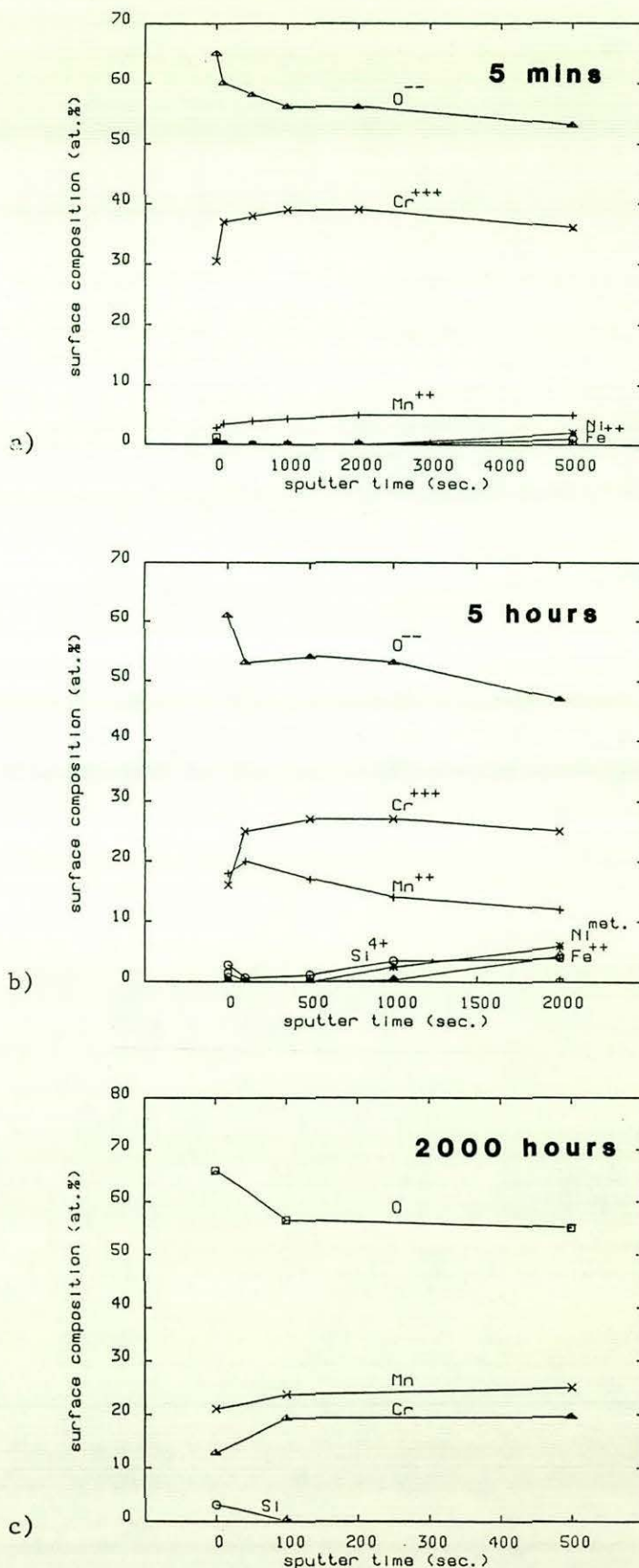


Figure 4.35

ESCA-AUGER analysis of the scale formed on the HP40Nb alloy exposed to the sulphur-free gas at 800°C (surface-worked '180 grit' condition).

HP40Nb, Oxide Spinel Lattice Parameters

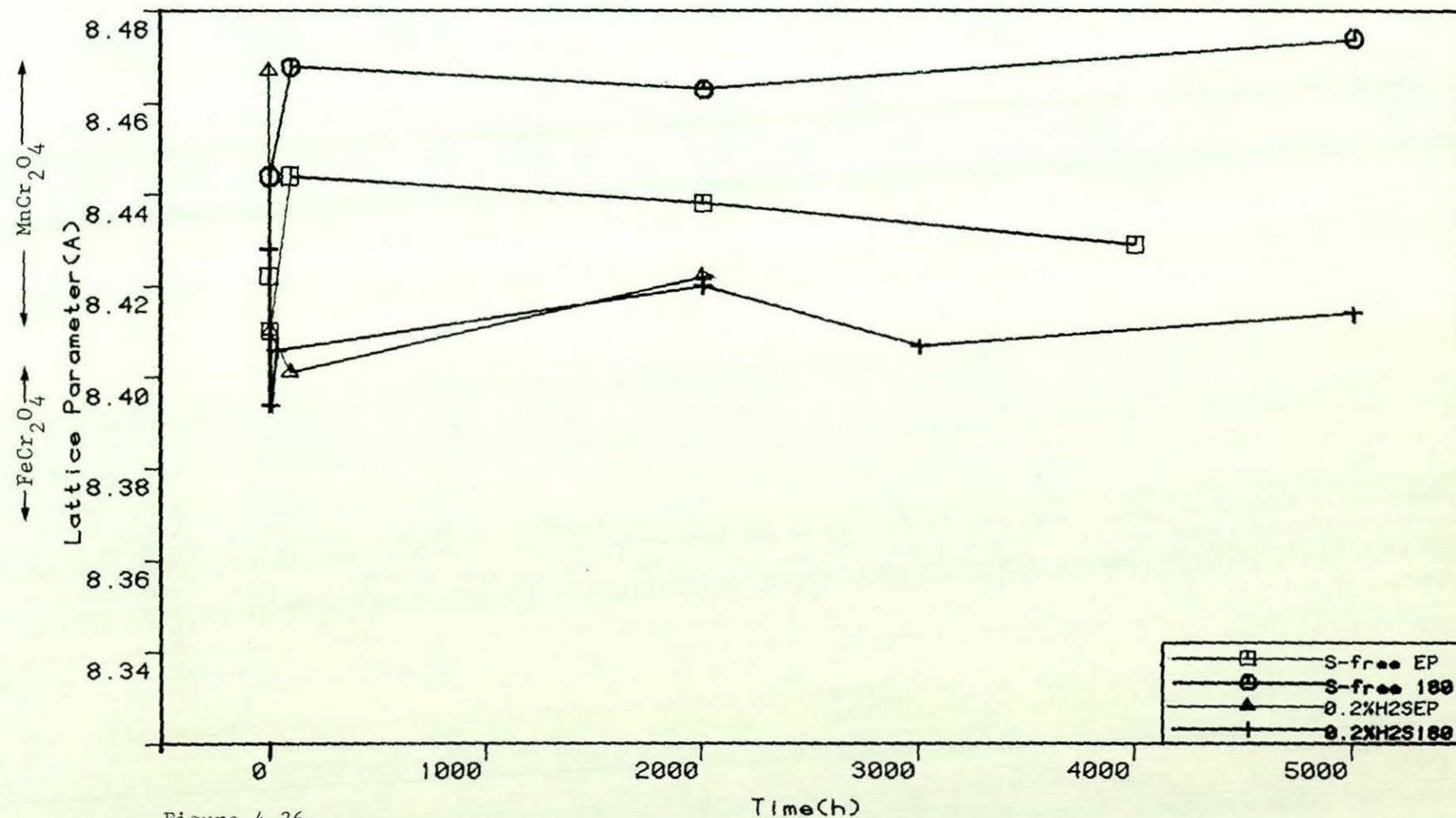


Figure 4.36

Plots of oxide spinel lattice parameter against time for the scale formed on HP40Nb exposed to the sulphur-free and 0.2% H₂S gases at 800°C.

HP40Nb, Cr2O3 Lattice Parameters

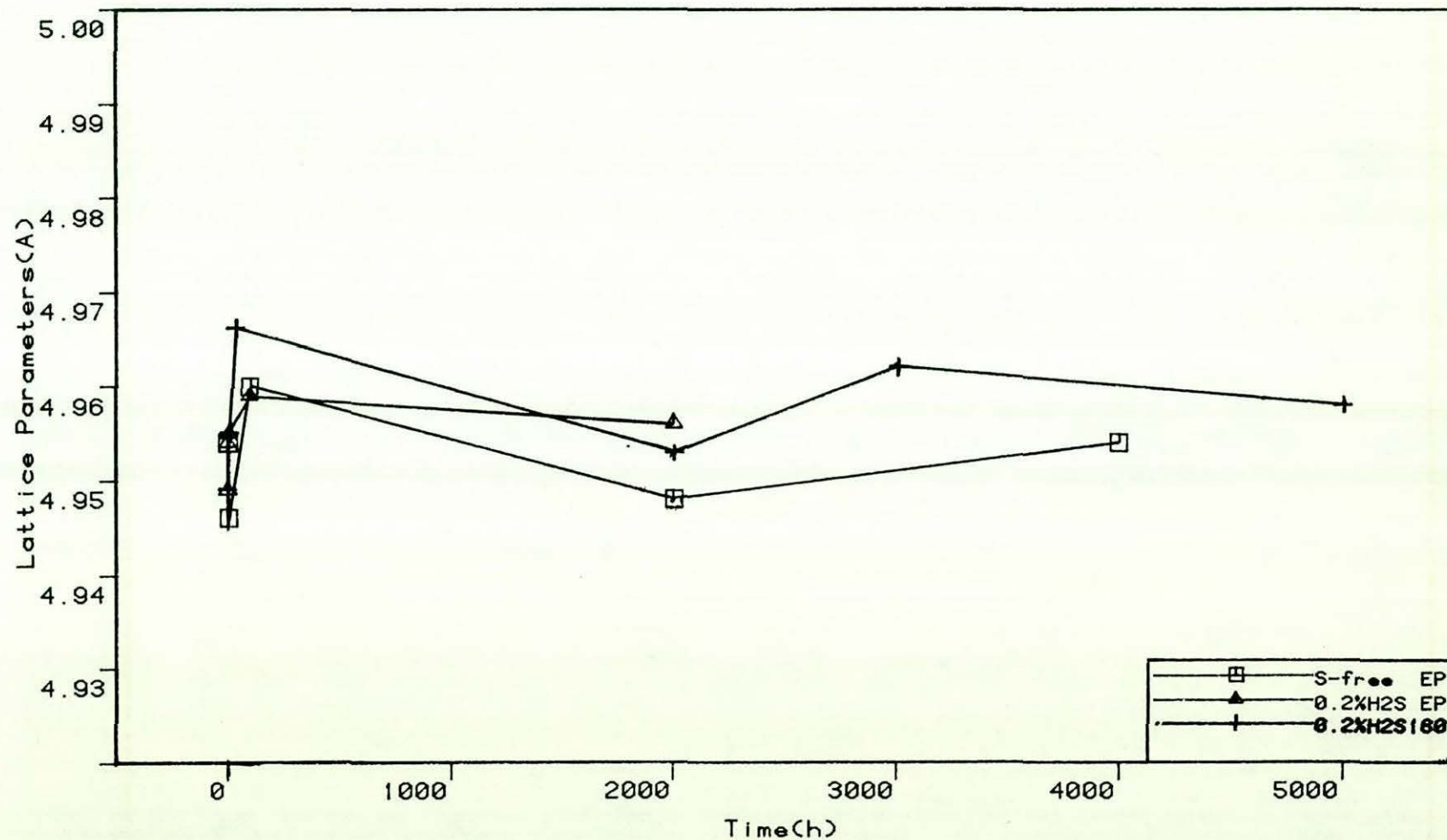


Figure 4.37

Plots of Cr₂O₃ lattice parameter against time for the scale formed on the HP40Nb alloy exposed to the sulphur-free and 0.2% H₂S gases at 800°C.

HP40Nb, S-free environment, 800 deg.C

electropolished

180 grit

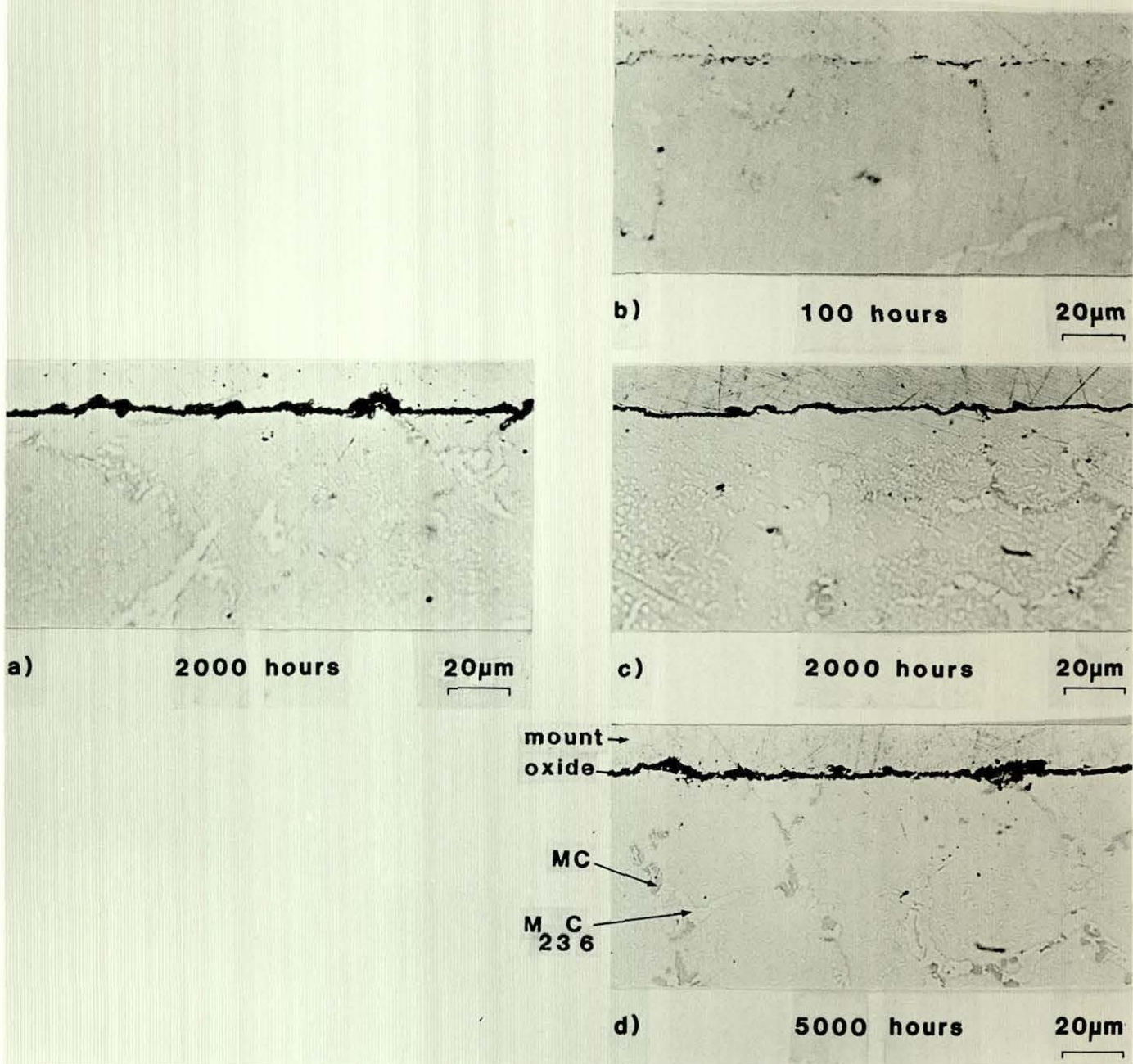


Figure 4.38

Cross-sectional metallographic examination of the HP40Nb alloy exposed to the sulphur-free gas at 800°C.

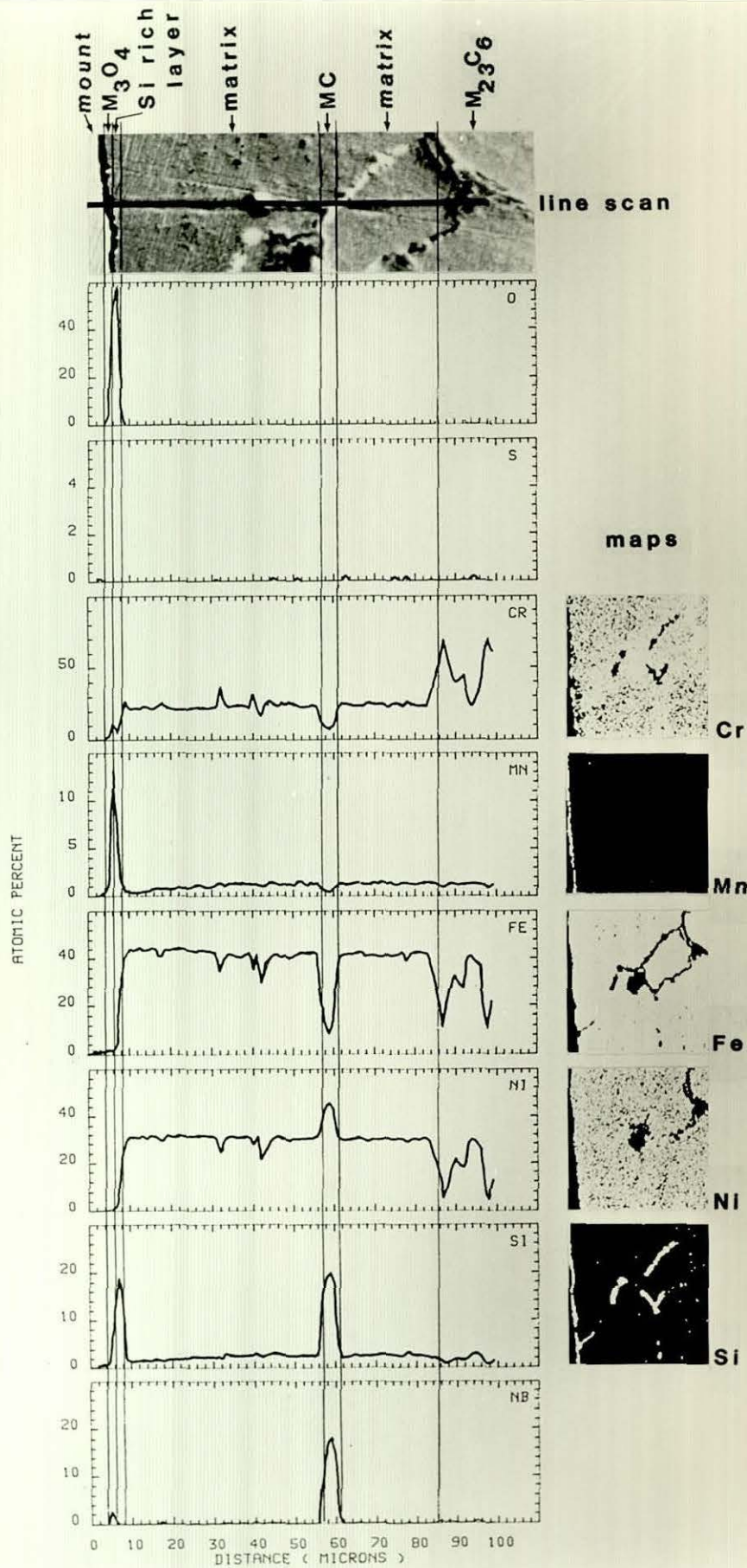
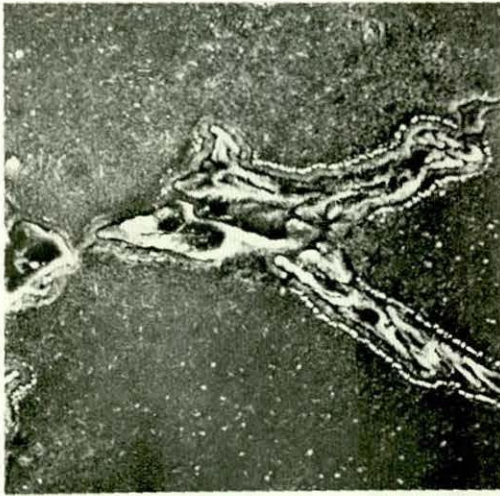


Figure 4.39

EPMA line scan and elemental concentration maps on the HP40Nb alloy exposed for 5000 hours in the S-free gas at 800°C (surface worked '180 grit' condition).



a) 5mins 10um

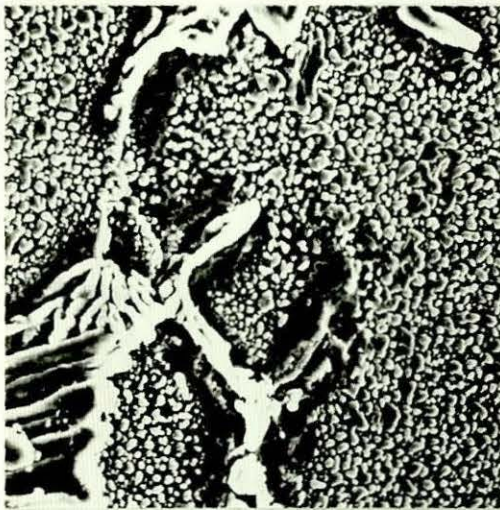
Surface SEM

HP40Nb

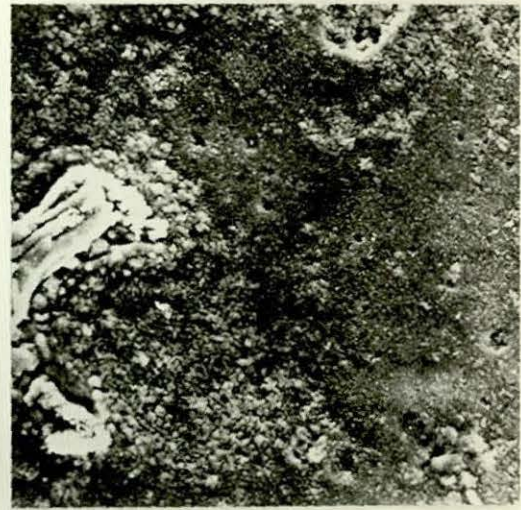
S-free environment

800 deg.C

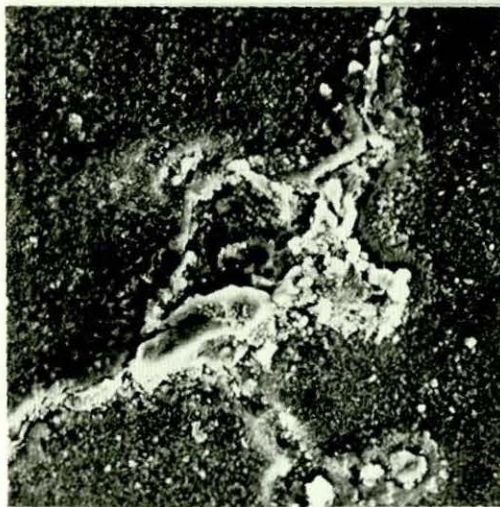
Electropolished



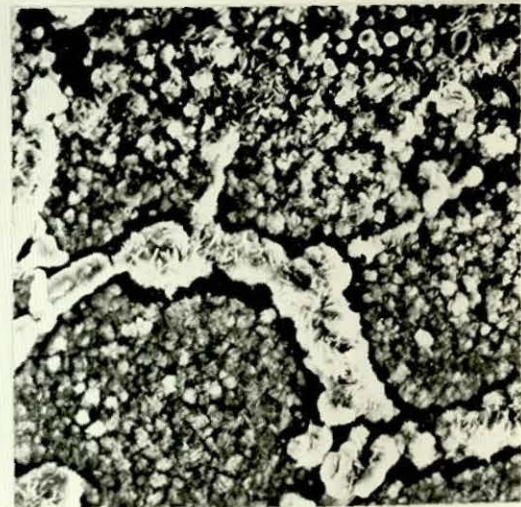
b) 0.5hour 10um



d) 100hours 10um



c) 5hours 10um



e) 2000hours 10um

Figure 4.40

Surface SEM examination of the HP40Nb alloy exposed to the sulphur-free gas at 800°C (electropolished condition).

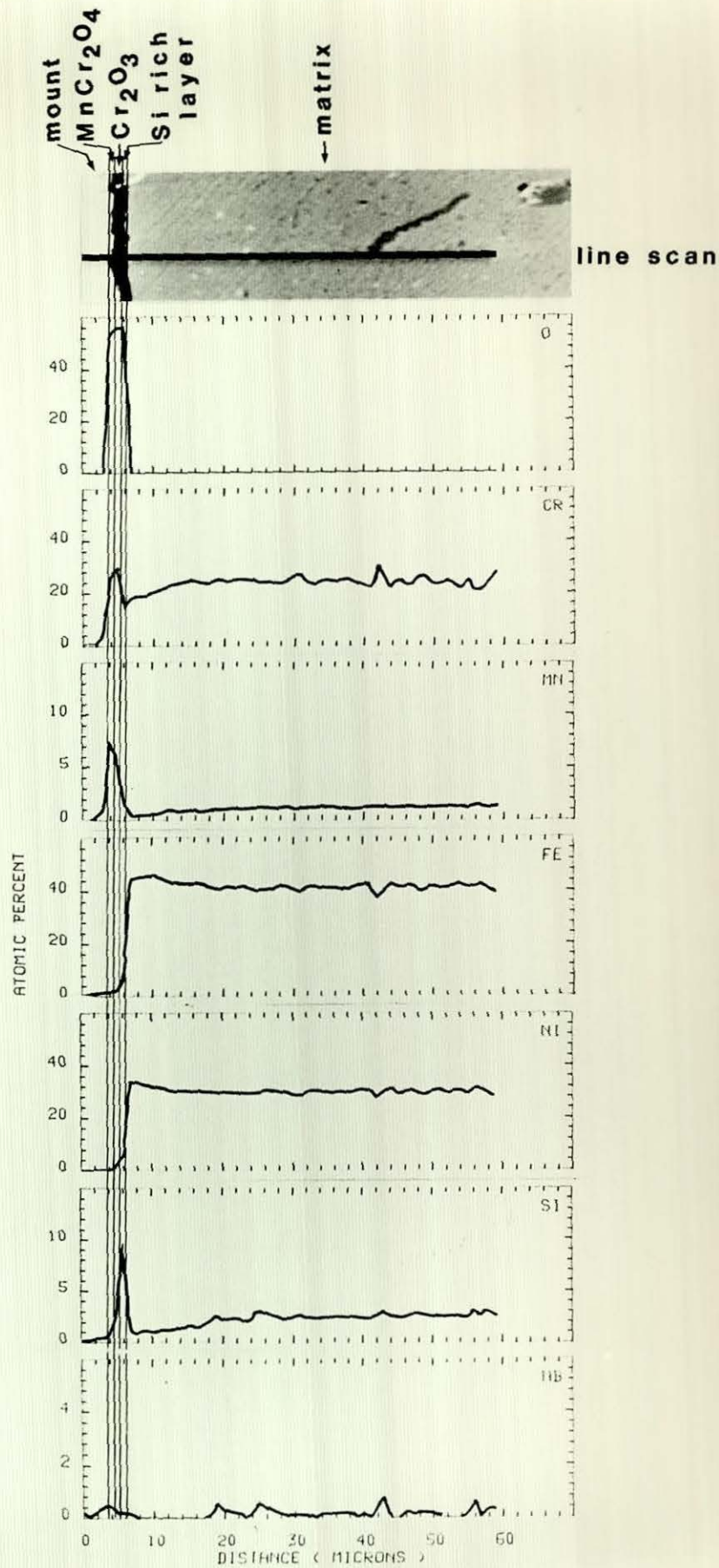


Figure 4.41

EPMA line scan through a normal section of the scale formed on the HP40Nb alloy exposed for 2000 hours in the sulphur-free gas at 800°C. (electropolished condition).

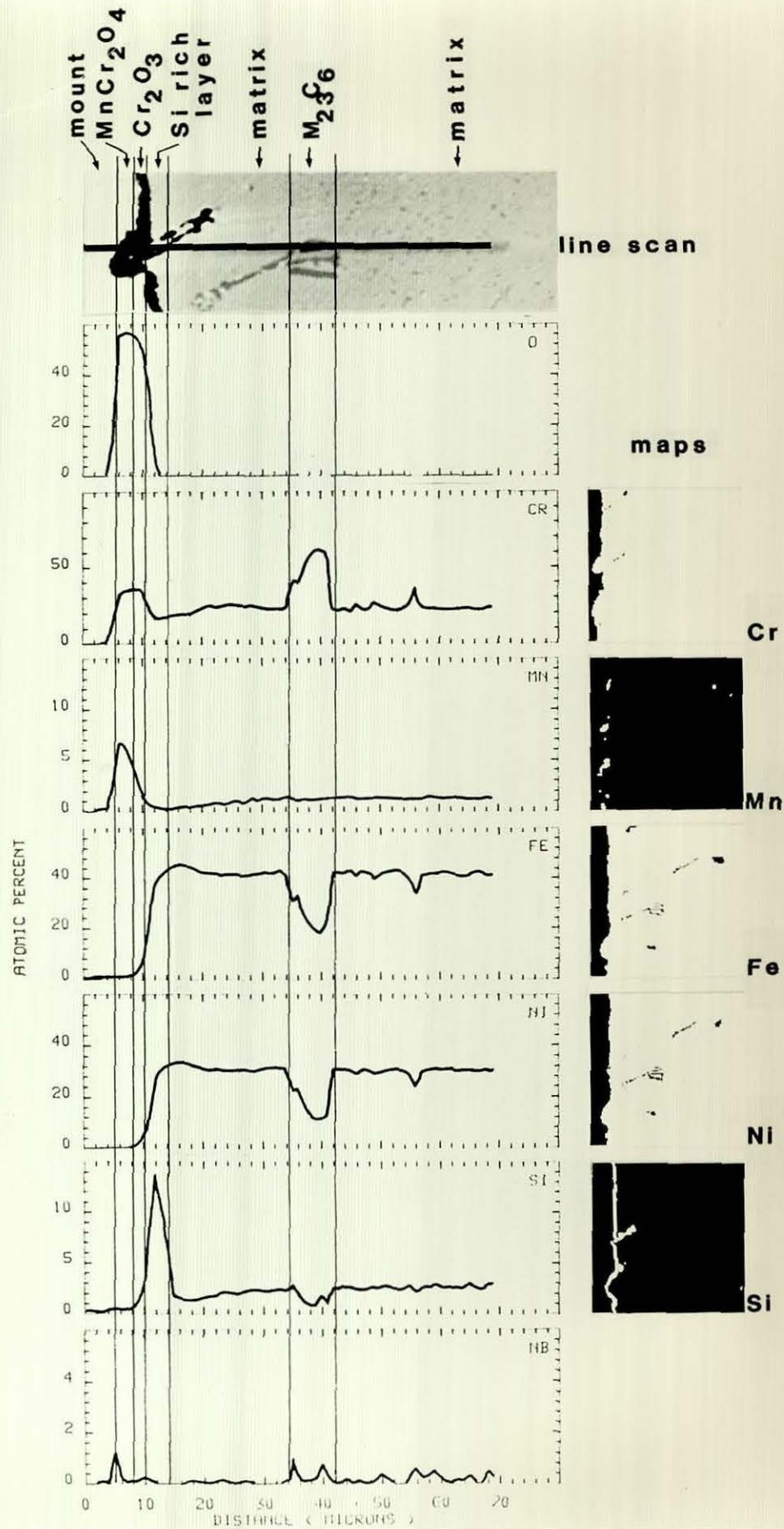


Figure 4.42

EPMA line scan and elemental concentration maps for a locally thickened area of scale formed on the HP40Nb alloy exposed for 2000 hours in the sulphur-free gas at 800°C (electropolished condition).

HP40Nb, $P_{O_2}=10^{-21}$ bar, $a_C=0.3$, 800degC

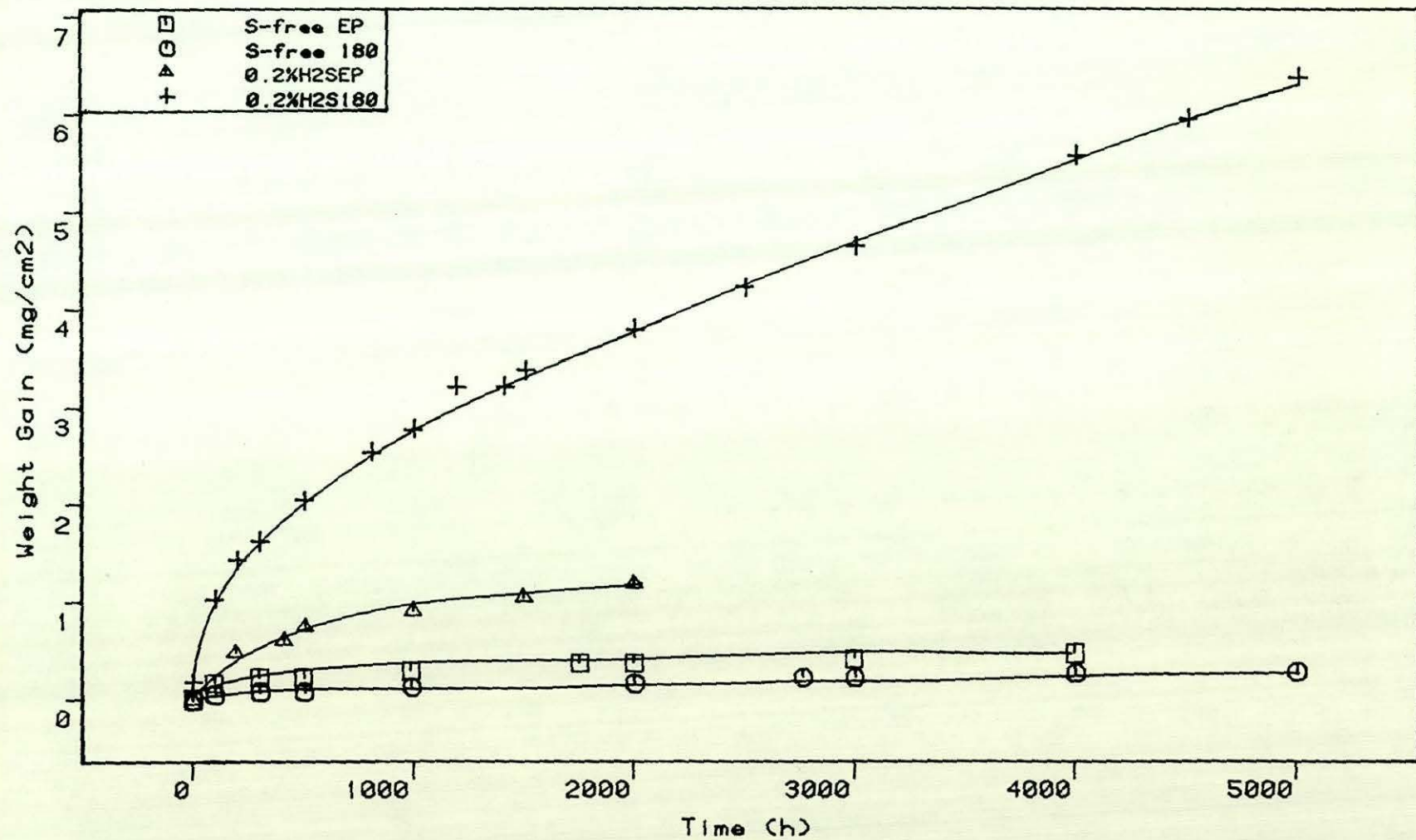


Figure 4.43

Kinetic data for the HP40Nb alloy exposed to the 0.2 % H_2S gas at 800°C.

0.2% H₂S, 800degC

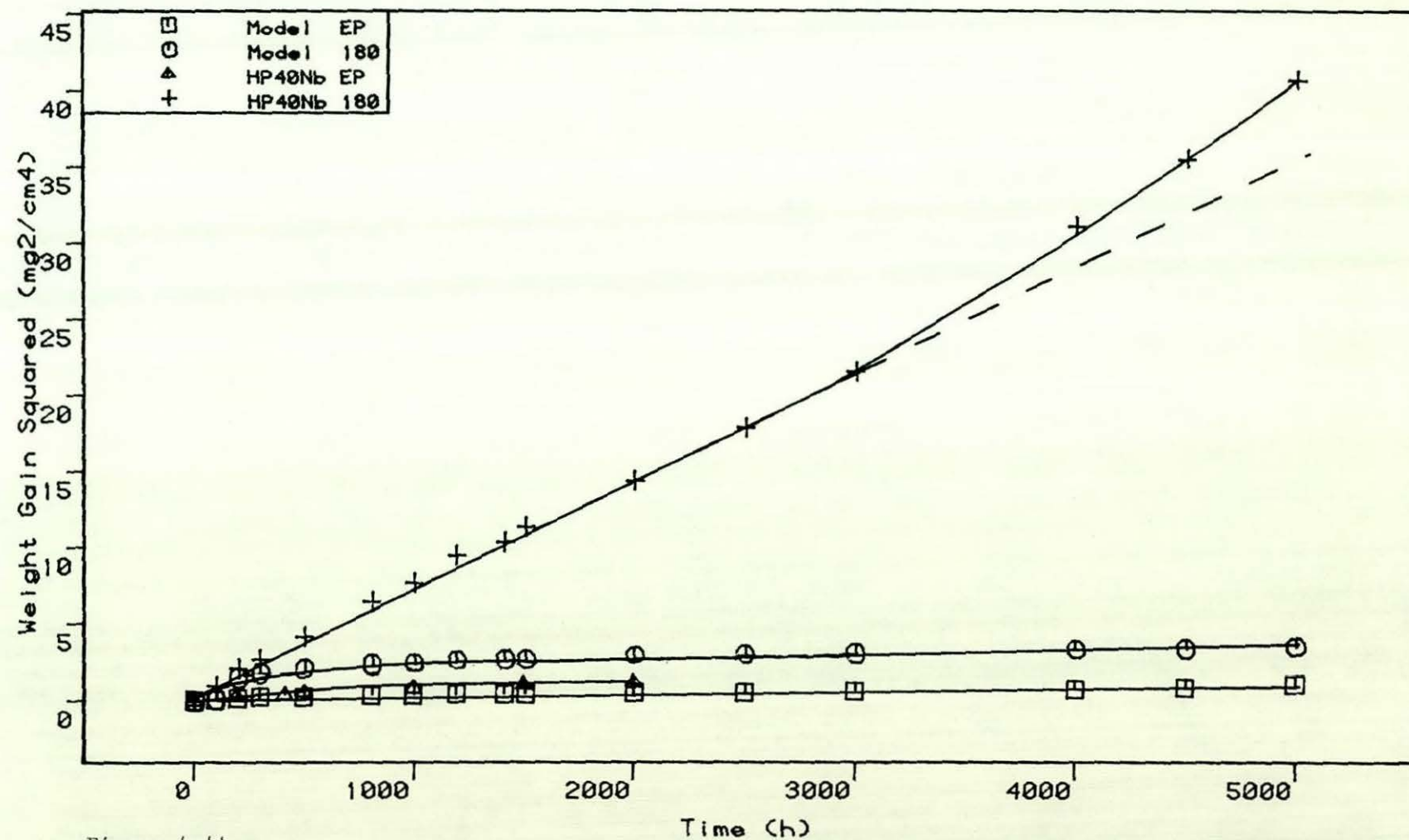


Figure 4.44

Plots of weight gain squared against time, which compare the corrosion behaviour of the Model 25Cr-35Ni-Fe alloy and HP40Nb in the 0.2% H₂S gas at 800°C.

HP40Nb , 0.2% H_2S , 800 deg.C

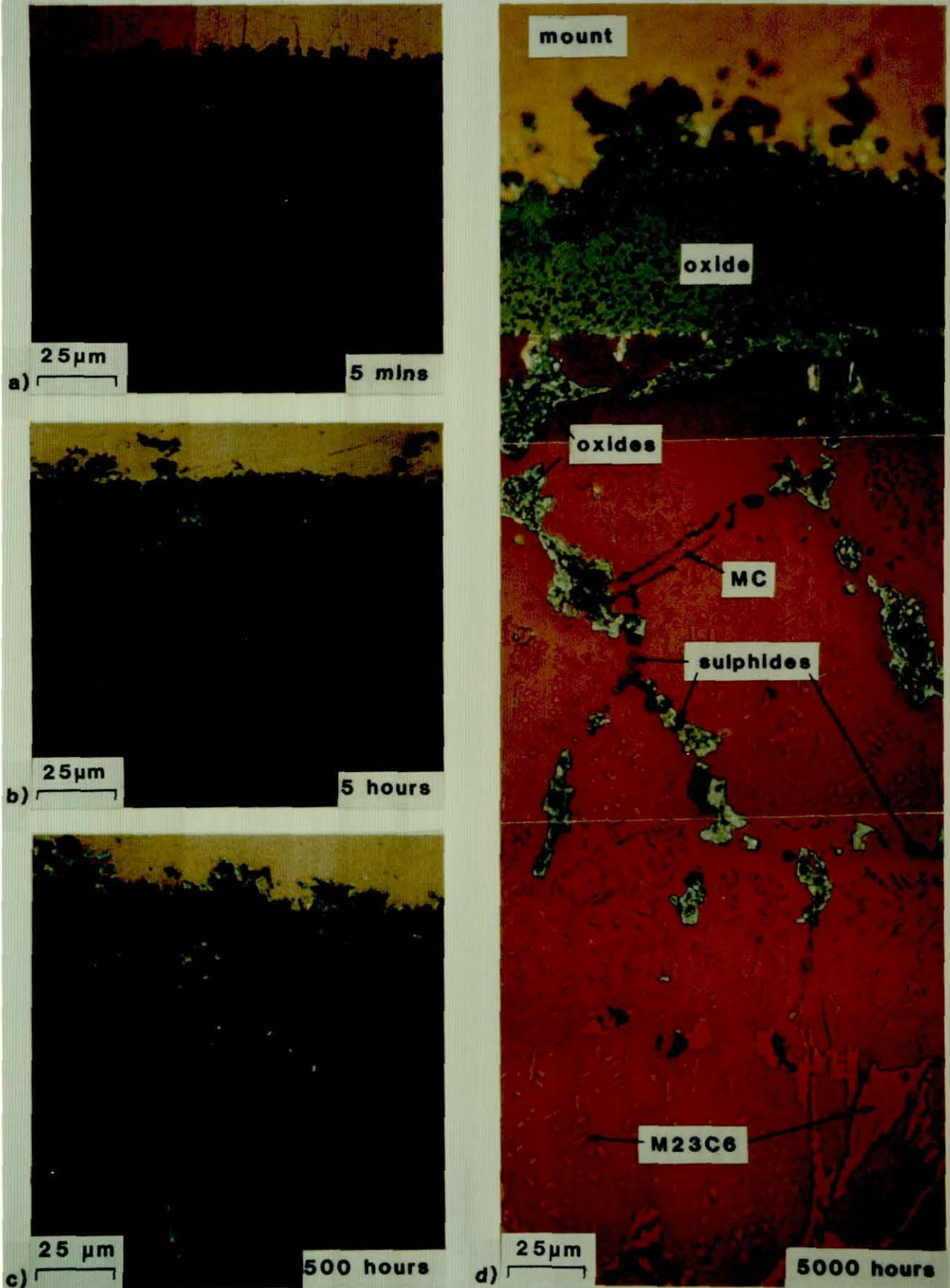
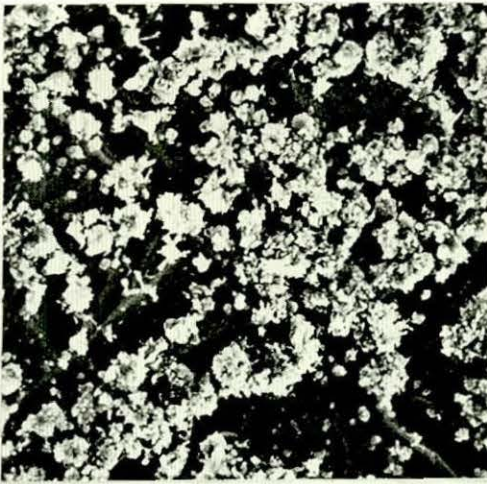
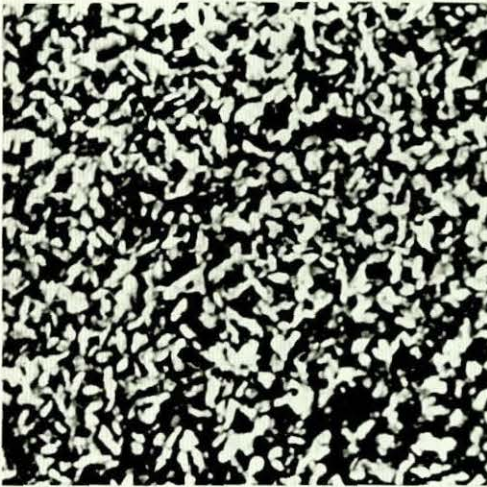


Figure 4.45

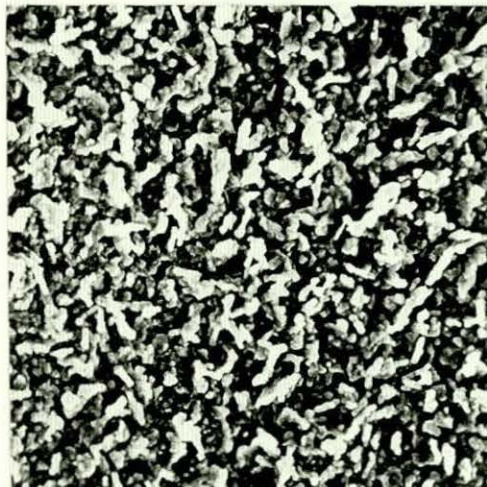
Cross-sectional metallographic examination using the Pepperhoff technique for the HP40Nb alloy exposed to the 0.2 % H_2S environment at 800°C (surface-worked '180 grit' condition).



a) 5mins 10μm



b) 1 hour 10μm



c) 32 hours 10μm

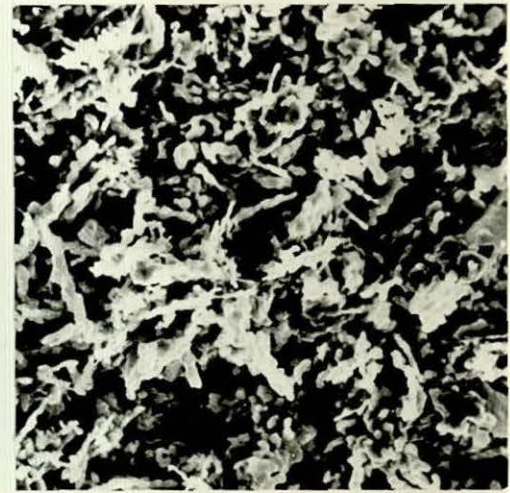
Surface SEM

HP40Nb

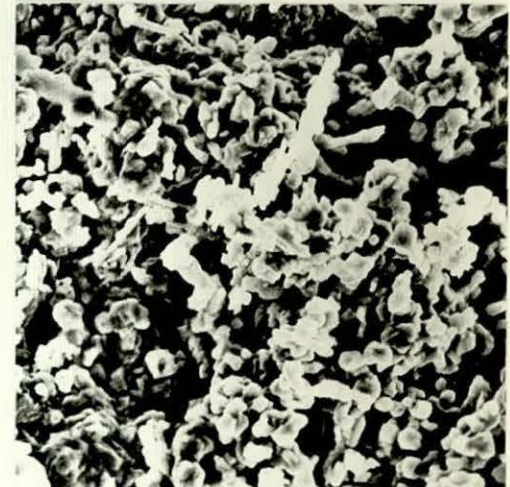
0.2% H_2S environment

800 deg.C

180 grit



d) 1000hours 10μm



e) 5000hours 10μm

Figure 4.46

Surface SEM examination of the scale formed on the HP40Nb alloy exposed to the 0.2 % H_2S environment at 800°C (surface worked '180 grit' condition).

HP40Nb 180 , 0.2% H₂S , 800 deg.C

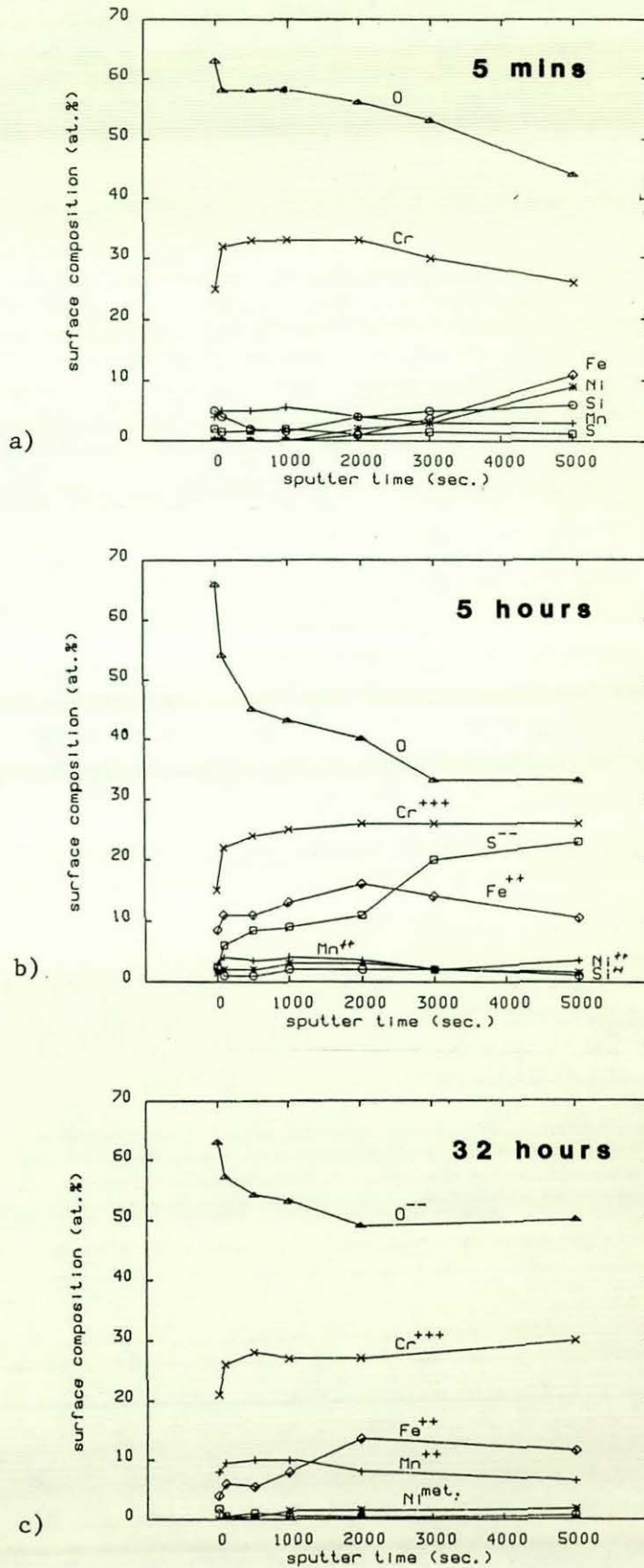


Figure 4.47

ESCA-AUGER analysis of the scale formed on the HP40Nb alloy exposed to the 0.2 % H₂S gas at 800°C (surface worked '180 grit' condition).

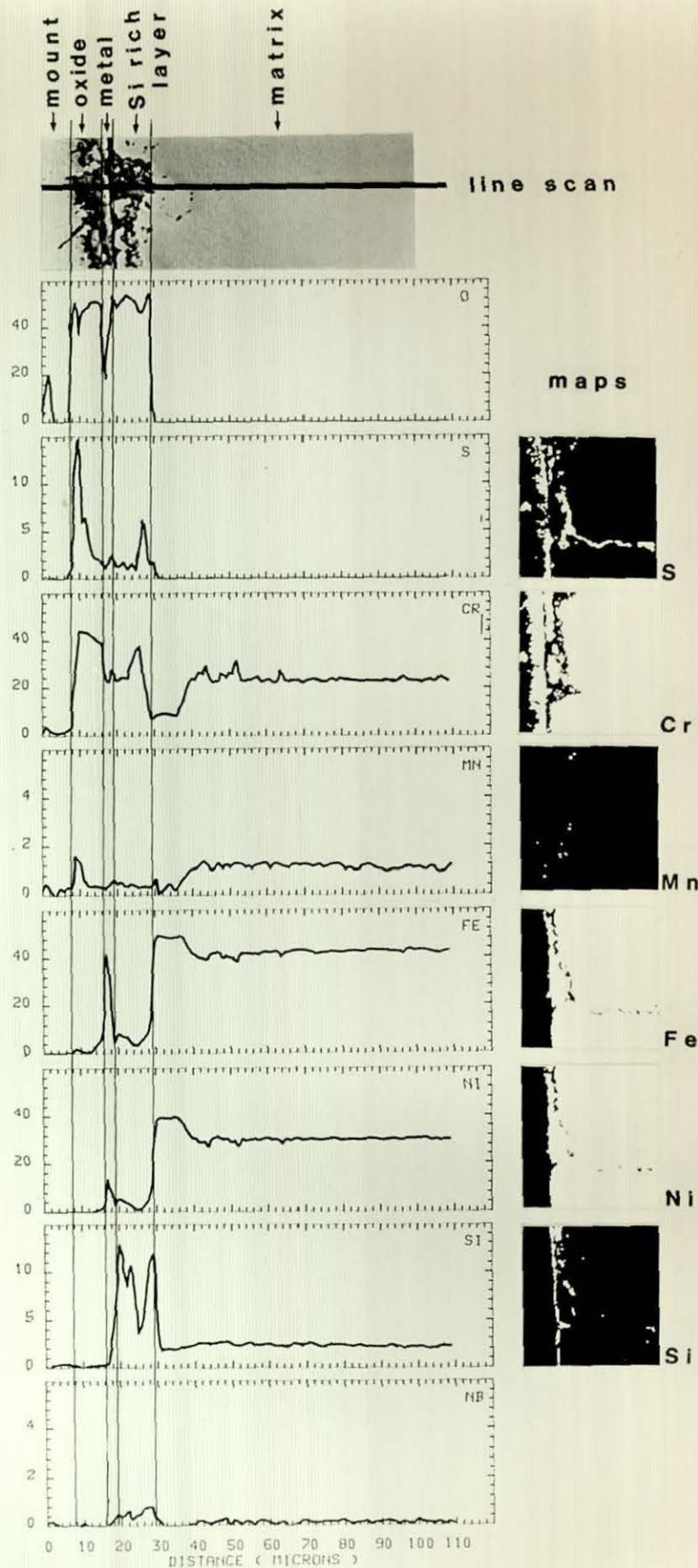


Figure 4.48

EPMA line scan and elemental concentration maps for the HP40Nb alloy exposed to the 0.2 % H_2S gas at 800°C for 100 hours (surface worked '180 grit' condition).

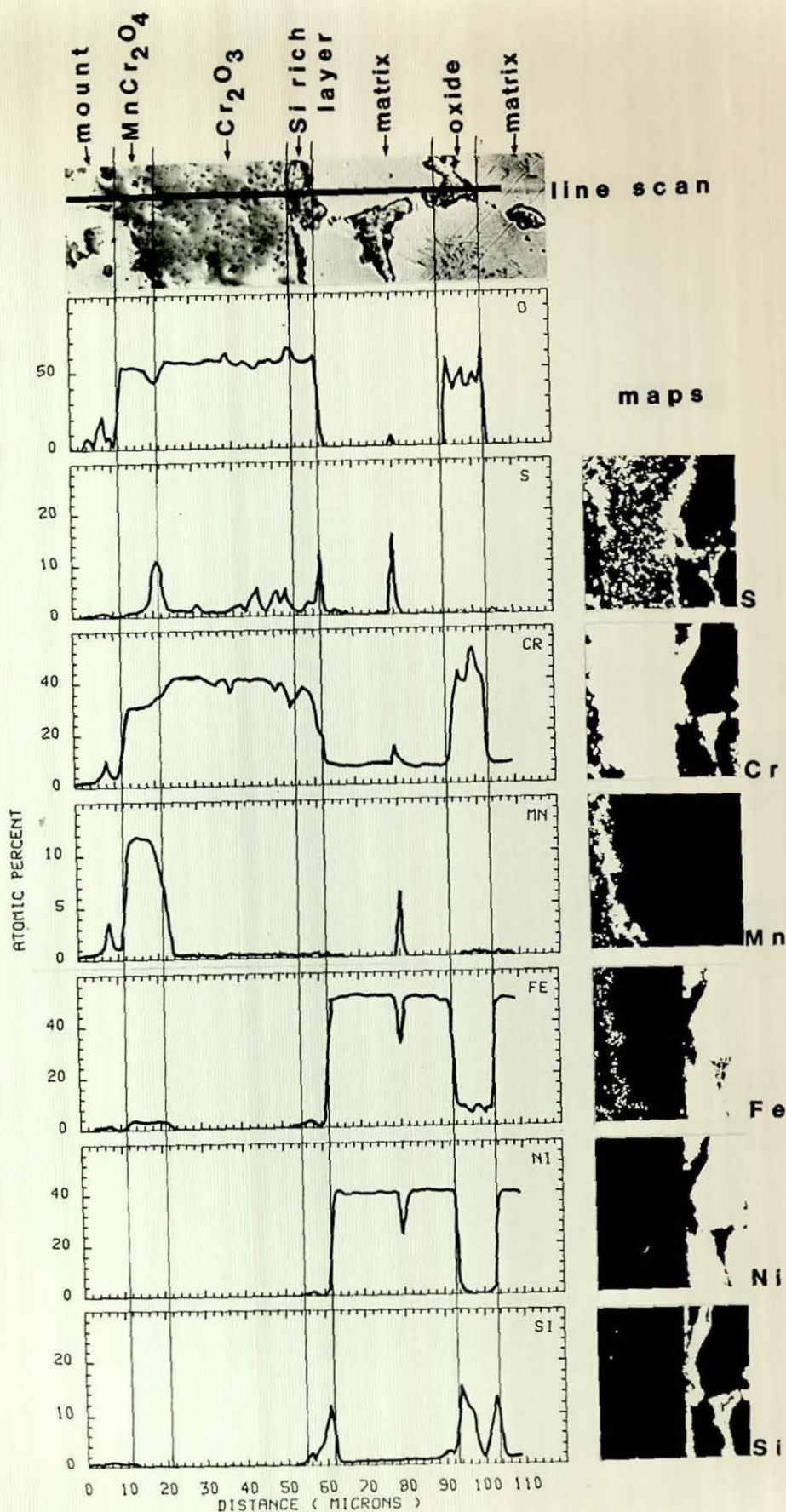


Figure 4.49

EPMA line scan and elemental concentration maps for the HP40Nb alloy exposed to the 0.2 % H₂S gas at 800°C for 5000 hours (surface worked '180 grit' condition).

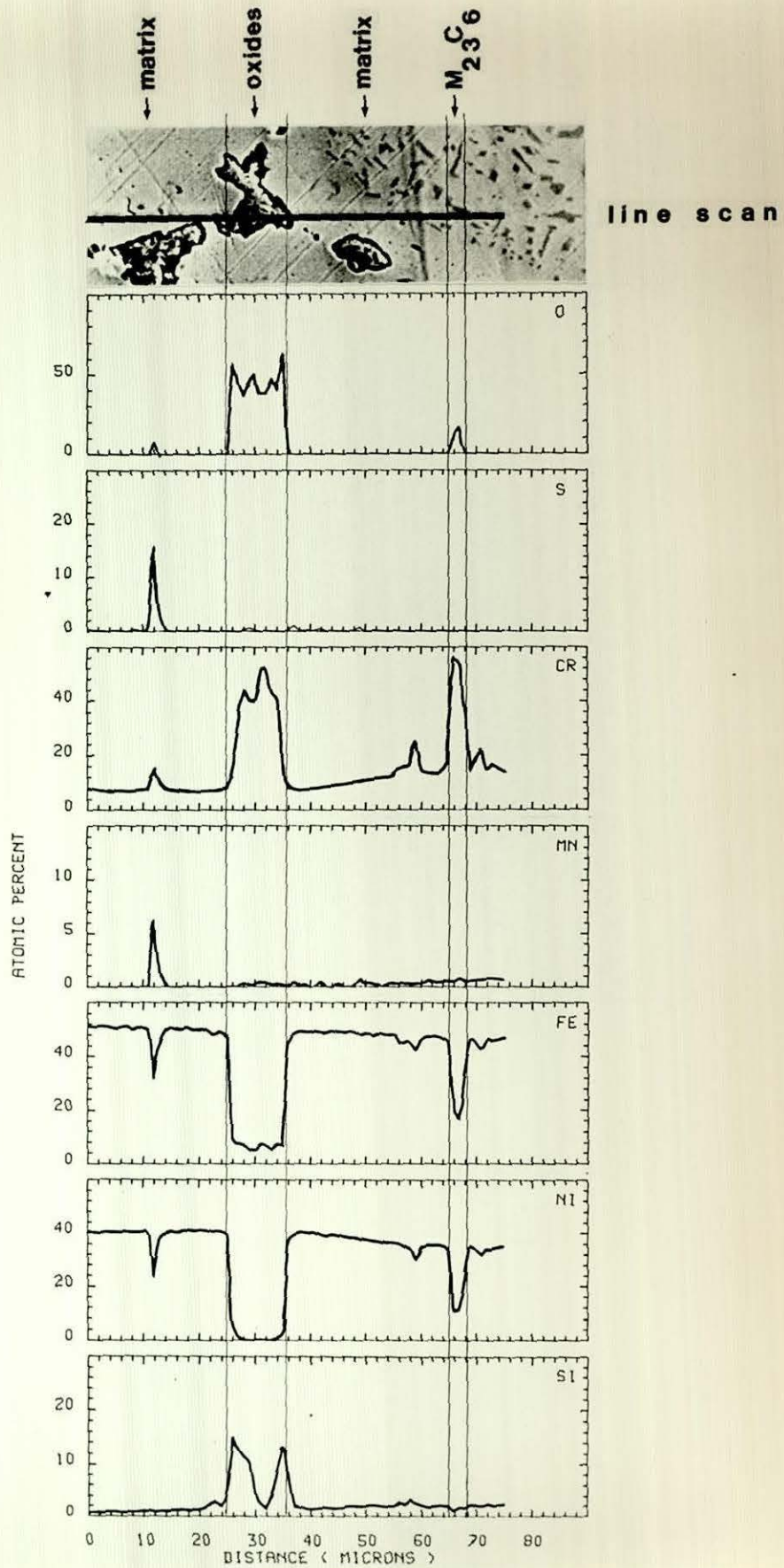


Figure 4.50
Continuation of the line scan shown in figure 4.49.

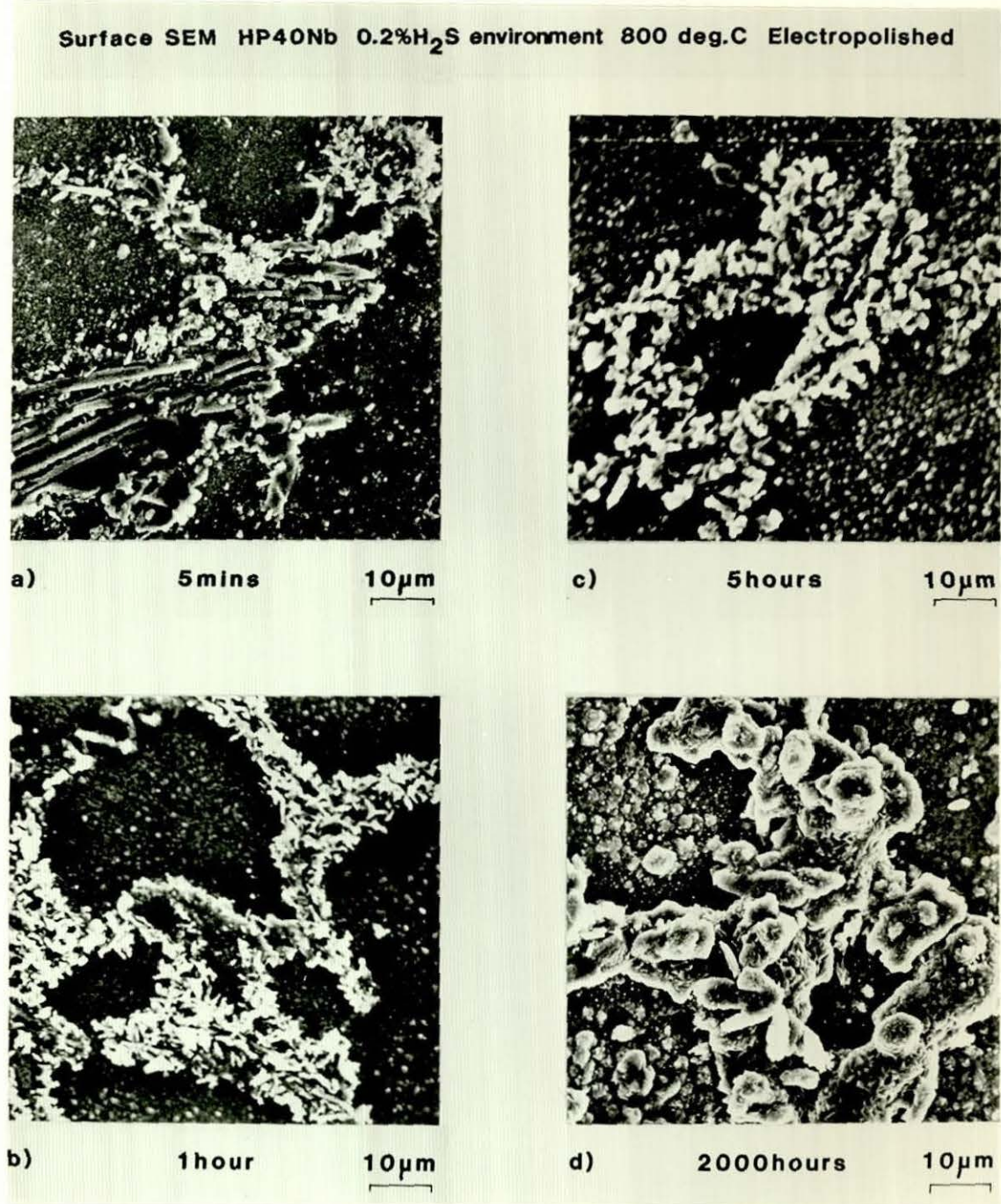


Figure 4.51

Surface SEM examination of the scale formed on the HP40Nb alloy exposed to the 0.2 % H_2S environment at 800°C (electropolished condition).

HP40Nb EP , 0.2% H_2S , 800 deg.C

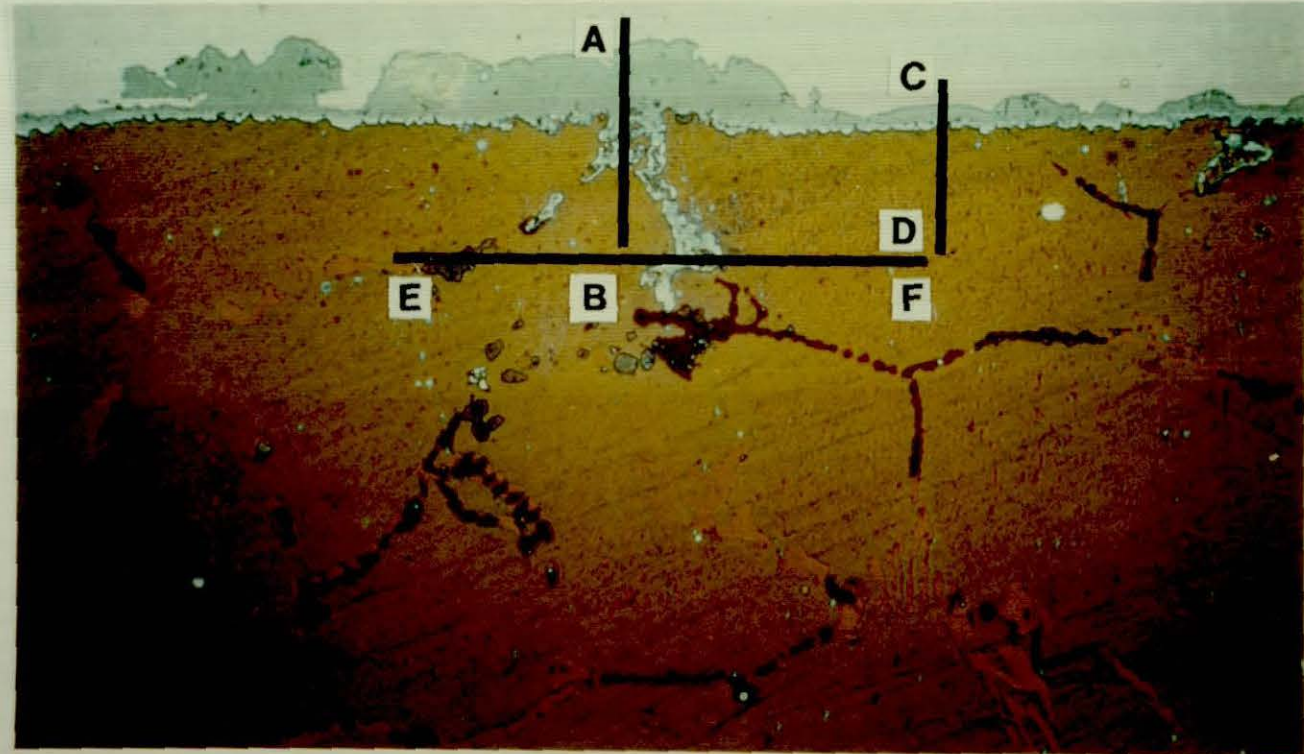


Figure 4.52

Cross-sectional examination using the Pepperhoff technique for the HP40Nb alloy exposed to the 0.2 % H_2S environment for 2000 hours at 800°C (electropolished condition).

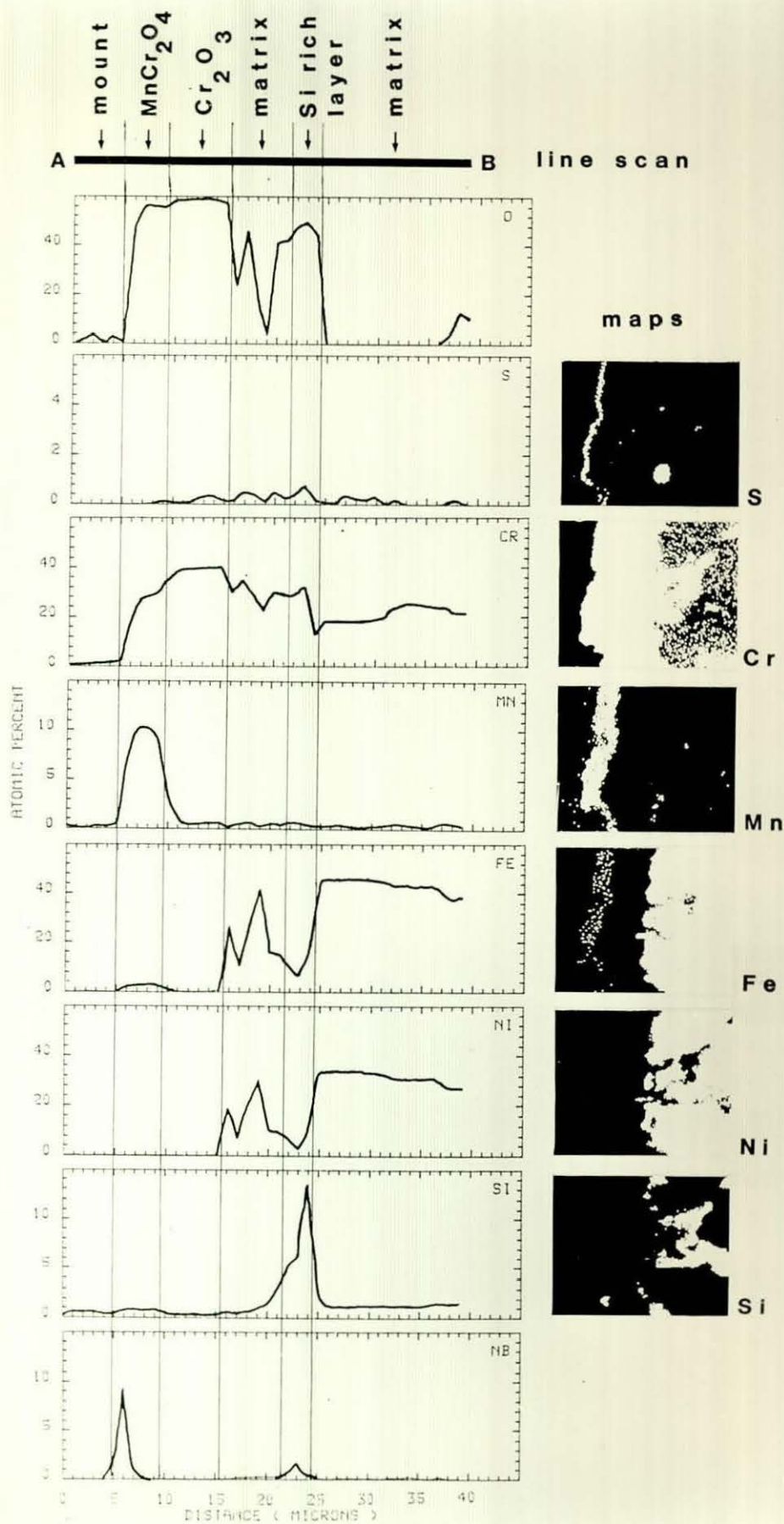


Figure 4.53

EPMA line scan corresponding to line AB on figure 4.52.

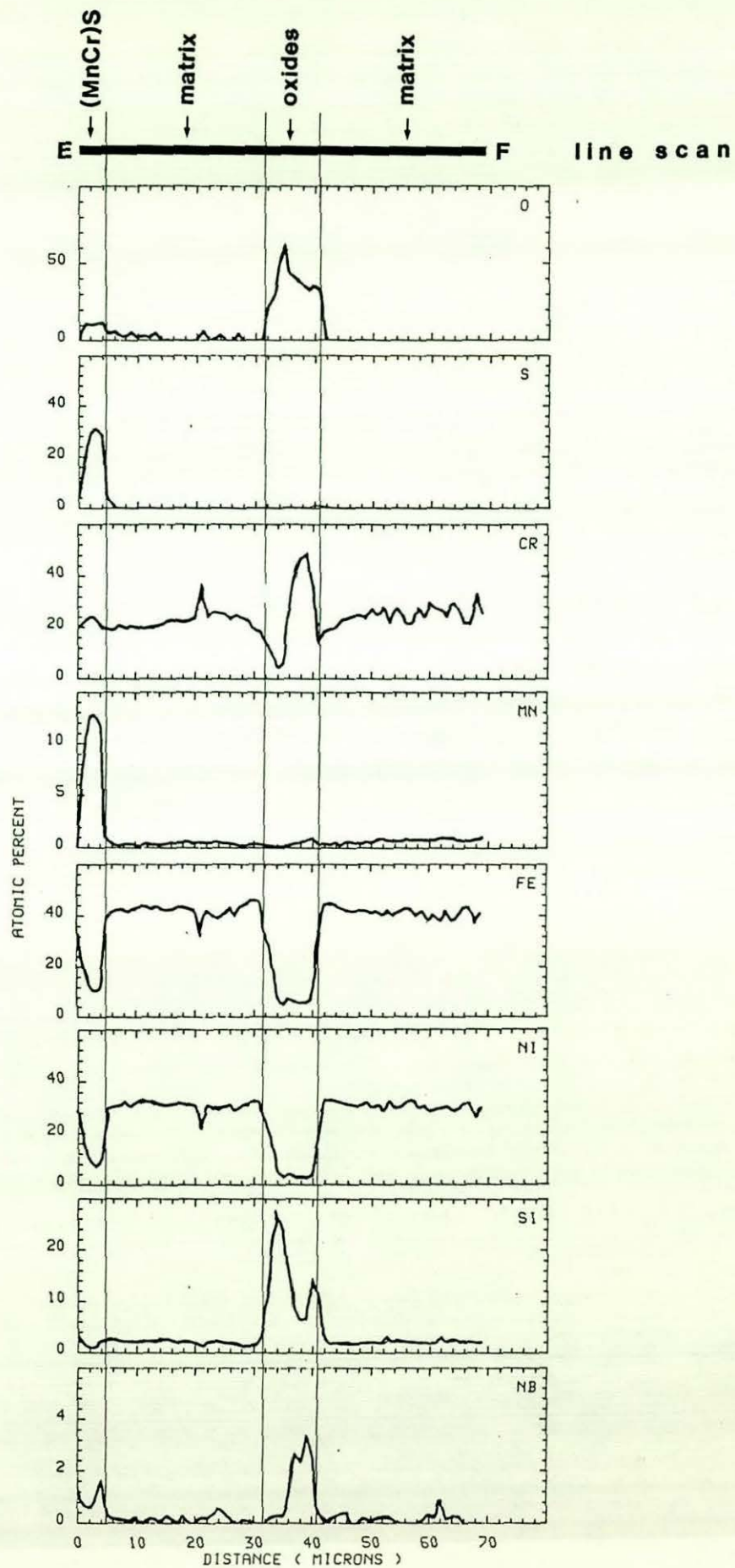


Figure 4.54
EPMA line scan corresponding to line EF on figure 4.52.

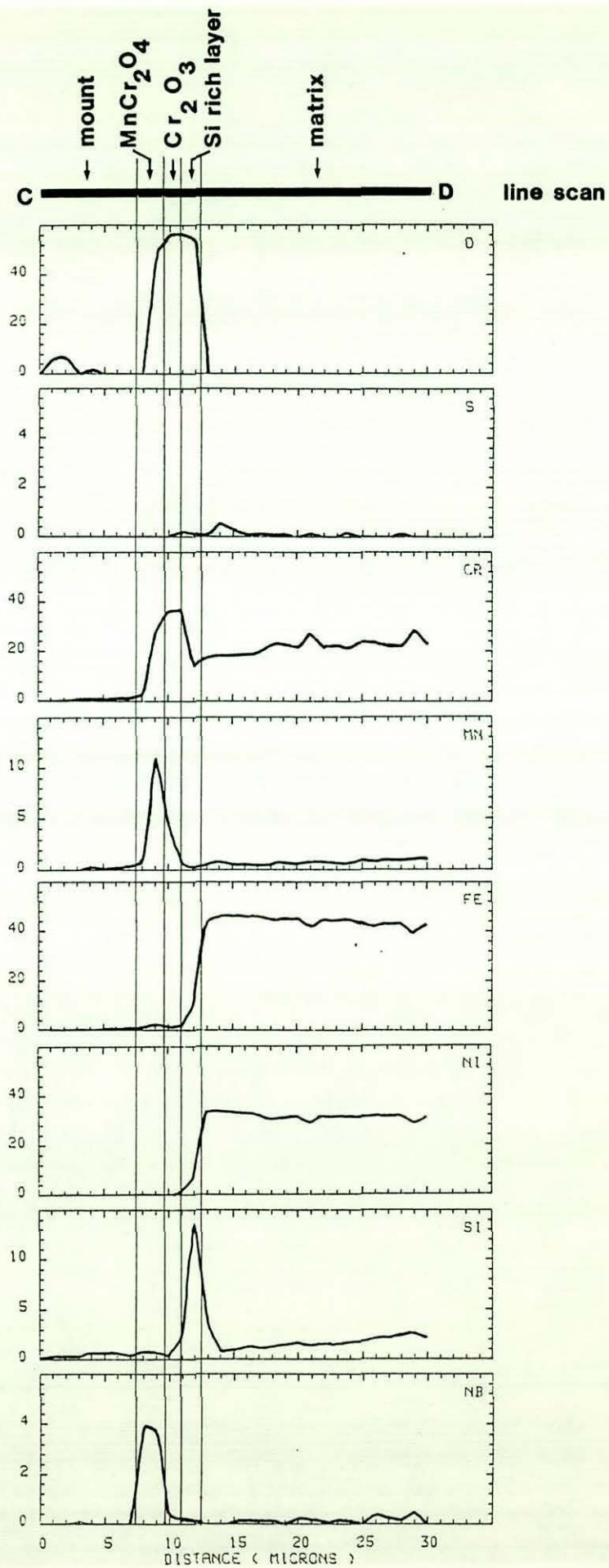


Figure 4.55

EPMA line scan corresponding to line CD on figure 4.52.

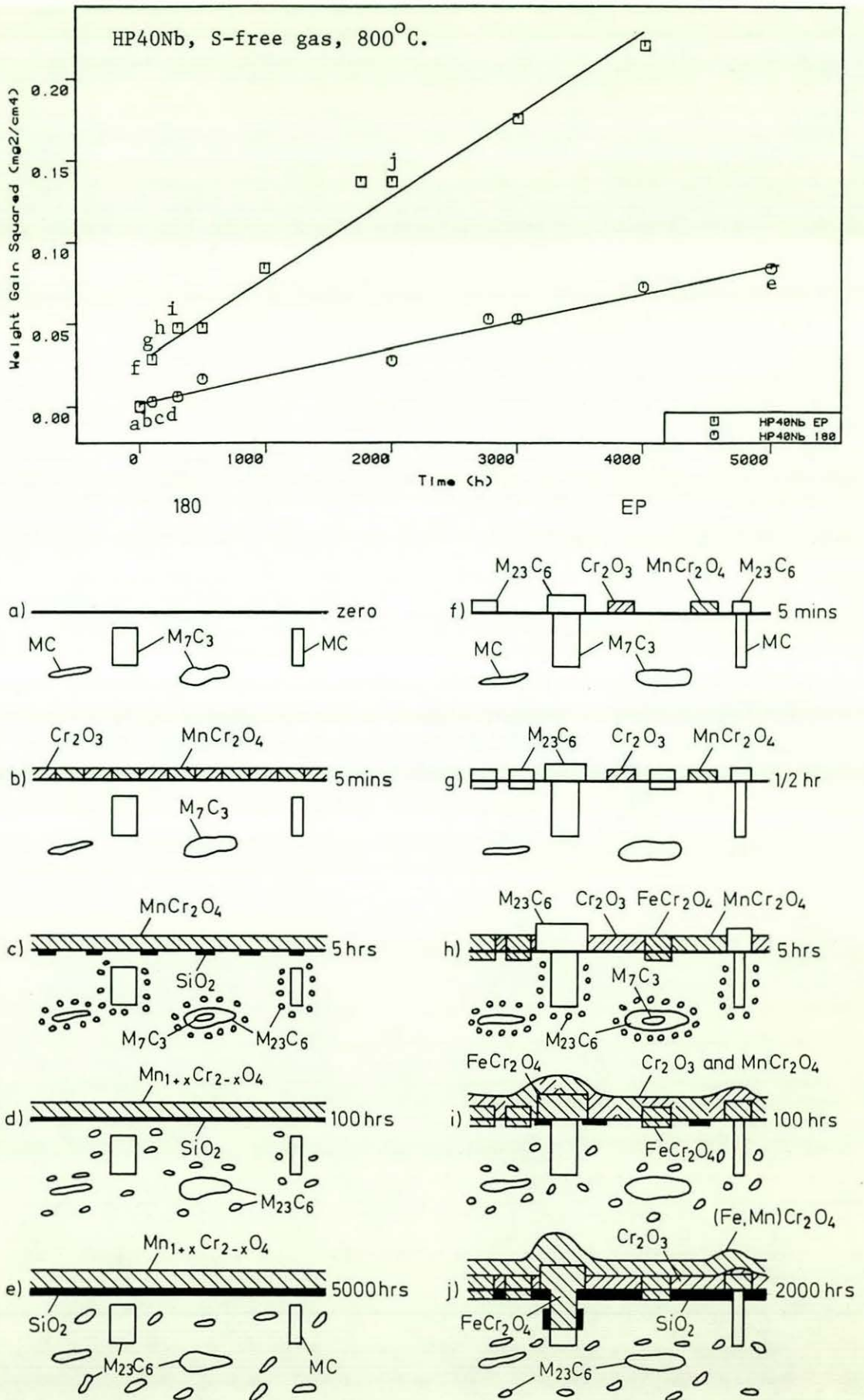


Figure 4.56

Schematic diagram summarising the corrosion process of HP40Nb in the sulphur-free gas at 800°C.

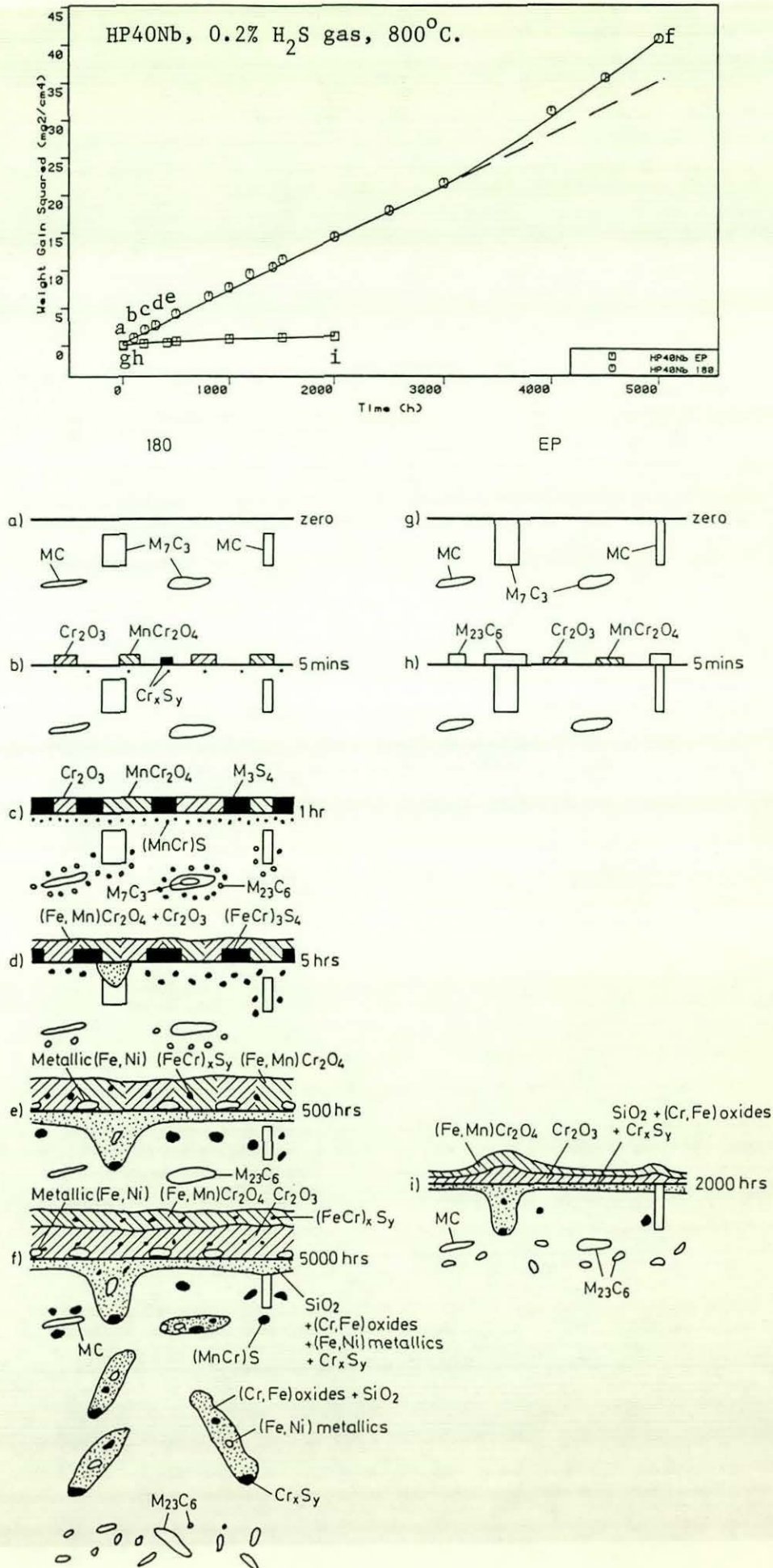


Figure 4.57

Schematic diagram summarising the corrosion process of HP40Nb in the 0.2 % H₂S gas at 800°C.

